

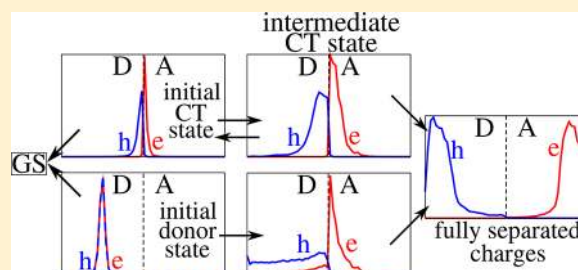
# Combination of Charge Delocalization and Disorder Enables Efficient Charge Separation at Photoexcited Organic Bilayers

Veljko Janković<sup>1</sup> and Nenad Vukmirović\*<sup>1</sup>

Scientific Computing Laboratory, Center for the Study of Complex Systems, Institute of Physics Belgrade, University of Belgrade, Pregrevica 118, Belgrade 11080, Serbia

## Supporting Information

**ABSTRACT:** We study incoherent charge separation in a lattice model of an all-organic bilayer. Charge delocalization is taken into account by working in the basis of electron–hole pair eigenstates, and the separation is described as a series of incoherent hops between these states. We find that relatively weak energetic disorder, in combination with good charge delocalization, can account for efficient and weakly field- and temperature-dependent separation of the strongly bound charge transfer (CT) state. The separation efficiency is determined by the competition between the recombination from the initial CT state and the escape toward intermediate CT states, from which free-charge states can be reached with certainty. The separation of donor excitons also exhibits quite high yields, less bound excitons separating more efficiently. Overall, our results support the notion that efficient charge separation can be achieved even out of strongly bound pair states without invoking coherent effects.



## INTRODUCTION

The outstanding problem of charge carrier photogeneration at an interface between an electron-donating (donor) and an electron-accepting (acceptor) organic material has inspired coordinated and interdisciplinary research efforts in the field of organic photovoltaics (OPVs).<sup>1–4</sup> A photoexcitation of such an interface creates strongly bound donor (or acceptor) excitons that, after the diffusion to the donor/acceptor (D/A) interface, dissociate forming the charge transfer (CT) state. Although the magnitude of the Coulomb interaction between the electron and hole in the CT state is much larger than the thermal energy at room temperature, the subsequent charge separation and eventual formation of free charges that can be extracted at the electrodes is very efficient.<sup>5,6</sup>

Numerous mechanisms have been invoked to understand the origins of such an efficient conversion of strongly bound excitons to free charges. One group of mechanisms (coherent mechanisms) suggests that free-charge generation occurs on an ultrafast (100 fs) time scale by virtue of the high-energy (“hot”) CT states in which electrons and holes are highly delocalized and spatially separated.<sup>7–10</sup> The charge separation competes with the subpicosecond exciton relaxation toward strongly bound and localized CT states, which are regarded as traps for further separation.<sup>7</sup> Another group of mechanisms (incoherent mechanisms) conceives charge separation as a much slower process that starts from the strongly bound (“cold”) CT states and converts them into free carriers by means of the hopping between localized states that is possibly assisted by the interfacial electric field.<sup>6,11–14</sup> The characteristic time scale for the incoherent charge separation is of the order of tens to hundreds of picoseconds.<sup>11,12</sup> However, what actually drives the

separation from “cold” CT states despite their strong binding and pronounced localization remains elusive.<sup>2</sup>

The coherent and incoherent separation mechanisms do not contradict each other, and both may be at play in an efficient OPV cell.<sup>15</sup> Indeed, from our recent theoretical studies,<sup>16,17</sup> which focus upon the ultrafast dynamics following photoexcitation of a model heterointerface, emerges that on picosecond time scales after photoexcitation the majority of charges are still bound in states of donor or CT excitons. In other words, there is some (coherent) charge separation on subpicosecond time scales, but the vast majority of charges remains in strongly bound states on picosecond time scales, which is in agreement with recent experimental results.<sup>13</sup> Therefore, examining charge separation on longer time scales is crucial to fully understand charge photogeneration in OPVs.

Recent theoretical studies have challenged the common view that the separation from the CT state requires surmounting an immense energy barrier.<sup>18–21</sup> These studies emphasize the influence of the entropy on charge separation. In this context, the entropy is related to the number of configurations in which an electron–hole pair may be arranged. It is suggested that the combined effect of entropy and disorder<sup>20</sup> or entropy and carrier delocalization<sup>21</sup> can substantially reduce (or even eliminate) the Coulomb barrier, so that the electron and hole in the CT state are not thermodynamically bound and thus might separate if there are no kinetic obstacles.

Received: April 2, 2018

Revised: April 19, 2018

Published: April 19, 2018

The charge separation from the strongly bound CT state has been extensively studied within the framework of the Onsager–Braun model<sup>22,23</sup> and its modifications.<sup>24</sup> Basically, the separation probability is determined by the competition between the electric field- and temperature-dependent dissociation of a localized electron–hole pair and its recombination to the ground state. While such a treatment has been revealed successful in reproducing experimental photodissociation yields in bulk molecular D/A crystals,<sup>25</sup> it has been recognized as unsuitable for conjugated polymer/fullerene blends.<sup>26</sup> The reasons for this inadequacy may be summarized as follows. First, the Onsager–Braun model employs the approximation of localized point charge carriers, which does not hold in a polymer/fullerene blend. In this regard, it has been proposed that the hole delocalization along conjugated segments of polymer chains can enhance charge separation<sup>27–29</sup> because the kinetic energy of hole oscillations along chains lowers the Coulomb barrier between the electron and hole. The combination of the effects due to the hole delocalization and the presence of dark interfacial dipoles<sup>30,31</sup> has been demonstrated to reproduce the essential features of experimental photocurrent data.<sup>32</sup> Furthermore, the combination of the on-chain hole delocalization and the dimensional (entropic) effects has been suggested as the main reason for weakly field-dependent and very efficient charge separation in polymer/fullerene bilayers.<sup>33</sup> Second, for the Onsager–Braun model to reproduce experimental data, the mobility-lifetime product should assume unrealistically high values, meaning that either carrier mobility or pair lifetime should be unrealistically large. Kinetic Monte Carlo (kMC) studies have demonstrated that efficient and weakly field- and temperature-dependent charge separation can be achieved when relevant parameters are carefully chosen on the basis of experimental data.<sup>34,35</sup> Third, the Onsager–Braun model does not capture the effects of the (energetic and/or spatial) disorder on charge separation. In ref 36, an analytical treatment of charge separation in a one-dimensional disordered chain is presented, and it was suggested that, at least at low interfacial electric fields, the disorder may enhance the separation of geminate electron–hole pairs. Recent kMC results also point toward the beneficial role of not too strong energetic disorder on charge separation.<sup>37</sup>

Here, we investigate the separation of geminate electron–hole pairs in a one-dimensional lattice model of a bilayer. The model takes into account energetic disorder, carrier delocalization, carrier–carrier interaction, carrier recombination, and the interaction of carriers with the phonon bath and the interfacial electric field. The carrier delocalization is properly taken into account by transferring the description of charge separation from the usually used position space to the space spanned by the exciton basis states, that is, by stationary states of an electron–hole pair on the model interface. The charge separation is then conceived as a sequence of transitions between exciton basis states that are mediated by the interaction with the phonon bath. The separation yield is computed from the stationary solution to the rate equations for basis states populations in two cases, for the separation starting from CT states and donor exciton states. We find that moderate energetic disorder and carrier delocalization promote efficient and relatively weakly field-dependent separation of the strongly bound CT exciton. In this process, the vital role is played by long-lived intermediate CT states, from which further charge separation proceeds practically without obstacles. The separation of the strongly bound donor exciton is also efficient,

but requires quite strong electric fields to occur with certainty. On the other hand, more separated and weakly bound donor excitons separate with efficiency close to 1.

## MODEL AND METHODS

**Model Hamiltonian, Exciton States, and Their Classification.** To describe the bilayer of two organic semiconductors, we employ the standard semiconductor model on a lattice with multiple single-electron and single-hole states per site. The model to be presented is quite general and may also be used (upon appropriate adjustments) to study the electric field-assisted charge generation in other D/A structures. The numerical computations are performed on a one-dimensional system consisting of  $2N$  sites located on a lattice of constant  $a$ . The sites  $0, \dots, N - 1$  represent the donor part, while sites  $N, \dots, 2N - 1$  represent the acceptor part of the bilayer. The single-electron levels on lattice site  $i$  are counted by index  $\beta_i$ , so that Fermi operators  $c_{i\beta_i}^\dagger$  ( $c_{i\beta_i}$ ) create (destroy) an electron on site  $i$  and in single-electron state  $\beta_i$ . The single-hole levels on site  $i$  are counted by index  $\alpha_i$  and Fermi operators  $d_{i\alpha_i}^\dagger$  ( $d_{i\alpha_i}$ ) create (annihilate) a hole in single-hole state  $\alpha_i$  on site  $i$ . The phonon bath is assumed to consist of a multitude of localized phonon modes on each lattice site, and the sets of phonon modes on all sites are identical. The Bose operators  $b_{i\lambda}^\dagger$  ( $b_{i\lambda}$ ) create (annihilate) a phonon on site  $i$  and in phonon mode  $\lambda$ . The model Hamiltonian assumes the form:

$$H = H_c + H_p + H_{c-p} + H_{c-f} \quad (1)$$

where  $H_c$  describes interacting carriers:

$$H_c = \sum_{\substack{i\beta_i \\ j\beta_j}} \epsilon_{(i\beta_i)(j\beta_j)}^c c_{i\beta_i}^\dagger c_{j\beta_j} - \sum_{\substack{i\alpha_i \\ j\alpha_j}} \epsilon_{(i\alpha_i)(j\alpha_j)}^v d_{i\alpha_i}^\dagger d_{j\alpha_j} + \frac{1}{2} \sum_{\substack{i\beta_i \\ j\beta_j}} V_{ij} c_{i\beta_i}^\dagger c_{j\beta_j}^\dagger c_{j\beta_j} c_{i\beta_i} + \frac{1}{2} \sum_{\substack{i\alpha_i \\ j\alpha_j}} V_{ij} d_{i\alpha_i}^\dagger d_{j\alpha_j}^\dagger d_{j\alpha_j} d_{i\alpha_i} - \sum_{\substack{i\beta_i \\ j\alpha_j}} V_{ij} c_{i\beta_i}^\dagger d_{j\alpha_j}^\dagger d_{j\alpha_j} c_{i\beta_i} \quad (2)$$

$$H_p = \sum_{i\lambda} \hbar \omega_\lambda b_{i\lambda}^\dagger b_{i\lambda} \quad (3)$$

describes the phonon bath,  $H_{c-p}$  accounts for the interaction of carriers with the phonon bath:

$$H_{c-p} = \sum_{i\beta_i} \sum_{\lambda} g_{i\beta_i\lambda}^c c_{i\beta_i}^\dagger c_{i\beta_i} (b_{i\lambda}^\dagger + b_{i\lambda}) - \sum_{i\alpha_i} \sum_{\lambda} g_{i\alpha_i\lambda}^v d_{i\alpha_i}^\dagger d_{i\alpha_i} (b_{i\lambda}^\dagger + b_{i\lambda}) \quad (4)$$

whereas  $H_{c-f}$  represents the interaction of carriers with the interfacial electric field  $\mathbf{F}$ , which is assumed to be uniform throughout the system:

$$H_{c-f} = \sum_{i\beta_i} q\mathbf{F} \cdot \mathbf{r}_i c_{i\beta_i}^\dagger c_{i\beta_i} - \sum_{i\alpha_i} q\mathbf{F} \cdot \mathbf{r}_i d_{i\alpha_i}^\dagger d_{i\alpha_i} \quad (5)$$

In eq 2, we take that quantities  $\epsilon_{(i\beta_i)(j\beta_j)}^c$  ( $\epsilon_{(i\alpha_i)(j\alpha_j)}^v$ ), which represent electron (hole) on-site energies and transfer integrals, assume nonzero values only for particular combinations of their

indices. In more detail, we assume that  $\varepsilon_{(i\beta)(j\beta')}^c \neq 0$  when it represents

- (1) on-site energy  $\varepsilon_{i\beta_i}^c$  of single-electron level  $\beta_i$  on site  $i$ , for  $i = j$  and  $\beta_i = \beta'_i$ ;
- (2) negative electron transfer integral between single-electron levels on nearest-neighboring sites belonging to the same band  $\beta_i$ ,  $-J_{i\beta_i}^{c,int}$ , for  $i$  and  $j$  both belonging to the same part of the bilayer,  $|i - j| = 1$ , and  $\beta_i = \beta'_j$ ;
- (3) negative electron transfer integral between single-electron levels on nearest-neighboring sites belonging to different bands,  $-J_{i\beta_i}^{c,ext}$ , for  $i$  and  $j$  both belonging to the same part of the bilayer,  $|i - j| = 1$ , and  $\beta_i \neq \beta'_j$ ; or
- (4) negative electron transfer integral between different parts of the bilayer,  $-J_{D,A}^c$ , for  $i = N - 1$  and  $j = N$  or vice versa.

The Coulomb interaction (eq 2) is taken into account in the lowest monopole–monopole approximation, and the interaction potential  $V_{ij}$  is assumed to be the Ohno potential:

$$V_{ij} = \frac{U}{\sqrt{1 + \left(\frac{r_{ij}}{r_0}\right)^2}} \quad (6)$$

where  $U$  is the on-site Coulomb interaction,  $r_{ij}$  is the distance between sites  $i$  and  $j$ ,  $r_0 = q^2/(4\pi\varepsilon_0\varepsilon_r U)$  is the characteristic length, and  $\varepsilon_r$  is the relative dielectric constant. Charge carriers are assumed to be locally and linearly coupled to the phonon bath (Holstein-type interaction), as given in eq 4. In eq 5,  $q > 0$  is the elementary charge,  $\mathbf{r}_i$  is the position vector of site  $i$ , and vector  $\mathbf{F}$  is assumed to be perpendicular to the interface and directed opposite the internal electric field of a space-separated electron–hole pair (vide infra). The interfacial electric field may originate from the different Fermi levels of the electrodes,<sup>38</sup> or from some other source.<sup>39</sup>

Similar to other numerical studies, which obtain charge separation efficiency by tracking the fate of a single electron–hole pair, we confine ourselves to the subspace of a single electron–hole pair. We describe charge separation in the exciton basis, whose basis vectors are stationary states of an electron–hole pair supported by the model interface. The most general state of an electron–hole pair can be written as  $|x\rangle = \sum_{i\alpha_i} \sum_{j\beta_j} \psi_{(i\alpha_i)(j\beta_j)}^x c_{j\beta_j}^\dagger d_{i\alpha_i}^\dagger |0\rangle$ , where  $|0\rangle$  is the vacuum of electron–hole pairs. The exciton basis states are obtained by solving the eigenvalue problem  $(H_c + H_{c-f})|x\rangle = \hbar\omega_x|x\rangle$ , which in the basis of single-particle states localized at lattice sites reads as

$$\sum_{\substack{i'\alpha'_i \\ j\beta'_j}} \left( \delta_{ii'} \delta_{\alpha_i\alpha'_i} \varepsilon_{(j\beta_j)(j'\beta'_j)}^c - \delta_{jj'} \delta_{\beta_j\beta'_j} \varepsilon_{(i\alpha_i)(i'\alpha'_i)}^v - \delta_{ii'} \delta_{\alpha_i\alpha'_i} \delta_{jj'} \delta_{\beta_j\beta'_j} \right) \psi_{(i'\alpha'_i)(j'\beta'_j)}^x \times (V_{ij} - q\mathbf{F} \cdot (\mathbf{r}_j - \mathbf{r}_i)) \psi_{(i\alpha_i)(j\beta_j)}^x = \hbar\omega_x \psi_{(i\alpha_i)(j\beta_j)}^x \quad (7)$$

We take into account the diagonal static disorder; that is, on-site energies  $\varepsilon_{i\beta_i}^c$  and  $\varepsilon_{i\alpha_i}^v$  depend on site index  $i$ . The disorder is the essential element of our model, because disorder-induced localization effects enable us to isolate exciton states that are similar to states of free charges, as will be detailed in the next paragraph.

It is convenient to classify the exciton basis states in a manner similar to that we employed in our previous studies,<sup>16,17</sup> where we differentiated between

- (1) donor exciton (XD) states, in which both carriers are mainly in the donor part of the bilayer,
- (2) acceptor exciton (XA) states, in which both carriers are mainly in the acceptor part of the bilayer, and
- (3) space-separated exciton states, in which the electron is mainly in the acceptor, while the hole is mainly in the donor part of the bilayer.

Here, we are interested in full charge separation, which results in almost free carriers capable of producing electric current. Therefore, we have to individuate exciton states of our model that resemble these free-carrier states. To this end, we introduce the notion of the contact region of the bilayer, which consists of sites  $0, \dots, l_c - 1$  in the donor part and sites  $2N - l_c, \dots, 2N - 1$  in the acceptor part of the bilayer. If both electron and hole are primarily located in the contact region (the electron in its acceptor part and the hole in its donor part), we consider them as fully separated carriers. More quantitatively, we say that space-separated exciton state  $x$  is a contact state (state of fully separated carriers) if

$$\sum_{i=0}^{l_c-1} \sum_j \sum_{\alpha\beta} |\psi_{(i\alpha)(j\beta)}^x|^2 \geq 0.7 \quad (8)$$

and

$$\sum_i \sum_{j=2N-l_c}^{2N-1} |\psi_{(i\alpha)(j\beta)}^x|^2 \geq 0.7 \quad (9)$$

The space-separated states that are not contact states will be further referred to as CT states. We point out that the localization induced by disorder is crucial to identify contact states. In the perfectly ordered system, there are no space-separated states that meet the criteria of spatial localization given in eqs 8 and 9.

**Theoretical Approach to Incoherent Charge Separation.** Our aim is to analyze the incoherent charge separation, that is, charge separation that occurs on long time scales so that coherent features are not pronounced and consequently carrier dynamics can be well described in terms of populations only. Here, we work in the basis of electron–hole pair states  $x$  and study charge separation by finding a stationary solution to an appropriate equation for populations  $f_x$  of exciton states. Similar to ref 36, we assume that contact states act as absorbing states in the course of charge separation; that is, once an exciton reaches a contact state, it is removed from the system. This removal may be interpreted as the extraction of the fully separated electron and hole at the electrodes. Therefore, we find the stationary solution to equations for populations  $f_x$  of exciton states  $x$  that do not belong to the group of contact states (further denoted as C). These equations are Pauli master equations in which the interaction with the phonon bath leads to transitions between exciton states. The time evolution of the population of exciton state  $x \notin C$  is described by

$$\frac{df_x}{dt} = g_x - \tau_x^{-1} f_x - \sum_{x'} w_{x'x} f_{x'} + \sum_{x' \notin C} w_{xx'} f_{x'} \quad (10)$$

where  $g_x$  is the generation rate of state  $x$  (the number of excitons generated per unit time in state  $x$ ),  $\tau_x$  is the lifetime of

exciton state  $x$ ,  $w_{x'x}$  is the rate of phonon bath-induced transition from state  $x$  to state  $x'$ , while the condition  $x' \notin C$  on the summation in the fourth term is due to the assumption of absorbing contact states.

We are searching for the stationary solution  $f_x^0$  to eq 10, which satisfies

$$0 = g_x - \tau_x^{-1} f_x^0 - \sum_{x'} w_{x'} f_{x'}^0 + \sum_{x' \notin C} w_{xx'} f_{x'}^0 \quad (11)$$

With the stationary populations of exciton states at hand, we can compute the separation probability:

$$\varphi = \frac{\sum_{x' \in C} \sum_{x \notin C} w_{x'} f_{x'}^0}{\sum_{x \notin C} g_x} \quad (12)$$

and the recombination probability:

$$\rho = \frac{\sum_{x \notin C} \tau_x^{-1} f_x^0}{\sum_{x \notin C} g_x} \quad (13)$$

Using eq 10, it can be shown that  $\varphi + \rho = 1$ . Different choices of  $g_x$  allow us to investigate incoherent charge separation starting from different initial states.

The phonon bath-assisted transition rates from exciton state  $x$  to exciton state  $x'$ ,  $w_{x'x}$  can be obtained using the Fermi golden rule. First, it is convenient to rewrite the carrier–phonon bath interaction  $H_{c-p}$  (eq 4) in the relevant subspace of single electron–hole excitations as<sup>16</sup>

$$H_{c-p} = \sum_{\substack{x'x \\ i\lambda}} \Gamma_{x'x}^{i\lambda} |x'\rangle \langle x| (b_{i\lambda}^\dagger + b_{i\lambda}) \quad (14)$$

where the interaction constants in the exciton basis read as

$$\begin{aligned} \Gamma_{x'x}^{i\lambda} = & \sum_{\beta_i} \sum_{j\alpha_j} g_{i\beta_j\lambda}^c \Psi_{(j\alpha_j)(i\beta_j)}^{x'*} \Psi_{(j\alpha_j)}^x \\ & - \sum_{\alpha_i} \sum_{j\beta_j} g_{i\alpha_j\lambda}^v \Psi_{(i\alpha_i)(j\beta_j)}^{x'*} \Psi_{(i\alpha_i)(j\beta_j)}^x \end{aligned} \quad (15)$$

Therefore, the phonon bath-assisted transition rate from state  $x$  to state  $x'$  is

$$\begin{aligned} w_{x'x} = & \frac{2\pi}{\hbar} \sum_{i\lambda} |\Gamma_{x'x}^{i\lambda}|^2 \delta(\hbar\omega_{x'} - \hbar\omega_x - \hbar\omega_\lambda) n_{\text{BE}}(\hbar\omega_\lambda) \\ & + \frac{2\pi}{\hbar} \sum_{i\lambda} |\Gamma_{x'x}^{i\lambda}|^2 \delta(\hbar\omega_{x'} - \hbar\omega_x + \hbar\omega_\lambda) (1 + n_{\text{BE}}(\hbar\omega_\lambda)) \end{aligned} \quad (16)$$

where  $n_{\text{BE}}(E) = (e^{\beta E} - 1)^{-1}$  is the Bose–Einstein occupation number at temperature  $T = (k_B\beta)^{-1}$ . The right-hand side of eq 16 can be simplified by assuming that all of the interaction constants  $g_{i\beta_j\lambda}^c$  and  $g_{i\alpha_j\lambda}^v$  are independent of site and band indices and equal to  $g_\lambda$ . Introducing the spectral density  $J(E)$  by

$$J(E) = \sum_{\lambda} |g_\lambda|^2 \delta(E - \hbar\omega_\lambda) \quad (17)$$

we obtain

$$w_{x'x} = \frac{2\pi}{\hbar} P_{x'x} J(|\hbar\omega_{x'} - \hbar\omega_x|) n(\hbar\omega_{x'} - \hbar\omega_x) \quad (18)$$

where

$$P_{x'x} = \sum_i \left| \sum_{\beta_i} \sum_{j\alpha_j} \Psi_{(j\alpha_j)(i\beta_j)}^{x'*} \Psi_{(j\alpha_j)(i\beta_j)}^x - \sum_{\alpha_i} \sum_{j\beta_j} \Psi_{(i\alpha_i)(j\beta_j)}^{x'*} \Psi_{(i\alpha_i)(j\beta_j)}^x \right|^2 \quad (19)$$

whereas

$$n(E) = \begin{cases} n_{\text{BE}}(E), & E > 0 \\ 1 + n_{\text{BE}}(-E), & E < 0 \end{cases} \quad (20)$$

The transition rates  $w_{x'x}$  do not depend solely on the energy difference  $\hbar\omega_{x'} - \hbar\omega_x$  between exciton states  $x'$  and  $x$ , but also on spatial properties (e.g., spatial localization and mutual overlap) of these states, which is described by quantity  $P_{x'x}$  (the so-called spatial proximity factor). The spatial proximity factor between exciton states of the same character is in general much larger than that between states of different characters. In other words, for the same energy difference  $\hbar\omega_{x'} - \hbar\omega_x$  the transition probability  $w_{x'x}$  (eq 18) is much larger when states  $x'$  and  $x$  are of the same character than when their characters are different. The last point will be repeatedly used in further discussion.

**Parametrization of the Model Hamiltonian.** The values of model parameters used in our computations are summarized in Table 1. They are selected so that the values of band gaps,

**Table 1. Values of Model Parameters Used in Computations**

parameter	value
$N$	30
$l_c$	11
$a$ (nm)	1.0
$U$ (eV)	0.65
$\epsilon_r$	3.0
$\epsilon_{D,0}^c$ (eV)	2.63
$J_{D,0}^{\text{int}}$ (eV)	0.1
$\epsilon_{D,0}^v$ (eV)	−0.3
$J_{D,0}^{\text{int}}$ (eV)	−0.15
$\epsilon_{A,0}^c$ (eV)	1.565
$\epsilon_{A,1}^c$ (eV)	1.865
$J_{A,0}^{\text{int}}$ (eV)	0.05
$J_{A,1}^{\text{int}}$ (eV)	0.025
$J_{A,0}^{\text{ext}}$ (eV)	0.02
$\epsilon_{A,0}^v$ (eV)	−1.03
$J_{A,0}^{\text{int}}$ (eV)	−0.15
$J_{DA}$ (eV)	0.1
$J_{DA}$ (eV)	−0.1
$\sigma$ (meV)	50
$\eta$	1.5
$E_c$ (meV)	10
$\tau_0$ (ps)	250
$A_{A/D}$	0.5
$T$ (K)	300

bandwidths, band offsets, and binding energies of the donor, acceptor, and CT exciton that emerge from our model are in agreement with the literature values for typical OPV materials. While the present values are largely chosen to be representative of the P3HT/PCBM interface, we emphasize that our aim is to unveil fundamental physical effects responsible for very efficient charge separation at an all-organic bilayer. Therefore, many of the parameters listed in Table 1 will be varied (within reasonable limits), and the effects of these variations on charge

separation yield will be rationalized. This is also of practical relevance, because the trends observed in such variations may suggest which material properties should be tuned to maximize the separation efficiency.

Actual computations are performed on the model system having one single-electron level per site in the donor and one single-hole level per site in both the donor and the acceptor. To mimic the presence of higher-than-LUMO orbitals energetically close to the LUMO level, which is a situation typical of fullerenes,<sup>40,41</sup> we take two single-electron levels per acceptor site. The HOMO level of the ordered donor material is taken as the zero of the energy scale. The model is schematically depicted in Figure 1. The choice of the values of model

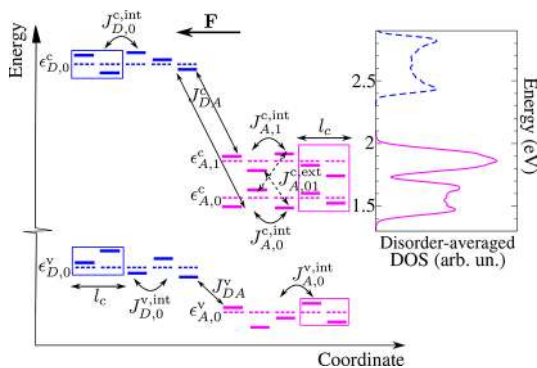


**Figure 1.** Schematic view of the model system indicating different transfer integrals and average on-site energies listed in Table 1. The dashed lines represent average on-site energies, while the solid lines represent actual on-site energies, which vary from site to site due to the diagonal static disorder. The contact region of the bilayer is denoted by rectangles.  $F$  is the vector of the interfacial electric field. The plot on the right presents the single-particle DOS for electrons in the isolated acceptor (full line) and donor (dashed line) regions of the bilayer averaged over different disorder realizations. For each disorder realization, the electronic states of the isolated regions are obtained by diagonalizing the free-electron Hamiltonian (the first term on the right-hand side of eq 2) in which the D/A coupling  $J_{DA}^c$  is set to 0. The DOS for that disorder realization is computed by broadening each of the single-electron states obtained by a Gaussian whose standard deviation is equal to 10 meV.

parameters is almost the same as in our recent investigation of ultrafast dynamics at a D/A heterointerface.<sup>16</sup> Therefore, here, we only briefly summarize the essential features of this parameter set, while the details can be found in our recent article.

Within each region of the bilayer, the on-site energies of electrons and holes are drawn from a Gaussian distribution function. For example, the probability density that the energy of the electron on donor site  $i$  ( $0 \leq i \leq N - 1$ ) is in the vicinity of  $\epsilon_{i,0}^c$  can be expressed as

$$f(\epsilon_{i,0}^c) = \frac{1}{\sigma\sqrt{2\pi}} \exp\left(-\frac{(\epsilon_{i,0}^c - \epsilon_{D,0}^c)^2}{2\sigma^2}\right) \quad (21)$$

where  $\epsilon_{D,0}^c$  is the average electron on-site energy in the donor, and  $\sigma$  is the standard deviation of the Gaussian distribution. We assume that the deviations of on-site energies from their average values are uncorrelated; this assumption regards both on-site energies of electrons (holes) on different sites and on-site energies of electrons and holes on the same site. The disorder strength is determined by parameter  $\sigma$ , which typically

assumes values of the order of 100 meV.<sup>42</sup> To obtain analytical insights into charge separation efficiency, we opt for a lower value of  $\sigma = 50$  meV, which does lead to localization effects, but does not completely destroy charge delocalization. Moreover, the disorder-averaged values of relevant quantities, such as exciton binding energies, LUMO–LUMO, and HOMO–HOMO offsets, assume values that are quite close (within few tens of meV) to the respective values in the ordered system, which will thus often be used in the discussion.

The lattice constant  $a$  is comparable to typical distances between neighboring constitutive elements of ordered polymers<sup>43</sup> (fullerene aggregates<sup>44</sup>). The number  $N$  of lattice sites in the donor and acceptor is then chosen so that the length of the model bilayer is similar to the linear dimensions of the polymer/fullerene bilayers used in experiments.<sup>26,29,32</sup> Our choice of the value of the hole transfer integral  $J_{D,0}^{v,int}$  is motivated by the literature values of the HOMO bandwidth along the  $\pi$ -stacking direction of the regioregular P3HT<sup>45,46</sup> and the values of the hole transfer integral along the  $\pi$ -stacking direction of the same material.<sup>47,48</sup> Such a choice tacitly assumes that the hole transport in the donor part of the bilayer takes place among different polymer chains. However, our Hamiltonian is quite general, so that a different selection of the values of its parameters can describe a different physical situation, for example, the hole transport along a polymer chain. The single-particle and optical gap of the ordered donor part of the bilayer are tuned to be around 2.43 and 2.0 eV, respectively,<sup>49,50</sup> so that the exciton binding energy of the ordered donor material is around 0.43 eV. The electronic parameters of the acceptor (transfer integrals  $J_{A,0}^{c,int}$ ,  $J_{A,1}^{c,int}$ , and  $J_{A,01}^{c,ext}$  and the energy difference  $\epsilon_{A,1}^c - \epsilon_{A,0}^c$  between average values of electronic on-site energies) are selected so that the single-electron density of states (DOS) of the ordered acceptor part reproduces the most important features of the DOS of fullerene aggregates.<sup>40,51</sup> The single-particle gap and the binding energy of the ordered acceptor part are tuned to the values of around 2.2 and 0.45 eV.<sup>49</sup> The values of the LUMO–LUMO (ca. 0.97 eV) and HOMO–HOMO (ca. 0.73 eV) offsets between the donor and acceptor part of the ordered bilayer are chosen by adjusting the energy differences  $\Delta_{XD-CT}$  and  $\Delta_{XA-CT}$  between the lowest excited state of the heterojunction (the lowest CT state) and the lowest exciton states in the donor and acceptor to the typical literature values.<sup>49,52,53</sup> The magnitudes of the transfer integrals  $J_{DA}^c$  and  $J_{DA}^v$  between the two materials are taken to be similar to the values obtained in ref 54.

For the spectral density of the phonon bath, we take the Ohmic spectral density:<sup>55</sup>

$$J(E) = \eta E e^{-E/E_c} \quad (22)$$

which is characterized by two parameters: the dimensionless parameter  $\eta$  describes the strength of the system–bath coupling, while  $E_c$  is the energy cutoff determining the energy range of phonon modes that are strongly coupled to the system. For the Holstein-like system–bath coupling and in the limiting case of a charge carrier localized on a single lattice site, the polaron binding energy is given by  $E_{\text{pol}} = \sum_{\lambda} |g_{\lambda}|^2 / (\hbar\omega_{\lambda})$ .<sup>56</sup> In terms of spectral density  $J(E)$ , and specifically for the Ohmic spectral density, the polaron binding energy can be expressed as

$$E_{\text{pol}} = \int_0^{+\infty} dE \frac{J(E)}{E} = \eta E_c \quad (23)$$

It is equal to the geometry relaxation energy  $\Lambda_{\text{rel}}$  upon charging a molecule and to one-half of the reorganization energy  $\Lambda_{\text{reorg}}$ .<sup>56</sup> In ref 40, the relaxation energy of the PC<sub>60</sub>BM anion was estimated to be  $\Lambda_{\text{rel}} = 15$  meV. The authors of ref 57 found that the polaron binding energy in a long straight polythiophene chain is of the order of 10 meV. We use these estimates and take the polaron binding energy  $E_{\text{pol}} = 15$  meV (the reorganization energy is then  $\Lambda_{\text{reorg}} = 30$  meV). We assume that the system–bath coupling is strongest for the low-frequency phonon modes and therefore take that  $E_c = 10$  meV and  $\eta = 1.5$ . All of these assumptions will be reassessed in the Discussion.

There are different kinds of recombination processes that limit the efficiency of organic solar cells.<sup>58</sup> The recombination of an electron–hole pair that originates from the absorption of a single photon is geminate recombination. On the other hand, an electron and a hole undergoing a nongeminate recombination event do not originate from the same photon. Here, we consider only geminate recombination, which at a D/A interface may occur as (a) the recombination of excitons photogenerated in a neat donor or acceptor material, or (b) the recombination of excitons in CT states. The recombination can be further classified as radiative or nonradiative. In neat polymers, recombination predominantly occurs via nonradiative processes.<sup>59</sup> In D/A blends, the major part of charges recombine nonradiatively either at the interface or in the donor material.<sup>60</sup> However, there is no simple model that describes the rate of nonradiative recombination in terms of microscopic material properties. It is intuitively clear that the smaller is the overlap between the electron and hole probability densities, the smaller is the rate of their recombination and the larger is the lifetime of the pair. In previous model studies of charge separation at D/A interfaces, the last point has been recognized as the steep dependence of the exciton lifetime on the electron–hole separation,<sup>61</sup> so that the recombination is assumed to occur exclusively from the strongly bound CT state,<sup>32,36,61</sup> or a formula describing the aforementioned distance dependence is proposed.<sup>33</sup> Here, to each exciton state  $x$ , be it a state in the neat material or a CT state, we assign the lifetime  $\tau_x$  that is inversely proportional to the weighted overlap of the electron and hole wave function moduli:

$$\tau_x = \tau_0 \left( \sum_{i=0}^{N-1} |\phi_i^{x,e}| |\phi_i^{x,h}| + A_{A/D} \sum_{i=N}^{2N-1} |\phi_i^{x,e}| |\phi_i^{x,h}| \right)^{-1} \quad (24)$$

In the last expression, the moduli of the wave function of the electron and hole in exciton state  $x$  are defined as

$$|\phi_i^{x,e}| = \sqrt{\sum_{\beta_i} \sum_{j\alpha_j} |\psi_{(j\alpha_j)(i\beta_i)}^x|^2} \quad (25)$$

$$|\phi_i^{x,h}| = \sqrt{\sum_{\alpha_i} \sum_{j\beta_j} |\psi_{(i\alpha_i)(j\beta_j)}^x|^2} \quad (26)$$

while  $\tau_0$  and  $A_{A/D}$  are constants that are determined so that the lifetimes of the lowest CT, XD, and XA states in the ordered system agree with the values reported in the literature. The expression for the lifetime given in eq 24 captures the previously described trend. Singlet exciton lifetimes in a variety of conjugated polymers used in organic solar cells are of the order of hundreds of picoseconds.<sup>59</sup> Time-resolved photoluminescence measurements yield the singlet exciton lifetime in neat P3HT around 470 ps and in neat PCBM around 740 ps.<sup>62</sup>

From the transient absorption measurements performed in blends of P3HT and different fullerenes, the lifetime of the CT state was determined to be around 3 ns.<sup>63</sup> For the values of model parameters listed in Table 1, the lifetime of the lowest CT state in the ordered system is  $\tau_{\text{CT}}^{\text{ord}} \approx 2.5$  ns, the lifetime of the lowest XD state in the ordered system is  $\tau_{\text{XD}}^{\text{ord}} \approx 400$  ps, and the lifetime of the lowest XA state in the ordered system is  $\tau_{\text{XA}}^{\text{ord}} \approx 800$  ps.

## NUMERICAL RESULTS

In this section, we present the results concerning the yield of charge separation starting from CT and donor states. In all of the computations, we average over different disorder realizations, and all of the results to be presented are averaged over 256 disorder realizations. To facilitate the discussion, in Figure 2a–e we present disorder-averaged DOS for different

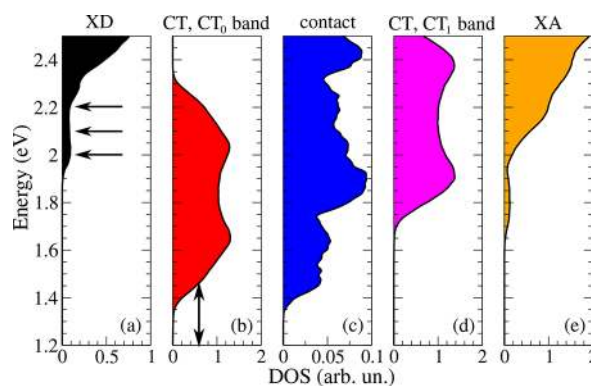


**Figure 2.** Disorder-averaged exciton DOS (in arbitrary units and at  $F = 0$ ) for (a) donor exciton states, (b) CT states belonging to CT<sub>0</sub> band, (c) contact states, (d) CT states belonging to CT<sub>1</sub> band, and (e) acceptor exciton states. The horizontal arrows in (a) indicate approximate energies of XD states serving as initial states of charge separation. The vertical double-sided arrow in (b) indicates the energy range of the CT states acting as initial states of charge separation. The DOS in a single disorder realization is obtained by broadening each exciton level by a Gaussian whose standard deviation is equal to 10 meV.

groups of exciton states. Similar to our recent study, we discriminate between CT states belonging to CT<sub>0</sub> and CT<sub>1</sub> bands.<sup>16</sup> We say that a CT state belongs to the CT<sub>0</sub> (CT<sub>1</sub>) band if its electron primarily belongs to the electronic band in the acceptor part of the bilayer arising from the single-electron level of average energy  $\epsilon_{A,0}^c$  ( $\epsilon_{A,1}^c$ ).

### Charge Separation from the Strongly Bound CT State.

As starting states for the charge separation process, here we consider CT states belonging to the CT<sub>0</sub> band. One particular CT state out of all of the states in the CT<sub>0</sub> band is chosen by requiring that the mean electron–hole separation, which for exciton state  $x$  reads as

$$\langle r_{e-h} \rangle_x = \sum_{\substack{i\alpha_i \\ j\beta_j}} |i - j| |\psi_{(i\alpha_i)(j\beta_j)}^x|^2 \quad (27)$$

be minimal. We will further refer to such a state as the strongly bound CT state. The strongly bound CT state is located on the lower edge of the disorder-averaged DOS of CT excitons belonging to the CT<sub>0</sub> band; see the vertical double-sided arrow in Figure 2b. We set the generation rate  $g_x$  appearing in eq 10 to be different from zero only for the strongly bound CT state.

The field-dependent separation yield from this state is presented by circles in Figure 3a. The separation yield is above

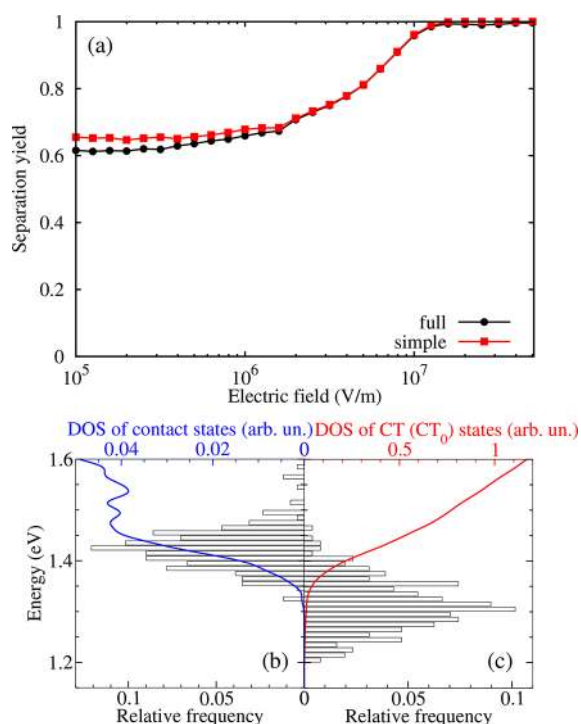


**Figure 3.** (a) Field-dependent yield of charge separation from the strongly bound CT state. The data labeled by “full” are obtained by numerically solving eq 10, while the data labeled by “simple” are computed using eq 34. The low-energy edges of the disorder-averaged DOS (full lines) for (b) contact states and (c) CT states belonging to the  $CT_0$  band. The bars depict histograms of the distribution of the energy of (b) the lowest-energy contact state and (c) the initial strongly bound CT state. The width of the bins on the energy axis is 10 meV, while  $F = 0$ .

0.6 for all of the examined values of the electric field down to  $F = 0$ . Figure 3b presents the low-energy tail of the DOS of contact states (see Figure 2c) along with the distribution of energies of the lowest-energy contact state. Figure 3c shows the low-energy tail of the DOS of CT states (see Figure 2b) together with the distribution of energies of the initial strongly bound CT state. The disorder-averaged energy difference between the lowest-energy contact state and the initial CT state may serve as an estimate of the average energy barrier that an electron–hole pair in the initial CT state has to surmount to reach the nearest free-charge state. We obtain the average barrier of approximately 0.13 eV ( $\sim 5 k_B T$  at room temperature), which is lower (at least by a factor of 2) than usually assumed when considering separation of the strongly bound CT exciton.<sup>64</sup> Further discussion reveals that the actual barrier to be overcome is smaller than the energy difference between the lowest-energy contact state and the initial CT state. The intermediate CT states, lying between the initial CT state and the lowest-energy contact state and exhibiting larger electron–hole distances as compared to the initial CT state, are crucial to the successful separation of the initial strongly bound pairs. Stronger electric field is beneficial to exciton separation, which, combined with the fact that the separation yield is above 0.5 even at  $F = 0$ , implies that it exhibits relatively weak dependence on the magnitude of the electric field.

It is instructive to analyze the results presented in Figure 3a from the viewpoint of single disorder realizations. In Figure 4a–d we present distributions of the separation yield in single

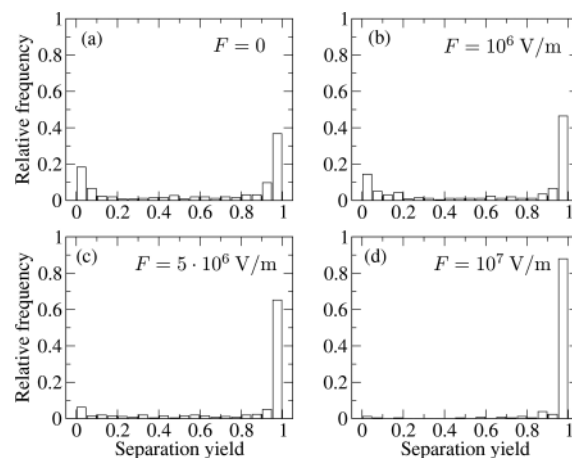


**Figure 4.** Histograms showing the distribution of the yield of charge separation from the strongly bound CT state for different strengths of the electric field: (a)  $F = 0$ , (b)  $F = 10^6$  V/m, (c)  $F = 5 \times 10^6$  V/m, and (d)  $F = 10^7$  V/m. The width of the bins for the separation yield is 0.05.

disorder realizations at different strengths of the electric field. A distinctive feature of all of the histograms is a quite small number of disorder realizations for which the separation yield assumes values in an intermediate range (say between 0.2 and 0.8). Even at zero electric field, the number of disorder realizations in which the separation yield is high (above 0.8) is greater than the number of those in which the separation yield is low (below 0.2), which can account for the mean separation yield above 0.5 even at zero field. As the electric field is increased, the number of disorder realizations in which the separation yield is low or intermediate decreases, while the number of disorder realizations in which the separation yield is high increases; see Figure 4b–d. At  $F = 10^7$  V/m, the separation yield is between 0.95 and 1 for somewhat less than 90% of disorder realizations, see Figure 4d, meaning that the mean yield is close to 1. Relevant to this discussion are also the relative positions of the lower-energy tails of the DOS of CT states belonging to the  $CT_0$  band and the DOS of contact states, which are presented in Figure S1a–d. We observe that the effect of increasing  $F$  on the DOS tails consists of decreasing the energy difference between the edges of CT and contact DOS. For sufficiently strong field, the lowest contact state is situated energetically below the strongly bound CT state.

We now establish which factors primarily determine the separation yield and propose an analytical formula that is capable of reproducing the separation yield in single disorder realizations (and consequently the mean separation yield) quite well. Let us begin by noticing that the initial CT state is usually strongly coupled (by means of phonon bath-assisted transitions) to only a couple of exciton states, which are of CT character and whose electron–hole separation (and consequently the lifetime) is larger than in the initial CT state. We further refer to these states as intermediate states. Moreover, intermediate states are in general very well coupled to other space-separated states, meaning that, in principle, there is no kinetic obstacle for an exciton in the intermediate state to

undergo a series of phonon bath-assisted transitions in which the electron–hole separation gradually increases, and finally reach a contact state. However, because the coupling among the initial state and intermediate states is appreciable, the “implosion” of the pair, that is, the back-transfer from intermediate states to the initial CT state followed by the recombination event, should not be omitted from the analysis. The recombination from intermediate states, as well as from all of the subsequent states paving the way toward contact states, is not probable, because the lifetimes of all of these states are quite long as compared to the inverse transition rates among them. In other words, the recombination occurs almost exclusively from the initial CT state. We may therefore assume that the only rate-limiting step during charge separation is the escape from the initial strongly bound CT state  $x_{\text{init}}$ . The separation yield is then determined by the competition between the recombination rate in the initial CT state, the escape rate from the initial CT state toward intermediate states, and the back-transfer rate from intermediate states to the initial CT state. This competition may be described using a simple kinetic model whose variables are populations of the initial CT state and intermediate states (which are considered as a single state). Recombination is possible only from the initial CT state, while contact states may be reached from intermediate states. The stationarity of the initial CT state population  $f_{\text{init}}^0$  demands that

$$g_{\text{init}} = (\tau_{\text{init}}^{-1} + w_{\text{inter,init}})f_{\text{init}}^0 - w_{\text{init,inter}}f_{\text{inter}}^0 \quad (28)$$

while a similar condition for the stationary population  $f_{\text{inter}}^0$  of intermediate states reads as

$$(w_{\text{init,inter}} + w_{\text{contact,inter}})f_{\text{inter}}^0 = w_{\text{inter,init}}f_{\text{init}}^0 \quad (29)$$

In eqs 28 and 29,  $g_{\text{init}}$  is the generation rate of the initial CT state,  $\tau_{\text{init}}$  is its lifetime,  $w_{\text{inter,init}}$  is the total escape rate from the initial CT state  $x_{\text{init}}$  toward intermediate states  $x_{\text{inter}}$ :

$$w_{\text{inter,init}} = \sum_{x_{\text{inter}}} w_{x_{\text{inter}},x_{\text{init}}} \quad (30)$$

and  $w_{\text{init,inter}}$  is the total back-transfer rate to the initial CT state from intermediate states:

$$w_{\text{init,inter}} = \sum_{x_{\text{inter}}} w_{x_{\text{init}},x_{\text{inter}}} \quad (31)$$

The total escape rate from all of the intermediate states toward contact states is

$$w_{\text{contact,inter}} = \sum_{x_{\text{inter}}} \sum_{x_f} w_{x_f,x_{\text{inter}}} \quad (32)$$

where, for each intermediate state  $x_{\text{inter}}$ , the summation over final states  $x_f$  is carried out only over the states from which further transitions toward contact states are possible (it should not include the transitions back to the initial CT state). An adaptation of eq 12 to the problem at hand gives the following expression for the separation yield:

$$\varphi = \frac{w_{\text{contact,inter}}f_{\text{inter}}^0}{g_{\text{init}}} \quad (33)$$

Combining eqs 28, 29, and 33, we obtain the following expression for the separation yield:

$$\varphi = \frac{1}{1 + (\tau_{\text{init}}w_{\text{inter,init}})^{-1} \left(1 + \frac{w_{\text{init,inter}}}{w_{\text{contact,inter}}}\right)} \quad (34)$$

We point out that all four quantities ( $\tau_{\text{init}}$ ,  $w_{\text{inter,init}}$ ,  $w_{\text{init,inter}}$ , and  $w_{\text{contact,inter}}$ ) entering eq 34 are characteristic of each disorder realization; that is, eq 34 contains no free parameters. It is then remarkable that it reproduces quite well the field-dependent separation yield for each disorder realization, and consequently the disorder-averaged separation yield, which is presented by squares in Figure 3a.

The preceding discussion suggests that the barrier the initial CT exciton has to surmount to reach a contact state is determined by the energy difference  $\hbar\omega_{\text{inter}} - \hbar\omega_{\text{init}}$  between the initial CT state and the intermediate CT state exhibiting strongest coupling to the initial state. In Figure 5a,b we present

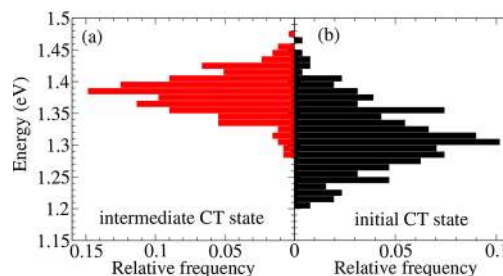


**Figure 5.** Histograms showing distributions of energies of (a) the intermediate CT state (which is most strongly coupled to the initial CT state) and (b) the initial CT state. The histograms are computed for  $F = 0$ .

distributions of energies of the intermediate (Figure 5a) and the initial (Figure 5b) CT state at  $F = 0$ . We estimate that the average energy difference  $\langle \hbar\omega_{\text{inter}} - \hbar\omega_{\text{init}} \rangle$  is around 0.07 eV, which is smaller than the average energy difference between the lowest contact state and the initial CT state. Therefore, already at  $F = 0$ , the average energy barrier opposing the separation from the initial CT state is  $\sim 3 k_B T$  at room temperature. For stronger  $F$ , the height of the barrier decreases, and the barrier is almost eliminated at  $F \gtrsim 10^7$  V/m, as is presented in more detail in Figure S2a–d.

Equation 34 gives the separation yield that is always an upper bound to the true separation yield obtained by numerically solving rate equations embodied in eq 10. Deriving eq 34, we assume that there is only one rate-limiting step in the process of charge separation from the initial CT state (the escape from the initial CT state to intermediate states), while further transitions from intermediate states toward contact states occur with certainty. However, in reality, some of these further transitions may present another obstacle to full charge separation, and, to fully reproduce the numerical data, eq 34 should be corrected so as to take other rate-limiting steps into account (it turns out that such corrections are really important only for strong enough disorder, vide infra). We can elaborate more on the last point by noticing that eq 34 is actually a version of the Rubel’s formula<sup>36</sup> that describes the separation of an exciton initially in state 1 through a series of incoherent hops  $1 \rightleftharpoons 2 \rightleftharpoons \dots \rightleftharpoons n \rightarrow n + 1$  among localized states, which terminates when free-charge state  $n + 1$  is reached:

$$\varphi_{\text{Rubel}} = \frac{1}{1 + (\tau_1 w_{21})^{-1} \left( 1 + \sum_{i=2}^n \prod_{j=2}^i \frac{w_{j-1,j}}{w_{j+1,j}} \right)} \quad (35)$$

One of the main assumptions behind the Rubel's formula is that the recombination event is possible only from the initial CT state 1, its rate being  $\tau_1^{-1}$ . This assumption is satisfied in our computations, as we obtain that the major part of recombination events occurs from the initial CT state, so that we may identify  $\tau_{\text{init}}$  in eq 34 with  $\tau_1$  in eq 35. The first rate-limiting step is the escape from the initial CT state to more separated (and thus longer-lived) intermediate states, which justifies the identification of  $w_{i,\text{inter,init}}$  in eq 34 with  $w_{21}$  in eq 35. Further rate-limiting steps are taken into account in eq 35 by the term  $\sum_{i=2}^n \prod_{j=2}^i \frac{w_{j-1,j}}{w_{j+1,j}}$ , which takes care of the fact that, at each step  $j$  that has to be completed to reach state  $i$ , there is a competition between the escape rate  $w_{j+1,j}$  toward the free-charge state  $n+1$  and the back-transfer rate  $w_{j-1,j}$  toward the initial state 1. Rubel et al. have assumed that the pathway from the initial to the final state is such that hops are possible only between neighboring states in the sequence  $1 \rightleftharpoons 2 \rightleftharpoons \dots \rightleftharpoons n \rightarrow n+1$ , while in our model hops are in principle possible among any two exciton states. Thus, in our model it is difficult to isolate particular separation paths and ensure that they do not interfere among themselves. Nevertheless, as evidenced by quite good agreement between the results presented in Figure 3a, taking into account only the first rate-limiting step is a reasonable approximation to the full numerical data. This approximation is, however, plausible only for not too strong disorder. For stronger disorder, disorder-induced localization effects become more pronounced, and, on its way toward contact states, an exciton may reach a state exhibiting strong localization. Because of its strong localization, this state is poorly coupled to other states, meaning that it may act as another recombination center, or it may "reflect" excitons toward the initial state; that is, it acts as a trap state for charge separation. Neither of these two possibilities is captured by eq 34; therefore, it cannot accurately reproduce the separation yield for stronger disorder, as we discuss in the next paragraph.

We continue our discussion on the effects of disorder by investigating the separation yield for different disorder strengths  $\sigma$  at zero electric field. Along with the data emerging from numerically solving eq 10, in Figure 6 we present the data obtained by means of eq 34. We observe that the dependence of  $\varphi$  on  $\sigma$  is not monotonic. For very low values of  $\sigma$  (typically  $\sigma < 20$  meV in our one-dimensional model), contact states are generally absent from the spectrum (the disorder is so weak that disorder-induced localization effects are not pronounced), and consequently the separation yield within our model is exactly equal to zero in the majority of disorder realizations. This is different from predictions of other models describing incoherent charge separation,<sup>36,37</sup> according to which the separation yield is different from zero for all of the values of disorder strength down to  $\sigma = 0$ . Therefore, the predictions of our model are not reliable for too low disorder. Bearing in mind that typical disorder strength in organic semiconductors is considered to be of the order of 100 meV,<sup>42</sup> the aforementioned feature of our model does not compromise its relevance. For stronger disorder (typically  $\sigma > 20$  meV), contact states start to appear in the spectrum, and their number grows with increasing  $\sigma$ . At the same time, the average energy difference  $\langle \hbar\omega_{\text{inter}} - \hbar\omega_{\text{init}} \rangle$  between the intermediate state and

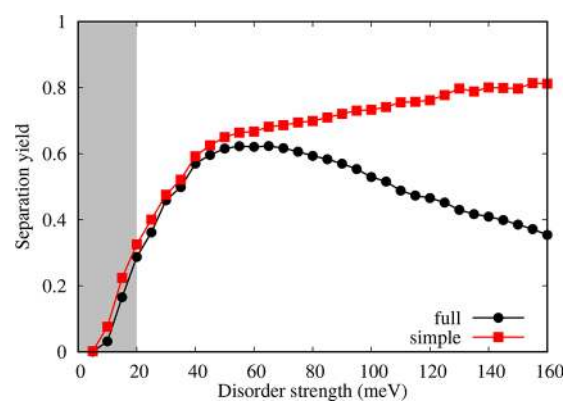


**Figure 6.** Yield of charge separation from the strongly bound CT state at  $F = 0$  for different strengths  $\sigma$  of the diagonal static disorder. The gray area indicates the range of disorder strength in which the predictions of our model are not reliable. The data labeled by "full" are obtained by numerically solving rate equations (eq 10), while the data labeled by "simple" are computed using eq 34.

the initial CT state decreases (see Figure S3), and the escape rate  $w_{i,\text{inter,init}}$  from the initial CT state to intermediate states increases (see eq 18). Because the disorder is still not too strong, further separation from intermediate states is much more probable than the "implosion" of the pair, meaning that typically  $w_{\text{init,inter}}/w_{\text{contact,inter}} \ll 1$ . The last statement, combined with the fact that  $\tau_{\text{init}}$  essentially does not depend on  $\sigma$ , gives that the separation yield determined by eq 34 increases with increasing  $\sigma$ . However, there exists an optimal disorder strength  $\sigma_{\text{opt}}$  for which the separation yield attains a maximum value, so that for  $\sigma > \sigma_{\text{opt}}$  an increase in the disorder strength leads to a decreased separation yield. In our numerical computations,  $\sigma_{\text{opt}}$  is around 60 meV, in good agreement with the results of ref 37, which also point toward the existence of the optimal disorder strength. Although for strong disorder the number of contact states is large, the pronounced disorder-induced localization starts to impede phonon-assisted transitions among exciton states. The number of trap states for charge separation (cf., previous paragraph) increases, meaning that there is more than just a single rate-limiting step during the separation of the initial electron-hole pair. This leads to an increased probability of the "implosion" of the pair into the initial CT state or the pair recombination directly from trap states. Therefore, the separation yield is decreased. As can be inferred from Figure 6, the yield computed using eq 34 (circles) is again an upper bound to the separation yield obtained by numerically solving rate equations (eq 10, squares) and approximates it quite well only for  $\sigma \lesssim \sigma_{\text{opt}}$  while for  $\sigma > \sigma_{\text{opt}}$  the two separation yields exhibit opposite trends with increasing disorder strength. While the true separation yield decreases for  $\sigma > \sigma_{\text{opt}}$ , the yield given by eq 34 monotonically increases in the entire examined range of disorder strength, consistent with the fact that  $\langle \hbar\omega_{\text{inter}} - \hbar\omega_{\text{init}} \rangle$  monotonically decreases with increasing  $\sigma$ . Equation 34 does not capture further rate-limiting steps in the course of charge separation, and the highly successful escape from the initial CT state to intermediate states does not guarantee full charge separation.

The apparent simplicity of our model enables us to systematically study the effects of variations of different model parameters on the efficiency of charge separation starting from the strongly bound CT state. Let us first examine how the variations in the electron delocalization in the acceptor

(mimicked by variations in the transfer integral  $J_{A,0}^{\text{int}}$ ) and in the hole delocalization in the donor (mimicked by variations in the transfer integral  $J_{D,0}^{\text{int}}$ ) affect the separation yield. We obtain that better delocalization of carriers promotes higher separation yields; see Figure 7a,b. This can be rationalized using eq 34,

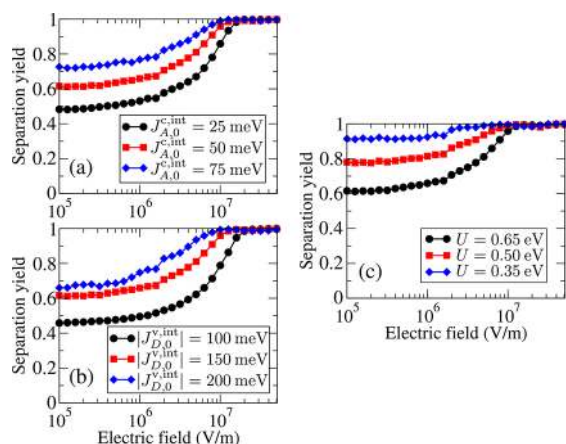


**Figure 7.** Field-dependent separation yield from the strongly bound CT state for different values of (a) the electron transfer integral  $J_{A,0}^{\text{int}}$  in the acceptor, (b) the hole transfer integral  $J_{D,0}^{\text{int}}$  in the donor, and (c) the on-site Coulomb interaction  $U$ .

which determines the separation yield as a function of only a couple of parameters, and following the variation of these parameters with varying carrier delocalization. When the separation yield is high (greater than 0.8 already at zero field and for the lowest investigated values of  $J_{A,0}^{\text{int}}$  and  $J_{D,0}^{\text{int}}$ , cf., the discussion of Figure 4a–d), reasonable variations in  $J_{A,0}^{\text{int}}$  and  $J_{D,0}^{\text{int}}$  do not dramatically influence the separation yield, which remains high. When the separation yield is low or intermediate (less than 0.8 at zero field and for the lowest investigated values of  $J_{A,0}^{\text{int}}$  and  $J_{D,0}^{\text{int}}$ ), it exhibits a pronounced increase with increasing transfer integrals  $J_{A,0}^{\text{int}}$  and  $J_{D,0}^{\text{int}}$ . Better carrier delocalization leads to an increase in the escape rate  $w_{\text{inter,init}}$  from the initial CT state, which, along with the fact that  $\tau_{\text{init}}$  remains largely unaffected by variations in  $J_{A,0}^{\text{int}}$  and  $J_{D,0}^{\text{int}}$ , means that the separation yield determined by eq 34 is higher.

Next, we comment on the variations that the separation yield undergoes when the magnitude of the on-site Coulomb interaction  $U$  is changed. In Figure 7c we observe that weaker electron–hole interaction leads to more efficient charge separation from the strongly bound CT state. Again, this beneficial effect of weaker Coulomb interaction may be attributed to the product  $\tau_{\text{init}}w_{\text{inter,init}}$  being (on average) larger for weaker Coulomb interaction. On a more intuitive level, the trends in the separation yield presented in Figure 7a–c may be rationalized by following the changes in the disorder-averaged energy difference  $\langle \hbar\omega_{\text{inter}} - \hbar\omega_{\text{init}} \rangle$  with changing the degree of carrier delocalization and the strength of the electron–hole interaction. In Figure S4a1–c3, we compare values of  $\langle \hbar\omega_{\text{inter}} - \hbar\omega_{\text{init}} \rangle$ , as well as the energy distributions of the initial and intermediate CT state, for different  $J_{A,0}^{\text{int}}$ ,  $J_{D,0}^{\text{int}}$ , and  $U$ . We conclude that better carrier delocalization and weaker electron–hole interaction favor lower values of  $\langle \hbar\omega_{\text{inter}} - \hbar\omega_{\text{init}} \rangle$ , or, in other words, lower the separation barrier from the CT state. Let us also note that each of the effects studied can on its own improve the separation from the strongly bound CT state, because its binding energy strongly depends both on the

degree of carrier delocalization and on the Coulomb interaction; compare to the discussion of the results (Figure 11a–c) concerning charge separation from the closely separated donor exciton state.

We have also studied the temperature dependence of the process of charge separation from the strongly bound CT state. We observe an approximately 6-fold decrease in the separation yield when the temperature is decreased from 300 to 100 K; see Figure 8a. On temperature reduction from 300 to below 50 K,

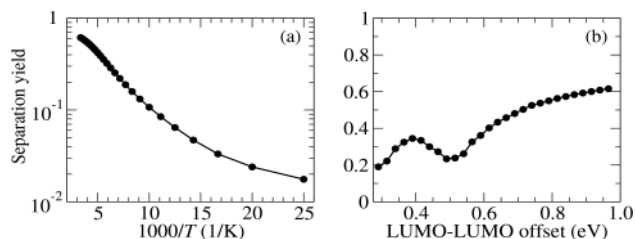


**Figure 8.** Yield of charge separation from the strongly bound CT state at zero electric field as a function of (a) the temperature (in Arrhenius representation) and (b) the LUMO–LUMO offset. The reported values of the LUMO–LUMO offset refer to the ordered system.

the separation yield reduces for more than an order of magnitude. These observations are in agreement with other numerical studies of charge separation from the strongly bound CT state,<sup>34</sup> and with experimentally obtained temperature dependence of the photocurrent under an excitation at the low-energy edge of the CT manifold.<sup>65</sup>

The effect of the variations in the LUMO–LUMO offset on the separation yield was studied by changing average on-site energies  $\epsilon_{A,0}^c$ ,  $\epsilon_{A,1}^c$ , and  $\epsilon_{A,0}^v$  in the acceptor part of the bilayer (see Figure 1) by the same amount, keeping all of the other model parameters listed in Table 1 unchanged. In first approximation, these variations manifest themselves in Figure 2a–e as rigid translations of the DOS of space-separated exciton states (Figure 2b–d) with respect to the DOS of donor and acceptor exciton states (Figure 2a,e). Figure 8b presents the dependence of the separation yield at zero electric field on the LUMO–LUMO offset. For the LUMO–LUMO offset greater than approximately 0.5 eV, we observe that the separation yield monotonically decreases with decreasing the LUMO–LUMO offset; see Figure 8b. A decrease in the LUMO–LUMO offset leads to a decreased energy difference between the lowest acceptor (and also donor) state and the initial CT state; see also Figure 2a–e. We may thus expect that a sufficient decrease in the LUMO–LUMO offset results in the involvement of acceptor and donor states in the separation from the strongly bound CT state. The transitions from the space-separated manifold toward the acceptor (donor) manifold are in general much less probable than those inside the space-separated manifold. However, once an exciton enters the acceptor (donor) manifold, it can easily recombine, because the typical lifetime of acceptor (donor) states is shorter than the lifetime of the initial CT state. In other words, the fact that acceptor (donor) states participate in the separation of the strongly bound CT exciton is seen as a decrease in the separation yield, which is due to the enhanced recombination from acceptor (donor) states. This is shown in more detail in Figure S5a,b, which provide data on recombination from different groups of exciton states. While the recombination from acceptor states can partially account for the decrease in

the separation yield observed for LUMO–LUMO offsets below 0.65 eV, the recombination from donor states is reflected in the decrease seen for LUMO–LUMO offsets below 0.4 eV. We can estimate these numbers using Figure 2a–e and having in mind that the LUMO–LUMO offset for that arrangement of exciton energies is ca. 0.97 eV. A rigid translation of Figure 2b–d by approximately 0.3 eV (upward in energy) makes the initial CT state energetically close to the acceptor states in the low-energy tail of the acceptor DOS, meaning that they can participate in the separation of the initial CT state. Similarly, a rigid translation of Figure 2b–d by approximately 0.55 eV makes the initial CT state energetically close to the donor states in the low-energy tail of the donor DOS. However, to understand the behavior of the separation yield in the whole range of LUMO–LUMO offsets displayed in Figure 8b, we have to remember that lower LUMO–LUMO offset promotes better coupling between the two parts of the bilayer, which is mediated by the D/A couplings  $J_{DA}^E$  and  $J_{DA}^H$ . As a consequence, reducing the LUMO–LUMO offset enhances the electron–hole overlap in CT states, thus decreasing their lifetime and increasing the recombination from CT states, which is shown in Figures S6 and S5b. Therefore, enhanced recombination from CT states can explain the decrease in the separation yield observed for LUMO–LUMO offsets above approximately 0.65 eV.

**Charge Separation from a Donor Exciton State.** Here, we aim at understanding which factors control charge separation starting from a donor exciton state. In numerical computations, the generation rate  $g_x$  appearing in eq 10 is set to a nonzero value only for donor states. We have noted in our previous publications that the low-energy (closely separated and strongly bound) donor states are essentially isolated from the manifold of space-separated states and thus act as trap states for the separation of the initial donor excitons on subpicosecond time scales.<sup>16,17</sup> On the contrary, higher-energy (more separated and loosely bound) donor states exhibit appreciable coupling to the space-separated manifold, and we may thus expect that charge separation starting from these states should be more probable than that starting from closely separated donor states.

We perform computations of the yield of the separation of donor excitons of different energies. We focus on the energy windows centered around  $E_{\text{init}} = 2.0$  eV (the optical gap of the ordered donor material),  $E_{\text{init}} = 2.1$  eV, and  $E_{\text{init}} = 2.2$  eV (significantly above the optical gap of the ordered donor material), which is indicated by horizontal arrows in Figure 2a. Because the precise energies of donor states are determined by the disorder, we choose the initial donor state among the states that lie in the 50 meV-wide energy windows centered around the aforementioned energies. One particular donor state out of the chosen states is selected by the requirement that the squared modulus of the dipole moment for the direct generation of donor exciton state  $x$ , which is proportional to  $\left| \sum_{i \in D; \alpha, \beta} \psi_{(i\alpha)(i\beta)}^x \right|^2$ ,<sup>16</sup> be maximum. In other words, among donor states in a given energy window, we select the state whose direct generation from the ground state is most probable. Such a choice of the initial donor state is motivated by our recent computations in which we have observed that quite a high fraction of photogenerated excitons remain in the initially photoexcited donor state on a picosecond time scale following the excitation.<sup>16</sup>

In Figure 9, we compare the yields of charge separation starting from donor states of different energies. As we have

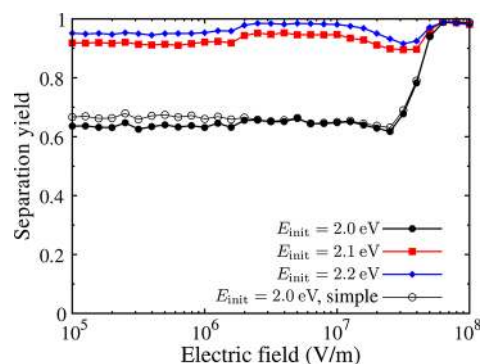


**Figure 9.** Field-dependent yield of charge separation starting from donor exciton states of different energies. The data represented by filled symbols are obtained by solving the full set of rate equations (eq 10). The data represented by empty circles are obtained by solving the reduced set of rate equations (eq 36) in case  $E_{\text{init}} = 2.0$  eV.

expected, charge separation starting from a higher-energy donor state is more efficient than that starting from a closely separated donor state. The yield of the separation from a donor state situated around  $E_{\text{init}} = 2.2$  eV is practically field-independent and greater than 0.9 for all of the examined values of the electric field down to  $F = 0$ . The yield is somewhat higher for  $E_{\text{init}} = 2.2$  eV than for  $E_{\text{init}} = 2.1$  eV. On the other hand, the yield of the separation from a closely separated donor state ( $E_{\text{init}} = 2.0$  eV) is lower: it is almost constant for electric fields  $F \lesssim 5 \times 10^7$  V/m, its value being around 0.6, after which it rises and reaches values close to 1 at  $F \sim 10^8$  V/m. The value of the electric field at which the separation from a closely separated donor state occurs with certainty is almost an order of magnitude larger than in the case of charge separation from the strongly bound CT state, see Figure 3a, which is consistent with the fact that the binding energy of the donor exciton is larger than the binding energy of the CT exciton.

Let us now analyze in more detail the separation of the closely separated donor exciton ( $E_{\text{init}} = 2.0$  eV). Our data suggest that the major part of recombination events occur from donor exciton states. This is consistent with the fact that phonon bath-assisted transitions starting from the closely separated donor exciton state couple it most strongly to other donor states, while coupling to the space-separated manifold is in principle much weaker (we note that its coupling to an acceptor state is practically negligible). The states of the space-separated manifold to which the closely separated donor state can couple are typically well spatially separated, long-lived, and exhibit good coupling to other space-separated states. In other words, despite the weak coupling, once an exciton in the closely separated donor state performs a transition to the space-separated manifold, it is highly probable that it will eventually reach a fully separated state. Instead of finding the stationary solution to the full set of rate equations (eq 10) for all exciton states (excluding contact states), we may compute the separation yield by solving the rate equations in which we explicitly consider only donor states  $x \in XD$  and treat exciton states  $x'$  that are not of donor character as absorbing states:

$$0 = g_x - \tau_x^{-1} f_x^0 - \sum_{x'} w_{x',x} f_x^0 + \sum_{x' \in XD} w_{xx'} f_{x'}^0 \quad (36)$$

The separation yield, computed by inserting the solution to eq 36 into an expression analogous to eq 12, which reads as

$$\varphi = \frac{\sum_{x' \notin \text{XD}} \sum_{x \in \text{XD}} w_{x'} f_x^0}{\sum_{x \in \text{XD}} g_x} \quad (37)$$

is presented in case  $E_{\text{init}} = 2.0$  eV by empty circles in Figure 9. We note that the agreement between the two results (full and empty circles in Figure 9) is quite good, thus validating our simple picture of charge separation from a low-energy donor state. The same procedure can be repeated when considering the separation starting from higher-energy donor states, but the agreement between the results obtained by solving eq 36 and the full system of rate equations (eq 10) is worse. An analysis of recombination events suggests that, in these cases, the acceptor exciton states are an equally important recombination channel as the donor exciton states. When the initial donor state is loosely bound, its direct coupling to acceptor states cannot be neglected. Further discussion on the limits of validity of the simple picture of charge separation from donor states embodied in eq 36 is presented in the next paragraph.

We now turn to the influence of the diagonal static disorder on the yield of charge separation starting from donor exciton states of different energies at zero electric field. We focus our attention on the initial donor states whose energies are around  $E_{\text{init}} = 2.0$  eV and  $E_{\text{init}} = 2.2$  eV. Together with the separation yield emerging from numerically solving the full set of rate equations given in eq 10 (the true separation yield), in Figure 10a,b we also present the data obtained by solving the reduced

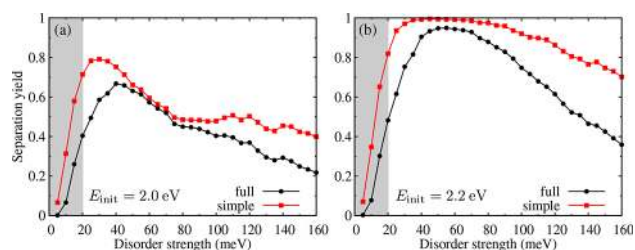


**Figure 10.** Separation yield at zero electric field for different strengths  $\sigma$  of the diagonal static disorder. The initial state of charge separation is a donor exciton state of energy around (a)  $E_{\text{init}} = 2.0$  eV and (b)  $E_{\text{init}} = 2.2$  eV. The data labeled by “full” are obtained by numerically solving the full set of rate equations (eq 10), whereas the data labeled by “simple” emerge from the numerical solution to the reduced set of rate equations (eq 36). Similar to Figure 6, the gray area indicates the range of disorder strength in which the predictions of our model are not reliable.

set of rate equations (eq 36). We observe that the separation yield exhibits similar trends with varying disorder strength as when the separation starts from the strongly bound CT state (cf., Figure 6). In particular, for not too strong disorder, the yield increases with increasing disorder strength, it attains the maximum value when the disorder assumes its optimal value, after which it decreases. For all of the examined values of disorder strength, the yield of the separation starting from the donor state of energy  $E_{\text{init}} = 2.2$  eV is higher than in the case  $E_{\text{init}} = 2.0$  eV; compare data represented by circles in Figure 10a,b, which again suggests that excitons initially in higher-energy donor states separate more efficiently than those initially in lower-energy donor states. While the maximum yield of separation starting from the donor state of energy  $E_{\text{init}} = 2.0$  eV is around 0.7, the maximum yield in the case  $E_{\text{init}} = 2.2$  eV is above 0.9. For both initial states of charge separation, the yield computed by numerically solving the reduced set of rate

equations (squares in Figure 10a,b) is an upper bound to the true separation yield (circles in Figure 10a,b) for all of the examined values of  $\sigma$ . For  $E_{\text{init}} = 2.0$  eV, the separation yield computed by solving the reduced set of rate equations reproduces the true separation yield very well when the disorder strength is from around 40 meV to around 90 meV, while for stronger disorder the agreement between the yields computed in two manners deteriorates. This suggests that, for moderate disorder strength, our simple picture of charge separation from the closely separated donor state, embodied in eq 36, is plausible. At stronger disorder, the localization effects become more important, and recombination may occur from states that do not belong to the donor manifold as well. On the other hand, the agreement between the two separation yields in case  $E_{\text{init}} = 2.2$  eV, see Figure 10b, is less satisfactory than that in case  $E_{\text{init}} = 2.0$  eV.

We have also examined the dependence of the separation yield starting from the closely separated donor state on the magnitude of electron ( $J_{D,0}^{c,\text{int}}$ ) and hole ( $J_{D,0}^{v,\text{int}}$ ) transfer integrals in the donor part of the bilayer. We find that reasonable variations in these quantities do not induce major changes in the separation yield; see Figure 11a,b. The reason for this

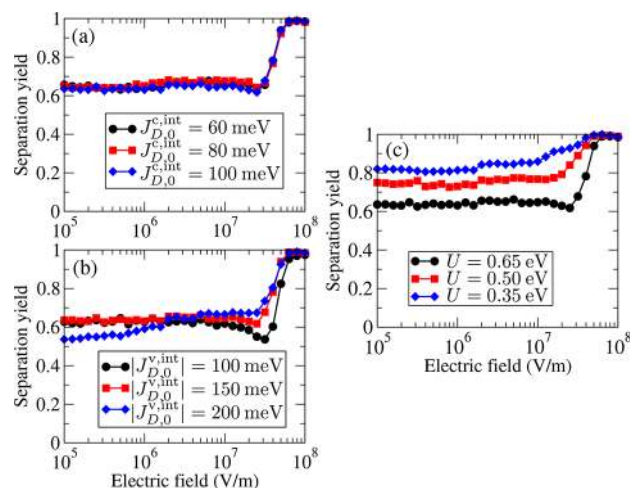


**Figure 11.** Field-dependent yield of charge separation starting from the closely separated donor exciton state ( $E_{\text{init}} = 2.0$  eV) for different values of (a) the electron transfer integral  $J_{D,0}^{c,\text{int}}$  in the donor, (b) the hole transfer integral  $J_{D,0}^{v,\text{int}}$  in the donor, and (c) the on-site Coulomb interaction  $U$ .

behavior is the fact that the donor exciton binding energy, which is a rough measure of the energy barrier that has to be overcome for free charges to form, is not strongly dependent on the carrier delocalization in the donor. The factor that primarily determines the binding energy of the donor exciton is the strength of the Coulomb interaction. In Figure 11c we present the field-dependent separation yield for different values of the on-site Coulomb interaction  $U$ . As anticipated, we find that lowering  $U$  leads to a higher separation yield.

The temperature-dependent separation yield at zero electric field is shown in Figure 12a. We see that lower temperature leads to lower separation yield because the phonon bath-assisted processes transferring an exciton in a donor state to the space-separated manifold (and, eventually, to a state of fully separated charges) are weaker. The separation yield exhibits a 6-fold decrease when the temperature is lowered from the room temperature to around 50 K. The intensity of the temperature

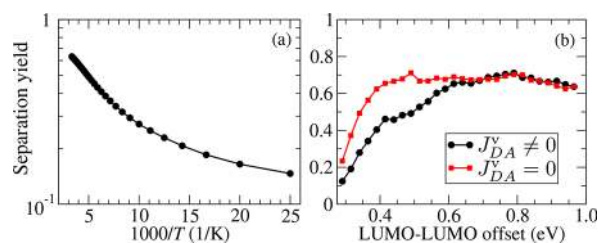


**Figure 12.** Yield of charge separation starting from the closely separated donor state ( $E_{\text{init}} = 2.0$  eV) at zero electric field as a function of (a) the temperature (in Arrhenius representation) and (b) the LUMO–LUMO offset. The reported values of the LUMO–LUMO offset refer to the ordered system. In (b), we present results in which acceptor states are included ( $J_{\text{DA}}^v \neq 0$ ) and excluded ( $J_{\text{DA}}^v = 0$ ) from the computation.

variation-induced effect on the separation yield is somewhat smaller than in case of the separation starting from the strongly bound CT state; compare to Figure 8a.

In the end, we examine how the value of the LUMO–LUMO offset affects charge separation from the closely separated donor state. Figure 12b presents the separation yield as a function of the LUMO–LUMO offset for the values of model parameters listed in Table 1 ( $J_{\text{DA}}^v \neq 0$ , circles), as well as for  $J_{\text{DA}}^v = 0$  (squares), that is, when states of acceptor excitons are excluded from the computation. For the LUMO–LUMO offset above approximately 0.6 eV, we observe that the separation yield in both cases is essentially the same and weakly dependent on the particular value of the LUMO–LUMO offset. This indicates that, in this range of LUMO–LUMO offsets, charge separation starting from the closely separated donor state does not involve acceptor exciton states, which once again validates our simple picture of charge separation from that state (formally embodied in eq 36). However, when the LUMO–LUMO offset is below 0.6 eV, the separation yield in case  $J_{\text{DA}}^v \neq 0$  starts to decrease with decreasing the LUMO–LUMO offset. On the other hand, in case  $J_{\text{DA}}^v = 0$ , a similar decrease in the separation yield is observed only when the LUMO–LUMO offset is lower than approximately 0.4 eV. The different behavior of the separation yield in the two cases signals that, when the LUMO–LUMO offset assumes values lower than ca. 0.6 eV, states of acceptor excitons are involved in charge separation, and the observed decrease is due to the recombination from acceptor states. As we have already noted in the analysis of Figure 8b, when the LUMO–LUMO offset is around 0.6 eV, the low-energy tails of the CT and acceptor exciton DOS become energetically close. Further analysis of recombination events from different groups of exciton states, which is presented in Figure S7, shows that the contribution of the recombination from acceptor states to the total recombination probability becomes appreciable when the LUMO–LUMO offset is around 0.6 eV. When acceptor states are excluded from the computation, the independence of the separation yield on the LUMO–LUMO offset is disturbed when the energy of the strongly bound CT state is approximately equal to the energy of the initial donor state, which occurs for the LUMO–LUMO offset below around 0.4 eV. For even smaller values of the LUMO–LUMO offset, all of the space-separated states are energetically above the initial donor state, meaning that full charge separation can be achieved only by means of energetically upward processes. The decrease in the separation yield with decreasing LUMO–LUMO offset

can then be attributed to an increased probability of recombination from donor states.

## DISCUSSION

This section is devoted to a more detailed discussion of some aspects of our model.

Let us start by commenting on our results in view of the reduced dimensionality of our model. Although formally one-dimensional, the proposed model of a bilayer can be regarded as a two (or three)-dimensional model consisting of periodically repeated chains similar to that shown in Figure 1 that are isolated from each other; that is, the transfer integrals between (neighboring) chains are equal to zero. We have established that, within our one-dimensional model, the degree of charge delocalization, quantified by the values of the electron and hole transfer integrals, is one of the factors influencing the (CT exciton) separation efficiency; see Figure 7a,b. On simple grounds, better delocalization is beneficial to charge separation because it increases the mean distance (in the direction of a single chain, which is perpendicular to the D/A interface) between the electron and hole located in the acceptor and donor, respectively. If we assigned nonzero values to transfer integrals coupling different chains, the charges could also delocalize along the direction perpendicular to the chains (parallel to the D/A interface) and further increase their separation. Therefore, it may be expected that the separation yield would be enhanced in such a genuinely two (or three)-dimensional model. This line of reasoning is supported by studies highlighting the beneficial role of hole delocalization along polymer chains in charge separation,<sup>28,33</sup> particularly if we keep in mind that the values of the intrachain transfer integrals are typically larger than those employed in this study. We may also say that the separation yields we obtain using an effectively one-dimensional model are the lower limit to those that would be obtained in a higher-dimensional system. Another possible interpretation of our results is that they suggest that, to describe fundamental reasons for efficient charge separation at all-organic bilayers, it is more important to properly account for charge delocalization than for dimensionality effects.

Next, we discuss our assumptions concerning the strength of the carrier–bath interaction. We take that the polaron binding energy is  $E_{\text{pol}} = 15$  meV, which is significantly lower than values commonly reported in electronic-structure studies of single PCBM molecules.<sup>44,66</sup> The selection of the values of model parameters implicitly suggests that each lattice site may be imagined to substitute a polymer chain or a group of fullerene molecules. In this regard, carrier transfer from one site to another should not be interpreted as transfer between single molecules supporting localized carrier states, but rather as transfer between two aggregates of molecules supporting delocalized carrier states. It has been demonstrated recently that, in such a case, the definition of  $E_{\text{pol}}$  (given in the text between eqs 22 and 23) should be corrected so as to take into account delocalization effects, which can substantially reduce  $E_{\text{pol}}$ .<sup>67</sup> Having all of these things considered, we believe that our choice of the magnitude of  $E_{\text{pol}}$  is reasonable. Larger  $E_{\text{pol}}$  (while keeping all other model parameters fixed) would result in a higher separation yield, because the phonon bath-induced transition rates (eq 18) would be larger. In this sense, our results may also be regarded as the lower limit to the separation yield computed for larger  $E_{\text{pol}}$ .

Another common choice for the spectral density  $J(E)$  (eq 17) when studying charge separation in photosynthetic<sup>55</sup> and

OPV systems<sup>51,68</sup> is the so-called Drude–Lorentz spectral density. Because of its algebraic decay at high energies, the Drude–Lorentz spectral density generally favors coupling to a wider range of phonon modes than does the Ohmic spectral density employed here. In Figure S8a–d, we find that the Drude–Lorentz spectral density promotes higher separation yield than the ohmic spectral density.

The next comment concerns the number of disorder realizations over which the averaging is performed and our definition of the contact region and contact states (eqs 8 and 9). In Figure S9a,b, we present the dependence of the (average) separation yield at zero electric field on the number of disorder realizations over which we average. We see that averaging over more than 200–300 disorder realizations does not lead to substantial changes in the separation yield. Figure S10a,b confirms that our results remain qualitatively (and to a good extent quantitatively) the same when the linear dimension  $l_c$  of the contact region and the threshold probability on the right-hand sides of eqs 8 and 9 are varied within reasonable limits.

In the end, we note that an approach to the separation of strongly bound CT state similar to ours (eq 34) has been recently implemented in ref 37. We point out that eq 34 can, for moderate disorder, reproduce the separation yield in single disorder realizations without any tunable parameters. On the other hand, the authors of ref 37 reproduce the nonmonotonic dependence of the separation yield on the disorder strength using a formula similar to eq 34, which contains disorder-averaged transition rates and a tunable parameter. Let us also mention that eq 34 bears certain similarity to the exciton dissociation probability in unintentionally doped polymer materials proposed by Arkhipov et al.<sup>69</sup> These authors also assumed that the formation of free carriers is a two-step process: the initial exciton dissociates by the electron transfer to the dopant, while the subsequent charge separation is due to combined effects of the internal electric field, hole delocalization, and carrier recombination. However, the phenomenon of our interest, that is, the formation of free charges at D/A interfaces, is significantly different from free-charge formation in lightly doped conjugated polymers. The model introduced in ref 69 was devised to rationalize the weak field and temperature dependence exhibited by the free-charge yield in doped polymers, which is much smaller than unity. To understand very efficient charge separation at organic D/A interfaces, this model was further amended in refs 28 and 30–32.

## CONCLUSION

Using a one-dimensional model of an all-organic bilayer, we have modeled and investigated the process of incoherent charge separation. Our model is microscopic, its parameters have clear physical significance, and their values are selected on the basis of literature data on OPV materials. The main advantage of our model is that it properly takes into account carrier delocalization, whose importance for efficient charge separation in OPV systems has been repeatedly recognized.<sup>26–28,30,32,33</sup> However, many studies on charge separation at organic heterointerfaces either employ the approximation of point-like charges,<sup>34,35,61,70</sup> or account for delocalization effects in an effective way (e.g., by introducing the carrier effective mass<sup>26,28,30,32,33</sup> or evenly smearing charge throughout the delocalization region<sup>27</sup>). On the other hand, here, carrier delocalization is fully and naturally taken into account by working in the exciton basis. The charge separation is then conceived as a sequence of environment-assisted transitions

among exciton basis states that terminates once a free-charge state is reached. Another important ingredient of our model is the diagonal static disorder, which is crucial to identify the counterparts of free-charge states within our description. We emphasize that the model and method employed in this study are very general. They may be potentially used, upon appropriate Hamiltonian modifications and suitable choice of the values of model parameters, to describe field-dependent charge generation in many different physical systems, for example, in a neat polymer material,<sup>14,71</sup> or at an interface between two polymer materials.

We obtain that the synergy between moderate energetic disorder and carrier delocalization can explain quite high and relatively weakly field-dependent separation efficiencies observed in solar cells photoexcited at the low-energy edge of the CT manifold,<sup>6</sup> see Figure 3a. At electric fields typically encountered in a working organic solar cell ( $F \sim 5\text{--}10\text{ V}/\mu\text{m}$ ), the efficiency of the separation of the strongly bound CT exciton is above 0.8. Our analytical treatment, which is sensible for not too strong disorder, reveals that the separation of the strongly bound CT exciton is actually governed by only a couple of parameters, see eq 34, among which the most important are the recombination rate from the initial CT state and the escape rate toward more separated and long-lived intermediate states. Because further separation from intermediate states can proceed without kinetic obstacles, the competition between the two aforementioned rates describes the separation quite well. However, strong disorder destroys this simple picture, because full charge separation then involves more than just a single rate-limiting step; compare the two curves in Figure 6. The remedy may then be enhancing carrier delocalization; see Figure 7a,b. This result is also in agreement with conclusions of ref 6, which emphasize that, in most efficient solar cells, the “cold” CT state is only weakly bound and quite delocalized. Moreover, we observe a much milder temperature dependence of the separation yield than the (predominantly) exponential one predicted by the Onsager–Braun model, see Figure 8a, in agreement with experimental<sup>65</sup> and theoretical studies.<sup>34</sup> The fact that larger LUMO–LUMO offsets favor more efficient free-charge generation out of the strongly bound CT state is attributed to an increased recombination probability from acceptor and donor states observed for smaller LUMO–LUMO offsets; see Figure 8b.

The separation of donor excitons is also quite efficient, and its yield depends on the exciton energy; see Figure 9. The electric field required to separate the closely separated donor exciton with certainty is almost an order of magnitude higher than that needed to separate the strongly bound CT exciton. Our results suggest that the separation of the closely separated donor exciton exhibits only one rate-limiting step, that is, the escape to the space-separated manifold. Carrier delocalization does not strongly influence this escape; see Figure 11a,b. The donor exciton separation shows weak temperature dependence, see Figure 12a, while its decrease with decreasing the LUMO–LUMO offset is attributed to the recombination from acceptor states, as in Figure 12b. Relatively weak disorder is beneficial to donor exciton separation, while strong disorder suppresses it; see Figure 10a,b.

In summary, our results provide unambiguous evidence that efficient charge separation can be achieved even out of strongly bound pair states and are supported by experiments<sup>6,13</sup> suggesting that free-charge generation predominantly occurs on long time scales, from localized initial conditions.

**■ ASSOCIATED CONTENT****■ Supporting Information**

The Supporting Information is available free of charge on the ACS Publications website at DOI: 10.1021/acs.jpcc.8b03114.

Numerical data complementing the discussion on the influence of various model parameters on the separation yield (PDF)

**■ AUTHOR INFORMATION****Corresponding Author**

\*Phone: +381 (0)11 3713152. E-mail: [nenad.vukmirovic@ipb.ac.rs](mailto:nenad.vukmirovic@ipb.ac.rs).

**ORCID**

Veljko Janković: 0000-0002-0297-2167

Nenad Vukmirović: 0000-0002-4101-1713

**Notes**

The authors declare no competing financial interest.

**■ ACKNOWLEDGMENTS**

We gratefully acknowledge the support by the Ministry of Education, Science and Technological Development of the Republic of Serbia (project no. ON171017) and the European Commission under H2020 project VI-SEEM, grant no. 675121, as well as the contribution of the COST Action MP1406. Numerical computations were performed on the PARADOX supercomputing facility at the Scientific Computing Laboratory of the Institute of Physics Belgrade.

**■ REFERENCES**

- (1) Gao, F.; Inganäs, O. Charge Generation in Polymer-Fullerene Bulk-Heterojunction Solar Cells. *Phys. Chem. Chem. Phys.* **2014**, *16*, 20291–20304.
- (2) Bäessler, H.; Köhler, A. "Hot or Cold": How do Charge Transfer States at the Donor-Acceptor Interface of an Organic Solar Cell Dissociate? *Phys. Chem. Chem. Phys.* **2015**, *17*, 28451–28462.
- (3) Ostroverkhova, O. Organic Optoelectronic Materials: Mechanisms and Applications. *Chem. Rev.* **2016**, *116*, 13279–13412.
- (4) Ponceca, C. S.; Chábera, P.; Uhlig, J.; Persson, P.; Sundström, V. Ultrafast Electron Dynamics in Solar Energy Conversion. *Chem. Rev.* **2017**, *117*, 10940–11024.
- (5) Park, S. H.; Roy, A.; Beaupré, S.; Cho, S.; Coates, N.; Moon, J. S.; Moses, D.; Leclerc, M.; Lee, K.; Heeger, A. J. Bulk Heterojunction Solar Cells with Internal Quantum Efficiency Approaching 100%. *Nat. Photonics* **2009**, *3*, 297–303.
- (6) Vandewal, K.; Albrecht, S.; Hoke, E. T.; Graham, K. R.; Widmer, J.; Douglas, J. D.; Schubert, M.; Mateker, W. R.; Bloking, J. T.; Burkhard, G. F.; et al. Efficient Charge Generation by Relaxed Charge-Transfer States at Organic Interfaces. *Nat. Mater.* **2014**, *13*, 63–68.
- (7) Jailaubekov, A. E.; Willard, A. P.; Tritsch, J. R.; Chan, W.-L.; Sai, N.; Gearba, R.; Kaake, L. G.; Williams, K. J.; Leung, K.; Rossky, P. J.; et al. Hot Charge-Transfer Excitons Set the Time Limit for Charge Separation at Donor/Acceptor Interfaces in Organic Photovoltaics. *Nat. Mater.* **2013**, *12*, 66–73.
- (8) Grancini, G.; Maiuri, M.; Fazzi, D.; Petrozza, A.; Egelhaaf, H.-J.; Brida, D.; Cerullo, G.; Lanzani, G. Hot Exciton Dissociation in Polymer Solar Cells. *Nat. Mater.* **2013**, *12*, 29–33.
- (9) Bakulin, A. A.; Rao, A.; Pavelyev, V. G.; van Loosdrecht, P. H. M.; Pshenichnikov, M. S.; Niedzialek, D.; Cornil, J.; Beljonne, D.; Friend, R. H. The Role of Driving Energy and Delocalized States for Charge Separation in Organic Semiconductors. *Science* **2012**, *335*, 1340–1344.
- (10) Falke, S. M.; Rozzi, C. A.; Brida, D.; Maiuri, M.; Amato, M.; Sommer, E.; de Sio, A.; Rubio, A.; Cerullo, G.; Molinari, E.; et al. Coherent Ultrafast Charge Transfer in an Organic Photovoltaic Blend. *Science* **2014**, *344*, 1001–1005.
- (11) Vithanage, D. A.; Devižis, A.; Abramavičius, V.; Infahsaeng, Y.; Abramavičius, D.; MacKenzie, R. C. I.; Keivanidis, P. E.; Yartsev, A.; Hertel, D.; Nelson, J.; et al. Visualizing Charge Separation in Bulk Heterojunction Organic Solar Cells. *Nat. Commun.* **2013**, *4*, 2334.
- (12) Devižis, A.; De Jonghe-Risse, J.; Hany, R.; Nüesch, F.; Jenatsch, S.; Gulbinas, V.; Moser, J.-E. Dissociation of Charge Transfer States and Carrier Separation in Bilayer Organic Solar Cells: A Time-Resolved Electroabsorption Spectroscopy Study. *J. Am. Chem. Soc.* **2015**, *137*, 8192–8198.
- (13) Grupp, A.; Ehrenreich, P.; Kalb, J.; Budweg, A.; Schmidt-Mende, L.; Brida, D. Incoherent Pathways of Charge Separation in Organic and Hybrid Solar Cells. *J. Phys. Chem. Lett.* **2017**, *8*, 4858–4864.
- (14) Gerhard, M.; Arndt, A. P.; Bilal, M.; Lemmer, U.; Koch, M.; Howard, I. A. Field-Induced Exciton Dissociation in PTB7-Based Organic Solar Cells. *Phys. Rev. B: Condens. Matter Mater. Phys.* **2017**, *95*, 195301.
- (15) Gerhard, M.; Arndt, A. P.; Howard, I. A.; Rahimi-Iman, A.; Lemmer, U.; Koch, M. Temperature- and Energy-Dependent Separation of Charge-Transfer States in PTB7-Based Organic Solar Cells. *J. Phys. Chem. C* **2015**, *119*, 28309–28318.
- (16) Janković, V.; Vukmirović, N. Identification of Ultrafast Photophysical Pathways in Photoexcited Organic Heterojunctions. *J. Phys. Chem. C* **2017**, *121*, 19602–19618.
- (17) Janković, V.; Vukmirović, N. Origin of Space-Separated Charges in Photoexcited Organic Heterojunctions on Ultrafast Time Scales. *Phys. Rev. B: Condens. Matter Mater. Phys.* **2017**, *95*, 075308.
- (18) Clarke, T. M.; Durrant, J. R. Charge Photogeneration in Organic Solar Cells. *Chem. Rev.* **2010**, *110*, 6736–6767.
- (19) Gregg, B. A. Entropy of Charge Separation in Organic Photovoltaic Cells: The Benefit of Higher Dimensionality. *J. Phys. Chem. Lett.* **2011**, *2*, 3013–3015.
- (20) Hood, S. N.; Kassal, I. Entropy and Disorder Enable Charge Separation in Organic Solar Cells. *J. Phys. Chem. Lett.* **2016**, *7*, 4495–4500.
- (21) Ono, S.; Ohno, K. Combined Impact of Entropy and Carrier Delocalization on Charge Transfer Exciton Dissociation at the Donor-Acceptor Interface. *Phys. Rev. B: Condens. Matter Mater. Phys.* **2016**, *94*, 075305.
- (22) Onsager, L. Initial Recombination of Ions. *Phys. Rev.* **1938**, *54*, 554–557.
- (23) Braun, C. L. Electric Field Assisted Dissociation of Charge Transfer States as a Mechanism of Photocarrier Production. *J. Chem. Phys.* **1984**, *80*, 4157–4161.
- (24) Wojcik, M.; Tachiya, M. Accuracies of the Empirical Theories of the Escape Probability Based on Eigen Model and Braun Model Compared with the Exact Extension of Onsager Theory. *J. Chem. Phys.* **2009**, *130*, 104107.
- (25) Goliber, T. E.; Perlstein, J. H. Analysis of Photogeneration in a Doped Polymer System in Terms of a Kinetic Model for Electric-Field-Assisted Dissociation of Charge-Transfer States. *J. Chem. Phys.* **1984**, *80*, 4162–4167.
- (26) Schwarz, C.; Tscheuschner, S.; Frisch, J.; Winkler, S.; Koch, N.; Bäessler, H.; Köhler, A. Role of the Effective Mass and Interfacial Dipoles on Exciton Dissociation in Organic Donor-Acceptor Solar Cells. *Phys. Rev. B: Condens. Matter Mater. Phys.* **2013**, *87*, 155205.
- (27) Deibel, C.; Strobel, T.; Dyakonov, V. Origin of the Efficient Polaron-Pair Dissociation in Polymer-Fullerene Blends. *Phys. Rev. Lett.* **2009**, *103*, 036402.
- (28) Nenashev, A. V.; Baranovskii, S. D.; Wiemer, M.; Jansson, F.; Österbacka, R.; Dvurechenskii, A. V.; Gebhard, F. Theory of Exciton Dissociation at the Interface Between a Conjugated Polymer and an Electron Acceptor. *Phys. Rev. B: Condens. Matter Mater. Phys.* **2011**, *84*, 035210.
- (29) Schwarz, C.; Bäessler, H.; Bauer, I.; Koenen, J.-M.; Preis, E.; Scherf, U.; Köhler, A. Does Conjugation Help Exciton Dissociation? A Study on Poly(p-phenylene)s in Planar Heterojunctions with C<sub>60</sub> or TNF. *Adv. Mater.* **2012**, *24*, 922–925.
- (30) Arkhipov, V. I.; Heremans, P.; Bäessler, H. Why is Exciton Dissociation So Efficient at the Interface Between a Conjugated

Polymer and an Electron Acceptor? *Appl. Phys. Lett.* **2003**, *82*, 4605–4607.

(31) Baranovskii, S. D.; Wiemer, M.; Nenashev, A. V.; Jansson, F.; Gebhard, F. Calculating the Efficiency of Exciton Dissociation at the Interface between a Conjugated Polymer and an Electron Acceptor. *J. Phys. Chem. Lett.* **2012**, *3*, 1214–1221.

(32) Tscheuschner, S.; Bäessler, H.; Huber, K.; Köhler, A. A Combined Theoretical and Experimental Study of Dissociation of Charge Transfer States at the Donor-Acceptor Interface of Organic Solar Cells. *J. Phys. Chem. B* **2015**, *119*, 10359–10371.

(33) Athanasopoulos, S.; Tscheuschner, S.; Bäessler, H.; Köhler, A. Efficient Charge Separation of Cold Charge-Transfer States in Organic Solar Cells Through Incoherent Hopping. *J. Phys. Chem. Lett.* **2017**, *8*, 2093–2098.

(34) van Eersel, H.; Janssen, R. A. J.; Kemerink, M. Mechanism for Efficient Photoinduced Charge Separation at Disordered Organic Heterointerfaces. *Adv. Funct. Mater.* **2012**, *22*, 2700–2708.

(35) Burke, T. M.; McGehee, M. D. How High Local Charge Carrier Mobility and an Energy Cascade in a Three-Phase Bulk Heterojunction Enable > 90% Quantum Efficiency. *Adv. Mater.* **2014**, *26*, 1923–1928.

(36) Rubel, O.; Baranovskii, S. D.; Stolz, W.; Gebhard, F. Exact Solution for Hopping Dissociation of Geminate Electron-Hole Pairs in a Disordered Chain. *Phys. Rev. Lett.* **2008**, *100*, 196602.

(37) Shi, L.; Lee, C. K.; Willard, A. P. The Enhancement of Interfacial Exciton Dissociation by Energetic Disorder Is a Nonequilibrium Effect. *ACS Cent. Sci.* **2017**, *3*, 1262–1270.

(38) Hoppe, H.; Sariciftci, N. S. Organic Solar Cells: An Overview. *J. Mater. Res.* **2004**, *19*, 1924–1945.

(39) Yuan, Y.; Reece, T. J.; Sharma, P.; Poddar, S.; Ducharme, S.; Gruverman, A.; Yang, Y.; Huang, J. Efficiency Enhancement in Organic Solar Cells with Ferroelectric Polymers. *Nat. Mater.* **2011**, *10*, 296–302.

(40) Savoie, B. M.; Rao, A.; Bakulin, A. A.; Gelin, S.; Movaghar, B.; Friend, R. H.; Marks, T. J.; Ratner, M. A. Unequal Partnership: Asymmetric Roles of Polymeric Donor and Fullerene Acceptor in Generating Free Charge. *J. Am. Chem. Soc.* **2014**, *136*, 2876–2884.

(41) Liu, T.; Troisi, A. What Makes Fullerene Acceptors Special as Electron Acceptors in Organic Solar Cells and How to Replace Them. *Adv. Mater.* **2013**, *25*, 1038–1041.

(42) Bäessler, H. Charge Transport in Disordered Organic Photovoltaics: A Monte Carlo Simulation Study. *Phys. Status Solidi B* **1993**, *175*, 15–56.

(43) Mladenović, M.; Vukmirović, N. Effects of Thermal Disorder on the Electronic Properties of Ordered Polymers. *Phys. Chem. Chem. Phys.* **2014**, *16*, 25950–25958.

(44) Cheung, D. L.; Troisi, A. Theoretical Study of the Organic Photovoltaic Electron Acceptor PCBM: Morphology, Electronic Structure, and Charge Localization. *J. Phys. Chem. C* **2010**, *114*, 20479–20488.

(45) Northrup, J. E. Atomic and Electronic Structure of Polymer Organic Semiconductors: P3HT, PQT, and PBTTT. *Phys. Rev. B: Condens. Matter Mater. Phys.* **2007**, *76*, 245202.

(46) Maillard, A.; Rochefort, A. Structural and Electronic Properties of Poly(3-hexylthiophene)  $\pi$ -stacked Crystals. *Phys. Rev. B: Condens. Matter Mater. Phys.* **2009**, *79*, 115207.

(47) Lan, Y.-K.; Huang, C.-I. A Theoretical Study of the Charge Transfer Behavior of the Highly Regioregular Poly-3-hexylthiophene in the Ordered State. *J. Phys. Chem. B* **2008**, *112*, 14857–14862.

(48) Cheung, D. L.; McMahon, D. P.; Troisi, A. Computational Study of the Structure and Charge-Transfer Parameters in Low-Molecular-Mass P3HT. *J. Phys. Chem. B* **2009**, *113*, 9393–9401.

(49) Street, R. A.; Hawks, S. A.; Khlyabich, P. P.; Li, G.; Schwartz, B. J.; Thompson, B. C.; Yang, Y. Electronic Structure and Transition Energies in Polymer-Fullerene Bulk Heterojunctions. *J. Phys. Chem. C* **2014**, *118*, 21873–21883.

(50) Bhatta, R. S.; Tsige, M. Chain Length and Torsional Dependence of Exciton Binding Energies in P3HT and PTB7

Conjugated Polymers: A First-Principles Study. *Polymer* **2014**, *55*, 2667–2672.

(51) Smith, S. L.; Chin, A. W. Phonon-Assisted Ultrafast Charge Separation in the PCBM Band Structure. *Phys. Rev. B: Condens. Matter Mater. Phys.* **2015**, *91*, 201302.

(52) Grancini, G.; Polli, D.; Fazzi, D.; Cabanillas-Gonzalez, J.; Cerullo, G.; Lanzani, G. Transient Absorption Imaging of P3HT:PCBM Photovoltaic Blend: Evidence For Interfacial Charge Transfer State. *J. Phys. Chem. Lett.* **2011**, *2*, 1099–1105.

(53) Liu, T.; Troisi, A. Absolute Rate of Charge Separation and Recombination in a Molecular Model of the P3HT/PCBM Interface. *J. Phys. Chem. C* **2011**, *115*, 2406–2415.

(54) Kanai, Y.; Grossman, J. C. Insights on Interfacial Charge Transfer Across P3HT/Fullerene Photovoltaic Heterojunction from Ab Initio Calculations. *Nano Lett.* **2007**, *7*, 1967–1972.

(55) Kell, A.; Feng, X.; Reppert, M.; Jankowiak, R. On the Shape of the Phonon Spectral Density in Photosynthetic Complexes. *J. Phys. Chem. B* **2013**, *117*, 7317–7323.

(56) Coropceanu, V.; Cornil, J.; da Silva Filho, D. A.; Olivier, Y.; Silbey, R.; Brédas, J.-L. Charge Transport in Organic Semiconductors. *Chem. Rev.* **2007**, *107*, 926–952.

(57) Meisel, K. D.; Vocks, H.; Bobbert, P. A. Polarons in Semiconducting Polymers: Study within an Extended Holstein Model. *Phys. Rev. B: Condens. Matter Mater. Phys.* **2005**, *71*, 205206.

(58) Proctor, C. M.; Kuik, M.; Nguyen, T.-Q. Charge Carrier Recombination in Organic Solar Cells. *Prog. Polym. Sci.* **2013**, *38*, 1941–1960.

(59) Dimitrov, S. D.; Schroeder, B. C.; Nielsen, C. B.; Bronstein, H.; Fei, Z.; McCulloch, I.; Heeney, M.; Durrant, J. R. Singlet Exciton Lifetimes in Conjugated Polymer Films for Organic Solar Cells. *Polymers* **2016**, *8*, 14.

(60) Kirchartz, T.; Taretto, K.; Rau, U. Efficiency Limits of Organic Bulk Heterojunction Solar Cells. *J. Phys. Chem. C* **2009**, *113*, 17958–17966.

(61) Offermans, T.; Meskers, S. C. J.; Janssen, R. A. J. Monte-Carlo Simulations of Geminate Electron-Hole Pair Dissociation in a Molecular Heterojunction: A Two-Step Dissociation Mechanism. *Chem. Phys.* **2005**, *308*, 125–133.

(62) Arndt, A. P.; Gerhard, M.; Quintilla, A.; Howard, I. A.; Koch, M.; Lemmer, U. Time-Resolved Charge-Transfer State Emission in Organic Solar Cells: Temperature and Blend Composition Dependences of Interfacial Traps. *J. Phys. Chem. C* **2015**, *119*, 13516–13523.

(63) Choi, J. H.; Son, K.-L.; Kim, T.; Kim, K.; Ohkubo, K.; Fukuzumi, S. Thienyl-Substituted Methanofullerene Derivatives for Organic Photovoltaic Cells. *J. Mater. Chem.* **2010**, *20*, 475–482.

(64) Deibel, C.; Strobel, T.; Dyakonov, V. Role of the Charge Transfer State in Organic Donor-Acceptor Solar Cells. *Adv. Mater.* **2010**, *22*, 4097–4111.

(65) Lee, J.; Vandewal, K.; Yost, S. R.; Bahlke, M. E.; Goris, L.; Baldo, M. A.; Manca, J. V.; Voorhis, T. V. Charge Transfer State Versus Hot Exciton Dissociation in Polymer-Fullerene Blended Solar Cells. *J. Am. Chem. Soc.* **2010**, *132*, 11878–11880.

(66) Idé, J.; Fazzi, D.; Casalegno, M.; Meille, S. V.; Raos, G. Electron Transport in Crystalline PCBM-Like Fullerene Derivatives: A Comparative Computational Study. *J. Mater. Chem. C* **2014**, *2*, 7313–7325.

(67) Taylor, N. B.; Kassal, I. Generalised Marcus Theory for Multi-Molecular Delocalised Charge Transfer. *Chem. Sci.* **2018**, *9*, 2942–2951.

(68) Yan, Y.; Song, L.; Shi, Q. Understanding the Free Energy Barrier and Multiple Timescale Dynamics of Charge Separation in Organic Photovoltaic Cells. *J. Chem. Phys.* **2018**, *148*, 084109.

(69) Arkhipov, V.; Emelianova, E.; Bäessler, H. Dopant-Assisted Charge Carrier Photogeneration in Conjugated Polymers. *Chem. Phys. Lett.* **2003**, *372*, 886–892.

(70) Peumans, P.; Forrest, S. R. Separation of Geminate Charge-Pairs at Donor-Acceptor Interfaces in Disordered Solids. *Chem. Phys. Lett.* **2004**, *398*, 27–31.

(71) Menšík, M.; Pflieger, J.; Rybak, A.; Jung, J.; Ulański, J.; Halašová, K.; Vohlídal, J. Photogeneration of Free Charge Carriers in Tenuously Packed  $\pi$  Conjugated Polymer Chains. *Polym. Adv. Technol.* **2011**, *22*, 2075–2083.

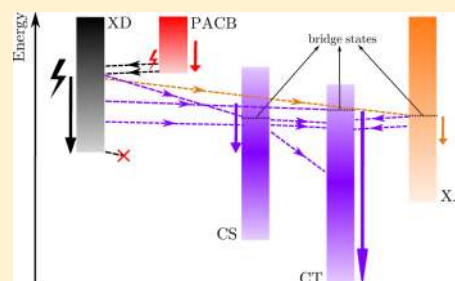
# Identification of Ultrafast Photophysical Pathways in Photoexcited Organic Heterojunctions

Veljko Janković<sup>1</sup> and Nenad Vukmirović\*

Scientific Computing Laboratory, Center for the Study of Complex Systems, Institute of Physics Belgrade, University of Belgrade, Pregrevica 118, 11080 Belgrade, Serbia

## Supporting Information

**ABSTRACT:** The exciton dissociation and charge separation occurring on subpicosecond time scales following the photoexcitation are studied in a model donor/acceptor heterojunction using a fully quantum approach. Higher-than-LUMO acceptor orbitals which are energetically aligned with the donor LUMO orbital participate in the ultrafast interfacial dynamics by creating photon-absorbing charge-bridging states in which charges are spatially separated and which can be directly photoexcited. Along with the states brought about by single-particle resonances, the two-particle (exciton) mixing gives rise to bridge states in which charges are delocalized. Bridge states open up a number of photophysical pathways that indirectly connect the initial donor states with states of spatially separated charges and compete with the efficient progressive deexcitation within the manifold of donor states. The diversity and efficiency of these photophysical pathways depend on a number of factors, such as the precise energy alignment of exciton states, the central frequency of the excitation, and the strength of carrier–phonon interaction.



## INTRODUCTION

Tremendous research efforts have been devoted to understanding the microscopic mechanisms governing efficient and ultrafast (happening on a  $\lesssim 100$  fs time scale) free-charge generation observed in time-resolved experiments on donor/acceptor (D/A) heterojunction organic photovoltaic (OPV) devices.<sup>1–4</sup> The photogenerated exciton in the donor material is commonly believed to transform into the charge transfer (CT) exciton.<sup>5,6</sup> In the CT exciton, the electron and hole are tightly bound and localized at the D/A interface. The Coulomb barrier preventing the electron and hole in the CT state from further charge separation and formation of a charge separated (CS) state is much higher than the thermal energy at room temperature, so that the actual mechanism of the emergence of spatially separated charges on such short time scales remains an open question.<sup>7–10</sup>

Electronically hot CT states, which are essentially resonant with the initial states of donor excitons and exhibit significant charge delocalization,<sup>11,12</sup> are believed to be precursors to separated charges present on ultrafast time scales following the excitation.<sup>1,2,13–16</sup> The delocalization of carriers can also reduce the Coulomb barrier and allow the transition from CT to CS exciton.<sup>3,17–19</sup> The ultrafast exciton dissociation and charge separation are not purely electronic processes, but are instead mediated by the carrier–phonon coupling.<sup>17,20–26</sup> The phonon-mediated ultrafast exciton dissociation and charge separation can proceed via the so-called intermediate bridge states,<sup>20,25</sup> the vibronically hot CT states,<sup>17</sup> or can occur without any intermediate CT state.<sup>24</sup> The exciton states of mixed donor and CS character are found to open up different photophysical pathways for ultrafast dissociation of initial

donor excitons, which are concurrent with vibronically assisted transitions within the donor exciton manifold.<sup>23</sup>

We have recently investigated the exciton dynamics occurring on a subpicosecond time scale following the excitation of the model D/A heterojunction.<sup>27</sup> Our model explicitly takes into account the physical mechanisms regarded as highly relevant for the ultrafast heterojunction dynamics, such as the carrier delocalization and the carrier–phonon interaction. Moreover, the exciton generation, exciton dissociation, and further charge separation are treated on equal footing and on a fully quantum level, which is essential to correctly describe processes taking place on ultrafast time scales. For the model parameters representative of a low-bandgap polymer/fullerene blend, we found that the major part of space-separated charges present on 100 fs time scales after the excitation originates from the direct optical generation from the ground state rather than from the ultrafast population transfer from initially generated donor excitons. The resonant mixing between single-electron states in the two materials leads to the redistribution of oscillator strengths between states of donor excitons and space-separated charges, the latter becoming accessible by direct photoexcitation.

In this study, we aim at giving a more detailed description of the ultrafast heterojunction dynamics in terms of particular photophysical pathways along which it proceeds. In order to keep the numerical effort within reasonable limits, we still use one-dimensional model of a heterojunction, but we extend it by

Received: June 7, 2017

Revised: August 3, 2017

Published: August 17, 2017



taking into account more than only one single-electron (single-hole) state per site. The model parameters are chosen to be representative of the prototypical blend of poly-3-hexylthiophene (P3HT) and [6,6]-phenyl-C<sub>61</sub> butyric acid methyl ester (PCBM). The aforementioned extension of the model is important in many aspects. First, the degeneracy of the LUMO, LUMO+1, and LUMO+2 orbitals of the C<sub>60</sub> molecule is broken in its functionalized derivative PCBM,<sup>28–30</sup> giving rise to three energetically close bands of electronic states of PCBM aggregates. This fact was shown to be important for efficient and ultrafast charge separation observed in D/A blends containing PCBM as the acceptor.<sup>14,25,31</sup> Upon the functionalization of C<sub>60</sub>, together with the degeneracy of its LUMO, LUMO+1, and LUMO+2 orbitals, the degeneracy of its LUMO+3, LUMO+4, and LUMO+5 orbitals, which are situated at around 1 eV above the LUMO, LUMO+1, and LUMO+2 orbitals, is also broken. Second, according to the results of Ma and Troisi,<sup>32</sup> the precise energy alignment of higher-than-LUMO orbitals of the acceptor can modulate the exciton dissociation rate by orders of magnitude by opening up new exciton dissociation channels. The LUMO–LUMO offset in the P3HT/PCBM blend can be quite large (around 1 eV)<sup>33–35</sup> and thus comparable to the energy separation between LUMO and LUMO+3 orbitals of the PCBM molecule. It can therefore be expected that the electronic states of a PCBM aggregate, which arise from LUMO+3, LUMO+4, and LUMO+5 orbitals of the PCBM molecule may play nontrivial role in the ultrafast interfacial dynamics. Surprisingly, it seems that the effect of these orbitals has not received enough attention in previous model studies of the P3HT/PCBM heterojunction. The ultrafast electron transfer observed in ref 36 has been ascribed to the energy overlap between the state of the photoexcited electron and the electronic states of the fullerene aggregate. The result presented in Figure 3e of ref 36 suggests that this overlap involves the electronic states of the fullerene aggregate stemming from the LUMO+3, LUMO+4, and LUMO+5 orbitals of the PCBM molecule.

Our results indicate that the exciton states in which the charges are delocalized throughout the heterojunction play a crucial role in the ultrafast heterojunction dynamics. In the low-energy part of the exciton spectrum, such states emerge due to the resonant mixing between different exciton (i.e., two-particle) states, and we denote them as bridge states. However, in the high-energy region of the exciton spectrum, such states form as a consequence of the resonant mixing between single-electron states in the donor and acceptor (states originating from LUMO+3, LUMO+4, and LUMO+5 orbitals of the PCBM molecule). The relevant exciton states of this kind are those in which the charges are spatially separated (the electron is mainly in the acceptor, while the hole is mainly in the donor) and we denote them as photon-absorbing charge-bridging (PACB) states,<sup>28,37,38</sup> since they can be directly reached by a photoexcitation. Exciting well above the lowest donor state, we find that excitons are generated in both donor and PACB states, while the major part of space-separated charges present on a 100 fs time scale following the excitation resides in PACB states. The deexcitation of initial PACB excitons proceeds via the donor exciton manifold, while single-phonon-assisted processes involving a PACB state and CT and CS states belonging to the low-energy part of the spectrum are virtually absent. The donor excitons mainly deexcite within the donor exciton manifold and, before reaching the lowest donor exciton state, may perform transitions to bridge states, which are

gateways into the space-separated manifold. The lowest donor state, being essentially decoupled from the space-separated manifold, is a trap state for exciton dissociation. The bridge states can be either intermediate or final states in the course of the charge separation. Once a space-separated state is reached, the gradual energy loss within the space-separated manifold leads to the population of low-energy CT states on a picosecond time scale. The participation of PACB excitons in the total exciton population strongly depends on the central frequency of the excitation. The probability of a bridge state being accessed during the exciton deexcitation sensitively depends on the distribution of initially generated excitons, the energy level alignment, and the carrier–phonon interaction strength.

## MODEL AND METHODS

**Model Hamiltonian.** We use the standard semiconductor Hamiltonian with multiple single-electron/single-hole states per site. The model heterojunction consists of  $2N$  sites located on a one-dimensional lattice of constant  $a$ : sites  $0, \dots, N-1$  belong to the donor part, while sites  $N, \dots, 2N-1$  belong to the acceptor part of the heterojunction. The single-electron levels on site  $i$  are counted by index  $\beta_i$ , so that Fermi operators  $c_{i\beta_i}^\dagger$  ( $c_{i\beta_i}$ ) create (destroy) electrons on site  $i$  and in single-electron state  $\beta_i$ . Analogously, single-hole levels on site  $i$  are counted by index  $\alpha_i$ , so that Fermi operators  $d_{i\alpha_i}^\dagger$  ( $d_{i\alpha_i}$ ) create (destroy) holes on site  $i$  and in single-hole state  $\alpha_i$ . Each site contributes a number of localized phonon modes and the corresponding Bose operators  $b_{i\lambda_i}^\dagger$  ( $b_{i\lambda_i}$ ) create (annihilate) phonons belonging to mode  $\lambda_i$  on site  $i$ . The Hamiltonian has the form

$$H = H_c + H_p + H_{c-p} + H_{c-f} \quad (1)$$

where  $H_c$  describes interacting carriers

$$H_c = \sum_{\substack{i\beta_i \\ j\beta_j}} \epsilon_{(i\beta_i)(j\beta_j)}^c c_{i\beta_i}^\dagger c_{j\beta_j} - \sum_{\substack{i\alpha_i \\ j\alpha_j}} \epsilon_{(i\alpha_i)(j\alpha_j)}^v d_{i\alpha_i}^\dagger d_{j\alpha_j} + \frac{1}{2} \sum_{\substack{i\beta_i \\ j\beta_j}} V_{ij} c_{i\beta_i}^\dagger c_{j\beta_j}^\dagger c_{j\beta_j} c_{i\beta_i} + \frac{1}{2} \sum_{\substack{i\alpha_i \\ j\alpha_j}} V_{ij} d_{i\alpha_i}^\dagger d_{j\alpha_j}^\dagger d_{j\alpha_j} d_{i\alpha_i} - \sum_{\substack{i\beta_i \\ j\alpha_j}} V_{ij} c_{i\beta_i}^\dagger d_{j\alpha_j}^\dagger d_{j\alpha_j} c_{i\beta_i} \quad (2)$$

$$H_p = \sum_{i\lambda_i} \hbar\omega_{i\lambda_i} b_{i\lambda_i}^\dagger b_{i\lambda_i} \quad (3)$$

is the phonon part of the Hamiltonian,  $H_{c-p}$  accounts for the carrier–phonon interaction

$$H_{c-p} = \sum_{i\beta_i} \sum_{\lambda_i} g_{i\beta_i\lambda_i}^c c_{i\beta_i}^\dagger c_{i\beta_i} (b_{i\lambda_i}^\dagger + b_{i\lambda_i}) - \sum_{i\alpha_i} \sum_{\lambda_i} g_{i\alpha_i\lambda_i}^v d_{i\alpha_i}^\dagger d_{i\alpha_i} (b_{i\lambda_i}^\dagger + b_{i\lambda_i}) \quad (4)$$

whereas  $H_{c-f}$  represents the interaction of carriers with the external electric field  $E(t)$

$$H_{c-f} = -E(t) \sum_{i\alpha\beta_i} d_{i\alpha\beta_i}^{cv} (c_{i\beta_i}^\dagger d_{i\alpha}^\dagger + d_{i\alpha} c_{i\beta_i}) \quad (5)$$

In our model, quantities  $\epsilon_{(i\beta_i)(j\beta_j)}^c$  ( $\epsilon_{(i\alpha_i)(j\alpha_j)}^v$ ), which represent electron (hole) on-site energies and transfer integrals, are

nonzero only for certain combinations of their indices. Namely,  $\epsilon_{(i\beta)(j\beta')}^c$  is nonzero when it represents

- (1) on-site energy  $\epsilon_{i\beta_i}^c$  of electron level  $\beta_i$  on site  $i$  for  $i = j$  and  $\beta_i = \beta'_i$ ;
- (2) negative electron transfer integral between nearest neighbors of band  $\beta_j - J_{i\beta_i}^{\text{int}}$ , for  $i$  and  $j$  both belonging to the same part of the heterojunction,  $|i - j| = 1$ , and  $\beta_i = \beta'_i$ ;
- (3) negative electron transfer integral between nearest neighbors of different bands,  $-J_{i\beta_i\beta'_i}^{\text{ext}}$ , for  $i$  and  $j$  both belonging to the same part of the heterojunction,  $|i - j| = 1$ , and  $\beta_i \neq \beta'_i$ ;
- (4) negative electron transfer integral between different parts of the heterojunctions,  $-J_{DA}^c$  for  $i = N - 1$  and  $j = N$  or vice versa.

The Coulomb interaction described by eq 2 is taken into account in the lowest monopole–monopole approximation and the interaction potential  $V_{ij}$  is assumed to be the Ohno potential

$$V_{ij} = \frac{U}{\sqrt{1 + \left(\frac{r_{ij}}{r_0}\right)^2}} \quad (6)$$

where  $U$  is the on-site Coulomb interaction,  $r_{ij}$  is the distance between sites  $i$  and  $j$ ,  $r_0 = e^2/(4\pi\epsilon_0\epsilon_r U)$  is the characteristic length, and  $\epsilon_r$  is the relative dielectric constant. Charge carriers are assumed to be locally and linearly coupled to the set of phonon modes (Holstein-type interaction), as given in eq 4. We assume that the frequency of the external electric field is such that it creates electron–hole excitations, the interband matrix elements of the dipole moment being  $d_{i\alpha\beta}^{\text{cv}}$ , and neglect all intraband dipole matrix elements.

**Theoretical Framework.** Ultrafast exciton dynamics governed by the model Hamiltonian defined in eqs 1–5 is treated using the density matrix formalism complemented with the dynamics controlled truncation (DCT) scheme.<sup>27,39–42</sup> Exciton generation (from initially unexcited heterojunction) by means of a pulsed excitation and subsequent evolution of thus created nonequilibrium state of the system are treated on equal footing. We consider the case of weak excitation and low carrier densities. The carrier branch of the hierarchy of equations produced by the density matrix formalism can then be truncated retaining only contributions up to the second order in the exciting field. The truncation of the phonon branch of the hierarchy is performed to ensure the conservation of the particle-number and energy after the pulsed excitation.<sup>42</sup>

It is advantageous to formulate theory in the subspace of single electron–hole excitations, which is spanned by the so-called exciton basis. The most general electron–hole pair state is of the form  $|x\rangle = \sum_{i\alpha_j} \psi_{(i\alpha)(j\beta)}^x c_{j\beta}^\dagger d_{i\alpha}^\dagger |0\rangle$ , where  $|0\rangle$  is the vacuum of electron–hole pairs. The exciton basis states are obtained by solving the eigenvalue problem  $H_c|x\rangle = \hbar\omega_x|x\rangle$ ,

which in the basis of single-particle states localized at lattice sites reads as

$$\sum_{\substack{i'\alpha'_i \\ i'\beta'_j}} (\delta_{ii'}\delta_{\alpha\alpha'}\epsilon_{(j\beta)(j'\beta')}^c - \delta_{jj'}\delta_{\beta\beta'}\epsilon_{(i\alpha)(i'\alpha')}^v) \psi_{(i'\alpha')(j'\beta')}^x - \delta_{ii'}\delta_{\alpha\alpha'}\delta_{jj'}\delta_{\beta\beta'}V_{ij})\psi_{(i'\alpha')(j'\beta')}^x = \hbar\omega_x\psi_{(i\alpha)(j\beta)}^x \quad (7)$$

The operator which creates an exciton in state  $x$  is defined through

$$X_x^\dagger = \sum_{\substack{i\alpha_i \\ j\beta_j}} \psi_{(i\alpha)(j\beta)}^x c_{j\beta}^\dagger d_{i\alpha}^\dagger \quad (8)$$

The total Hamiltonian (eq 1), in which we keep only operators whose expectation values are at most of the second order in the exciting field, can be expressed in terms of exciton creation and annihilation operators as

$$H = \sum_x \hbar\omega_x X_x^\dagger X_x + \sum_{i\lambda_i} \hbar\omega_{i\lambda_i} b_{i\lambda_i}^\dagger b_{i\lambda_i} + \sum_{\substack{\bar{x}x \\ i\lambda_i}} (\Gamma_{\bar{x}x}^{i\lambda_i} X_{\bar{x}}^\dagger X_x b_{i\lambda_i}^\dagger + \Gamma_{\bar{x}x}^{i\lambda_i*} X_x^\dagger X_{\bar{x}} b_{i\lambda_i}) - E(t) \sum_x (M_x^* X_x + M_x X_x^\dagger). \quad (9)$$

Dipole-moment matrix elements for the direct generation (from the ground state) of excitons in state  $x$  are given as

$$M_x = \sum_i \sum_{\alpha\beta} \psi_{(i\alpha)(i\beta)}^{x*} d_{i\alpha\beta}^{\text{cv}} \quad (10)$$

while exciton–phonon matrix elements describing transitions from exciton state  $x$  to exciton state  $\bar{x}$  assisted by phonon ( $i\lambda_i$ ) are

$$\Gamma_{\bar{x}x}^{i\lambda_i} = \sum_{\beta_i} \sum_{j\alpha_j} g_{i\beta_j\lambda_i}^c \psi_{(j\alpha)(i\beta)}^{\bar{x}*} \psi_{(j\alpha)(i\beta)}^x - \sum_{\alpha_i} \sum_{j\beta_j} g_{i\alpha_j\lambda_i}^v \psi_{(i\alpha)(j\beta)}^{\bar{x}*} \psi_{(i\alpha)(j\beta)}^x \quad (11)$$

Active variables in our formalism are electronic density matrices  $y_x = \langle X_x \rangle$  and  $n_{\bar{x}x} = \langle X_{\bar{x}}^\dagger X_x \rangle$ , along with their single-phonon-assisted counterparts  $y_{x(i\lambda_i)^-} = \langle X_x b_{i\lambda_i} \rangle$ ,  $y_{x(i\lambda_i)^+} = \langle X_x b_{i\lambda_i}^\dagger \rangle$ , and  $n_{\bar{x}x(i\lambda_i)^+} = \langle X_{\bar{x}}^\dagger X_x b_{i\lambda_i}^\dagger \rangle$ . The equations of motion for these variables are given in the Supporting Information. Since the phonon branch of the hierarchy is truncated at the level of second-order phonon assistance, our treatment of the electron–phonon interaction does not capture properly the processes with higher-order phonon assistance, which are important for stronger electron–phonon interaction. In this case, the feedback effects of electronic excitations on phonons would have to be taken into account as well. To this end, in our recent publication<sup>27</sup> we performed a computation of subpicosecond dynamics using surface hopping approach (which, however, treats lattice dynamics classically) and found that the feedback effects were not very pronounced. In order to treat the electron–phonon interaction more accurately, other approaches based on state-of-the-art multiconfigurational techniques,<sup>23</sup> infinite resummation within Green's function formalism<sup>43,44</sup> or variational ansätze for the wave function of electron–phonon system<sup>45</sup> can be used.

The early stages of our numerical experiment (during and immediately after the pulsed excitation) are dominated by exciton coherences with the ground state  $y_x$  and their phonon-assisted counterparts. The corresponding coherent exciton populations  $|y_x|^2$  are not a measure of the number of truly bound electron–hole pairs and generally decay quickly after the pulsed excitation, converting into incoherent exciton populations. This conversion from coherent to incoherent exciton populations is in our model mediated by the carrier–phonon interaction. The incoherent exciton populations are defined as

$$\bar{n}_{xx} = n_{xx} - |y_x|^2 \quad (12)$$

They represent numbers of Coulomb-correlated electron–hole pairs and typically exist for a long time after the decay of coherent populations. The incoherent populations of various groups  $X$  of exciton states are defined as

$$N_X^{\text{incoh}} = \sum_{x \in X} \bar{n}_{xx} \quad (13)$$

and are frequently and conveniently normalized to the total exciton population

$$N_{\text{tot}} = \sum_x n_{xx} \quad (14)$$

which is conserved after the excitation. Once created from coherent populations, incoherent populations redistribute among various exciton states, the redistribution being mediated by the carrier–phonon interaction. In order to gain insight into the pathways along which these redistribution processes proceed, we define energy- and time-resolved exciton populations  $\varphi_X(E, t)$  of states belonging to group  $X$  as

$$\varphi_X(E, t) = \frac{1}{N_{\text{tot}}} \sum_{x \in X} n_{xx}(t) \delta(E - \hbar\omega_x) \quad (15)$$

so that  $\varphi_X(E, t) \Delta E$  is the number (normalized to  $N_{\text{tot}}$ ) of excitons from group  $X$  residing in the states whose energies are between  $E$  and  $E + \Delta E$ . Bearing in mind eq 12, relating the coherent, incoherent, and total exciton population of state  $x$ , quantity  $\varphi_X(E, t)$  can be decomposed into its coherent

$$\varphi_X^{\text{coh}}(E, t) = \frac{1}{N_{\text{tot}}} \sum_{x \in X} |y_x(t)|^2 \delta(E - \hbar\omega_x) \quad (16)$$

and incoherent part

$$\varphi_X^{\text{incoh}}(E, t) = \frac{1}{N_{\text{tot}}} \sum_{x \in X} \bar{n}_{xx}(t) \delta(E - \hbar\omega_x) \quad (17)$$

The plots of  $\varphi_X^{\text{coh}}$  as a function of  $E$  and  $t$  provide information about states in which excitons are initially generated (the initial exciton distribution) and the time scale on which the conversion from coherent to incoherent exciton populations takes place. The plots of  $\varphi_X^{\text{incoh}}$  as a function of  $E$  and  $t$  reveal actual pathways along which (incoherent) excitons are redistributed, starting from the initial exciton distribution.

**Parameterization of the Model Hamiltonian.** Our model is parametrized with the aim of describing ultrafast exciton dissociation and charge separation in the direction perpendicular to the D/A interface. This is motivated by recent studies of ultrafast exciton dissociation<sup>46</sup> and charge separation<sup>19</sup> in two-dimensional models of a D/A polymeric heterojunction which have suggested that these processes crucially depend on the electronic properties and geometry in the direction

perpendicular to the interface. In actual computations, we take one single-electron level per site in the donor and one single-hole level per site in both the donor and acceptor. In order to mimic the presence of higher-than-LUMO orbitals energetically close to the LUMO level (which is a situation typical of fullerenes), as well as to investigate the effects of single-electron levels situated at around 1.0 eV above the LUMO level on the exciton dissociation, we take four single-electron levels per site in the acceptor. Different types of electronic couplings are schematically indicated in Figure 1, while the values of model parameters

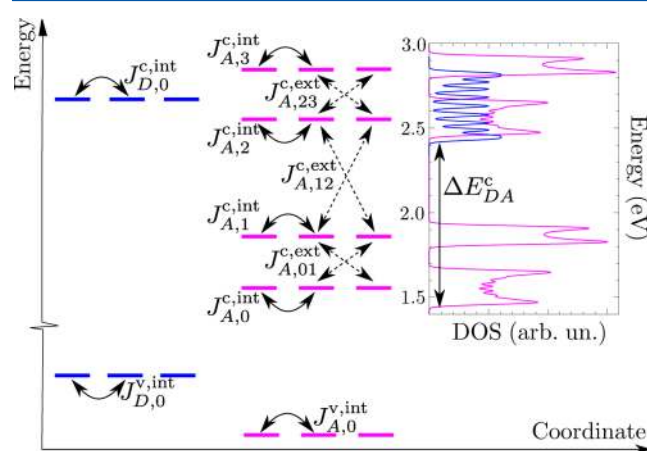


**Figure 1.** Illustration of the model system indicating different transfer integrals present in Table 1. The plot on the right shows the single-particle DOS for electrons in the neat donor (blue curve) and acceptor (magenta curve) materials obtained using the values of relevant parameters listed in Table 1. The electronic states of the isolated materials are computed by diagonalizing the free-electron Hamiltonian (the first term on the right-hand side of eq 2) in which the D/A coupling is set to 0. The DOS was then calculated by broadening each of the states obtained by a Gaussian with the standard deviation of 10 meV.

used in computations are summarized in Table 1. These values are selected so that the main characteristics of the single-particle and exciton spectrum (band widths, band alignments, exciton and charge transfer state binding energies) within the model correspond to the ones observed in P3HT/PCBM material system. We take the HOMO level of the donor material to be the zero of the energy scale.

The value of the lattice spacing  $a$  agrees with the typical distance between constitutive elements of organic semiconductors. The number of sites in a single material  $N = 11$  is reasonable since typical linear dimensions of phase segregated domains in bulk heterojunction morphology are 10–20 nm.<sup>47</sup> The value of the transfer integral  $J_{D,0}^{v,int}$  was chosen so as to agree with the HOMO bandwidth along the  $\pi$ -stacking direction of the regioregular P3HT<sup>48,49</sup> and the values of the hole transfer integral along the  $\pi$ -stacking direction of the same material.<sup>50,51</sup> The electron transfer integral  $J_{D,0}^{c,int}$  should be of similar magnitude as the hole transfer integral along the  $\pi$ -stacking direction.<sup>50</sup> Energies of the single-electron and single-hole levels in the donor, as well as the on-site Coulomb interaction  $U$ , were chosen so that the lowest donor exciton state is located at around 2.0 eV, while the HOMO–LUMO gap (single-particle gap) is around 2.4 eV, i.e., the binding energy of the donor exciton is around 0.4 eV.<sup>52,53</sup>

Electron transfer integrals in the acceptor  $J_{A,0}^{c,int}$ ,  $J_{A,1}^{c,int}$  and  $J_{A,0}^{c,ext}$ , together with the energy difference  $\epsilon_{A,1}^c - \epsilon_{A,0}^c$  between

Table 1. Values of Model Parameters Used in Computations

parameter	value
$N$	11
$a$ (nm)	1.0
$U$ (eV)	0.65
$\epsilon_r$	3.0
$\epsilon_{D,0}^c$ (eV)	2.63
$J_{D,0}^{\text{int}}$ (eV)	0.1
$\epsilon_{D,0}^v$ (eV)	-0.3
$J_{D,0}^{\text{int}}$ (eV)	-0.15
$\epsilon_{A,0}^c$ (eV)	1.565
$\epsilon_{A,1}^c$ (eV)	1.865
$\epsilon_{A,2}^c$ (eV)	2.565
$\epsilon_{A,3}^c$ (eV)	2.865
$J_{A,0}^{\text{int}}$ (eV)	0.05
$J_{A,1}^{\text{int}}$ (eV)	0.025
$J_{A,2}^{\text{int}}$ (eV)	0.05
$J_{A,3}^{\text{int}}$ (eV)	0.025
$J_{A,01}^{\text{ext}}$ (eV)	0.02
$J_{A,12}^{\text{ext}}$ (eV)	0.02
$J_{A,23}^{\text{ext}}$ (eV)	0.02
$\epsilon_{A,0}^v$ (eV)	-1.03
$J_{A,0}^{\text{int}}$ (eV)	-0.15
$J_{DA}^c$ (eV)	0.1
$J_{DA}^v$ (eV)	-0.1
$\hbar\omega_{p,1}$ (meV)	10.0
$g_1$ (meV)	42.0
$\hbar\omega_{p,2}$ (meV)	185.0
$g_2$ (meV)	94.0
$T$ (K)	300.0

single-electron states, are chosen to reproduce the most important features of the low-energy part of the electronic density of states (DOS) of fullerene aggregates,<sup>14,25</sup> such as the combined (total) bandwidth of 0.4–0.5 eV and the presence of two separated groups of allowed states. Let us note that, because of the reduced dimensionality of our model, we cannot expect to reproduce details of the actual DOS, but only its gross features. We therefore believe that taking two instead of three orbitals energetically close to the LUMO orbital is reasonable within our model. The electronic DOS in the acceptor produced by our model is shown in the inset of Figure 1. Magnitudes of transfer integrals in the acceptor are also in agreement with the values reported in the literature.<sup>54,55</sup> We have also included the single-electron fullerene states which are located at around 1 eV above the lowest single-electron state. It is well-known that these states in  $C_{60}$  are also triply degenerate and that this degeneracy is lifted in  $PC_{60}BM$ . Since we use a model system, we take, for simplicity, that the degeneracy is lifted in the same manner as in the case of lowest single-electron levels, i.e., we take  $J_{A,0}^{\text{int}} = J_{A,2}^{\text{int}} = J_{A,1}^{\text{int}} = J_{A,3}^{\text{int}}$ ,  $J_{A,01}^{\text{int}} = J_{A,23}^{\text{int}}$ , and  $\epsilon_{A,3}^c - \epsilon_{A,2}^c = \epsilon_{A,1}^c - \epsilon_{A,0}^c$ , while  $\epsilon_{A,2}^c - \epsilon_{A,0}^c = 1.0$  eV. For the magnitudes of the energy difference  $\epsilon_{A,0}^c - \epsilon_{A,0}^v$  and the transfer integral  $J_{A,0}^{\text{int}}$  listed in Table 1, the single-particle gap in the acceptor part of the heterojunction assumes the value of 2.2 eV, which is similar to the literature values for  $PCBM$ .<sup>52</sup>

The energy differences  $\Delta_{XD-CT}$  and  $\Delta_{XA-CT}$  between the lowest excited state of the heterojunction (the lowest CT state) and the lowest exciton states in the donor and acceptor respectively, are directly related to LUMO–LUMO and HOMO–HOMO energy offsets between the materials. Literature values of  $\Delta_{XD-CT}$  representative of P3HT/PCBM

blends are usually calculated for the system consisting of one PCBM molecule and one oligomer and range from 0.7 eV<sup>33</sup> to 1.3 eV.<sup>34</sup> Liu and Troisi<sup>35</sup> obtained  $\Delta_{XD-CT} = 0.97$  eV and pointed out that taking into account partial electron delocalization over fullerene molecules can significantly lower the XD-CT energy difference. For parameters listed in Table 1,  $\Delta_{XD-CT} = 0.68$  eV, which is a reasonable value, since we do account for carrier delocalization effects. The LUMO–LUMO offset  $\Delta E_{DA}^c$  (see Figure 1) produced by the model parameters is around 0.96 eV and the lowest CT state is located at 1.32 eV. The energy difference  $\Delta_{XA-CT} = 0.42$  eV, so that the HOMO–HOMO offset is around 0.73 eV and the lowest XA state is approximately at 1.74 eV, both of which compare well with the available data.<sup>52</sup> The magnitudes of the transfer integrals  $J_{DA}^c$  and  $J_{DA}^v$  between the two materials are taken to be similar to the values obtained in ref 28.

Interband matrix elements of the dipole moment  $d_{i\alpha\beta}^{cv}$  are assumed not to depend on band indices  $\alpha, \beta, i$  and to be equal on all sites belonging to the single material,  $d_{i\alpha\beta}^{cv} = d_D^{cv}$  for  $i = 0, \dots, N - 1$  and  $d_{i\alpha\beta}^{cv} = d_A^{cv}$  for  $i = N, \dots, 2N - 1$ . Since the focus of our study is on the dissociation of donor excitons, in all the computations we set  $d_A^{cv} = 0$ .

We assume that each site contributes one low-frequency and one high-frequency phonon mode. The energies of the phonon modes, as well as the carrier–phonon interaction constants, are taken to be equal in both parts of the heterojunction. The phonon mode of energy 185 meV, present in both materials, was shown to be important for ultrafast charge transfer in the P3HT/PCBM blend,<sup>26</sup> while low-energy ( $\lesssim 10$  meV) phonon modes of P3HT exhibit strong coupling to carriers.<sup>56</sup> The strength of the carrier–phonon interaction can be quantified by the polaron binding energy, which can be estimated using the result of the second-order weak-coupling perturbation theory at  $T = 0$  in the vicinity of the point  $k = 0$ :<sup>57</sup>

$$\epsilon_b^{\text{pol}} = \sum_{i=1}^2 \epsilon_{b,i}^{\text{pol}} = \sum_{i=1}^2 \frac{g_i^2}{2|J|} \frac{1}{\sqrt{\left(1 + \frac{\hbar\omega_{p,i}}{2|J|}\right)^2 - 1}} \quad (18)$$

where  $\epsilon_{b,i}^{\text{pol}}$  are the contributions of high- and low-frequency phonon modes to the polaron binding energy. The values of  $g_1$  and  $g_2$  in Table 1 are obtained assuming that  $\epsilon_b^{\text{pol}} = 50$  meV and  $\epsilon_{b,1}^{\text{pol}} = \epsilon_{b,2}^{\text{pol}}$  and setting  $|J| = 125$  meV.

**Classification of Exciton States.** The classification of exciton states is unambiguous only for  $J_{DA}^c = J_{DA}^v = 0$  (noninteracting heterojunction), when each exciton state  $\psi_{(i\alpha)(j\beta)}^{x(0)}$  can be classified as a donor exciton state (XD), a space-separated state, an acceptor exciton state (XA) or a state in which the electron is in the donor, while the hole is in the acceptor (eDhA). Because eDhA states are very well separated (in energy) from other groups of exciton states, we will not further consider them. In the group of space-separated states, CT and CS states can further be distinguished by the mean electron–hole distance

$$\langle r_{e-h} \rangle_{x(0)} = \sum_{\substack{i\alpha_i \\ j\beta_j}} |\psi_{(i\alpha)(j\beta)}^{x(0)}|^2 |i - j| \quad (19)$$

If the electron–hole interaction is set to zero, the mean electron–hole distance for all the space-separated states is equal to  $N$ . For the nonzero Coulomb interaction, we consider a

space-separated state as a CS state if its mean electron–hole distance is larger than (or equal to)  $N$ , otherwise we consider it as a CT state.

In general case, when at least one of  $J_{DA}^c, J_{DA}^v$  is different from zero (interacting heterojunction), it is useful to explicitly separate the D/A interaction from the interacting-carrier part of the Hamiltonian (eq 2),

$$H_c = H_c^{(0)} + H_{DA} \quad (20)$$

where

$$H_{DA} = -J_{DA}^c \sum_{\substack{\beta_{N-1} \\ \beta_N}} \left( c_{(N-1)\beta_{N-1}}^\dagger c_{N\beta_N} + \text{H. c.} \right) + J_{DA}^v \sum_{\substack{\alpha_{N-1} \\ \alpha_N}} \left( d_{(N-1)\alpha_{N-1}}^\dagger d_{N\alpha_N} + \text{H. c.} \right) \quad (21)$$

is the D/A interaction, and  $H_c^{(0)}$  describes interacting carriers at the noninteracting heterojunction. Exciton states of the noninteracting heterojunction  $\psi_{(i\alpha_i)(j\beta_j)}^{x(0)}$  and corresponding exciton energies  $\hbar\omega_x^{(0)}$  are obtained solving the electron–hole pair eigenproblem of  $H_c^{(0)}$ . Exciton states of the interacting heterojunction  $\psi_{(i\alpha_i)(j\beta_j)}^x$  are linear combinations of exciton states of the noninteracting heterojunction

$$\psi_{(i\alpha_i)(j\beta_j)}^x = \sum_{x^{(0)}} C_{xx^{(0)}} \psi_{(i\alpha_i)(j\beta_j)}^{x^{(0)}} \quad (22)$$

and their character is obtained using this expansion. Namely, for each group  $X^{(0)}$  of the exciton states of the noninteracting heterojunction, we compute the overlap of state  $x$  (of the interacting heterojunction) with states belonging to this group

$$C_{X^{(0)}}^x = \sum_{x^{(0)} \in X^{(0)}} |C_{xx^{(0)}}|^2 \quad (23)$$

The character of state  $x$  is then the character of the group  $X^{(0)}$  for which the overlap  $C_{X^{(0)}}^x$  is maximum.

The electron in a space-separated state is predominantly located in the acceptor part of the heterojunction, while the hole is located in the donor part. Since there is a number of single-electron levels per acceptor site, the electron in a space-separated state can be in different electronic bands originating from these single-electron levels. A useful quantity for further classification of space-separated states is

$$p_x(\beta) = \sum_{j=N}^{2N-1} \sum_{i\alpha_i} |\psi_{(i\alpha_i)(j\beta)}^x|^2 \quad (24)$$

which represents the conditional probability that, given that the electron in state  $x$  is in the acceptor, it belongs to the electronic band stemming from the single-electron level  $\beta$ . The index of the electronic band  $\beta_x$  to which the electron in space-separated state  $x$  predominantly belongs is then the value of  $\beta$  for which the conditional probability  $p_x$  is maximal. In other words, space-separated state  $x$  belongs to the  $CT_{\beta_x}$  band.

Let us note here that, because of the large energy separation between the lower two (0 and 1) and the higher two (2 and 3) single-electron levels in the acceptor, the electronic coupling  $J_{A,12}^{\text{ext}}$ , which couples space-separated states belonging to  $CT_0$  and  $CT_1$  bands to the ones belonging to  $CT_2$  and  $CT_3$  bands, is not effective. Therefore, the space-separated states from  $CT_0$  and  $CT_1$  bands are very weakly mixed with (and essentially

isolated from) space-separated states of  $CT_2$  and  $CT_3$  bands, which permits us to separately analyze these two subgroups of space-separated states.

**Role of the Donor–Acceptor Coupling and the Resonant Mixing Mechanism.** In this section, we show that the D/A coupling is at the root of the resonant mixing mechanism, which explains the presence of space-separated (and XA) states that have a certain amount of donor character, can be reached by means of a photoexcitation, and act as gateways to the space-separated manifold for the initial donor excitons. However, the precise role of the D/A coupling is different in different energy regions of the exciton spectrum. In the low-energy region of the exciton spectrum, which is dominated by the space-separated states belonging to  $CT_0$  and  $CT_1$  bands, this coupling leads to the resonant mixing of two-particle (exciton) states. On the other hand, in the high-energy region of the exciton spectrum, in which space-separated states belong to  $CT_2$  and  $CT_3$  bands, it gives rise to the resonant mixing of single-electron states in the donor and acceptor.

To better appreciate the role of couplings  $J_{DA}^c, J_{DA}^v$ , it is convenient to schematically represent exciton wave functions  $\psi_{(i\alpha_i)(j\beta_j)}^{x(0)}$  and  $\psi_{(i\alpha_i)(j\beta_j)}^x$  in the coordinate space. For the clarity of the discussion, we assume that we have only one single-electron and single-hole state per site throughout the system. This assumption does not compromise the validity of the conclusions to be presented in the case of more single-particle states per site. On the abscissa of our coordinate space is the hole coordinate, while the electron coordinate is on the ordinate.

The wave functions of exciton states  $x^{(0)}$  of the noninteracting heterojunction are confined to a single quadrant of our coordinate space, see Figure 2a. For example, the wave

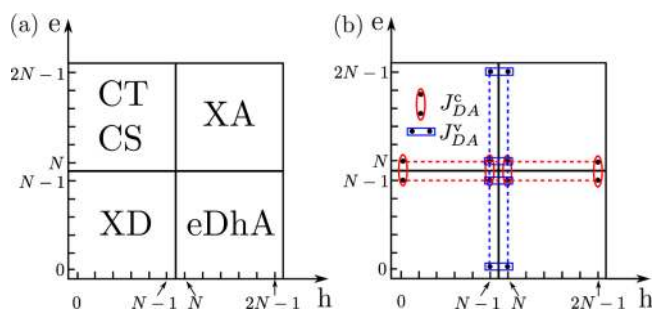


**Figure 2.** (a) At the noninteracting heterojunction, the wave function of each exciton state is confined to a single quadrant in the position space of the electron and hole. (b) The points at which the sums in eq 26 are evaluated: the points relevant to the computation of the first and the second sum are grouped by red ellipses, the points relevant to the computation of the third and the fourth sum are grouped by blue rectangles.

function of a donor exciton state is nonzero only when both electron and hole coordinates are between 0 and  $N - 1$ , and similarly for other groups of exciton states. Because of the D/A interaction  $H_{DA}$  (eq 21), exciton states  $x$  of the interacting heterojunction are mixtures of different exciton states  $x^{(0)}$  of the noninteracting heterojunction, see eq 22. Therefore, the wave function of a general exciton state at the interacting heterojunction is not confined to the quadrant which is in Figure 2a labeled by its prevalent character, but is nonzero also in other quadrants. The D/A interaction  $H_{DA}$  is written in the noninteracting-heterojunction exciton basis as

$$H_{\text{DA}} = \sum_{\bar{x}^{(0)}, x^{(0)}} h_{\bar{x}^{(0)}, x^{(0)}} |\bar{x}^{(0)}\rangle \langle x^{(0)}| \quad (25)$$

with

$$\begin{aligned} h_{\bar{x}^{(0)}, x^{(0)}} = & -J_{\text{DA}}^{\text{c}} \sum_{k\alpha_k} \psi_{(k\alpha_k)(N-1, \beta_{N-1})}^{\bar{x}^{(0)*}} \psi_{(k\alpha_k)(N\beta_N)}^{x^{(0)}} \\ & - J_{\text{DA}}^{\text{c}} \sum_{k\alpha_k} \psi_{(k\alpha_k)(N\beta_N)}^{\bar{x}^{(0)*}} \psi_{(k\alpha_k)(N-1, \beta_{N-1})}^{x^{(0)}} \\ & + J_{\text{DA}}^{\text{v}} \sum_{k\beta_k} \psi_{(N-1, \alpha_{N-1})(k\beta_k)}^{\bar{x}^{(0)*}} \psi_{(N\alpha_N)(k\beta_k)}^{x^{(0)}} \\ & + J_{\text{DA}}^{\text{v}} \sum_{k\beta_k} \psi_{(N\alpha_N)(k\beta_k)}^{\bar{x}^{(0)*}} \psi_{(N-1, \alpha_{N-1})(k\beta_k)}^{x^{(0)}} \end{aligned} \quad (26)$$

The points at which the sums in the last equation (disregarding band indices) are to be evaluated are presented in Figure 2b. The first two sums in eq 26 are nonzero only when one state is of XD, and the other is of space-separated character. Similarly, the other two sums in eq 26 are nonzero only when one state is of XA, and the other is of space-separated character. Therefore, if  $J_{\text{DA}}^{\text{c}} \neq 0$  and  $J_{\text{DA}}^{\text{v}} = 0$ , XA states of the interacting heterojunction are identical to XA states of the noninteracting heterojunction, while XD (space-separated) states of the interacting heterojunction are generally combinations of XD and space-separated states of the noninteracting heterojunction. Similarly, if  $J_{\text{DA}}^{\text{c}} = 0$  and  $J_{\text{DA}}^{\text{v}} \neq 0$ , XD states of the interacting heterojunction are identical to XD states of the noninteracting heterojunction, while XA (space-separated) states of the interacting heterojunction are generally combinations of XA and space-separated states of the noninteracting heterojunction.

The exact mechanism of this mixing is different in different parts of the exciton spectrum. Let us start with the lower-energy part of the spectrum, which contains space-separated states belonging to CT<sub>0</sub> and CT<sub>1</sub> bands. Single-electron states in the acceptor which originate from levels 0 and 1 do not exhibit strong resonant mixing with single-electron states in the donor, thanks to the large energy separation between these two groups of states. Therefore, the relevant partitioning of the interacting-carrier Hamiltonian  $H_{\text{c}}$  is the one embodied in eq 20. Coefficients  $C_{xx}^{(0)}$  in the expansion of exciton state  $x$  (of the interacting heterojunction) in terms of exciton states  $x^{(0)}$  (of the noninteracting heterojunction) are obtained as solutions to the eigenvalue problem

$$\sum_{x^{(0)}} (\delta_{x^{(0)}, \bar{x}^{(0)}} \hbar\omega_{x^{(0)}} + h_{\bar{x}^{(0)}, x^{(0)}}) C_{xx}^{(0)} = \hbar\omega_x C_{x\bar{x}}^{(0)} \quad (27)$$

Since  $h_{\bar{x}^{(0)}, x^{(0)}}$  contains products of two exciton wave functions,  $|h_{\bar{x}^{(0)}, x^{(0)}}|$  is generally much smaller than  $|J_{\text{DA}}^{\text{c}}|$ . Therefore, most of the states in the lower-energy part of the interacting heterojunction are almost identical to the respective states of the noninteracting heterojunction. However, whenever  $|h_{\bar{x}^{(0)}, x^{(0)}}| \sim |\hbar\omega_{\bar{x}^{(0)}} - \hbar\omega_{x^{(0)}}|$ , there exists at least one state of the interacting heterojunction which is a mixture of states  $\bar{x}^{(0)}$  and  $x^{(0)}$  (which have different characters!) of the noninteracting heterojunction. In other words, states  $\bar{x}^{(0)}$  and  $x^{(0)}$ , which are virtually resonant in energy, exhibit resonant mixing to form the so-called bridge states of the interacting heterojunction. Apart from their dominant character, which is obtained as previously explained, bridge states also have nontrivial overlaps

with noninteracting-heterojunction states of other characters. For example, if  $J_{\text{DA}}^{\text{c}} = 0$ , all the bridge states of the interacting heterojunction are of mixed XD and space-separated character; if  $J_{\text{DA}}^{\text{v}} = 0$ , all the bridge states of the interacting heterojunction are of mixed XA and space-separated character; if both couplings are nonzero, bridge states of the interacting heterojunction are of mixed XD, XA, and space-separated character. The emergence of bridge states in the low-energy part of the exciton spectrum requires subtle energy alignment of exciton, i.e., two-particle, states. Bridge states formed by resonances between two-particle states are thus rather scarce. Having a certain amount of the donor character, bridge states acquire oscillator strengths from donor states and can thus be directly generated from the ground state. In the rest of our paper, it is convenient to consider as a bridge state any state (in the lower-energy part of the exciton spectrum) of dominant CS, CT, or XA character whose amount of donor character is at least 0.01.

On the other hand, in the high-energy region of the exciton spectrum, which contains space-separated states belonging to CT<sub>2</sub> and CT<sub>3</sub> bands, there is significant mixing between single-electron states in the acceptor stemming from levels 2 and 3 and single-electron states in the donor. In this case, instead of the decomposition of the interacting-carrier part of the Hamiltonian given in eq 20, it is more convenient to separate the carrier-carrier interaction (last three terms in eq 2) from the part describing noninteracting carriers (first two terms in eq 2). The latter part of the interacting-carrier Hamiltonian then gives rise to single-electron states of the whole heterojunction which are delocalized on both the donor and acceptor as a consequence of the resonant mixing between single-electron states in the two materials. Since one single-electron state of the entire system generally participates in many two-particle states, exciton states having at least one carrier delocalized throughout the heterojunction are ubiquitous in the high-energy region of the spectrum. They also generally have greater amount of donor character than the bridge states in the low-energy part of the spectrum, *vide infra*, making them easily accessible from the ground state by a (suitable) photoexcitation. The dominant character of these states can be different and to our further discussion are relevant space-separated (CT and CS) states of CT<sub>2</sub> and CT<sub>3</sub> bands with partial donor character, which will be further termed photon-absorbing charge-bridging (PACB) states. This term has been repeatedly used in the literature to denote space-separated states in which charges are delocalized throughout the system.<sup>28,37,38</sup> We note that the PACB states within our model do not have any other immediate relationship with PACB states reported in ab initio studies of D/A interfaces apart from the charge-bridging property and relatively large oscillator strengths permitting their direct optical generation.

The bridge states owe their name to the fact that they indirectly connect, via phonon-assisted processes, a state of pure XD character to a state of pure space-separated character. In our model, these two states cannot be involved in a single-phonon-assisted process because of the form of exciton-phonon matrix elements  $\Gamma_{\bar{x}x}^{i\lambda_i}$  (eq 11), which contain products of exciton wave functions taken at the same point. Therefore, single-phonon-assisted transitions among exciton states of the same character are most intensive and probable. A state of pure XD character can, however, also be coupled (via processes mediated by a donor phonon) to a bridge state, which can then be coupled to a state of pure space-separated character (via single-phonon processes mediated by acceptor phonons).

In the remaining part of our study, we will for ease of presentation adopt the following classification of the exciton states. Since space-separated states belonging to CT<sub>2</sub> and CT<sub>3</sub> bands which are relevant to our study are PACB states, we will not discriminate between CT and CS states in CT<sub>2</sub> and CT<sub>3</sub> bands, but rather refer to all of them as PACB states. We will, however, distinguish between CS and CT states in CT<sub>0</sub> and CT<sub>1</sub> bands and, for brevity of discussion, we will denote them simply as CS and CT states. This classification facilitates the understanding of the role that PACB states play in ultrafast interfacial dynamics by enabling direct comparison between results obtained with all four and only two lower orbitals per acceptor site, *vide infra*. The comparison is plausible since there is a well-defined correspondence between XA, CT, and CS states in the lower-energy part of the exciton spectrum (four orbitals per acceptor site) and the corresponding states when only two orbitals per acceptor site are taken into account. The part of the exciton spectrum which is relevant for our study is shown in Figure 3.

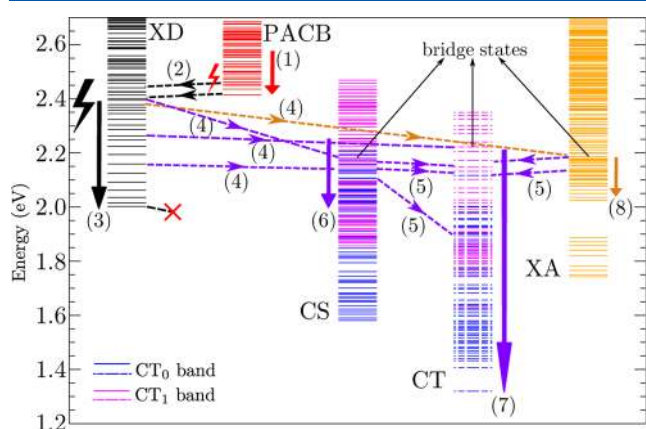


**Figure 3.** Exciton states relevant for our study divided in different groups. In the third (the fourth) column (from the left), blue and magenta lines denote CS (CT) states belonging to CT<sub>0</sub> and CT<sub>1</sub> band, respectively. Ultrafast exciton dynamics proceeds along the photophysical pathways denoted by (1)–(8), which are further specified in the Numerical Results section. The solid arrows [pathways (1), (3), (6), (7), and (8)] indicate the deexcitation processes occurring within one group of exciton states, whereas the dashed arrows [pathways (2), (4), and (5)] denote transitions among different groups of exciton states. The black (red) bolt denotes the direct photoexcitation of excitons in donor (PACB) states.

## NUMERICAL RESULTS

In this section, we present results for the exciton dynamics at the model heterojunction during and after its pulsed excitation. The form of the excitation is

$$E(t) = E_0 \cos(\omega_c t) \exp\left(-\frac{t^2}{\tau_G^2}\right) \theta(t + t_0) \theta(t_0 - t) \quad (28)$$

where  $\omega_c$  is its central frequency,  $2t_0$  is its duration,  $\tau_G$  is the characteristic time of the Gaussian envelope, and  $\theta(t)$  is the Heaviside step function. In all the computations, we set  $t_0 = 50$  fs and  $\tau_G = 20$  fs. Computing the energy- and time-resolved exciton populations  $\varphi_X(E, t)$  (eqs 16 and 17) or the exciton DOS, we represent  $\delta$  functions by a Gaussian with the standard deviation of 10 meV.

We start with the analysis of the ultrafast exciton dynamics when model parameters assume the values listed in Table 1 and

the system is excited at the bright donor state located around  $\hbar\omega_c = 2.35$  eV, which is significantly above the lowest donor state. We also present the results obtained taking into account only two lower single-electron levels (of energies  $\epsilon_{A,0}^c$  and  $\epsilon_{A,1}^c$ ) in the acceptor per site, while the values of all other model parameters are as listed in Table 1. The comparison of these results helps us understand the effects that the presence of two higher single-electron levels in the acceptor has on ultrafast exciton dynamics in our model.

In Figure 4a we show the time dependence of the total coherent exciton population  $N_{\text{tot}}^{\text{coh}} = \sum_x |y_x|^2$ , total incoherent exciton population  $N_{\text{tot}}^{\text{incoh}} = \sum_x \bar{n}_{x,v}$  and total exciton population  $N_{\text{tot}}$  (eq 14). Exciting well above the lowest donor state, the conversion from coherent to incoherent exciton populations is rapid and is completed in a couple of tens of femtoseconds after the end of the pulsed excitation. Figure 5a–e presents density plots of energy- and time-resolved distributions  $\varphi_X^{\text{coh}}(E, t)$  of coherent exciton populations for different groups of exciton states X. Comparing the ranges of color bars in Figure 5a–e, we conclude that the excitation predominantly generates donor excitons. We observe in Figure 5a that the initially populated donor states are the states located around 2.35 and 2.42 eV, together with the lowest donor state at around 2 eV. Even though we pump well above the lowest donor state, this state is prone to the direct optical generation because of its very large dipole moment  $M_x$  (eq 10) for direct generation from the ground state and the spectral width of the pulse. Apart from donor states, PACB states are also initially populated (see Figure 5b). In Figure 5c–e we see that energy positions of the bright spots in the density plots on the left correspond very well to the energy positions of red bars, which indicate bridge states of dominant CS, CT, and XA character, on the right. In other words, these states can be directly optically generated from the ground state, as already discussed.

The time dependence of normalized incoherent populations of different groups of exciton states is presented in Figure 4b. Figure 4c shows normalized incoherent populations in the model with only two accessible electronic states (of energies  $\epsilon_{A,0}^c$  and  $\epsilon_{A,1}^c$ ) at each acceptor site. Comparing panels b and c of Figure 4, we conclude that the presence of PACB states significantly affects exciton dynamics on ultrafast time scales. In the presence of only two lower electronic levels in the acceptor, the number of donor excitons decreases, while the numbers of CS, CT, and XA excitons increase after the excitation (see Figure 4c). On the other hand, taking into account the presence of higher-lying electronic orbitals in the acceptor and pumping well above the lowest donor exciton, the populations of XD, XA, CT, and CS states increase, while the population of PACB states decreases after the excitation. The fact that donor states acquire population after the end of the pulse may at first seem counterintuitive, since initially generated donor excitons are expected to dissociate, performing transitions to the space-separated manifold. Having significant amount of donor character, PACB states are well coupled (via single-phonon-assisted processes) to the manifold of donor excitons, while their coupling to space-separated states belonging to CT<sub>0</sub> and CT<sub>1</sub> bands is essentially negligible (see also the paragraph following eq 24). Therefore, instead of performing single-phonon-assisted transitions to lower-energy space-separated states, initially generated PACB excitons perform transitions toward donor states, i.e., the number of donor excitons increases at the expense of excitons initially generated in PACB states. While, at the end of the pulse, excitons in PACB states comprise

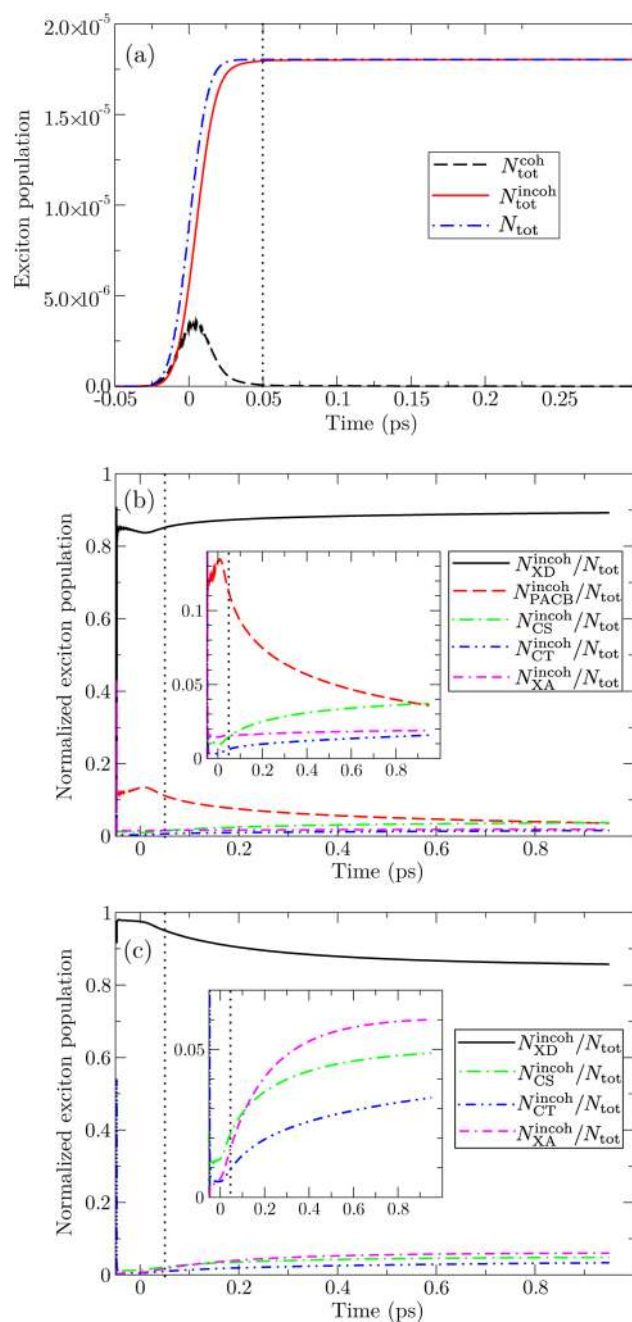


**Figure 4.** Time dependence of (a) the total exciton population and its coherent and incoherent parts, (b,c) normalized incoherent populations of different groups of exciton states. In panels a and b, we take four single-electron levels per acceptor site, while in panel c we take only two lower single-electron levels ( $\epsilon_{A,0}^x$  and  $\epsilon_{A,1}^x$ ) per acceptor site. The dotted vertical lines denote the end of the excitation.

around 11% of the total exciton population, 900 fs after the pulse their participation in the total population reduces to 4%. At the same time, the normalized number of donor excitons increases from around 85% to around 89% of the total exciton population, meaning that some of the donor excitons are converted into XA, CT, and CS states, which is seen in Figure 4b as the increase in the populations of these states.

In the model with four accessible electronic orbitals per acceptor site, the major part of space-separated states that are populated on 100 fs time scales following the excitation are directly generated PACB states. This conclusion is in line with

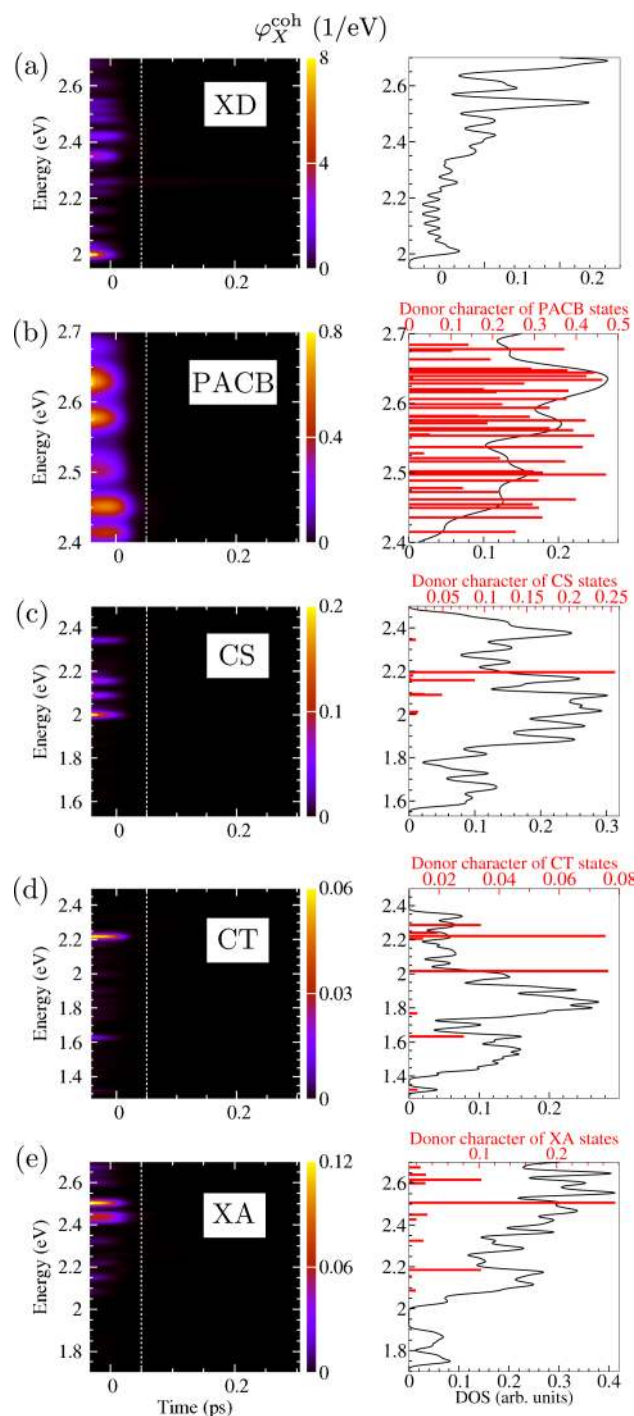


**Figure 5.** Density plots of  $\varphi_X^{\text{coh}}(E,t)$  for (a) XD, (b) PACB, (c) CS, (d) CT, and (e) XA states. Each density plot is complemented with the plot of the corresponding exciton DOS. In panels b–e, exciton DOS plots contain amounts of the donor character of exciton states (see eq 23) [in panels c–e, as long as it is greater than 0.01].

our recent results regarding ultrafast photophysics in a model where the LUMO–LUMO offset is comparable to the effective bandwidth of the LUMO band of the acceptor.<sup>27</sup> Namely, we have recognized that the resonant mixing between single-electron states in the LUMO bands of the two materials is at the root of the ultrafast direct optical generation of space-separated charges. Here, the same mechanism is responsible for the observed direct generation of excitons in PACB states, which now acquire nonzero oscillator strengths due to the

energy alignment between single-electron states stemming from the donor LUMO orbital and higher-than-LUMO acceptor orbitals. On the contrary, if only electronic orbitals close to the LUMO orbital are taken into account, populations of space-separated states present on 100 fs time scales after the excitation mainly reside in bridge states, which are formed by two-particle resonant mixing. The populations of bridge states are dominantly built by phonon-assisted transitions from initially generated donor excitons (since the direct generation of excitons in bridge states is not very pronounced for the excitation studied). Therefore, in our model, the PACB states can enhance the generation of space-separated charges on ultrafast time scales by allowing for their direct optical generation and not by acting as intermediate states of charge separation starting from initial donor excitons.

In order to understand the photophysical pathways of ultrafast exciton dynamics, in Figure 6a–e we depict the density plots of  $\varphi_X^{\text{incoh}}(E,t)$  for various groups  $X$  of exciton states. For the completeness of the discussion, in the Supporting Information we provide the density plots of  $\varphi_X^{\text{incoh}}(E,t)$  in the model with only two lower electronic orbitals per acceptor site and compare them to the plots presented here. As already explained, the excitons initially generated in PACB states (red bolt in Figure 3) undergo deexcitation within the PACB manifold (pathway (1) in Figure 3) followed by phonon-mediated transitions toward the manifold of donor states (pathway (2) in Figure 3; see Figure 6b). Donor excitons (either the ones initially generated in higher-lying bright states (black bolt in Figure 3) or the ones originating from PACB excitons) are involved in a series of ultrafast phonon-assisted transitions toward lower-energy states. Most of these transitions happen within the XD manifold (pathway (3) in Figure 3; see the series of more or less bright bands in the density plot of Figure 6a), which is consistent with the fact that donor excitons comprise the largest part of the total exciton population at every instant. The deexcitation within the XD manifold proceeds until the lowest XD state is reached. In fact, we see that already for  $t \gtrsim 250$  fs, XD population resides mainly in the lowest donor state at around 2 eV and the donor state at around 2.13 eV. The lowest donor state is almost uncoupled from the space-separated manifold, acting as a trap state for exciton dissociation, which is in line with other studies.<sup>23</sup> The other donor state (at around 2.13 eV) acting as a trap state for exciton dissociation is specific to our computation.

In the course of the deexcitation from the higher-lying donor states and before reaching a trap state for exciton dissociation, a donor exciton can perform a transition to a bridge state (pathway (4) in Figure 3). As seen in Figure 6c–e, the energy positions of the bright bands in the density plots on the left match exactly the energy positions of red bars displaying the amount of donor character of dominantly space-separated or XA states on the right. Figure 7b–d depicts probability distributions of the electron and hole in representative bridge states of different dominant characters, while Figure 7a shows the same quantities for particular PACB states. All the bridge states exhibit carrier delocalization throughout the system; this property makes them accessible from the initial states of donor excitons. The same holds for PACB states: since the carriers in these states are delocalized throughout the heterojunction, these states inherit oscillator strengths from donor excitons and may thus be directly accessed by an optical excitation. Moreover, this property enables efficient phonon-assisted coupling between PACB states and donor states. The bridge

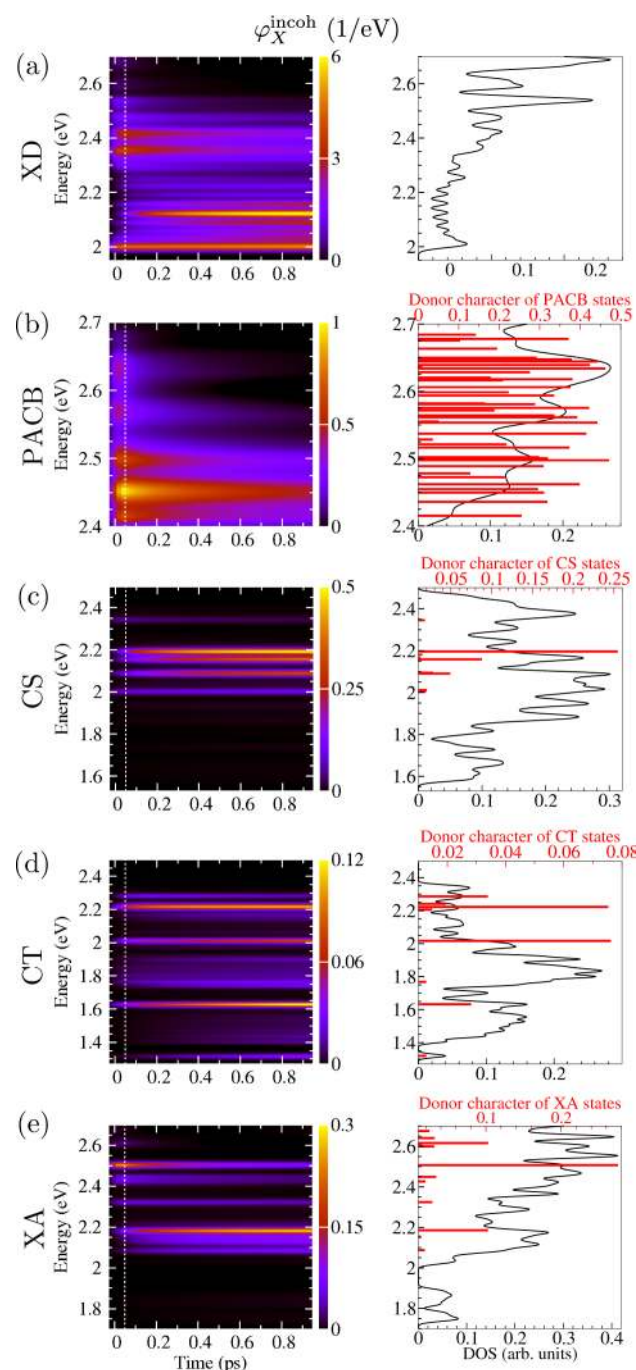


**Figure 6.** Density plots of  $\varphi_X^{\text{incoh}}(E,t)$  for (a) XD, (b) PACB, (c) CS, (d) CT, and (e) XA states. Each density plot is accompanied by the plot of the corresponding exciton DOS. In panels b–e, the exciton DOS plots contain the amount of the donor character of exciton states (see eq 23) [in panels c–e, as long as it is greater than 0.01].

states gain significant populations during the first 100 fs following the excitation (pathway (4) in Figure 3) and concomitantly the excitons initially generated in PACB states perform phonon-mediated transitions toward donor states (pathway (2) in Figure 3).

Once the exciton has reached a bridge state, it can deexcite within the manifold of its dominant character (pathways (6)–(8) in Figure 3) or it can perform a transition to the CT manifold (pathway (5) in Figure 3) followed by a number of downward transitions within this manifold (pathway (7) in Figure 3; see the

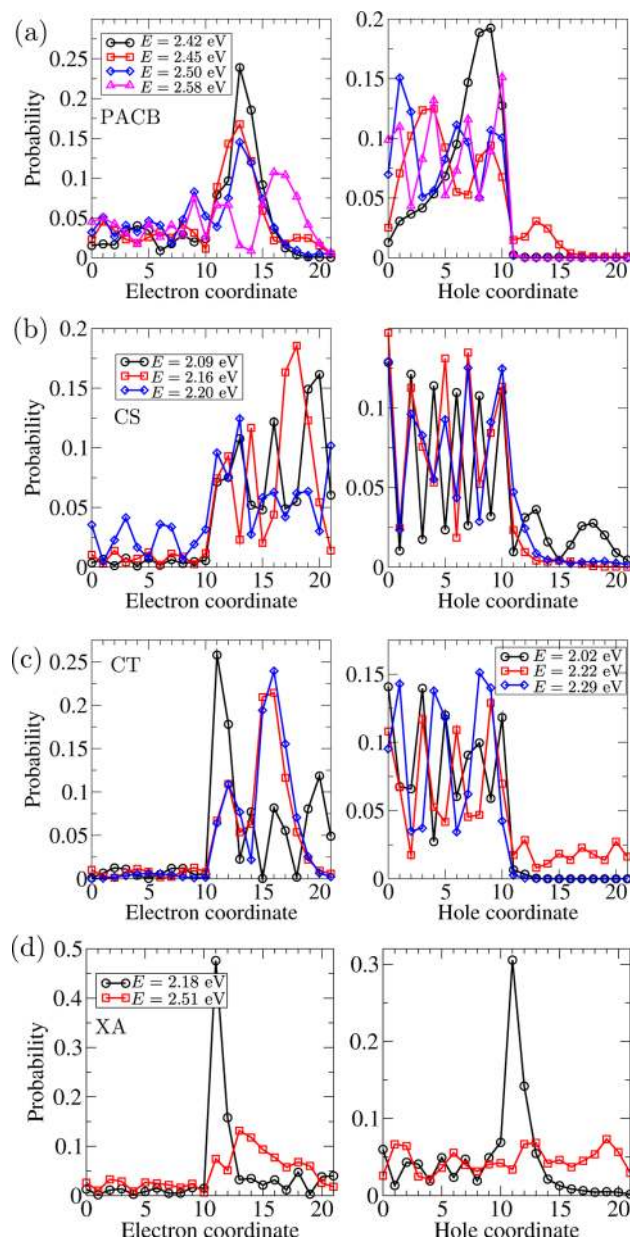


**Figure 7.** Probability distributions of the electron (left) and hole (right) in representative (a) PACB states and bridge states of dominant (b) CS, (c) CT, and (d) XA character.

series of more or less bright bands between 1.3 and 2.2 eV in the density plot of Figure 6d). The gradual deexcitation within the CT manifold leads to the delayed buildup of populations of low-energy CT states (pathway (7) in Figure 3; see bright bands at around 1.62 and 1.32 eV in the density plot in Figure 6d), which happens on a picosecond time scale. Apart from mediating the charge separation, bridge states can also act as competing final states. In our computation, at every instant, virtually all CS excitons reside in bridge states of dominant CS character, and the progressive deexcitation within the CS manifold (pathway (6) in Figure 3) is not pronounced (see Figure 6c). Analogous situation is observed analyzing the energy- and time-resolved populations of XA states (pathway (8) in Figure 3) in Figure 6e. This 2-fold role of bridge states observed in our computations is in agreement with conclusions of previous studies.<sup>20</sup>

**Ultrafast Exciton Dynamics for Various Central Frequencies.** The exact photophysical pathways along which

the exciton dynamics proceeds on ultrafast time scales strongly depend on the frequency of the excitation, the exciton dissociation being more pronounced for larger excess energy.<sup>1,58</sup> Here, we examine ultrafast exciton dynamics for three different excitations of central frequencies  $\hbar\omega_c = 2.35$ , 2.25, and 2 eV (excitation at the lowest donor state). As the central frequency of the excitation is decreased, i.e., as the initially generated donor excitons are closer in energy to the lowest donor state, the conversion from coherent to incoherent exciton population is slower and the time scale on which exciton coherences with the ground state dominate the interfacial dynamics is longer (see Figure 8b). At the same time, the participation of excitons

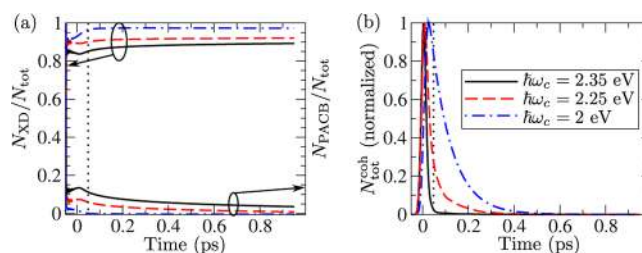


**Figure 8.** Time dependence of (a) the normalized number of excitons in donor and PACB states, and (b) the total coherent exciton population, for different central frequencies of the excitation. For convenience, the total coherent population shown in panel b is normalized so that its maximal value is equal to 1.

in PACB states in the total exciton population is decreased, whereas donor excitons comprise larger part of the total population (see Figure 8a). Namely, as the central frequency is lowered toward the lowest donor state, the initial optical generation of excitons in PACB states is less pronounced and the pathways (1) and (2) in Figure 3 become less important, while the possible photophysical pathways of the initially generated donor excitons become less diverse. Therefore, the phonon-assisted processes responsible for the conversion from coherent to incoherent exciton populations and for the ultrafast phonon-mediated transitions from donor states toward space-separated states are less effective. As a consequence, the conversion from coherent to incoherent exciton populations is slower, and initially generated donor excitons tend to remain within the manifold of donor states (pathway (3) in Figure 3, down to the lowest donor state, is preferred to pathways (4)–(7), which may lead to space-separated states). The latter fact is especially pronounced exciting at the lowest donor state, which is very weakly coupled to the space-separated manifold, when around 80% of the total exciton population lies in the lowest donor state, meaning that the ultrafast charge transfer upon excitation at this state is not significant. In the Supporting Information, we present the density plots of  $\phi_X^{\text{incoh}}(E,t)$  for different groups of exciton states  $X$  and excitations of different central frequencies.

**Influence of Small Variations of the LUMO–LUMO Offset on Ultrafast Exciton Dynamics.** In this work, we deal with rather large LUMO–LUMO offsets, when the bridge states emerge as a consequence of the energy resonance between two-particle (exciton) states. The energies of these states, as well as their number and amount of the donor character, are therefore very sensitive to the particular exciton energy level alignment at the heterojunction. On the other hand, the properties of PACB states are not expected to be particularly sensitive to the details of the energy level alignment,

since they originate from resonances between single-electron states in the donor and acceptor. In order to demonstrate this difference between bridge states and PACB states, we performed computations with different, but very close, values of the LUMO–LUMO offset. The LUMO–LUMO offset is varied by changing all the parameters  $\epsilon_{A,0}^c, \epsilon_{A,1}^c, \epsilon_{A,2}^c, \epsilon_{A,3}^c, \epsilon_{A,0}^v$  in Table 1 by the same amount, keeping all the other model parameters fixed. The effects of small variations of LUMO–LUMO offset are studied for  $J_{DA}^v = 0$ , when all the bridge states are of mixed XD and space-separated character and, since  $d_A^{cv} = 0$ , XA states do not participate in the ultrafast exciton dynamics. The exclusion of XA states from the dynamics significantly decreases the numerical effort and at the same time allows us to concentrate on the dynamics of ultrafast electron transfer, instead of considering both electron transfer and exciton transfer. The main qualitative features of the ultrafast exciton dynamics described earlier remain the same, as detailed in the Supporting Information.

The system is excited at  $\hbar\omega_c = 2.35$  eV. Figure 9a presents the time dependence of the normalized number excitons in

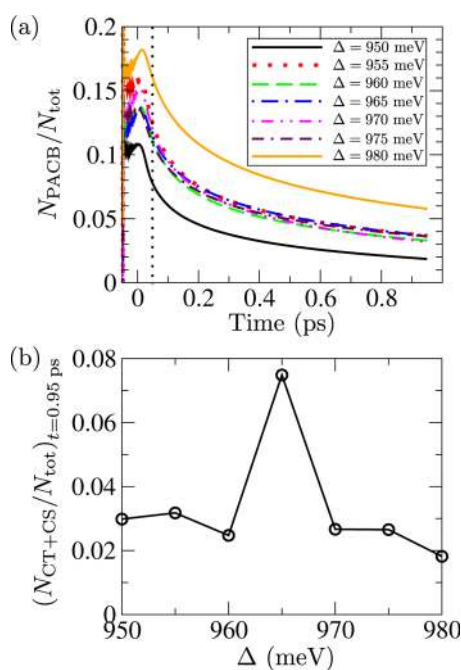


**Figure 9.** (a) Time dependence of the normalized number of PACB excitons for different LUMO–LUMO offsets  $\Delta$ . (b) The relative number of excitons in space-separated (CT and CS) states 900 fs after the excitation for different LUMO–LUMO offsets  $\Delta$ .

PACB states, while Figure 9b shows the normalized number of excitons in space-separated states 900 fs after the excitation for different LUMO–LUMO offsets ranging from 950 to 980 meV in steps of 5 meV. Small variations of the LUMO–LUMO offset between 955 and 975 meV weakly affect the portion of PACB excitons in the total exciton population. However, for the LUMO–LUMO offset of 980 meV, the normalized number of excitons in PACB states is somewhat higher than for the other considered values, while this number is somewhat smaller for the LUMO–LUMO offset of 950 meV. Namely, for larger LUMO–LUMO offsets, the lowest state of  $\text{CT}_2$  band is closer to the central frequency of the excitation, and the direct optical generation of excitons in PACB states is more pronounced. For smaller LUMO–LUMO offsets, the initial generation of

excitons in PACB states is to a certain extent suppressed because the energy difference between the lowest state of  $\text{CT}_2$  band and the central frequency of the excitation is larger. On the other hand, the relative number of space-separated excitons can change up to three times as a result of small changes in the LUMO–LUMO offset. The different behavior displayed by the relative numbers of PACB excitons and space-separated excitons is a consequence of different mechanisms by which PACB states and bridge states emerge. The peak in the normalized number of space-separated excitons observed for the LUMO–LUMO offset of 965 meV signals that the exciton-level alignment at this point favors either (i) formation of more bridge states of dominant space-separated character than at other points or (ii) formation of bridge states that couple more strongly to initial donor states than bridge states at other points.

#### Influence of Carrier–Phonon Interaction Strength and Temperature on Ultrafast Exciton Dynamics.

We have analyzed the ultrafast exciton dynamics for different strengths of the carrier–phonon coupling, exciting the system at  $\hbar\omega_c = 2.35$  eV. The polaron binding energy  $\epsilon_{\text{pol}}^b$  (eq 18), which is a measure of the carrier–phonon interaction strength, assumes values of 20, 50, and 70 meV.

Since the carrier–phonon interaction mediates the conversion from coherent to incoherent exciton populations, weaker carrier–phonon coupling makes this conversion somewhat slower (see Figure 10a). We note that, for all the interaction strengths considered, the total coherent population decays 100 times (compared to its maximal value) in  $\lesssim 100$  fs following the excitation, meaning that the conversion is in all three cases relatively fast.

The normalized number of excitons in PACB states is smaller for stronger carrier–phonon interaction (see Figure 10b). The characteristic time scale for the decay of the population of PACB states is shorter for stronger carrier–phonon interaction, which is a consequence of stronger phonon-mediated coupling among PACB states and donor states (pathway (2) in Figure 3). For larger interaction strength, the populations of CS and CT states comprise larger part of the total exciton population (see Figure 10d,e). Namely, the stronger the carrier–phonon interaction, the more probable the transitions from donor excitons to bridge states (pathway (4) in Figure 3) and the larger the populations of CS and CT states (pathways (5)–(7) in Figure 3). The relative number of acceptor excitons does not change very much with the carrier–phonon interaction strength (see Figure 10b). The variation in the relative number of donor excitons brought about by the changes in the interaction strength is governed by a number of competing factors. First, stronger carrier–phonon interaction favors larger number of donor excitons, since phonon-assisted transitions from PACB to XD states (pathway (2) in Figure 3) are more pronounced. Second, for stronger interaction, the transitions from XD to bridge states are more probable (pathway (4) in Figure 3). Third, since phonon-mediated transitions are most pronounced between exciton states of the same character, stronger interaction may also favor deexcitation of donor populations within the XD manifold (down to the lowest XD state, pathway (3) in Figure 3) to possible transitions (via bridge states) to the space-separated manifold (pathways (4)–(7) in Figure 3). From Figure 10c we see that, as a result of all these factors, the relative number of donor excitons does not change monotonously with the interaction strength.

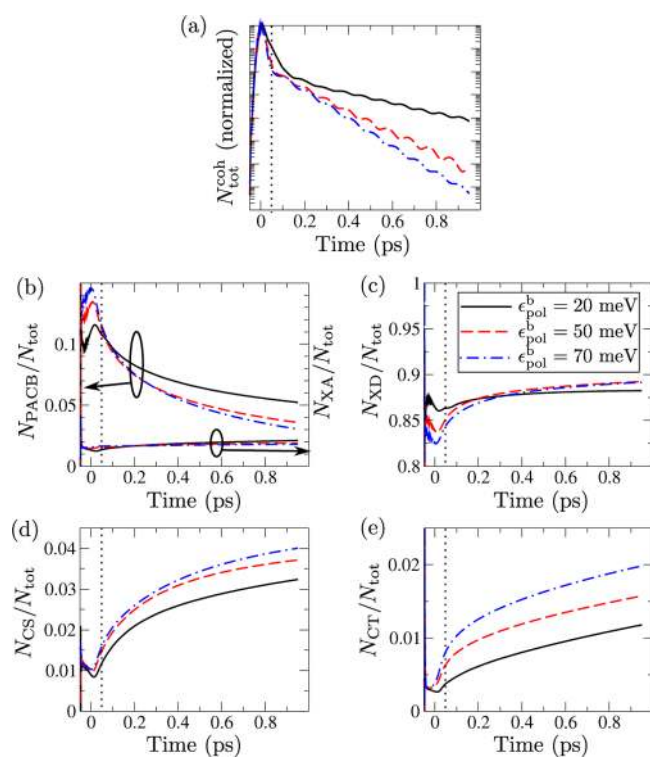


**Figure 10.** (a) Time dependence of the total coherent exciton population  $N_{\text{tot}}^{\text{coh}}$  for different carrier–phonon interaction strengths. For convenience,  $N_{\text{tot}}^{\text{coh}}$  is normalized so that its maximum assumes the same value for all studied interaction strengths. Dynamics of normalized incoherent excitation populations of (b) PACB and XA, (c) XD, (d) CS, and (e) CT states, for different interaction strengths.

In order to understand how the changes in carrier–phonon interaction strength affect the photophysical pathways along which the ultrafast exciton dynamics proceeds, in Figure 11a–l we present energy- and time-resolved incoherent populations of various groups of exciton states (in different rows) and for different interaction strengths (in different columns).

While for the strongest studied interaction initially generated higher-lying donor excitons and excitons in PACB states leave the initial states rapidly (see Figure 11i,j), for the weakest studied interaction strength, significant exciton population remains in these states during the first picosecond of the exciton dynamics (see Figure 11a,b). The deexcitation of donor excitons takes place predominantly within the XD manifold (pathway (3) in Figure 3) for all three interaction strengths (compare the ranges of color bars in Figure 11a,e,i). For the weakest studied interaction, the lowest donor state, which is a trap for the exciton dissociation, is largely bypassed in the course of the deexcitation, whereas for stronger carrier–phonon interactions, this state acquires significant population already from the beginning of the excitation. Energy- and time-resolved populations of CS states are very nearly the same for all three interaction strengths studied (see Figure 11c,g,k). The major part of the CS population resides in bridge states, and the deexcitation within the subset of CS states (pathway (6) in Figure 3) is not very pronounced. On the other hand, the deexcitation within the subset of CT states (pathway (7) in Figure 3), down to the lowest CT state, is observed for all the interaction strengths considered (see the series of more or less bright bands in Figure 11d,h,l). While for the weakest interaction the largest portion of the CT population resides in

the bridge state of CT character located at around 2.2 eV, for the strongest interaction, the major part of the CT population is located in the lowest state of  $\text{CT}_1$  band at around 1.63 eV.

The carrier–phonon coupling thus acts in two different ways. On the one hand, stronger carrier–phonon interaction enhances exciton dissociation and subsequent charge separation by (i) enabling phonon-assisted transitions from a donor state to space-separated states via bridge states (pathways (4) and (5) in Figure 3) and (ii) enabling phonon-assisted transitions within the space-separated manifold once a space-separated state is reached (pathways (6) and (7) in Figure 3). On the other hand, stronger carrier–phonon coupling is detrimental to exciton dissociation and further charge separation because (i) it makes donor states more easily accessible from initially generated PACB excitons (pathway (2) in Figure 3), and, similarly, it may favor backward transitions from a bridge state to a donor state with respect to transitions to the space-separated manifold and (ii) downward phonon-assisted transitions make low-energy CT states, which are usually considered as traps for charge separation, populated on a picosecond time scale following the excitation (pathway (7) in Figure 3).

In the Supporting Information we examine the temperature dependence of the ultrafast heterojunction dynamics. We find that the effect of temperature variations on exciton dynamics occurring on subpicosecond time scales is not particularly pronounced, as has been repeatedly recognized in the literature.<sup>59–61</sup>

## DISCUSSION AND CONCLUSION

Using a relatively simple, but physically grounded model of an all-organic heterointerface, we have investigated subpicosecond dynamics of exciton dissociation and charge separation in the framework of the density matrix theory complemented with the DCT scheme. Our model is constructed as an effective model intended to describe the dynamics of excitation transport in the direction perpendicular to the interface, and it is parametrized using the literature data for the P3HT/PCBM blend.

Apart from the electronic states of the fullerene aggregate that originate from molecular orbitals close to the LUMO orbital of PCBM, we also account for the electronic states stemming from orbitals situated at around 1 eV above the LUMO orbital. Our analysis reveals the importance of the space-separated states that inherit nonzero oscillator strengths from donor states (bridge states and PACB states) and exhibit charge delocalization in ultrafast exciton dynamics. Depending on the energy region of the exciton spectrum, the origin of these states is different. In the low-energy region of the spectrum, bridge states are formed as a consequence of the resonant mixing among exciton (i.e., two-particle) states, while in the opposite part of the spectrum the resonant mixing between single-electron states in the two materials brings about the formation of PACB states.

The resonant mixing has been suggested to be the key physical mechanism responsible for the presence of separated charges on ultrafast time scales following the excitation of a D/A heterojunction.<sup>1,11,12,62–65</sup> Employing the model of reduced dimensionality and studying its subpicosecond dynamics on a fully quantum level, we reach similar conclusions, and thus believe that our one-dimensional model is capable of describing the essential physics behind ultrafast interfacial processes. Our one-dimensional model does not provide a detailed description of, e.g., the role of fullerene cluster size and packing in the ultrafast dynamics. However, it takes into account the most important consequences of the aforementioned effects, i.e., the

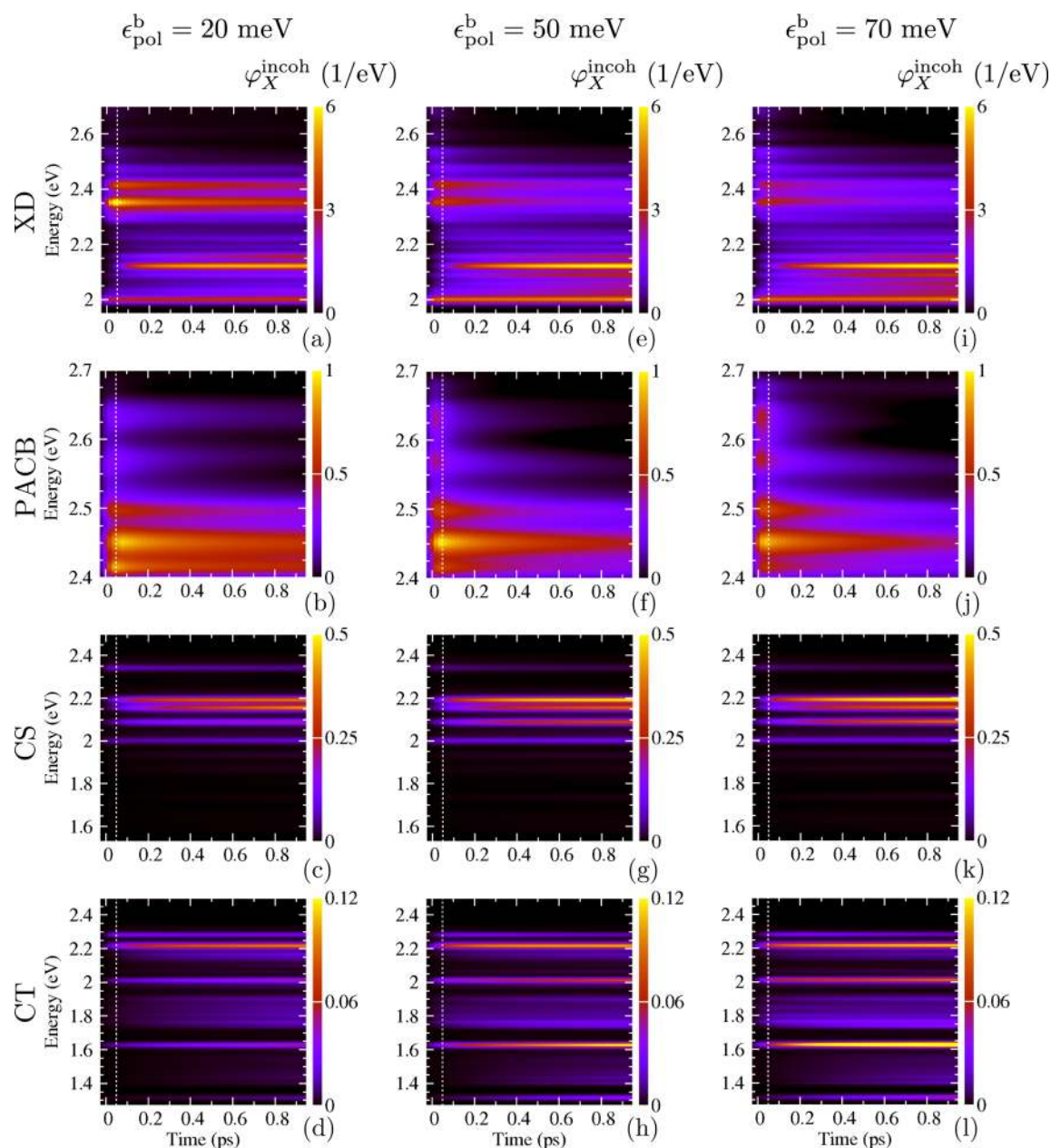


**Figure 11.** Energy- and time-resolved incoherent exciton populations  $\phi_X^{\text{incoh}}(E, t)$  for different carrier–phonon interaction strengths: (a–d)  $g_1 = 26.7$  meV,  $g_2 = 59.7$  meV; (e–h)  $g_1 = 42.2$  meV,  $g_2 = 94.3$  meV; (i–l)  $g_1 = 54.0$  meV,  $g_2 = 111.6$  meV. Groups of exciton states: (a,e,i) XD states; (b,f,j) PACB states; (c,g,k) CS states; (d,h,l) CT states.

delocalization of electronic states and the accessibility of delocalized states of space-separated charges from the states of donor excitons.<sup>64</sup> The effects of the dimensionality of the model become crucial on somewhat longer time and length scales. Namely, on  $\gtrsim 10$  ps time scales, the diffusion-controlled charge separation by incoherent hops throughout the respective materials takes place,<sup>66</sup> and one has to take into consideration all possible separation paths the electron and hole can follow, which can be done correctly only within a three-dimensional model of the heterojunction. The effects of electric polarization and screening at realistic interfaces are rather complex and strongly dependent on the details of the interface.<sup>67</sup> Here, however, we take a minimal model of the electron–hole interaction that reproduces the most important features of the energetics of exciton states obtained from experimental data or from more sophisticated models of polarization and screening

at interfaces. In that sense, our model can be considered as an effective model whose parameters were adjusted to yield realistic energetics of relevant exciton states.

While the PACB states in our model enhance ultrafast charge separation by acting as additional interfacial photon-absorbing states, the most important characteristic of the bridge states is not their direct accessibility from the ground state, but their good coupling with the manifold of donor states. Therefore, for donor excitons, the bridge states act as gateways to the space-separated manifold, so that the populations of low-lying space-separated states are built by progressive deexcitation within the space-separated manifold on a picosecond time scale following the excitation.

The ultrafast exciton dynamics strongly depends on the central frequency of the excitation. While exciting well above the lowest donor state, there are a number of photophysical

pathways enabling subpicosecond exciton dissociation, exciting at the lowest donor state, the major part of generated excitons reside in this state, and ultrafast exciton dissociation is not pronounced. Stronger carrier–phonon interaction enhances phonon-mediated transitions from donor states to bridge states and is thus beneficial to exciton dissociation on ultrafast time scales.

Our results indicate that the number of space-separated charges that are present 1 ps after photoexcitation is rather small, being typically less than 10% of the number of excited electron–hole pairs (see, e.g., Figures 4 and 10). On the other hand, in most efficient solar cell devices internal quantum efficiencies (IQE) close to 100% have been reported. In light of an ongoing debate on the origin of high IQE and the time scale necessary for the charge separation process to occur, our results indicate that longer time scales are needed to separate the charges. Many of the photophysical pathways that we identify eventually lead to occupation of low-lying CT states (e.g., in Figure 3, the pathway starting from initial donor excitons (black bolt) [  $\rightarrow$  (3) ]  $\rightarrow$  (4)  $\rightarrow$  (5)  $\rightarrow$  (7) or the pathway starting from initial PACB excitons (red bolt) [  $\rightarrow$  (1) ]  $\rightarrow$  (2) [  $\rightarrow$  (3) ]  $\rightarrow$  (4)  $\rightarrow$  (5)  $\rightarrow$  (7)). We also find that on subpicosecond time scales a large portion of excitons remains in donor states. Therefore, a mechanism that leads to escape of charges from low-lying CT states and donor states on longer time scales and consequently to high IQE needs to exist. Several recent experimental<sup>68,69</sup> and theoretical<sup>70–72</sup> studies have provided evidence that the separation of charges residing in these states is indeed possible. Along these lines, our model could potentially be part of a multiscale model of the OPV devices, as it yields the populations of different states at  $\sim$ 1 ps after photoexcitation. The output of our model could then be used as input for a semiclassical model that would consider the charge separation and transport on a longer time scale.

## ■ ASSOCIATED CONTENT

### Supporting Information

The Supporting Information is available free of charge on the ACS Publications website at DOI: 10.1021/acs.jpcc.7b05582.

Equations of motion for active density matrices and further details on ultrafast exciton dynamics complementing the main discussion (PDF)

## ■ AUTHOR INFORMATION

### Corresponding Author

\*E-mail: nenad.vukmirovic@ipb.ac.rs; Phone: +381 (0)11 3713152.

### ORCID

Veljko Janković: 0000-0002-0297-2167

### Notes

The authors declare no competing financial interest.

## ■ ACKNOWLEDGMENTS

We gratefully acknowledge the support by the Ministry of Education, Science and Technological Development of the Republic of Serbia (Project No. ON171017) and the European Commission under H2020 project VI-SEEM, Grant No. 675121, as well as the contribution of the COST Action MP1406. Numerical computations were performed on the PARADOX supercomputing facility at the Scientific Computing Laboratory of the Institute of Physics Belgrade.

## ■ REFERENCES

- (1) Grancini, G.; Maiuri, M.; Fazzi, D.; Petrozza, A.; Egelhaaf, H.-J.; Brida, D.; Cerullo, G.; Lanzani, G. Hot Exciton Dissociation in Polymer Solar Cells. *Nat. Mater.* **2013**, *12*, 29–33.
- (2) Jailaubekov, A. E.; Willard, A. P.; Tritsch, J. R.; Chan, W.-L.; Sai, N.; Gearba, R.; Kaake, L. G.; Williams, K. J.; Leung, K.; Rossky, P. J.; et al. Hot Charge-Transfer Excitons Set the Time Limit for Charge Separation at Donor/Acceptor Interfaces in Organic Photovoltaics. *Nat. Mater.* **2013**, *12*, 66–73.
- (3) Gélinas, S.; Rao, A.; Kumar, A.; Smith, S. L.; Chin, A. W.; Clark, J.; van der Poll, T. S.; Bazan, G. C.; Friend, R. H. Ultrafast Long-Range Charge Separation in Organic Semiconductor Photovoltaic Diodes. *Science* **2014**, *343*, 512–516.
- (4) Paracattil, A. A.; Banerji, N. Charge Separation Pathways in a Highly Efficient Polymer: Fullerene Solar Cell Material. *J. Am. Chem. Soc.* **2014**, *136*, 1472–1482.
- (5) Clarke, T. M.; Durrant, J. R. Charge Photogeneration in Organic Solar Cells. *Chem. Rev.* **2010**, *110*, 6736–6767.
- (6) Deibel, C.; Strobel, T.; Dyakonov, V. Role of the Charge Transfer State in Organic Donor-Acceptor Solar Cells. *Adv. Mater.* **2010**, *22*, 4097–4111.
- (7) Gao, F.; Inganäs, O. Charge Generation in Polymer-Fullerene Bulk-Heterojunction Solar Cells. *Phys. Chem. Chem. Phys.* **2014**, *16*, 20291–20304.
- (8) Few, S.; Frost, J. M.; Nelson, J. Models of Charge Pair Generation in Organic Solar Cells. *Phys. Chem. Chem. Phys.* **2015**, *17*, 2311–2325.
- (9) Bässlér, H.; Köhler, A. "Hot or Cold": How do Charge Transfer States at the Donor-Acceptor Interface of an Organic Solar Cell Dissociate? *Phys. Chem. Chem. Phys.* **2015**, *17*, 28451–28462.
- (10) Ostroverkhova, O. Organic Optoelectronic Materials: Mechanisms and Applications. *Chem. Rev.* **2016**, *116*, 13279–13412.
- (11) Troisi, A. How Quasi-Free Holes and Electrons are Generated in Organic Photovoltaic Interfaces. *Faraday Discuss.* **2013**, *163*, 377–392.
- (12) Vázquez, H.; Troisi, A. Calculation of Rates of Exciton Dissociation into Hot Charge-Transfer States in Model Organic Photovoltaic Interfaces. *Phys. Rev. B: Condens. Matter Mater. Phys.* **2013**, *88*, 205304.
- (13) Bakulin, A. A.; Rao, A.; Pavelyev, V. G.; van Loosdrecht, P. H. M.; Pshenichnikov, M. S.; Niedzialek, D.; Cornil, J.; Beljonne, D.; Friend, R. H. The Role of Driving Energy and Delocalized States for Charge Separation in Organic Semiconductors. *Science* **2012**, *335*, 1340–1344.
- (14) Savoie, B. M.; Rao, A.; Bakulin, A. A.; Gelinas, S.; Movaghar, B.; Friend, R. H.; Marks, T. J.; Ratner, M. A. Unequal Partnership: Asymmetric Roles of Polymeric Donor and Fullerene Acceptor in Generating Free Charge. *J. Am. Chem. Soc.* **2014**, *136*, 2876–2884.
- (15) Nan, G.; Zhang, X.; Lu, G. Do "Hot" Charge-Transfer Excitons Promote Free Carrier Generation in Organic Photovoltaics? *J. Phys. Chem. C* **2015**, *119*, 15028–15035.
- (16) Chen, K.; Barker, A. J.; Reish, M. E.; Gordon, K. C.; Hodgkiss, J. M. Broadband Ultrafast Photoluminescence Spectroscopy Resolves Charge Photogeneration via Delocalized Hot Excitons in Polymer-Fullerene Photovoltaic Blends. *J. Am. Chem. Soc.* **2013**, *135*, 18502–18512.
- (17) Tamura, H.; Burghardt, I. Ultrafast Charge Separation in Organic Photovoltaics Enhanced by Charge Delocalization and Vibronically Hot Exciton Dissociation. *J. Am. Chem. Soc.* **2013**, *135*, 16364–16367.
- (18) Smith, S. L.; Chin, A. W. Ultrafast Charge Separation and Nongeminate Electron-Hole Recombination in Organic Photovoltaics. *Phys. Chem. Chem. Phys.* **2014**, *16*, 20305–20309.
- (19) Sun, Z.; Stafström, S. Dynamics of Charge Separation at an Organic Donor-Acceptor Interface. *Phys. Rev. B: Condens. Matter Mater. Phys.* **2014**, *90*, 115420.
- (20) Tamura, H.; Ramon, J. G. S.; Bittner, E. R.; Burghardt, I. Phonon-Driven Ultrafast Exciton Dissociation at Donor-Acceptor Polymer Heterojunctions. *Phys. Rev. Lett.* **2008**, *100*, 107402.

- (21) Tamura, H.; Burghardt, I.; Tsukada, M. Exciton Dissociation at Thiophene/Fullerene Interfaces: The Electronic Structures and Quantum Dynamics. *J. Phys. Chem. C* **2011**, *115*, 10205–10210.
- (22) Tamura, H.; Martinazzo, R.; Ruckebauer, M.; Burghardt, I. Quantum Dynamics of Ultrafast Charge Transfer at an Oligothiophene-Fullerene Heterojunction. *J. Chem. Phys.* **2012**, *137*, 22A540.
- (23) Huix-Rotllant, M.; Tamura, H.; Burghardt, I. Concurrent Effects of Delocalization and Internal Conversion Tune Charge Separation at Regioregular Polythiophene-Fullerene Heterojunctions. *J. Phys. Chem. Lett.* **2015**, *6*, 1702–1708.
- (24) Bittner, E. R.; Silva, C. Noise-Induced Quantum Coherence Drives Photo-Carrier Generation Dynamics at Polymeric Semiconductor Heterojunctions. *Nat. Commun.* **2014**, *5*, 3119.
- (25) Smith, S. L.; Chin, A. W. Phonon-Assisted Ultrafast Charge Separation in the PCBM Band Structure. *Phys. Rev. B: Condens. Matter Mater. Phys.* **2015**, *91*, 201302.
- (26) Falke, S. M.; Rozzi, C. A.; Brida, D.; Maiuri, M.; Amato, M.; Sommer, E.; De Sio, A.; Rubio, A.; Cerullo, G.; Molinari, E.; et al. Coherent Ultrafast Charge Transfer in an Organic Photovoltaic Blend. *Science* **2014**, *344*, 1001–1005.
- (27) Janković, V.; Vukmirović, N. Origin of Space-Separated Charges in Photoexcited Organic Heterojunctions on Ultrafast Time Scales. *Phys. Rev. B: Condens. Matter Mater. Phys.* **2017**, *95*, 075308.
- (28) Kanai, Y.; Grossman, J. C. Insights on Interfacial Charge Transfer Across P3HT/Fullerene Photovoltaic Heterojunction from Ab Initio Calculations. *Nano Lett.* **2007**, *7*, 1967–1972.
- (29) Sheng, C.-Q.; Wang, P.; Shen, Y.; Li, Y.-J.; Zhang, W.-H.; Xu, F.-Q.; Zhu, J.-F.; Lai, G.-Q.; Li, H.-N. Electronic Structure of PCBM. *Chin. Phys. B* **2012**, *21*, 017102.
- (30) Idé, J.; Fazzi, D.; Casalegno, M.; Meille, S. V.; Raos, G. Electron Transport in Crystalline PCBM-Like Fullerene Derivatives: A Comparative Computational Study. *J. Mater. Chem. C* **2014**, *2*, 7313–7325.
- (31) Liu, T.; Troisi, A. What Makes Fullerene Acceptors Special as Electron Acceptors in Organic Solar Cells and How to Replace Them. *Adv. Mater.* **2013**, *25*, 1038–1041.
- (32) Ma, H.; Troisi, A. Modulating the Exciton Dissociation Rate by up to More than Two Orders of Magnitude by Controlling the Alignment of LUMO + 1 in Organic Photovoltaics. *J. Phys. Chem. C* **2014**, *118*, 27272–27280.
- (33) Grancini, G.; Polli, D.; Fazzi, D.; Cabanillas-Gonzalez, J.; Cerullo, G.; Lanzani, G. Transient Absorption Imaging of P3HT:PCBM Photovoltaic Blend: Evidence For Interfacial Charge Transfer State. *J. Phys. Chem. Lett.* **2011**, *2*, 1099–1105.
- (34) Yi, Y.; Coropceanu, V.; Bredas, J.-L. A Comparative Theoretical Study of Exciton-Dissociation and Charge-Recombination Processes in Oligothiophene/Fullerene and Oligothiophene/Perylenediimide Complexes for Organic Solar Cells. *J. Mater. Chem.* **2011**, *21*, 1479–1486.
- (35) Liu, T.; Troisi, A. Absolute Rate of Charge Separation and Recombination in a Molecular Model of the P3HT/PCBM Interface. *J. Phys. Chem. C* **2011**, *115*, 2406–2415.
- (36) Li, Z.; Zhang, X.; Lu, G. Electron Structure and Dynamics at Poly(3-hexylthiophene)/Fullerene Photovoltaic Heterojunctions. *Appl. Phys. Lett.* **2011**, *98*, 083303.
- (37) Liu, T.; Cheung, D. L.; Troisi, A. Structural Variability and Dynamics of the P3HT/PCBM Interface and its Effects on the Electronic Structure and the Charge-Transfer Rates in Solar Cells. *Phys. Chem. Chem. Phys.* **2011**, *13*, 21461–21470.
- (38) Fujii, M.; Shin, W.; Yasuda, T.; Yamashita, K. Photon-Absorbing Charge-Bridging States in Organic Bulk Heterojunctions Consisting of Diketopyrrolopyrrole Derivatives and PCBM. *Phys. Chem. Chem. Phys.* **2016**, *18*, 9514–9523.
- (39) Axt, V.; Stahl, A. A Dynamics-Controlled Truncation Scheme for the Hierarchy of Density Matrices in Semiconductor Optics. *Z. Phys. B: Condens. Matter* **1994**, *93*, 195–204.
- (40) Axt, V. M.; Victor, K.; Stahl, A. Influence of a Phonon Bath on the Hierarchy of Electronic Densities in an Optically Excited Semiconductor. *Phys. Rev. B: Condens. Matter Mater. Phys.* **1996**, *53*, 7244–7258.
- (41) Axt, V. M.; Mukamel, S. Nonlinear Optics of Semiconductor and Molecular Nanostructures; A Common Perspective. *Rev. Mod. Phys.* **1998**, *70*, 145–174.
- (42) Janković, V.; Vukmirović, N. Dynamics of Exciton Formation and Relaxation in Photoexcited Semiconductors. *Phys. Rev. B: Condens. Matter Mater. Phys.* **2015**, *92*, 235208.
- (43) Král, K.; Khás, Z. Electron Self-Energy in Quantum Dots. *Phys. Rev. B: Condens. Matter Mater. Phys.* **1998**, *57*, R2061–R2064.
- (44) Menšík, M.; Pflieger, J.; Toman, P. Dynamics of Photogenerated Polarons and Polaron Pairs in P3HT Thin Films. *Chem. Phys. Lett.* **2017**, *677*, 87–91.
- (45) Bera, S.; Gheeraert, N.; Fratini, S.; Ciuchi, S.; Florens, S. Impact of Quantized Vibrations on the Efficiency of Interfacial Charge Separation in Photovoltaic Devices. *Phys. Rev. B: Condens. Matter Mater. Phys.* **2015**, *91*, 041107.
- (46) Sun, Z.; Stafström, S. Dynamics of Exciton Dissociation in Donor-Acceptor Polymer Heterojunctions. *J. Chem. Phys.* **2013**, *138*, 164905.
- (47) Cowan, S. R.; Banerji, N.; Leong, W. L.; Heeger, A. J. Charge Formation, Recombination, and Sweep-Out Dynamics in Organic Solar Cells. *Adv. Funct. Mater.* **2012**, *22*, 1116–1128.
- (48) Northrup, J. E. Atomic and Electronic Structure of Polymer Organic Semiconductors: P3HT, PQT, and PBTBT. *Phys. Rev. B: Condens. Matter Mater. Phys.* **2007**, *76*, 245202.
- (49) Maillard, A.; Rochefort, A. Structural and Electronic Properties of Poly(3-hexylthiophene)  $\pi$ -stacked Crystals. *Phys. Rev. B: Condens. Matter Mater. Phys.* **2009**, *79*, 115207.
- (50) Lan, Y.-K.; Huang, C.-I. A Theoretical Study of the Charge Transfer Behavior of the Highly Regioregular Poly-3-hexylthiophene in the Ordered State. *J. Phys. Chem. B* **2008**, *112*, 14857–14862.
- (51) Cheung, D. L.; McMahon, D. P.; Troisi, A. Computational Study of the Structure and Charge-Transfer Parameters in Low-Molecular-Mass P3HT. *J. Phys. Chem. B* **2009**, *113*, 9393–9401.
- (52) Street, R. A.; Hawks, S. A.; Khlyabich, P. P.; Li, G.; Schwartz, B. J.; Thompson, B. C.; Yang, Y. Electronic Structure and Transition Energies in Polymer-Fullerene Bulk Heterojunctions. *J. Phys. Chem. C* **2014**, *118*, 21873–21883.
- (53) Bhatta, R. S.; Tsige, M. Chain Length and Torsional Dependence of Exciton Binding Energies in P3HT and PTB7 Conjugated Polymers: A First-Principles Study. *Polymer* **2014**, *55*, 2667–2672.
- (54) Cheung, D. L.; Troisi, A. Theoretical Study of the Organic Photovoltaic Electron Acceptor PCBM: Morphology, Electronic Structure, and Charge Localization. *J. Phys. Chem. C* **2010**, *114*, 20479–20488.
- (55) Tamura, H.; Tsukada, M. Role of Intermolecular Charge Delocalization on Electron Transport in Fullerene Aggregates. *Phys. Rev. B: Condens. Matter Mater. Phys.* **2012**, *85*, 054301.
- (56) Lücke, A.; Ortmann, F.; Panhans, M.; Sanna, S.; Rauls, E.; Gerstmann, U.; Schmidt, W. G. Temperature-Dependent Hole Mobility and Its Limit in Crystal-Phase P3HT Calculated from First Principles. *J. Phys. Chem. B* **2016**, *120*, 5572–5580.
- (57) Cheng, Y.-C.; Silbey, R. J. A Unified Theory for Charge-Carrier Transport in Organic Crystals. *J. Chem. Phys.* **2008**, *128*, 114713.
- (58) Schulze, M.; Hänsel, M.; Tegeder, P. Hot Excitons Increase the Donor/Acceptor Charge Transfer Yield. *J. Phys. Chem. C* **2014**, *118*, 28527–28534.
- (59) Pensack, R. D.; Asbury, J. B. Beyond the Adiabatic Limit: Charge Photogeneration in Organic Photovoltaic Materials. *J. Phys. Chem. Lett.* **2010**, *1*, 2255–2263.
- (60) Chenel, A.; Mangaud, E.; Burghardt, I.; Meier, C.; Desouter-Lecomte, M. Exciton Dissociation at Donor-Acceptor Heterojunctions: Dynamics Using the Collective Effective Mode Representation of the Spin-Boson Model. *J. Chem. Phys.* **2014**, *140*, 044104.
- (61) Hughes, K. H.; Cahier, B.; Martinazzo, R.; Tamura, H.; Burghardt, I. Non-Markovian Reduced Dynamics of Ultrafast Charge

Transfer at an Oligothiophene-Fullerene Heterojunction. *Chem. Phys.* **2014**, *442*, 111–118.

(62) D'Avino, G.; Muccioli, L.; Olivier, Y.; Beljonne, D. Charge Separation and Recombination at Polymer-Fullerene Heterojunctions: delocalization and Hybridization Effects. *J. Phys. Chem. Lett.* **2016**, *7*, 536–540.

(63) Ma, H.; Troisi, A. Direct Optical Generation of Long-Range Charge-Transfer States in Organic Photovoltaics. *Adv. Mater.* **2014**, *26*, 6163–6167.

(64) Savoie, B. M.; Rao, A.; Bakulin, A. A.; Gelinas, S.; Movaghar, B.; Friend, R. H.; Marks, T. J.; Ratner, M. A. Unequal Partnership: Asymmetric Roles of Polymeric Donor and Fullerene Acceptor in Generating Free Charge. *J. Am. Chem. Soc.* **2014**, *136*, 2876–2884.

(65) Yao, Y.; Xie, X.; Ma, H. Ultrafast Long-Range Charge Separation in Organic Photovoltaics: Promotion by Off-Diagonal Vibronic Couplings and Entropy Increase. *J. Phys. Chem. Lett.* **2016**, *7*, 4830–4835.

(66) Vithanage, D. A.; Devižis, A.; Abramavičius, V.; Infahsaeng, Y.; Abramavičius, D.; MacKenzie, R. C. I.; Keivanidis, P. E.; Yartsev, A.; Hertel, D.; Nelson, J.; et al. Visualizing Charge Separation in Bulk Heterojunction Organic Solar Cells. *Nat. Commun.* **2013**, *4*, 2334.

(67) D'Avino, G.; Mothy, S.; Muccioli, L.; Zannoni, C.; Wang, L.; Cornil, J.; Beljonne, D.; Castet, F. Energetics of Electron-Hole Separation at P3HT/PCBM Heterojunctions. *J. Phys. Chem. C* **2013**, *117*, 12981–12990.

(68) Vandewal, K.; Albrecht, S.; Hoke, E. T.; Graham, K. R.; Widmer, J.; Douglas, J. D.; Schubert, M.; Mateker, W. R.; Bloking, J. T.; Burkhard, G. F.; et al. Efficient Charge Generation by Relaxed Charge-Transfer States at Organic Interfaces. *Nat. Mater.* **2014**, *13*, 63–68.

(69) Gerhard, M.; Arndt, A. P.; Bilal, M.; Lemmer, U.; Koch, M.; Howard, I. A. Field-Induced Exciton Dissociation in PTB7-Based Organic Solar Cells. *Phys. Rev. B: Condens. Matter Mater. Phys.* **2017**, *95*, 195301.

(70) Burke, T. M.; McGehee, M. D. How High Local Charge Carrier Mobility and an Energy Cascade in a Three-Phase Bulk Heterojunction Enable > 90% Quantum Efficiency. *Adv. Mater.* **2014**, *26*, 1923–1928.

(71) Hood, S. N.; Kassal, I. Entropy and Disorder Enable Charge Separation in Organic Solar Cells. *J. Phys. Chem. Lett.* **2016**, *7*, 4495–4500.

(72) Athanasopoulos, S.; Tscheuschner, S.; Bäessler, H.; Köhler, A. Efficient Charge Separation of Cold Charge-Transfer States in Organic Solar Cells Through Incoherent Hopping. *J. Phys. Chem. Lett.* **2017**, *8*, 2093–2098.

**Origin of space-separated charges in photoexcited organic heterojunctions on ultrafast time scales**

Veljko Janković\* and Nenad Vukmirović†

*Scientific Computing Laboratory, Center for the Study of Complex Systems, Institute of Physics Belgrade, University of Belgrade, Pregrevica 118, 11080 Belgrade, Serbia*

(Received 29 December 2016; published 21 February 2017)

We present a detailed investigation of ultrafast (subpicosecond) exciton dynamics in the lattice model of a donor/acceptor heterojunction. Exciton generation by means of a photoexcitation, exciton dissociation, and further charge separation are treated on equal footing. The experimentally observed presence of space-separated charges at  $\lesssim 100$  fs after the photoexcitation is usually attributed to ultrafast transitions from excitons in the donor to charge-transfer and charge-separated states. Here, we show, however, that the space-separated charges appearing on  $\lesssim 100$ -fs time scales are predominantly directly optically generated. Our theoretical insights into the ultrafast pump-probe spectroscopy challenge usual interpretations of pump-probe spectra in terms of ultrafast population transfer from donor excitons to space-separated charges.

DOI: [10.1103/PhysRevB.95.075308](https://doi.org/10.1103/PhysRevB.95.075308)**I. INTRODUCTION**

The past two decades have seen rapidly growing research efforts in the field of organic photovoltaics (OPVs), driven mainly by the promise of economically viable and environmentally friendly power generation [1–5]. In spite of vigorous and interdisciplinary research activities, there is a number of fundamental questions that still have to be properly answered in order to rationally design more efficient OPV devices. It is commonly believed [1,6] that photocurrent generation in OPV devices is a series of the following sequential steps. Light absorption in the donor material creates an exciton, which subsequently diffuses towards the donor/acceptor (D/A) interface where it dissociates producing an interfacial charge transfer (CT) state. The electron and hole in this state are tightly bound and localized at the D/A interface. The CT state further separates into a free electron and a hole [the so-called charge-separated (CS) state], which are then transported to the respective electrodes. On the other hand, several recent spectroscopic studies [7–10] have indicated the presence of spatially separated electrons and holes on ultrafast ( $\lesssim 100$  fs) time scales after the photoexcitation. These findings challenge the described picture of free-charge generation in OPV devices as the following issues arise. (i) It is not expected that an exciton created in the donor can diffuse in such a short time to the D/A interface since the distance it can cover in 100 fs is rather small compared to the typical size of phase segregated domains in bulk heterojunctions. [11] (ii) The mechanism by which a CT state would transform into a CS state is not clear. The binding energy of a CT exciton is rather large [6,12] and there is an energy barrier preventing it from the transition to a CS state, especially at such short time scales.

To resolve question (ii), many experimental [7,8,13,14] and theoretical [15–19] studies have challenged the implicit assumption that the lowest CT state is involved in the process. These studies emphasized the critical role of electronically hot (energetically higher) CT states as intermediate states before the transition to CS states. Having significantly larger

electron-hole separations, i.e., more delocalized carriers, compared to the interface-bound CT states, these hot CT states are also more likely to exhibit ultrafast charge separation and thus bypass the relaxation to the lowest CT state. The time scale of the described hot exciton dissociation mechanism is comparable to the time scale of hot CT exciton relaxation to the lowest CT state [8,18]. Other studies suggested that electron delocalization in the acceptor may reduce the Coulomb barrier [9,20,21] and allow the transition from CT to CS states. Experimental results of Vandewal *et al.* [22], who studied the consequences of the direct optical excitation of the lowest CT state, suggest that the charge separation can occur very efficiently from this state. To resolve issue (i), it has been proposed that a direct transition from donor excitons to CS states provides an efficient route for charge separation [23,24].

All the aforementioned studies implicitly assume that an optical excitation creates a donor exciton and address the mechanisms by which it can evolve into a CT or CS state on a  $\sim 100$ -fs time scale. In this work, we demonstrate that the majority of space-separated charges that are present  $\sim 100$  fs after photoexcitation are directly optically generated, in contrast to the usual belief that they originate from optical generation of donor excitons followed by some of the proposed mechanisms of transfer to CT or CS states. We note that in a recent theoretical work Ma and Troisi [25] concluded that space-separated electron-hole pairs significantly contribute to the absorption spectrum of the heterojunction, suggesting the possibility of their direct optical generation. A similar conclusion was also obtained in the most recent study of D'Avino *et al.* [26]. These works, however, do not provide information about the relative importance of direct optical generation of space-separated charges in comparison to other hypothesized mechanisms of their generation. On the other hand, in the framework of a simple, yet physically grounded model, we simulate the time evolution of populations of various exciton states during and after optical excitation. Working with a model Hamiltonian whose parameters have clear physical meanings, we are able to vary model parameters and demonstrate that these variations do not violate our principal conclusion that the space-separated charges present at  $\sim 100$  fs following photoexcitation originate from direct optical generation. In addition, we numerically investigate the

\*veljko.jankovic@ipb.ac.rs

†nenad.vukmirovic@ipb.ac.rs

ultrafast pump-probe spectroscopy and find that the signal on ultrafast time scales is dominated by coherences rather than by state populations. This makes the interpretation of the experimental spectra in terms of state populations rather difficult.

The paper is organized as follows. Section II introduces the model, its parametrization, and the theoretical treatment of ultrafast exciton dynamics. The central conclusion of our study is presented in Sec. III, where we also assess its robustness against variations of most of the model parameters. Section IV is devoted to the theoretical approach to ultrafast pump-probe experiments and numerical computations of the corresponding pump-probe signals. We discuss our results and draw conclusions in Sec. V.

## II. THEORETICAL FRAMEWORK

In this section, we lay out the essential elements of the model (Sec. II A) and of the theoretical approach (Sec. II B) we use to study ultrafast exciton dynamics at a heterointerface. Section II C presents the parametrization of the model Hamiltonian and analyzes its spectrum.

### A. One-dimensional lattice model of a heterojunction

In this study, a one-dimensional two-band lattice semiconductor model is employed to describe a heterojunction. It takes into account electronic couplings, carrier-carrier, and carrier-phonon interactions, as well as the interaction of carriers with the external electric field. There are  $2N$  sites in total, see Fig. 2(a); first  $N$  sites (labeled by  $0, \dots, N-1$ ) belong to the donor part of the heterojunction, while sites labeled by  $N, \dots, 2N-1$  belong to the acceptor part. Each site  $i$  has one valence-band and one conduction-band orbital and also contributes localized phonon modes counted by index  $\lambda_i$ . The model Hamiltonian is pictorially presented in Fig. 1(a), the total Hamiltonian being

$$H = H_c + H_p + H_{c-p} + H_{c-f}. \quad (1)$$

Interacting carriers are described by

$$H_c = \sum_{i=0}^{2N-1} \left( H_c^i + H_h^i + \sum_{\substack{j=0 \\ j \neq i}}^{2N-1} (H_e^{ij} + H_h^{ij}) + \sum_{j=0}^{2N-1} H_{e-h}^{ij} \right), \quad (2)$$

the phonon Hamiltonian is

$$H_p = \sum_{i=0}^{2N-1} H_p^i, \quad (3)$$

the carrier-phonon interaction is

$$H_{c-p} = \sum_{i=0}^{2N-1} (H_{e-p}^i + H_{h-p}^i), \quad (4)$$

while the interaction of carriers with the external exciting field  $E(t)$  is given as

$$H_{c-f} = \sum_{i=0}^{2N-1} H_{c-f}^i. \quad (5)$$

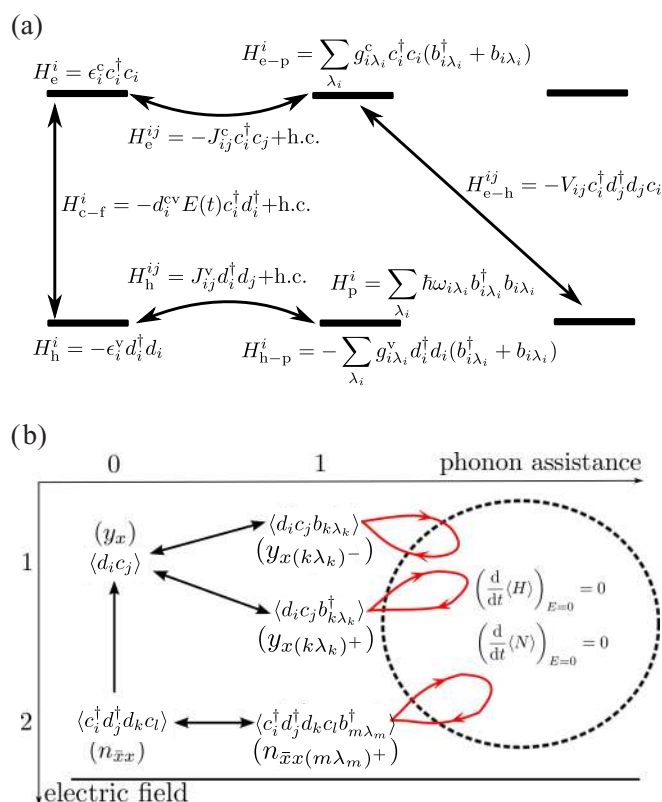


FIG. 1. (a) Illustration of the model Hamiltonian used in our study. (b) Active variables in the density matrix formalism and their interrelations in the resulting hierarchy of equations. The direction of a straight arrow indicates that in the equation for the variable at its start appears the variable at its end. Loops represent couplings to higher-order phonon-assisted density matrices which are truncated so that the particle number and energy of the free system are conserved.

In Fig. 1(a), Fermi operators  $c_i^\dagger$  and  $d_i^\dagger$  ( $c_i$  and  $d_i$ ) create (destroy) electrons and holes on site  $i$ , whereas Bose operators  $b_{i\lambda_i}^\dagger$  ( $b_{i\lambda_i}$ ) create (destroy) phonons in mode  $\lambda_i$  on site  $i$ .  $\epsilon_i^c$  and  $\epsilon_i^v$  are electron and hole on-site energies, while  $J_{ij}^c$  and  $J_{ij}^v$  denote electron and hole transfer integrals, respectively. The carrier-phonon interaction is taken to be of the Holstein form, where a charge carrier is locally and linearly coupled to dispersionless optical modes, and  $g_{i\lambda_i}^c$  and  $g_{i\lambda_i}^v$  are the interaction strengths with electrons and holes, respectively. Electron-hole interaction is accounted for in the lowest monopole-monopole approximation and  $V_{ij}$  is the carrier-carrier interaction potential. Interband dipole matrix elements are denoted by  $d_i^{cv}$ .

### B. Theoretical approach to exciton dynamics

We examine the ultrafast exciton dynamics during and after pulsed photoexcitation of a heterointerface in the previously developed framework of the density matrix theory complemented with the dynamics controlled truncation (DCT) scheme [27–29] (see Ref. [30] and references therein), starting from initially unexcited heterojunction. We confine ourselves to the case of weak optical field and low carrier densities, in which it is justified to work in the subspace of single-

exciton excitations (spanned by the so-called exciton basis) and truncate the carrier branch of the hierarchy of equations for density matrices retaining only contributions up to the second order in the optical field. The phonon branch of the hierarchy is truncated independently so as to ensure the particle-number and energy conservation after the pulsed excitation, as described in detail in Ref. [30].

In more detail, the exciton basis is obtained solving the eigenvalue problem

$$\sum_{i'j'} (\delta_{i'i} \epsilon_{jj'}^c - \delta_{j'j} \epsilon_{ii'}^v - \delta_{i'i} \delta_{j'j} V_{ij}) \psi_{i'j'}^x = \hbar \omega_x \psi_{ij}^x, \quad (6)$$

where indices  $i, i'$  ( $j, j'$ ) correspond to the position of the hole (electron) and quantities  $\epsilon_{mn}^c$  ( $\epsilon_{mn}^v$ ) denote on-site electron (hole) energies (for  $m = n$ ) or electron (hole) transfer integrals (for  $m \neq n$ ) in the donor, in the acceptor, or between the donor and the acceptor. The creation operator for the exciton in the state  $x$  is then defined as

$$X_x^\dagger = \sum_{ij} \psi_{ij}^x c_j^\dagger d_i^\dagger. \quad (7)$$

As we pointed out [30], the total Hamiltonian, in which only contributions whose expectation values are at most of the second order in the optical field are kept, can be expressed in terms of exciton operators  $X_x^\dagger, X_x$  as

$$\begin{aligned} H = & \sum_x \hbar \omega_x X_x^\dagger X_x + \sum_{i\lambda_i} \hbar \omega_{i\lambda_i} b_{i\lambda_i}^\dagger b_{i\lambda_i} \\ & + \sum_{\substack{\bar{x}x \\ i\lambda_i}} (\Gamma_{\bar{x}x}^{i\lambda_i} X_{\bar{x}}^\dagger X_x b_{i\lambda_i}^\dagger + \Gamma_{\bar{x}x}^{i\lambda_i*} X_x^\dagger X_{\bar{x}} b_{i\lambda_i}) \\ & - E(t) \sum_x (M_x^* X_x + M_x X_x^\dagger), \end{aligned} \quad (8)$$

where the exciton-phonon coupling constants are given as

$$\Gamma_{\bar{x}x}^{i\lambda_i} = g_{i\lambda_i}^c \sum_j \psi_{ji}^{\bar{x}*} \psi_{ji}^x - g_{i\lambda_i}^v \sum_j \psi_{ij}^{\bar{x}*} \psi_{ij}^x, \quad (9)$$

while the dipole moment for the generation of the state  $x$  from the ground state is

$$M_x = \sum_i \psi_{ii}^{x*} d_i^{cv}. \quad (10)$$

Active variables in our formalism are the coherences between exciton state  $x$  and the ground state,  $y_x = \langle X_x \rangle$ , exciton populations (for  $\bar{x} = x$ ), and exciton-exciton coherences (for  $\bar{x} \neq x$ )  $n_{\bar{x}x} = \langle X_{\bar{x}}^\dagger X_x \rangle$ , together with their single-phonon-assisted counterparts  $y_{x(i\lambda_i)^-} = \langle X_x b_{i\lambda_i} \rangle$ ,  $y_{x(i\lambda_i)^+} = \langle X_x b_{i\lambda_i}^\dagger \rangle$ , and  $n_{\bar{x}x(i\lambda_i)^+} = \langle X_{\bar{x}}^\dagger X_x b_{i\lambda_i}^\dagger \rangle$ . Their mutual interrelations in the resulting hierarchy are schematically shown in Fig. 1(b), while the equations themselves are presented in Ref. [31]. In order to quantitatively monitor ultrafast processes at the model heterojunction during and after its pulsed photoexcitation, the incoherent population of exciton state  $x$ , which gives the number of truly bound (Coulomb-correlated) electron-hole pairs in the state  $x$ ,

$$\bar{n}_{xx} = n_{xx} - |y_x|^2, \quad (11)$$

will be used. Coherent populations of exciton states,  $|y_x|^2$ , dominate early stages of the optical experiment, typically decay quickly due to different scattering mechanisms (in our case, the carrier-phonon interaction), and do not represent bound electron-hole pairs. The populations of truly bound electron-hole pairs build up on the expense of coherent exciton populations. We frequently normalize  $\bar{n}_{xx}$  to the total exciton population in the system,

$$N_{\text{tot}} = \sum_x n_{xx}, \quad (12)$$

which, together with the expectation value of the Hamiltonian  $\langle H \rangle$ , is conserved in the absence of the external field. Probabilities  $f_e(t, r)$  [ $f_h(t, r)$ ] that an electron (a hole) is located at site  $r$  at instant  $t$  can be obtained using the so-called contraction identities (see, e.g., Ref. [29]) and are given as

$$f_e(t, r) = \frac{\sum_{\bar{x}x} (\sum_{r_h} \psi_{r_h r}^{\bar{x}*} \psi_{r_h r}^x) n_{\bar{x}x}(t)}{\sum_x n_{xx}(t)}, \quad (13)$$

$$f_h(t, r) = \frac{\sum_{\bar{x}x} (\sum_{r_e} \psi_{r r_e}^{\bar{x}*} \psi_{r r_e}^x) n_{\bar{x}x}(t)}{\sum_x n_{xx}(t)}. \quad (14)$$

Consequently, the probability that an electron is in the acceptor at time  $t$  is

$$P_A^e(t) = \sum_{r=N}^{2N-1} f_e(t, r). \quad (15)$$

### C. Model parameters and Hamiltonian spectrum

The model Hamiltonian was parameterized to yield values of band gaps, bandwidths, band offsets, and exciton binding energies that are representative of typical OPV materials. The values of model parameters used in numerical computations are summarized in Table I. While these values largely correspond to the PCPDTBT/PCBM interface, we note that our goal is to reach general conclusions valid for a broad class of interfaces. Consequently, later in this study, we also vary most of the model parameters and study the effects of these variations. Figures 2(a) and 2(b) illustrate the meaning of some of the model parameters.

All electron and hole transfer integrals are restricted to nearest neighbors. The single-particle band gap of the donor  $E_{g,D}$ , as well as the offset  $\Delta E_{DA}^c$  between the lowest single-electron levels in the donor and acceptor, assume values that are representative of the low-band-gap PCPDTBT polymer used in the most efficient solar cells [32,33]. The single-particle band gap of the acceptor  $E_{g,A}$  and electron/hole transfer integrals  $J_A^{c/v}$  are tuned to values typical of fullerene and its derivatives [34,35]. Electron/hole transfer integrals  $J_D^{c/v}$  in the donor were extracted from the conduction and valence bandwidths of the PCPDTBT polymer. To obtain the bandwidths, an electronic structure calculation was performed on a straight infinite polymer. The calculation is based on the density functional theory (DFT) in the local density approximation (LDA), as implemented in the QUANTUM ESPRESSO [36] package. Transfer integrals were then obtained as 1/4 of the respective bandwidth. The values of the transfer integral between the two materials are chosen to be similar to the values obtained in the

TABLE I. Values of model parameters used in calculations.

Parameter <sup>a</sup>	Value
$E_{g,D}$ (meV)	1500
$E_{g,A}$ (meV)	1950
$\Delta E_{DA}^c$ (meV)	500
$ J_D^c $ (meV)	105
$ J_D^v $ (meV)	295
$ J_A^c $ (meV)	150
$ J_A^v $ (meV)	150
$ J_{DA}^c ,  J_{DA}^v $ (meV)	75
$\epsilon_r$	3.0
$N$	11
$a$ (nm)	1.0
$U$ (meV)	480
$\hbar\omega_{p,1}$ (meV)	10
$g_1$ (meV)	28.5
$\hbar\omega_{p,2}$ (meV)	185
$g_2$ (meV)	57.0
$T$ (K)	300
$t_0$ (fs)	50

<sup>a</sup> $E_{g,D}$  ( $E_{g,A}$ ) is the single-particle band gap in the donor (acceptor).  $\Delta E_{DA}^c$  denotes LUMO-LUMO energy offset.  $J_D^{c/v}$  ( $J_A^{c/v}$ ) are electron/hole transfer integrals in the donor (acceptor).  $J_{DA}^{c/v}$  are electron/hole transfer integrals between the donor and acceptor.  $\epsilon_r$  is the relative dielectric constant.  $N$  is the number of lattice sites in the donor and acceptor ( $2N$  sites in total).  $a$  is the lattice constant.  $U$  denotes the on-site Coulomb interaction.  $\hbar\omega_{p,1/2}$  are energies of local phonon modes, while  $g_{1/2}$  are carrier-phonon coupling constants.  $T$  denotes temperature. The duration of the pulse is  $2t_0$ .

*ab initio* study of P3HT/PCBM heterojunctions [37]. We set the number of sites in a single material to  $N = 11$ , which is reasonable having in mind that the typical dimensions of phase segregated domains in bulk heterojunction morphology are considered to be 10–20 nm [11]. The electron-hole interaction potential  $V_{ij}$  is modeled using the Ohno potential

$$V_{ij} = \frac{U}{\sqrt{1 + \left(\frac{r_{ij}}{a_0}\right)^2}}, \quad (16)$$

where  $r_{ij}$  is the distance between sites  $i$  and  $j$ , and  $a_0 = e^2/(4\pi\epsilon_0\epsilon_r U)$  is the characteristic length. The relative dielectric constant  $\epsilon_r$  assumes a value typical for organic materials, while the magnitude of the on-site Coulomb interaction  $U$  was chosen so that the exciton binding energy in both the donor and the acceptor is around 300 meV. Following common practice when studying all-organic heterojunctions [38,39], we take one low-energy and one high-energy phonon mode. For simplicity, we assume that energies of both phonon modes, as well as their couplings to carriers, have the same values in both materials. The high-frequency phonon mode of energy 185 meV ( $\approx 1500 \text{ cm}^{-1}$ ), which is present in both materials, was suggested to be crucial for ultrafast electron transfer in the P3HT/PCBM blend [40]. Recent theoretical calculations of the phonon spectrum and electron-phonon coupling constants in P3HT indicate the presence of low-energy phonon modes ( $\lesssim 10$  meV) that strongly couple to carriers [41]. The chosen

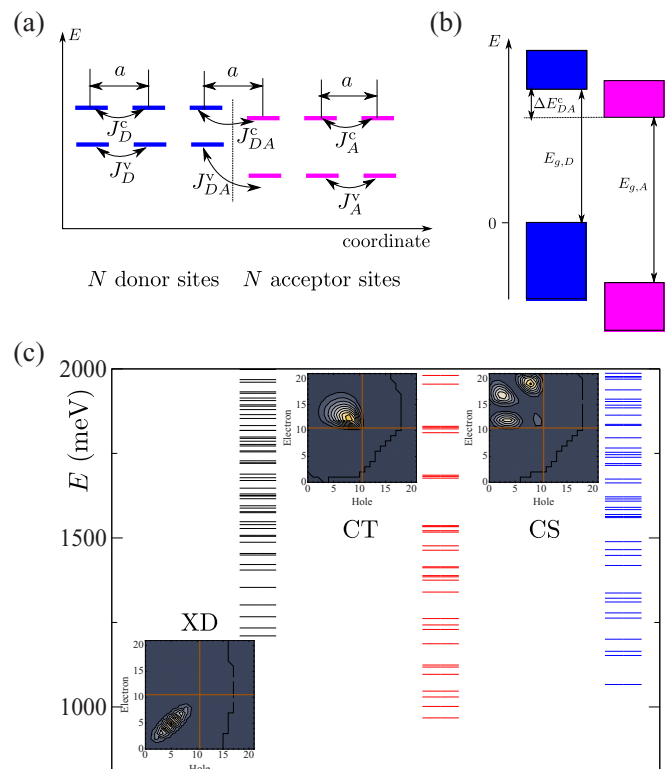


FIG. 2. (a) One-dimensional lattice model of a heterojunction. Various types of electronic couplings (in the donor, in the acceptor, and among them) are indicated. There is an energy offset between single-electron/hole levels in the donor and acceptor. (b) Band alignment produced by our model. (c) Energies of exciton states, in particular of donor excitons (black lines), CT (red lines), and CS (blue lines) states. Exciton wave function square moduli are shown for the lowest donor, CT, and CS state.

values of phonon-mode energies fall in the ranges in which the phonon density of states in conjugated polymers is large [42] and the local electron-vibration couplings in PCBM are pronounced [43]. We estimate the carrier-phonon coupling constants from the value of polaron binding energy, which can be estimated using the result of the second-order weak-coupling perturbation theory at  $T = 0$  in the vicinity of the point  $k = 0$  [44]:

$$\epsilon_b^{\text{pol}} = \sum_{i=1}^2 \frac{g_i^2}{2|J|} \frac{1}{\sqrt{\left(1 + \frac{\hbar\omega_{p,i}}{2|J|}\right)^2 - 1}}. \quad (17)$$

We took  $g_2/g_1 = 2$  and estimated the numerical values assuming that  $\epsilon_b^{\text{pol}} = 20$  meV and  $|J| = 125$  meV. The electric field is centered around  $t = 0$  and assumes the form

$$E(t) = E_0 \cos(\omega_c t) \theta(t + t_0) \theta(t_0 - t), \quad (18)$$

where  $\omega_c$  is its central frequency,  $\theta(t)$  is the step function, and the duration of the pulse is  $2t_0$ . The time  $t_0$  should be chosen large enough so that the pulse is spectrally narrow enough (the energy of the initially generated excitons is around the central frequency of the pulse). On the other hand, since our focus is on processes happening on subpicosecond time scale, the pulse should be as short as possible in order

to disentangle the carrier generation during the pulse from free-system evolution after the pulse. Trying to reconcile the aforementioned requirements, we choose  $t_0 = 50$  fs. We note that the results and conclusions to be presented do not crucially depend on the particular value of  $t_0$  nor on the wave form of the excitation. This is shown in greater detail in Ref. [31], see Figs. 1 and 2, where we present the dynamics for shorter pulses of wave forms given in Eqs. (18) and (33). Interband dipole matrix elements  $d_i^{cv}$  are zero in the acceptor ( $i = N, \dots, 2N - 1$ ), while in the donor they all assume the same value  $d^{cv}$  so that  $d^{cv} E_0 = 0.2$  meV (weak excitation).

Figure 2(c) displays part of the exciton spectrum produced by our model. Exciton states can be classified according to the relative position of the electron and the hole. The classification is straightforward only for the noninteracting heterojunction ( $J_{DA}^{c/v} = 0$ ), in which case any exciton state can be classified into four groups: (a) both the electron and the hole are in the donor [donor exciton (XD) state], (b) both the electron and the hole are in the acceptor (acceptor exciton state), (c) the electron is in the acceptor, while the hole is in the donor (space-separated exciton state), and (d) the electron is in the donor, while the hole is in the acceptor.

Space-separated excitons can be further discriminated according to their mean electron-hole distance defined as

$$\langle r_{e-h} \rangle_x = \sum_{ij} |i - j| |\psi_{ij}^x|^2. \quad (19)$$

When the electron-hole interaction is set to zero, the mean electron-hole distance for all the states from group (c) is equal to  $N$ . For the nonzero Coulomb interaction, we consider a space-separated exciton as a CS exciton if its mean electron-hole distance is larger than (or equal to)  $N$ , otherwise we consider it as a CT exciton. In the general case, the character of an exciton state is established by calculating its overlap with each of the aforementioned groups of the exciton states at the noninteracting heterojunction; this state then inherits the character of the group with which the overlap is maximal.

### III. NUMERICAL RESULTS

Here, the results of our numerical calculations on the model system defined in Sec. II are presented. In Sec. III A, we observe that the populations of CT and CS states predominantly build up during the action of the excitation, and that the changes in these populations occurring on  $\sim 100$ -fs time scales after the excitation are rather small. This conclusion, i.e., the direct optical generation as the principal source of space-separated charges on ultrafast time scales following the excitation, is shown in Sec. III B to be robust against variations of model parameters. Since the focus of our study is on the ultrafast exciton dynamics at photoexcited heterojunctions, all the computations are carried out for 1 ps in total (involving the duration of the pulse).

#### A. Interfacial dynamics on ultrafast time scales

Figure 3(a) shows the time dependence of the numbers of donor, CT, and CS excitons for the 100-fs-long excitation with central frequency  $\hbar\omega_c = 1500$  meV, which excites the system well above the lowest donor or space-separated exciton

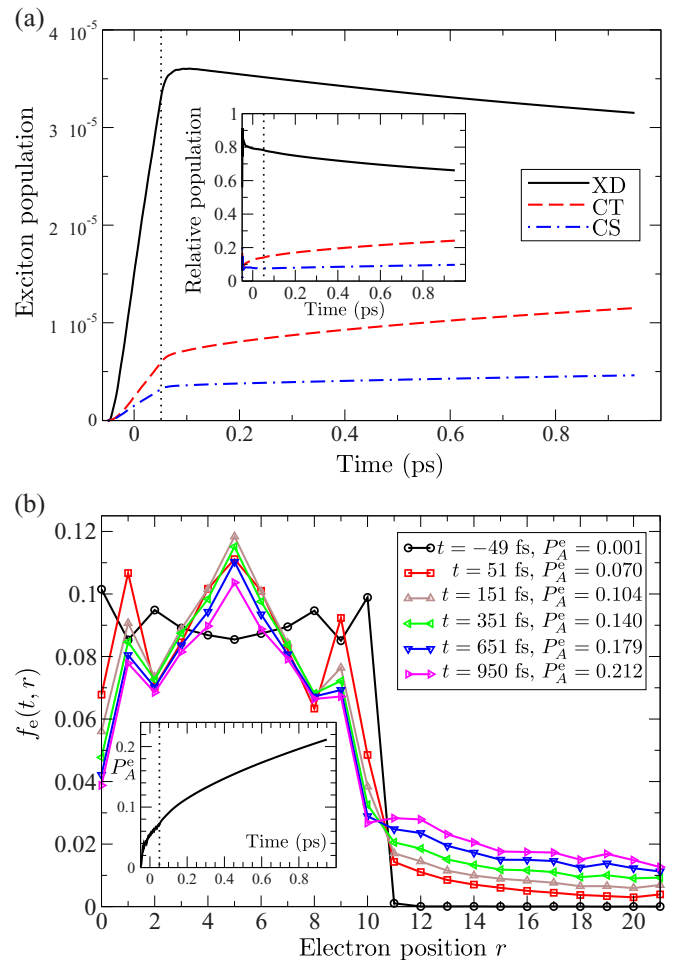


FIG. 3. (a) Time dependence of the numbers of donor (XD), CT, and CS excitons. The inset shows the time dependence of these quantities normalized to the total exciton population in the system. (b) Probability that at time  $t$  an electron is located at site  $r$  as a function of  $r$  for various values of  $t$ . In the legend, the probability that at instant  $t$  an electron is located in the acceptor is given, while the inset shows its full time dependence. Dotted vertical lines indicate the end of the excitation.

state, see Fig. 2(c). The number of all three types of excitons grows during the action of the electric field, whereas after the electric field has vanished, the number of donor excitons decreases and the numbers of CT and CS excitons increase. However, the changes in the exciton numbers brought about by the free-system evolution alone are much less pronounced than the corresponding changes during the action of the electric field, as is shown in Fig. 3(a). The population of CS excitons builds up during the action of the electric field, so that after the first 100 fs of the calculation, CS excitons comprise 7.6% of the total exciton population, see the inset of Fig. 3(a). In the remaining 900 fs, when the dynamics is governed by the free Hamiltonian, the population of CS excitons further increases to 9.6%. A similar, but less extreme, situation is also observed in the relative number of CT excitons, which at the end of the pulse form 14% of the total population and in the remaining 900 fs of the computation their number further grows to 24%. Therefore, if only the free-system

evolution were responsible for the conversion from donor to CT and CS excitons, the population of CT and CS states at the end of the pulsed excitation would assume much smaller values than we observe. We are led to conclude that the population of CT and CS excitons on ultrafast ( $\lesssim 100$ -fs) time scales is mainly established by direct optical generation. Transitions from donor to CT and CS excitons are present, but on this time scale are not as important as is currently thought.

Exciton dissociation and charge separation can also be monitored using the probabilities  $f_e(t,r)$  [ $f_h(t,r)$ ] that an electron (a hole) is located on site  $r$  at instant  $t$ , as well as the probability  $P_A^e(t)$  that an electron is in the acceptor at time  $t$ , see Eqs. (13)–(15). Figure 3(b) displays quantity  $f_e$  as a function of site index  $r$  at different times  $t$ . The probability of an electron being in the acceptor is a monotonically increasing function of time  $t$ , see the inset of Fig. 3(b). It increases, however, more rapidly during the action of the electric field than after the electric field has vanished: in the first 100 fs of the calculation, it increases from virtually 0 to 0.070, while in the next 100 fs it only rises from 0.070 to 0.104, and at the end of the computation it assumes the value 0.210. The observed time dependence of the probability that an electron is located in the acceptor further corroborates our hypothesis of direct optical generation as the main source of separated carriers on ultrafast time scales. If only transitions from donor to CT and CS excitons led to ultrafast charge separation starting from a donor exciton, the values of the considered probability would be smaller than we observe.

The rationale behind the direct optical generation of space-separated charges is the resonant coupling between donor excitons and (higher-lying) space-separated states, which stems from the resonant mixing between single-electron states in the donor and acceptor modulated by the electronic coupling between materials, see the level alignment in Fig. 2(b). This mixing leads to higher-lying CT and CS states having non-negligible amount of donor character and acquiring nonzero dipole moment from donor excitons; these states can thus be directly generated from the ground state. It should be stressed that the mixing, in turn, influences donor states, which have certain amount of space-separated character.

### B. Impact of model parameters on ultrafast exciton dynamics

Our central conclusion was so far obtained using only one set of model parameters and it is therefore important to check its sensitivity on system parameters. To this end, we vary one model parameter at a time, while all the other parameters retain the values listed in Table I.

We start by investigating the effect of the transfer integral between the donor and acceptor  $J_{DA}^{c/v}$ . Higher values of  $J_{DA}^{c/v}$  favor charge separation, since the relative numbers of CT and CS excitons, together with the probability that an electron is in the acceptor, increase, whereas the relative number of donor excitons decreases with increasing  $J_{DA}^{c/v}$ , see Figs. 4(a)–4(c). In light of the proposed mechanism of ultrafast direct optical generation of space-separated charges, the observed trends can be easily rationalized. Stronger electronic coupling between materials leads to stronger mixing between donor and space-separated states, i.e., a more pronounced donor character of

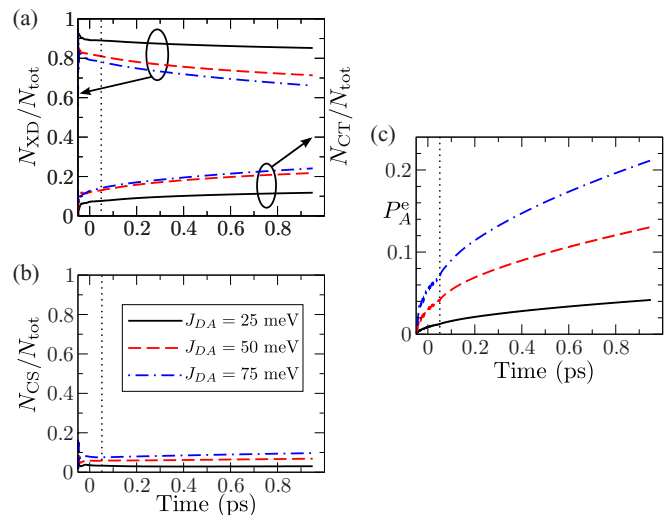


FIG. 4. Time dependence of the relative number of (a) donor and CT, (b) CS excitons, and (c) the probability  $P_A^e$  that an electron is in the acceptor, for different values of the transfer integrals  $|J_{DA}^c| = |J_{DA}^v| = J_{DA}$  between the donor and the acceptor. Dotted vertical lines indicate the end of the excitation.

CT and CS states and consequently a larger dipole moment for direct creation of CT and CS states from the ground state.

The results concerning the effects of the energy offset  $\Delta E_{DA}^c$  between LUMO levels in the donor and acceptor are summarized in Figs. 5(a)–5(c). The parameter  $\Delta E_{DA}^c$  determines the energy width of the overlap region between single-electron states in the donor and acceptor, see Fig. 2(b). The smaller is  $\Delta E_{DA}^c$ , the greater is the number of virtually resonant single-electron states in the donor and in the acceptor and therefore the greater is the number of (higher-lying) CT and CS states that inherit nonzero dipole moments from donor states and may thus be directly excited from the ground state.

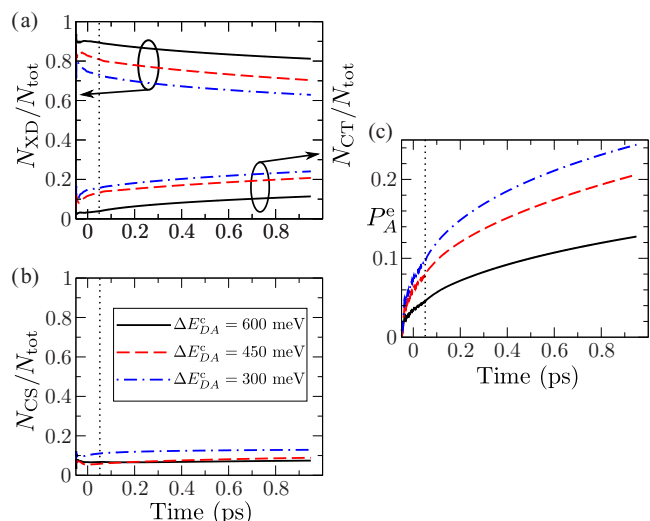


FIG. 5. Time dependence of the relative number of (a) donor and CT, (b) CS excitons, and (c) the probability  $P_A^e$  that an electron is in the acceptor, for different values of the LUMO-LUMO energy offset  $\Delta E_{DA}^c$ . Dotted vertical lines indicate the end of the excitation.

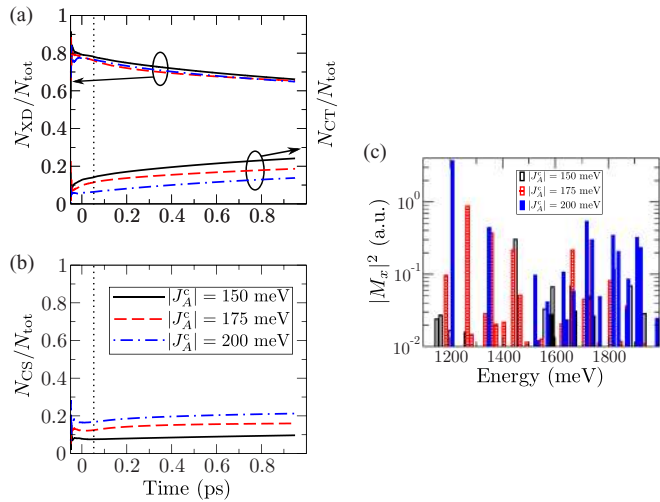


FIG. 6. Time dependence of the relative number of (a) donor and CT and (b) CS excitons, for different values of electronic coupling in the acceptor  $J_A^c$ . (c) Squared moduli of dipole matrix elements (in arbitrary units) for direct generation of CS excitons from the ground state for different values of electronic coupling in the acceptor  $J_A^c$ . Dotted vertical lines indicate the end of the excitation. Note that, globally, squared moduli of dipole matrix elements are largest for  $|J_A^c| = 200$  meV (completely filled bars).

This manifests as a larger number of CT and CS excitons, as well as a larger probability that an electron is in the acceptor, with decreasing  $\Delta E_{DA}^c$ .

Figures 6(a)–6(c) show the effects of electron delocalization in the acceptor on the ultrafast dynamics at the model heterojunction. Delocalization effects are mimicked by varying the electronic coupling in the acceptor. While increasing  $|J_A^c|$  has virtually no effect on the relative number of donor excitons, it leads to an increased participation of CS and a decreased participation of CT excitons in the total exciton population. CT states, in which the electron-hole interaction is rather strong, are mainly formed from lower-energy single-electron states in the acceptor and higher-energy single-hole states in the donor. These single-particle states are not subject to strong resonant mixing with single-particle states of the other material. However, CS states are predominantly composed of lower-energy single-hole donor states and higher-energy single-electron acceptor states; the mixing of the latter group of states with single-electron donor states is stronger for larger  $|J_A^c|$ , just as in case of smaller  $\Delta E_{DA}^c$ , see Fig. 2(b). Therefore the dipole moments for direct generation of CS excitons generally increase when increasing  $|J_A^c|$ , see Fig. 6(c), whereas the dipole moments for direct generation of CT excitons at the same time change only slightly, which can account for the trends of the participation of CS and CT excitons in Figs. 6(a) and 6(b).

We now turn our attention to the effects that the strength of the carrier-phonon interaction has on the ultrafast exciton dynamics at heterointerfaces. In Figs. 7(a)–7(d), we present the results with the fixed ratio  $g_2/g_1 = 2.0$  and the polaron binding energies defined in Eq. (17) assuming the values of approximately 20, 40, 60, and 140 meV, in ascending order of  $g_1$ . We note that it is not straightforward to predict the

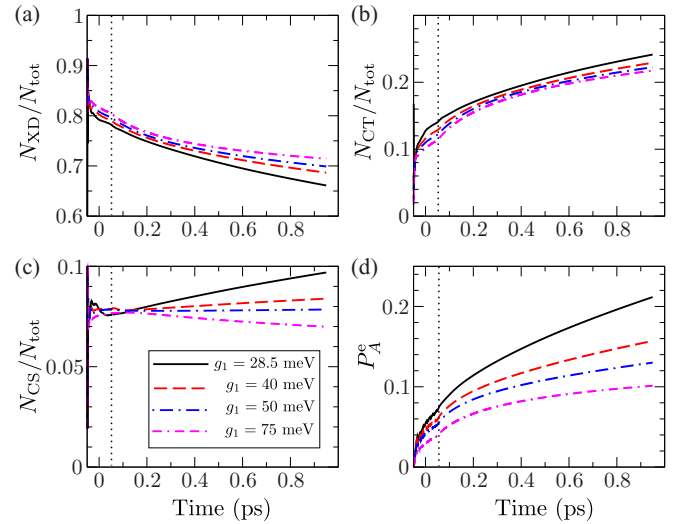


FIG. 7. Time dependence of the relative number of (a) donor, (b) CT, (c) CS excitons, and (d) the probability  $P_A^e$  that an electron is in the acceptor, for different strengths of the carrier-phonon interaction. Dotted vertical lines indicate the end of the excitation.

effect of the variations of carrier-phonon interaction strength on the population of space-separated states. Single-phonon-assisted processes preferentially couple exciton states of the same character, i.e., a donor exciton state is more strongly coupled to another donor state, than to a space-separated state. On the one hand, stronger carrier-phonon interaction implies more pronounced exciton dissociation and charge separation because of stronger coupling between donor and space-separated states. On the other hand, stronger carrier-phonon interaction leads to faster relaxation of initially generated donor excitons within the donor exciton manifold to low-lying donor states. Low-lying donor states are essentially uncoupled from space-separated states, i.e., they exhibit low probabilities of exciton dissociation and charge separation. Our results, shown in Figs. 7(a)–7(d), indicate that stronger carrier-phonon interaction leads to smaller number of CT and CS excitons, as well as the probability that an electron is in the acceptor, and to greater number of donor excitons. We also note that stronger carrier-phonon interaction changes the trend displayed by the population of CS states. While for the weakest interaction studied CS population grows after the excitation, for the strongest interaction studied CS population decays after the excitation. This is a consequence of more pronounced phonon-assisted processes leading to population of low-energy CT states once a donor exciton performs a transition to a space-separated state. This discussion can rationalize the changes in relevant quantities summarized in Figs. 7(a)–7(d); the magnitudes of the changes observed are, however, rather small. In previous studies [38,45], which did not deal with the initial exciton generation step, stronger carrier-phonon interaction is found to suppress quite strongly the charge separation process. The weak influence of the carrier-phonon interaction strength on ultrafast heterojunction dynamics that we observe supports the mechanism of ultrafast direct optical generation of space-separated charges. If the charge separation process at heterointerfaces were mainly

driven by the free-system evolution, greater changes in the quantities describing charge separation efficiency would be expected with varying carrier-phonon interaction strength.

Additionally, we have performed computations for a fixed value of  $\epsilon_b^{\text{pol}}$  [Eq. (17)] and different values of the ratio  $g_2/g_1$  among coupling constants of high- and low-frequency phonon modes. The result, which is presented in Ref. [31] (see Fig. 4), shows that the increase of the ratio  $g_2/g_1$  increases the number of CT excitons and decreases the number of donor excitons, while the population of CS states exhibits only a weak increase. Stronger coupling to the high-frequency phonon mode (with respect to the low-frequency one) enhances charge separation by decreasing the number of donor excitons, but at the same time promotes phonon-assisted processes towards more strongly bound CT states, so that the population of CS states remains nearly constant.

Our formalism takes into account the influence of phonons on excitons. However, if this influence were too strong, the hierarchy of equations would have to be truncated at a higher level, which would make it computationally intractable. When the effects of lattice motion on excitons are strong, one has, in turn, to consider the feedback of excitons on phonons, which is not captured by the current approach. The feedback of excitons on the lattice motion can be easily included in a mixed quantum/classical approach, where excitons are treated quantum mechanically, while the lattice motion is treated classically. To estimate the importance of the feedback of excitons on the lattice motion, we have performed the computation using the surface hopping approach [46,47] (see Ref. [31] for more details). In Fig. 3 of Ref. [31], we show the time dependence of the probability that an electron is in the acceptor obtained from simulations with and without feedback effects. The result is nearly the same in both cases, suggesting that feedback effects are small. As a consequence, our approach is sufficient for properly taking into account the influence of phonons on excitons.

We have also studied the influence of the temperature on the ultrafast exciton dynamics at a heterojunction. It exhibits a weak temperature dependence, see Fig. 5 of Ref. [31], which is consistent with existing theoretical [48] and experimental [49] insights, and also with the mechanism of direct optical generation of space-separated carriers.

Finally, the consequences of introducing diagonal static disorder in our model will be studied. It is done by drawing the (uncorrelated) on-site energies of electrons and holes in the donor and the acceptor from Gaussian distributions centered at the values that can be obtained from Table I. We have for simplicity assumed that the standard deviations of all the Gaussian distributions are equal to  $\sigma$ . As we do not intend to obtain any of the system properties by a statistical analysis of various realizations of disorder, but merely to check whether or not the presence of disorder may significantly alter qualitative features of the proposed picture of ultrafast exciton dynamics at heterointerfaces, we present our results only for a couple of different disorder realizations and compare them to the results for ordered system. In Figs. 8(a)–8(d), we show the time dependence of the relative number of space-separated (CS and CT) excitons and of the probability  $P_A^e$  for three different realizations of disorder with standard deviations  $\sigma = 50$  and 100 meV. For these disorder realizations, the quantities

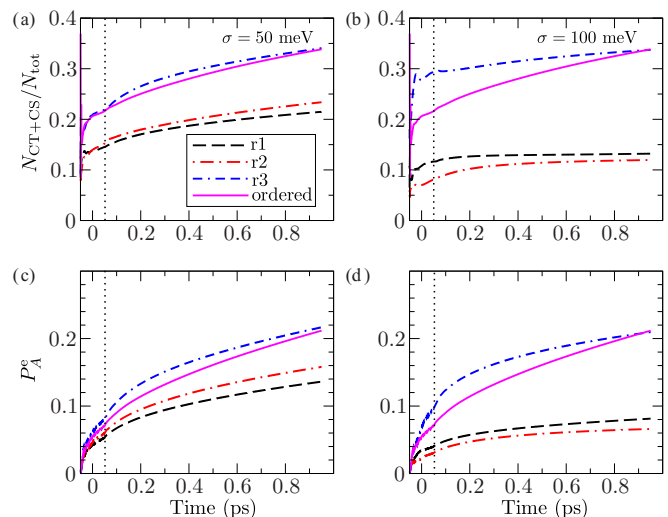


FIG. 8. (a) and (b) Time dependence of the relative number of space-separated (CT and CS) excitons for three different disorder realizations (r1, r2, and r3). (c) and (d) Time dependence of the probability that an electron is in the acceptor for three different disorder realizations. Time evolution of the respective quantities in ordered system is shown on each graph for comparison. Disorder is diagonal (affects only on-site energies), static, and Gaussian, standard deviations being  $\sigma = 50$  [(a) and (c)] and 100 meV [(b) and (d)].

we use to describe ultrafast heterojunction dynamics show qualitatively similar behavior to the case of the ordered system. Namely, changes in the relative number of space-separated excitons and the probability of an electron being in the acceptor are more pronounced during the action of the pulse than after its end. The characteristic time scales of these changes (for the disorder realizations studied) are not drastically different from the corresponding time scale in the ordered system. The presence of disorder in our model does not necessarily lead to less efficient charge separation as monitored by the two aforementioned quantities. Our results based on the considered disorder realizations are in agreement with the more detailed study of the effects of disorder on charge separation at model D/A interfaces [16], from which emerged that regardless of the degree of disorder, the essential physics of free hole and electron generation remains the same.

In summary, we find that regardless of the particular values of varied model parameters ( $J_{DA}^{c/v}$ ,  $\Delta E_{DA}^c$ ,  $J_A^c$ , carrier-phonon coupling constants), the majority of CT and CS states that are present at  $\sim 100$  fs after photoexcitation have been directly generated during the excitation. Trends in quantities describing ultrafast heterojunction dynamics that we observe varying model parameters can be explained by taking into consideration the proposed mechanism of ultrafast direct optical generation of space-separated charges.

#### IV. ULTRAFAST SPECTROSCOPY SIGNATURES

Exciton dynamics on ultrafast time scales is typically probed experimentally using the ultrafast pump-probe spectroscopy, see, e.g., Refs. [7,8]. In such experiments, the presence of space-separated charges on ultrafast time scales after photoexcitation has been established and the energy

resonance between donor exciton and space-separated states was identified as responsible for efficient charge generation [7], in agreement with our numerical results. However, while our results indicate that the majority of space-separated charges that are present at  $\sim 100$  fs after photoexcitation have been directly optically generated, interpretation of experiments [7] suggests that these states become populated by the transition from donor exciton states. To understand the origin of this apparent difference, we numerically compute ultrafast pump-probe signals in the framework of our heterojunction model. In Sec. IV A, we present the theoretical treatment of ultrafast pump-probe experiments adapted for the system at hand. Assuming that the probe pulse is deltalike, we obtain an analytic expression relating the differential transmission  $\Delta T$  to the nonequilibrium state of the system “seen” by the probe pulse. The expression provides a very clear and direct interpretation of the results of ultrafast pump-probe experiments and allows to distinguish between contributions stemming from exciton populations and coherences, challenging the existing interpretations. It is used in Sec. IV B to numerically compute differential transmission signals.

### A. Theoretical treatment of the ultrafast pump-probe spectroscopy

In a pump-probe experiment, the sample is firstly irradiated by an energetic pump pulse and the resulting excited (nonequilibrium) state of the sample is consequently examined using a second, weaker, probe pulse, whose time delay with respect to the pump pulse can be tuned [50–52]. Our theoretical approach to a pump-probe experiment considers the interaction with the pump pulse as described in Sec. II B and Ref. [30], i.e., within the density matrix formalism employing the DCT scheme up to the second order in the pump field. The interaction with the probe pulse is assumed not to change significantly the nonequilibrium state created by the pump pulse and is treated in the linear response regime. The corresponding nonequilibrium dipole-dipole retarded correlation function is then used to calculate pump-probe signals [52,53].

To study pump-probe experiments, we extended our two-band lattice semiconductor model including more single-electron (single-hole) energy levels per site. Multiple single-electron (single-hole) levels on each site should be dipole-coupled among themselves in order to enable probe-induced dipole transitions between various exciton states. We denote by  $c_{i\beta_i}^\dagger$  ( $c_{i\beta_i}$ ) creation (annihilation) operators for electrons on site  $i$  in conduction-band orbital  $\beta_i$ ; similarly,  $d_{i\alpha_i}^\dagger$  ( $d_{i\alpha_i}$ ) create (annihilate) a hole on site  $i$  in valence-band orbital  $\alpha_i$ . The dipole-moment operator in terms of electron and hole operators assumes the form

$$P = \sum_{i, \beta_i, \alpha_i} (d_i^{\text{cv}} c_{i\beta_i}^\dagger d_{i\alpha_i}^\dagger + \text{H.c.}) + \sum_{i, \beta_i \neq \beta_i'} d_i^{\text{cc}} c_{i\beta_i}^\dagger c_{i\beta_i'} - \sum_{i, \alpha_i \neq \alpha_i'} d_i^{\text{vv}} d_{i\alpha_i'}^\dagger d_{i\alpha_i}. \quad (20)$$

Intraband dipole matrix elements  $d_i^{\text{cc}}$  ( $d_i^{\text{vv}}$ ) describe electron (hole) transitions between different single-electron (single-hole) states on site  $i$ , as opposed to the interband matrix

elements  $d_i^{\text{cv}}$ , which are responsible for the exciton generation. Performing transition to the exciton basis, which is defined analogously to Eq. (6), dipole matrix elements for transitions from the ground state to exciton state  $x$  are

$$M_x = \sum_{i, \beta_i, \alpha_i} d_i^{\text{cv}} \psi_{(i\alpha_i)(i\beta_i)}^{x*}, \quad (21)$$

while those for transitions from exciton state  $x$  to exciton state  $\bar{x}$  are

$$M_{\bar{x}}^x = \sum_{i, \alpha_i \neq \alpha_i'} \sum_j \psi_{(i\alpha_i)(j\beta_j)}^{\bar{x}*} d_i^{\text{vv}} \psi_{(i\alpha_i')(j\beta_j)}^x - \sum_{i, \beta_i \neq \beta_i'} \sum_j \psi_{(j\alpha_j)(i\beta_i')}^{\bar{x}*} d_i^{\text{cc}} \psi_{(j\alpha_j)(i\beta_i)}^x. \quad (22)$$

Operator  $P$  [Eq. (20)] expressed in terms of operators  $X_x, X_x^\dagger$  assumes the form (keeping only contributions whose expectation values are at most of the second order in the pump field)

$$P = \sum_x (M_x X_x^\dagger + M_x^* X_x) - \sum_{\bar{x}} M_{\bar{x}}^x X_{\bar{x}}^\dagger X_x. \quad (23)$$

We concentrate on the so-called nonoverlapping regime [52], in which the probe pulse, described by its electric field  $e(t)$ , acts after the pump pulse. We take that our system meets the condition of optical thinness, i.e., the electromagnetic field originating from probe-induced dipole moment can be neglected compared to the electromagnetic field of the probe. In the following considerations, the origin of time axis  $t = 0$  is taken to be the instant at which the probe pulse starts. The pump pulse finishes at  $t = -\tau$ , where  $\tau$  is the time delay between (the end of) the pump and (the start of) the probe. The pump creates a nonequilibrium state of the system which is, at the moment when the probe pulse starts, given by the density matrix  $\rho(0)$ , which implicitly depends on the pump-probe delay  $\tau$ .

In the linear-response regime, the probe-induced dipole moment  $d_p(t)$  for  $t > 0$  is expressed as [52]

$$d_p(t) = \int dt' \chi(t, t') e(t'), \quad (24)$$

where  $\chi(t, t')$  is the nonequilibrium retarded dipole-dipole correlation function

$$\chi(t, t') = -\frac{i}{\hbar} \theta(t - t') \text{Tr}(\rho(0)[P(t), P(t')]). \quad (25)$$

Time dependence in Eq. (25) is governed by the Hamiltonian of the system in the absence of external fields [Eq. (8)]:

$$H_{E(t)=0} = H_0 + H_{\text{e-ph}}, \quad (26)$$

where  $H_0$  is the noninteracting Hamiltonian of excitons in the phonon field [the first two terms in Eq. (8)], while  $H_{\text{e-ph}}$  accounts for exciton-phonon interaction [the third term in Eq. (8)]. For an ultrashort probe pulse,  $e(t) = e_0 \delta(t)$ , the probe-induced dipole moment assumes the form

$$d_p(t) = e_0 \chi(t, 0) = e_0 \left( -\frac{i}{\hbar} \right) \text{Tr}(\rho(0)[P(t), P(0)]). \quad (27)$$

Probe pulse tests the possibility of transitions between various exciton states, i.e., it primarily affects carriers. Therefore,

as a reasonable approximation to the full time dependent operator  $P(t)$  appearing in Eq. (27), operator  $P^{(0)}(t)$ , evolving according to the noninteracting Hamiltonian  $H_0$  in Eq. (26), may be used. This leads us to the central result for the probe-induced dipole moment:

$$d_p(t) = e_0 \left( -\frac{i}{\hbar} \right) \text{Tr}(\rho(0)[P^{(0)}(t), P(0)]). \quad (28)$$

Deriving the commutator in Eq. (28), in the expression for  $d_p(t)$  we obtain two types of contributions, see Eq. (A3) in Appendix. Contributions of the first type oscillate at frequencies  $\omega_x$  corresponding to probe-induced transitions between the ground state and exciton state  $x$ , while those of the second type oscillate at frequencies  $\omega_{\bar{x}} - \omega_x$  corresponding to probe-induced transitions between exciton states  $\bar{x}$  and  $x$ . Here, we focus our attention to the process of photoinduced absorption (PIA), in which an exciton in state  $x$  performs a transition to another state  $\bar{x}$  under the influence of the probe field. Therefore we will further consider only the second type of contributions.

The frequency-dependent transmission coefficient  $T(\omega)$  is defined as (we use SI units)

$$T(\omega) = 1 + \frac{c\mu_0}{S\hbar} \text{Im} \left[ \hbar\omega \frac{d_p(\omega)}{e(\omega)} \right], \quad (29)$$

where  $d_p(\omega)$  and  $e(\omega)$  are Fourier transformations of  $d_p(t)$  and  $e(t)$ , respectively, while  $S$  is the irradiated area of the sample. The differential transmission is given as

$$\Delta T(\tau; \omega) = T^{\text{neq}}(\tau; \omega) - T^{\text{eq}}(\omega). \quad (30)$$

The transmission of a system, which is initially (before the action of the probe) unexcited, is denoted by  $T^{\text{eq}}(\omega)$ . The transmission of a pump-driven system  $T^{\text{neq}}(\tau; \omega)$  depends on the time delay  $\tau$  between the pump and the probe through the nonequilibrium density matrix  $\rho(0)$ . Since our aim is to study the process of PIA and since  $T^{\text{eq}}(\omega)$  is expected to reflect only transitions involving the ground state, we will not further consider this term. After a derivation, the details of which are given in Appendix, we obtain the expression for the part of the differential transmission signal  $\Delta T_{\text{PIA}}(\tau; \omega)$  accounting for the PIA:

$$\begin{aligned} \Delta T_{\text{PIA}}(\tau; \omega) \propto \text{Im} \left[ \sum_{xx'} \left( (M_x M_{x'})^* \frac{\hbar\omega}{\hbar\omega - (\hbar\omega_{x'} - \hbar\omega_x) + i\eta} y_{x'}(0) - M_x M_{x'}^* \frac{\hbar\omega}{\hbar\omega + (\hbar\omega_{x'} - \hbar\omega_x) + i\eta} y_{x'}^*(0) \right) \right. \\ + \sum_{\bar{x}xx'} \left( M_{x'}^x M_{\bar{x}}^{\bar{x}} \frac{\hbar\omega}{\hbar\omega + (\hbar\omega_{x'} - \hbar\omega_x) + i\eta} y_{x'}^*(0) y_{\bar{x}}(0) - M_x^{x'} M_{\bar{x}}^x \frac{\hbar\omega}{\hbar\omega - (\hbar\omega_{x'} - \hbar\omega_x) + i\eta} y_{\bar{x}}^*(0) y_{x'}(0) \right) \\ \left. + \sum_{\bar{x}xx'} \left( M_{x'}^x M_{\bar{x}}^{\bar{x}} \frac{\hbar\omega}{\hbar\omega + (\hbar\omega_{x'} - \hbar\omega_x) + i\eta} \bar{n}_{x'\bar{x}}(0) - M_x^{x'} M_{\bar{x}}^x \frac{\hbar\omega}{\hbar\omega - (\hbar\omega_{x'} - \hbar\omega_x) + i\eta} \bar{n}_{\bar{x}x'}(0) \right) \right]. \quad (31) \end{aligned}$$

In the last equation, we have explicitly separated the coherent contributions by introducing the correlated parts of exciton populations and exciton-exciton coherences  $\bar{n}_{\bar{x}x} = n_{\bar{x}x} - y_{\bar{x}}^* y_x$  [see also Eq. (11) defining incoherent exciton populations], while  $\eta$  is a positive parameter effectively accounting for the spectral line broadening [53].  $y_x(0)$  denotes the value of the electronic density matrix  $y_x$  at the moment when the probe pulse starts, and similarly for  $\bar{n}_{\bar{x}x}(0)$ . The coherences between exciton states and the ground state  $y_x(0)$ , as well as correlated parts of exciton-exciton coherences  $\bar{n}_{\bar{x}x}(0)$  ( $\bar{x} \neq x$ ), are expected to approach zero for sufficiently long time delays between the pump and the probe [54]. In this limit, Eq. (31) contains only the incoherent exciton populations  $\bar{n}_{xx}$ :

$$\Delta T_{\text{PIA}}(\tau; \omega) \propto \sum_{xx'} |M_{x'}^x|^2 \left[ -\frac{\eta \cdot \hbar\omega}{(\hbar\omega + (\hbar\omega_{x'} - \hbar\omega_x))^2 + \eta^2} + \frac{\eta \cdot \hbar\omega}{(\hbar\omega - (\hbar\omega_{x'} - \hbar\omega_x))^2 + \eta^2} \right] \bar{n}_{x'x}(0). \quad (32)$$

This expression is manifestly negative when it describes probe-induced transitions from exciton state  $x'$  to some higher-energy exciton state  $x$ . The last conclusion is in agreement with the usual experimental interpretation of pump-probe spectra, where a negative differential transmission signal corresponds either to PIA or to stimulated emission [51]. Our expression [Eq. (31)] demonstrates, however, that this correspondence can not be uniquely established in the ultrafast regime, where it is expected that both coherences between exciton states and the ground state  $y_x(0)$  and exciton-exciton coherences  $\bar{n}_{\bar{x}x}(0)$  ( $\bar{x} \neq x$ ), along with incoherent exciton populations  $\bar{n}_{xx}(0)$ , play significant role. This is indeed the case in our numerical computations of pump-probe spectra, which are presented in the following subsection. For each studied case, we separately show the total signal [full Eq. (31)], the  $y$ -part of the signal

[the first two terms in Eq. (31)], and the  $\bar{n}$ -part of the signal [the third term in Eq. (31)]. We note that it would be possible to further separate the  $\bar{n}$ -part of the signal into the contribution stemming from incoherent exciton populations  $\bar{n}_{xx}$  [Eq. (32)] and exciton-exciton coherences  $\bar{n}_{\bar{x}x}$  ( $\bar{x} \neq x$ ). As shown in more detail in Ref. [31] (see Fig. 7), the overall  $\bar{n}$ -part of the signal is qualitatively very similar to its contribution stemming from incoherent exciton populations. Therefore, for the simplicity of further discussion, we may consider the  $\bar{n}$ -part of the signal as completely originating from incoherent exciton populations.

## B. Numerical results: ultrafast pump-probe signals

In order to compute pump-probe signals and at the same time keep the numerics manageable, we extended our model

by introducing only one additional single-electron level both in the donor and in the acceptor and one additional single-hole level in the donor. Additional energy levels in the donor and the corresponding bandwidths are extracted from the aforementioned electronic structure calculation on the infinitely long PCPDTBT polymer. The additional single-electron level is located at 1160 meV above the single-electron level used in all the calculations and the bandwidth of the corresponding zone is estimated to be 480 meV. The additional single-hole level is located at 1130 meV below the single-hole level used in all the calculations and the bandwidth of the corresponding zone is estimated to be 570 meV. The additional single-electron level in the acceptor is extracted from an electronic structure calculation on the  $C_{60}$  molecule. The calculation is based on DFT using either LDA or B3LYP exchange-correlation functional (both choices give similar results) and 6-31G basis set and was performed using the NWCHEM package [55]. We found that the additional single-electron level lies around 1000 meV above the single-electron level used in all the calculations. The bandwidth of the corresponding zone is set to 600 meV, see Table I.

In this section, we assume that the waveform of the pump pulse is

$$E(t) = E_0 \cos(\omega_c t) \exp\left(-\frac{t^2}{\tau_G^2}\right) \theta(t + t_0) \theta(t_0 - t), \quad (33)$$

where we take  $\tau_G = 20$  fs and  $t_0 = 50$  fs, while the probe is

$$e(t) = e_0 \delta(t - (t_0 + \tau)), \quad (34)$$

with variable pump-probe delay  $\tau$ . The intraband dipole matrix elements  $d_i^{cc}, d_i^{vv}$  in Eq. (20) are assumed to be equal in the whole system:

$$d_i^{cc} = d_i^{vv} = d^{\text{intra}} = \frac{1}{2} d^{cv}. \quad (35)$$

The positive parameter  $\eta$ , which effectively accounts for the line broadening, is set to  $\eta = 50$  meV. We have checked that variations in  $\eta$  do not change the qualitative features of the presented PIA spectra, see Fig. 6 in Ref. [31]. In actual computations of the signal given in Eq. (31), we should remember that the pump pulse finishes at instant  $t_0$ , while in Eq. (31), all the quantities are taken at the moment when the probe starts, which is now  $t_0 + \tau$ ; in other words,  $y_x(0) \rightarrow y_x(t_0 + \tau)$ ,  $\bar{n}_{\bar{x}x}(0) \rightarrow \bar{n}_{\bar{x}x}(t_0 + \tau)$  when we compute pump-probe signals using Eq. (31) and the pump and probe are given by Eqs. (33) and (34), respectively.

In Figs. 9(a) and 9(b), we show the PIA signal from space-separated states after the excitation by the pump at 1500 meV. The frequency  $\omega$  in Eq. (31) is set to 1000 meV, which is (for the adopted values of model parameters) appropriate for observing PIA from space-separated states. At small pump-probe delays ( $\tau \lesssim 300$  fs), we see that the oscillatory features stemming from coherences between exciton states and the ground state ( $y$ -part of the signal) dominate the dynamics. At larger delays, the part originating from established (incoherent) exciton populations ( $\bar{n}$ -part of the signal) prevails, see Fig. 9(b), and the shape of the signal resembles the shapes of signals from space-separated states in Fig. 4(c) of Ref. [7]. The signal decreases at larger delays, which correlates very well with the fact that the numbers of CT and CS excitons increase,

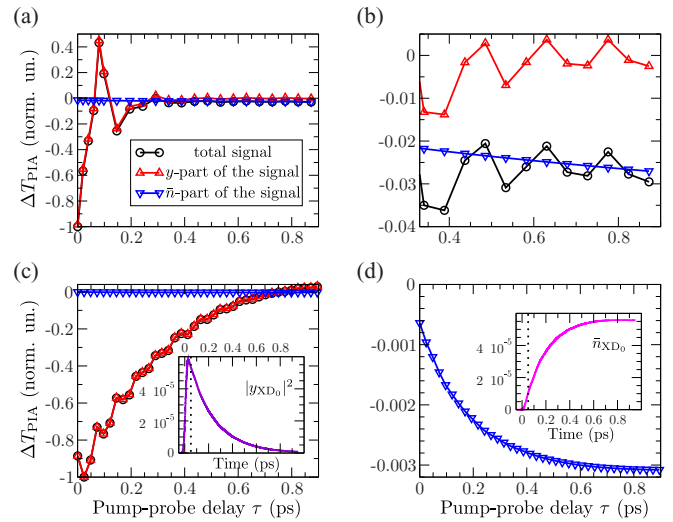


FIG. 9. Differential transmission signal  $\Delta T_{\text{PIA}}$  [Eq. (31)] as a function of the pump-probe delay for (a) pump at 1500 meV (826 nm) and probe at 1000 meV (1240 nm) testing PIA dynamics from space-separated states, and (c) pump resonant with the lowest donor exciton (1210 meV, 1025 nm) and probe at 1130 meV (1096 nm) testing PIA dynamics from donor states. The inset of (c) shows the coherent exciton population  $|y_{\text{XD}_0}|^2$  of the lowest donor state  $\text{XD}_0$ . (b) The same signal as in (a) at longer pump-probe delays ( $> 300$  fs). (d)  $\bar{n}$  part of the signal shown in (c); the inset displays the incoherent exciton population  $\bar{n}_{\text{XD}_0}$  of the lowest donor state.

see Fig. 3(a). In other words, at larger pump-probe delays, at which the influence of coherences between exciton states and the ground state is small, the signal can be unambiguously interpreted in terms of charge transfer from the donor to the acceptor.

Figures 9(c) and 9(d) display PIA signal from donor excitons following the pump excitation at the lowest donor exciton (1210 meV). The frequency  $\omega$  in Eq. (31) is set to 1130 meV. The overall signal shape is qualitatively similar to the shape of donor exciton PIA signal in Fig. 4(a) of Ref. [7], but its interpretation is rather different. While the authors of Ref. [7] suggest that the monotonically increasing PIA signal from donor excitons reflects their transfer to space-separated states, our signal predominantly originates from coherences between donor states and the ground state [ $y$ -part of the signal in Fig. 9(c)]. Furthermore, the shape of the total signal matches very well the decay of the coherent population of the lowest donor exciton, see the inset of Fig. 9(c), while the shape of the  $\bar{n}$ -part of the signal corresponds well to the changes in the incoherent population of the lowest donor state, see the inset of Fig. 9(d). This incoherent population does not decay during our computation: immediately after the pump pulse, it rises and at longer times it reaches a plateau, which signals that the donor exciton population is “blocked” in the lowest donor state. The lowest donor exciton is very strongly dipole-coupled to the ground state, its population comprising around 75% of the total generated population. Therefore, according to our numerical results, the observed PIA signal from donor excitons in this case mimics the conversion from coherent to incoherent exciton population

of the lowest donor state. This, however, does not necessarily mean that the concomitant charge transfer is completely absent in this case. Instead, the presence of coherences between exciton states and the ground state, which dominate the signal for all pump-probe delays we studied, prevents us from attributing the signal to the population transfer from donor excitons to space-separated states. The aforementioned conversion from coherent to incoherent exciton population of the lowest donor state is rather slow because of the relatively weak coupling between low-lying donor excitons on the one hand and space-separated states on the other hand (this weak coupling was also appreciated in Ref. [7]). On the other hand, pumping well above the lowest donor and space-separated states, the couplings between these species are stronger and more diverse than for the pump resonant with the lowest donor exciton; this situation resembles the one encountered for the excitation condition in Fig. 4(c) of Ref. [7].

In conclusion, our computations yield spectra which overall agree with experimental spectra [7], and we find that the shape of the spectrum in Figs. 9(c) and 9(d) originates from the decay of coherences between donor excitons and the ground state, rather than from transitions from donor excitons to space-separated states.

## V. DISCUSSION AND CONCLUSION

We studied ultrafast exciton dynamics in a one-dimensional model of a heterointerface. Even though similar theoretical models have been lately proposed [38,56], we believe that our theoretical treatment goes beyond the existing approaches, since it treats both the exciton generation and their further separation on equal footing and it deals with all the relevant interactions on a fully quantum level. Namely, the vast majority of the existing theoretical studies on charge separation at heterointerfaces does not treat explicitly the interaction with the electric field which creates excitons from an initially unexcited system [17,19,38,45,56], but rather assumes that the exciton has already been generated and then follows its evolution at the interface between two materials. If we are to explore the possibility of direct optical generation of space-separated charges, we should certainly monitor the initial process of exciton generation, which we are able to achieve with the present formalism. We find that the resonant electronic coupling between donor and space-separated states not only enhances transfer from the former to the latter group of states [7,15], but also opens up a new pathway to obtain space-separated charges: their direct optical generation [25,26]. While this mechanism has been proposed on the basis of electronic structure and model Hamiltonian calculations (which did not include any dynamics), our study is, to the best of our knowledge, the first to investigate the possibility of direct optical generation of separated charges studying the ultrafast exciton dynamics at a heterointerface. We conclude that the largest part of space-separated charges which are present  $\sim 100$  fs after the initial photoexcitation are directly optically generated, contrary to the general belief that they originate from ultrafast transitions from donor excitons. Although the D/A coupling in our model is restricted to only two nearest sites (labeled by  $N - 1$  and  $N$ ) in the donor and acceptor, there are space-separated states which

acquire nonzero dipole moment from donor excitons. The last point was previously highlighted in studies conducted on two- [25] and three-dimensional [26] heterojunction models, in which the dominant part of the D/A coupling involves more than a single pair of sites. We thus speculate that the main conclusions of our study would remain valid in a more realistic higher-dimensional model of a heterointerface. While there is absorption intensity transfer from donor to space-separated states brought about by their resonant mixing, the absorption still primarily occurs in the donor part of a heterojunction. Our results show that on ultrafast time scales the direct optical generation as a source of space-separated carriers is more important than transitions from donor to space-separated states. This, however, does not mean that initially generated donor excitons do not transform into space-separated states. They indeed do, see Figs. 3(a) and 3(b), but the characteristic time scale on which populations of space-separated states change due to the free-system evolution is longer than 100 fs.

The ultrafast generation of separated charges at heterointerfaces is more pronounced when the electronic coupling between materials is larger or when the energy overlap region between single-electron states in the donor and acceptor is wider, either by increasing the electronic coupling in the acceptor or decreasing the LUMO-LUMO offset between the two materials, see Fig. 2(b). Our results are therefore in agreement with studies emphasizing the beneficial effects of larger electronic couplings among materials [56], charge delocalization, [17,21,38,56], and smaller LUMO-LUMO offset [57] on charge separation. We find that strong carrier-phonon interaction suppresses charge separation, in agreement with previous theoretical studies [38,45] in which the effects of variations of carrier-phonon coupling constants have been systematically investigated. However, changes in the quantities we use to monitor charge separation with variations of carrier-phonon coupling strength are rather small, which we interpret to be consistent with the ultrafast direct optical generation of space-separated charges. Our theoretical treatment of ultrafast exciton dynamics is fully quantum, but it is expected to be valid for not too strong coupling of excitons to lattice vibrations, since the phonon branch of the hierarchy is truncated at a finite order, see Sec. I in Ref. [31]. Results of our mixed quantum/classical approach to exciton dynamics show that the feedback effect of excitons on the lattice motion, which is expected to be important for stronger exciton-phonon interaction, is rather small. We therefore expect that more accurate treatment of exciton-phonon interaction is not crucial to describe heterojunction dynamics on ultrafast time scales. If one wants to treat more accurately strong exciton-phonon interaction and yet remain in the quantum framework, other theoretical approaches, such as the one adopted in Ref. [45], have to be employed.

Despite a simplified model of organic semiconductors, our theoretical treatment takes into account all relevant effects. Consequently, our approach to ultrafast pump-probe experiments produces results that are in qualitative agreement with experiments and confirms the previously observed dependence of the exciton dynamics on the excess photon energy [7]. Our results indicate that the interpretation of ultrafast pump-probe signals is involved, as it is hindered by coherences (dominantly by those between exciton states and the ground state) which

cannot be neglected on the time scales studied. Time scales on which coherent features are prominent depend on the excess photon energy. We find that higher values of the excess photon energy enable faster disappearance of the coherent part of the signal since they offer diverse transitions between exciton states which make conversion from coherent to incoherent exciton populations faster. Pumping at the lowest donor exciton, our signal is (at subpicosecond pump-probe delays) dominated by its coherent part, conversion from coherent to incoherent exciton populations is slow, and therefore it cannot be interpreted in terms of exciton population transfer between various states.

### ACKNOWLEDGMENTS

We gratefully acknowledge the support by the Ministry of Education, Science and Technological Development of the Republic of Serbia (Project No. ON171017) and European Community FP7 Marie Curie Career Integration Grant

(ELECTROMAT), as well as the contribution of the COST Action MP1406. Numerical computations were performed on the PARADOX supercomputing facility at the Scientific Computing Laboratory of the Institute of Physics Belgrade.

### APPENDIX: DETAILS OF THE THEORETICAL TREATMENT OF PUMP-PROBE EXPERIMENTS

The commutator in Eq. (28) is to be evaluated in the nonequilibrium state  $\rho(0)$  at the moment when the probe pulse starts. Therefore, deriving this commutator, only contributions whose expectation values are at most of the second order in the pump field should be retained. The commutation relations of exciton operators, which are correct up to the second order in the pump field, read as

$$[X_x, X_{\bar{x}}^\dagger] = \delta_{x\bar{x}} - \sum_{\bar{x}'x'} C_{\bar{x}x}^{\bar{x}'x'} X_{\bar{x}'}^\dagger X_{x'}, \quad (\text{A1})$$

where four-index coefficients  $C_{\bar{x}x}^{\bar{x}'x'}$  are given as

$$C_{\bar{x}x}^{\bar{x}'x'} = \sum_{\substack{\bar{j}\bar{\beta}_j \\ j\beta_j}} \left( \sum_{i\alpha_i} \psi_{(i\alpha_i)(\bar{j}\bar{\beta}_j)}^{\bar{x}'*} \psi_{(i\alpha_i)(j\beta_j)}^{x'} \right) \left( \sum_{i\alpha_i} \psi_{(i\alpha_i)(\bar{j}\bar{\beta}_j)}^{\bar{x}} \psi_{(i\alpha_i)(j\beta_j)}^{x*} \right) + \sum_{\substack{\bar{i}\bar{\alpha}_i \\ i\alpha_i}} \left( \sum_{j\beta_j} \psi_{(\bar{i}\bar{\alpha}_i)(j\beta_j)}^{\bar{x}'*} \psi_{(i\alpha_i)(j\beta_j)}^{x'} \right) \left( \sum_{j\beta_j} \psi_{(\bar{i}\bar{\alpha}_i)(j\beta_j)}^{\bar{x}} \psi_{(i\alpha_i)(j\beta_j)}^{x*} \right). \quad (\text{A2})$$

The final result for the commutator  $[P^{(0)}(t), P(0)]$  is

$$\begin{aligned} [P^{(0)}(t), P(0)] &= \sum_x |M_x|^2 (e^{-i\omega_x t} - e^{i\omega_x t}) - \sum_{\bar{x}_1 x_1} \sum_{x x'} (M_x^* M_{x'} C_{x'x}^{\bar{x}_1 x_1} e^{-i\omega_x t} - M_x M_{x'}^* C_{xx'}^{\bar{x}_1 x_1} e^{i\omega_x t}) X_{\bar{x}_1}^\dagger X_{x_1} \\ &\quad - \sum_{x x'} (M_x M_{x'}^*)^* e^{-i\omega_x t} X_{x'} + \sum_{x x'} M_x M_{x'}^* e^{i\omega_x t} X_{x'}^\dagger + \sum_{x x'} (M_x M_{x'}^x)^* e^{-i(\omega_{x'} - \omega_x)t} X_{x'} \\ &\quad - \sum_{x x'} M_x M_{x'}^x e^{i(\omega_{x'} - \omega_x)t} X_{x'}^\dagger + \sum_{\bar{x} x x'} M_{x'}^x M_x^{\bar{x}} e^{i(\omega_{x'} - \omega_x)t} X_{x'}^\dagger X_{\bar{x}} - \sum_{\bar{x} x x'} M_x^{x'} M_{\bar{x}}^x e^{-i(\omega_{x'} - \omega_x)t} X_{\bar{x}}^\dagger X_{x'}. \quad (\text{A3}) \end{aligned}$$

The expectation values [with respect to  $\rho(0)$ ] of the operators appearing in the last equation are simply the active purely electronic density matrices of our formalism computed when the probe pulse starts, i.e.,  $\text{Tr}(\rho(0)X_x) = y_x(0)$  and  $\text{Tr}(\rho(0)X_{\bar{x}}^\dagger X_x) = n_{\bar{x}x}(0)$ .

As already mentioned, in order to study the process of PIA, in Eq. (A3) only terms which oscillate at differences of two exciton frequencies should be retained. Computing the Fourier transformation of  $d_p(t)$  [Eq. (28)], we obtain integrals of the type

$$\int_0^{+\infty} dt e^{i(\omega - \Omega + i\eta)t} = \frac{i}{\omega - \Omega + i\eta}, \quad (\text{A4})$$

where we have introduced a positive infinitesimal parameter  $\eta$  to ensure the integral convergence. Physically, introducing  $\eta$  effectively accounts for the line broadening. For simplicity, we assume that only one value of  $\eta$  is used in all the integrals of the type (A4). Using the computed Fourier transformation  $d_p(\omega)$  in Eqs. (29) and (30), we obtain the result for  $\Delta T_{\text{PIA}}(\tau; \omega)$  given in Eq. (31).

- 
- [1] T. M. Clarke and J. R. Durrant, Charge photogeneration in organic solar cells, *Chem. Rev.* **110**, 6736 (2010).  
 [2] C. Deibel and V. Dyakonov, Polymer-fullerene bulk heterojunction solar cells, *Rep. Prog. Phys.* **73**, 096401 (2010).  
 [3] F. Gao and O. Inganäs, Charge generation in polymer-fullerene bulk-heterojunction solar cells, *Phys. Chem. Chem. Phys.* **16**, 20291 (2014).

- [4] A. Zhugayevych and S. Tretiak, Theoretical description of structural and electronic properties of organic photovoltaic materials, *Annu. Rev. Phys. Chem.* **66**, 305 (2015).  
 [5] H. Bässler and A. Köhler, "Hot or cold": how do charge transfer states at the donor-acceptor interface of an organic solar cell dissociate? *Phys. Chem. Chem. Phys.* **17**, 28451 (2015).

- [6] J. L. Brédas, J. E. Norton, J. Cornil, and V. Coropceanu, Molecular understanding of organic solar cells: the challenges, *Acc. Chem. Res.* **42**, 1691 (2009).
- [7] G. Grancini, M. Maiuri, D. Fazzi, A. Petrozza, H.-J. Egelhaaf, D. Brida, G. Cerullo, and G. Lanzani, Hot exciton dissociation in polymer solar cells, *Nat. Mater.* **12**, 29 (2013).
- [8] A. E. Jailaubekov, A. P. Willard, J. R. Tritsch, W.-L. Chan, N. Sai, R. Gearba, L. G. Kaake, K. J. Williams, K. Leung, P. J. Rossky, and X.-Y. Zhu, Hot charge-transfer excitons set the time limit for charge separation at donor/acceptor interfaces in organic photovoltaics, *Nat. Mater.* **12**, 66 (2013).
- [9] S. Gélinas, A. Rao, A. Kumar, S. L. Smith, A. W. Chin, J. Clark, T. S. van der Poll, G. C. Bazan, and R. H. Friend, Ultrafast long-range charge separation in organic semiconductor photovoltaic diodes, *Science* **343**, 512 (2014).
- [10] A. A. Paraecattil and N. Banerji, Charge separation pathways in a highly efficient polymer:fullerene solar cell material, *J. Am. Chem. Soc.* **136**, 1472 (2014).
- [11] S. R. Cowan, N. Banerji, W. L. Leong, and A. J. Heeger, Charge formation, recombination, and sweep-out dynamics in organic solar cells, *Adv. Funct. Mater.* **22**, 1116 (2012).
- [12] C. Deibel, T. Strobel, and V. Dyakonov, Role of the charge transfer state in organic donor-acceptor solar cells, *Adv. Mater.* **22**, 4097 (2010).
- [13] A. A. Bakulin, A. Rao, V. G. Pavelyev, P. H. M. van Loosdrecht, M. S. Pshenichnikov, D. Niedzialek, J. Cornil, D. Beljonne, and R. H. Friend, The role of driving energy and delocalized states for charge separation in organic semiconductors, *Science* **335**, 1340 (2012).
- [14] K. Chen, A. J. Barker, M. E. Reish, K. C. Gordon, and J. M. Hodgkiss, Broadband ultrafast photoluminescence spectroscopy resolves charge photogeneration via delocalized hot excitons in polymer:fullerene photovoltaic blends, *J. Am. Chem. Soc.* **135**, 18502 (2013).
- [15] A. Troisi, How quasi-free holes and electrons are generated in organic photovoltaic interfaces, *Faraday Discuss.* **163**, 377 (2013).
- [16] H. Vázquez and A. Troisi, Calculation of rates of exciton dissociation into hot charge-transfer states in model organic photovoltaic interfaces, *Phys. Rev. B* **88**, 205304 (2013).
- [17] Z. Sun and S. Stafström, Dynamics of charge separation at an organic donor-acceptor interface, *Phys. Rev. B* **90**, 115420 (2014).
- [18] G. Nan, X. Zhang, and G. Lu, Do “hot” charge-transfer excitons promote free carrier generation in organic photovoltaics? *J. Phys. Chem. C* **119**, 15028 (2015).
- [19] S. L. Smith and A. W. Chin, Phonon-assisted ultrafast charge separation in the PCBM band structure, *Phys. Rev. B* **91**, 201302 (2015).
- [20] H. Tamura and I. Burghardt, Ultrafast charge separation in organic photovoltaics enhanced by charge delocalization and vibronically hot exciton dissociation, *J. Am. Chem. Soc.* **135**, 16364 (2013).
- [21] S. L. Smith and A. W. Chin, Ultrafast charge separation and nongeminate electron-hole recombination in organic photovoltaics, *Phys. Chem. Chem. Phys.* **16**, 20305 (2014).
- [22] K. Vandewal, S. Albrecht, E. T. Hoke, K. R. Graham, J. Widmer, J. D. Douglas, M. Schubert, W. R. Mateker, J. T. Bloking, G. F. Burkhard, A. Sellinger, J. M. J. Fréchet, A. Amassian, M. K. Riede, M. D. McGehee, D. Neher, and A. Salleo, Efficient charge generation by relaxed charge-transfer states at organic interfaces, *Nat. Mater.* **13**, 63 (2014).
- [23] E. R. Bittner and C. Silva, Noise-induced quantum coherence drives photo-carrier generation dynamics at polymeric semiconductor heterojunctions, *Nat. Commun.* **5**, 3119 (2014).
- [24] B. M. Savoie, A. Rao, A. A. Bakulin, S. Gélinas, B. Movaghar, R. H. Friend, T. J. Marks, and M. A. Ratner, Unequal partnership: Asymmetric roles of polymeric donor and fullerene acceptor in generating free charge, *J. Am. Chem. Soc.* **136**, 2876 (2014).
- [25] H. Ma and A. Troisi, Direct optical generation of long-range charge-transfer states in organic photovoltaics, *Adv. Mater.* **26**, 6163 (2014).
- [26] G. D’Avino, L. Muccioli, Y. Olivier, and D. Beljonne, Charge separation and recombination at polymer-fullerene heterojunctions: delocalization and hybridization effects, *J. Phys. Chem. Lett.* **7**, 536 (2016).
- [27] V.M. Axt and A. Stahl, A dynamics-controlled truncation scheme for the hierarchy of density matrices in semiconductor optics, *Z. Phys. B* **93**, 195 (1994).
- [28] V. M. Axt, K. Victor, and A. Stahl, Influence of a phonon bath on the hierarchy of electronic densities in an optically excited semiconductor, *Phys. Rev. B* **53**, 7244 (1996).
- [29] V. M. Axt and S. Mukamel, Nonlinear optics of semiconductor and molecular nanostructures; a common perspective, *Rev. Mod. Phys.* **70**, 145 (1998).
- [30] V. Janković and N. Vukmirović, Dynamics of exciton formation and relaxation in photoexcited semiconductors, *Phys. Rev. B* **92**, 235208 (2015).
- [31] See Supplemental Material at <http://link.aps.org/supplemental/10.1103/PhysRevB.95.075308> for equations of motion of active density matrices, further results concerning the impact of model parameters on ultrafast exciton dynamics, the mixed quantum/classical approach to exciton dynamics, and additional details regarding numerical computations of ultrafast pump-probe spectra.
- [32] I.-W. Hwang, C. Soci, D. Moses, Z. Zhu, D. Waller, R. Gaudiana, C. J. Brabec, and A. J. Heeger, Ultrafast electron transfer and decay dynamics in a small band gap bulk heterojunction material, *Adv. Mater.* **19**, 2307 (2007).
- [33] D. Mühlbacher, M. Scharber, M. Morana, Z. Zhu, D. Waller, R. Gaudiana, and C. Brabec, High photovoltaic performance of a low-bandgap polymer, *Adv. Mater.* **18**, 2884 (2006).
- [34] R. A. Street, S. A. Hawks, P. P. Khlyabich, G. Li, B. J. Schwartz, B. C. Thompson, and Y. Yang, Electronic structure and transition energies in polymer-fullerene bulk heterojunctions, *J. Phys. Chem. C* **118**, 21873 (2014).
- [35] H. Tamura and M. Tsukada, Role of intermolecular charge delocalization on electron transport in fullerene aggregates, *Phys. Rev. B* **85**, 054301 (2012).
- [36] P. Giannozzi *et al.*, Quantum espresso: a modular and open-source software project for quantum simulations of materials, *J. Phys.: Condens. Matter* **21**, 395502 (2009).
- [37] Y. Kanai and J. C. Grossman, Insights on interfacial charge transfer across P3HT/fullerene photovoltaic heterojunction from ab initio calculations, *Nano Lett.* **7**, 1967 (2007).
- [38] M. H. Lee, J. Aragón, and A. Troisi, Charge dynamics in organic photovoltaic materials: Interplay between quantum diffusion and quantum relaxation, *J. Phys. Chem. C* **119**, 14989 (2015).

- [39] E. R. Bittner and J. G. S. Ramon, Exciton and charge-transfer dynamics in polymer semiconductors, in *Quantum Dynamics of Complex Molecular Systems*, edited by D. A. Micha and I. Burghardt (Springer-Verlag, Berlin Heidelberg, 2007).
- [40] S. M. Falke, C. A. Rozzi, D. Brida, M. Maiuri, M. Amato, E. Sommer, A. De Sio, A. Rubio, G. Cerullo, E. Molinari, and C. Lienau, Coherent ultrafast charge transfer in an organic photovoltaic blend, *Science* **344**, 1001 (2014).
- [41] A. Lücke, F. Ortmann, M. Panhans, S. Sanna, E. Rauls, U. Gerstmann, and W. G. Schmidt, Temperature-dependent hole mobility and its limit in crystal-phase P3HT calculated from first principles, *J. Phys. Chem. B* **120**, 5572 (2016).
- [42] N. Vukmirović and L.-W. Wang, Charge carrier motion in disordered conjugated polymers: A multiscale ab initio study, *Nano Lett.* **9**, 3996 (2009).
- [43] D. L. Cheung and A. Troisi, Theoretical study of the organic photovoltaic electron acceptor PCBM: Morphology, electronic structure, and charge localization, *J. Phys. Chem. C* **114**, 20479 (2010).
- [44] Y.-C. Cheng and R. J. Silbey, A unified theory for charge-carrier transport in organic crystals, *J. Chem. Phys.* **128**, 114713 (2008).
- [45] S. Bera, N. Gheeraert, S. Fratini, S. Ciuchi, and S. Florens, Impact of quantized vibrations on the efficiency of interfacial charge separation in photovoltaic devices, *Phys. Rev. B* **91**, 041107 (2015).
- [46] J. C. Tully, Molecular dynamics with electronic transitions, *J. Chem. Phys.* **93**, 1061 (1990).
- [47] L. Wang and O. V. Prezhdo, A simple solution to the trivial crossing problem in surface hopping, *J. Phys. Chem. Lett.* **5**, 713 (2014).
- [48] A. Chenel, E. Mangaud, I. Burghardt, C. Meier, and M. Desouter-Lecomte, Exciton dissociation at donor-acceptor heterojunctions: Dynamics using the collective effective mode representation of the spin-boson model, *J. Chem. Phys.* **140**, 044104 (2014).
- [49] R. D. Pensack and J. B. Asbury, Beyond the adiabatic limit: Charge photogeneration in organic photovoltaic materials, *J. Phys. Chem. Lett.* **1**, 2255 (2010).
- [50] S. Mukamel, *Principles of Nonlinear Optical Spectroscopy* (Oxford University Press, New York, 1995).
- [51] J. Cabanillas-Gonzalez, G. Grancini, and G. Lanzani, Pump-probe spectroscopy in organic semiconductors: Monitoring fundamental processes of relevance in optoelectronics, *Adv. Mater.* **23**, 5468 (2011).
- [52] E. Perfetto and G. Stefanucci, Some exact properties of the nonequilibrium response function for transient photoabsorption, *Phys. Rev. A* **91**, 033416 (2015).
- [53] J. Walkenhorst, U. De Giovannini, A. Castro, and A. Rubio, Tailored pump-probe transient spectroscopy with time-dependent density-functional theory: controlling absorption spectra, *Eur. Phys. J. B* **89**, 128 (2016).
- [54] Coherences between exciton states and the ground state  $y_x$  typically decay on  $\lesssim 100$ -fs time scale after the pump field has vanished, while exciton-exciton coherences typically decay on picosecond time scales or longer. Therefore, in our computations, we expect to see the decay of coherences between exciton states and the ground state, but not of the exciton-exciton coherences, and time scales on which Eq. (32) is valid are in principle at least picosecond or longer.
- [55] M. Valiev, E. J. Bylaska, N. Govind, K. Kowalski, T. P. Straatsma, H. J. J. Van Dam, D. Wang, J. Nieplocha, E. Apra, T. L. Windus, and W. A. de Jong, NWChem: A comprehensive and scalable open-source solution for large scale molecular simulations, *Comput. Phys. Commun.* **181**, 1477 (2010).
- [56] A. A. Kocherzhenko, D. Lee, M. A. Forsuelo, and K. B. Whaley, Coherent and incoherent contributions to charge separation in multichromophore systems, *J. Phys. Chem. C* **119**, 7590 (2015).
- [57] L. J. A. Koster, V. D. Mihailetchi, and P. W. M. Blom, Ultimate efficiency of polymer/fullerene bulk heterojunction solar cells, *Appl. Phys. Lett.* **88**, 093511 (2006).

**Dynamics of exciton formation and relaxation in photoexcited semiconductors**

Veljko Janković\* and Nenad Vukmirović†

*Scientific Computing Laboratory, Institute of Physics Belgrade, University of Belgrade, Pregrevica 118, 11080 Belgrade, Serbia*

(Received 21 October 2015; revised manuscript received 4 December 2015; published 22 December 2015)

We investigate the dynamics of the exciton formation and relaxation on a picosecond time scale following a pulsed photoexcitation of a semiconductor. The study is conducted in the framework of the density matrix theory complemented with the dynamics controlled truncation scheme. We truncate the phonon branch of the resulting hierarchy of equations and propose the form of coupling among single-phonon-assisted and higher-order phonon-assisted density matrices so as to ensure the energy and particle-number conservation in a closed system. Time scales relevant for the exciton formation and relaxation processes are determined from numerical investigations performed on a one-dimensional model for the values of model parameters representative of a typical organic and inorganic semiconductor. The exciton dynamics is examined for different values of central frequency of the exciting field, temperature, and microscopic model parameters, such as the strengths of carrier-carrier and carrier-phonon couplings. We find that for typical organic semiconductor parameters, formation of bound excitons occurs on a several-hundred-femtosecond time scale, while their subsequent relaxation and equilibration take at least several picoseconds. These time scales are consistent with recent experimental studies of the exciton formation and relaxation in conjugated polymer-based materials.

DOI: [10.1103/PhysRevB.92.235208](https://doi.org/10.1103/PhysRevB.92.235208)

PACS number(s): 71.35.-y, 71.10.-w

**I. INTRODUCTION**

The continual and ever-increasing demand for economic and efficient ways of utilizing solar energy drives a huge part of current research activities. In particular, organic solar cells have developed rapidly in the past decade and have become promising candidates for economically viable large-scale power generation due to their flexibility, cost effectiveness, relatively simple fabrication techniques, and mass production [1,2]. Processes upon which the operation of solar cells is based are the light absorption in a semiconducting material and the subsequent conversion of photons into mobile charge carriers that produce an electric current [3,4]. An optical excitation of a semiconductor creates an exciton, i.e., an electron-hole pair in which Coulomb attraction between oppositely charged electron and hole prevents their separation. In a conventional inorganic semiconductor, relatively weak Coulomb interaction (primarily due to large dielectric constant) results in the exciton binding energy of the order of 10 meV [5–7]. Thus, thermal excitations are likely to split the exciton in an electron and a hole. On the other hand, in a typical organic semiconductor, the attraction between an electron and a hole is much stronger (mainly due to low dielectric constant), the exciton binding energy being of the order of or larger than 500 meV [3,8]. Therefore, while optical absorption in an inorganic semiconductor results in almost immediate generation of free charges, in an organic semiconductor it leads to formation of tightly bound electron-hole pairs, which should be separated in order to generate current [1,3,4]. This last conclusion has an enormous impact on the design and geometry of organic photovoltaic devices.

Photoexcitation of a semiconductor creates electron-hole pairs in a highly nonequilibrium state. Apart from the Coulomb interaction, which primarily induces correlations, the carrier-phonon interaction is also vital for a thorough understanding

of nonequilibrium processes taking place in photoexcited semiconductors. Theoretical approaches for treating these processes are most often based on the density matrix theory [9,10] or the nonequilibrium Green's functions formalism [11]. Density matrix theory has become the preferred technique in the treatment of experiments with ultrashort pulses since it deals with quantities that depend on one time argument and are directly related to observables.

Previous theoretical studies of the exciton formation process after an ultrafast optical excitation of a semiconductor were typically focused on inorganic semiconductors. Early studies were conducted in the framework of the semiclassical Boltzmann approach [12,13]. The fully microscopic and quantum theory for the interacting system of electrons, holes, photons, and phonons, capable of treating a wide variety of optical and excitonic effects after an ultrafast optical excitation of a semiconductor, was elaborated in Refs. [14–18]. On the other hand, the exciton formation from an initial state of two opposite charges in organic semiconductors was typically modeled by simulating the time evolution of empirical Hamiltonians applied to small systems, where the effects of the lattice are not included or are treated classically [19,20].

The main aim of this work was to investigate the dynamics of exciton formation on short (up to several ps) time scale. This time scale is of particular relevance for the operation of organic solar cells since it has been well established that the exciton separation at the interface of donor and acceptor materials occurs on a subpicosecond time scale [21,22]. However, the details of the exciton formation and separation process and the factors that determine its efficiency are still not well understood. In recent years, significant insights have been obtained from subpicosecond time-resolved experiments performed both on neat materials [23,24] and blends [25–29]. The results of all these experiments highlight the importance of nonequilibrium nature of excitons formed after photoexcitation.

In our study, we employ the Hamiltonian which includes all relevant physical effects in the system: electronic coupling which leads to band formation, electron-hole interaction

\*veljko.jankovic@ipb.ac.rs

†nenad.vukmirovic@ipb.ac.rs

which causes exciton formation, electron-phonon interaction that leads to relaxation, and the interaction with external electromagnetic field. We do not, however, include the effects of stimulated emission which lead to radiative recombination of excitons since we are interested in the exciton dynamics on a short time scale, where these effects are negligible. From the time evolution of relevant quantities, we identify the time scale of the processes of formation of free charges and bound excitons and their subsequent relaxation. Rather than focusing on the details of one particular material system, we have chosen a Hamiltonian whose parameters can be easily varied so that we can identify the influence of different physical effects on relevant time scales. The study is conducted in the framework of the density matrix formalism combined with the so-called dynamics controlled truncation (DCT) scheme, first developed in 1994 by Axt and Stahl [30,31]. This method is particularly suited for a system described by a pair-conserving Hamiltonian which is initially unexcited and was successfully applied to study the dynamics of exciton formation for near-band-gap excitations and low-excitation densities [32–34]. Here, we truncate the phonon branch of the hierarchy so as to ensure that the resulting equations are compatible with the energy and particle-number conservation in a closed system. Furthermore, we propose the form of coupling between single-phonon-assisted and higher-order phonon-assisted electronic density matrices which is compatible with the energy conservation in a closed system.

The paper is organized as follows. In Sec. II, the general form of the Hamiltonian, along with the equations which describe the exciton formation process, is presented. Section III is devoted to the results of our numerical investigations of the exciton formation process which are carried out on a one-dimensional model system. The discussion of our results in light of recent experimental investigations of ultrafast exciton dynamics is presented in Sec. IV, whereas concluding remarks are given in Sec. V.

## II. THEORETICAL FRAMEWORK

We use the standard two-band semiconductor model which takes into account the interaction of carriers with the external electromagnetic field applied to the semiconductor, as well as carrier-carrier and carrier-phonon interactions. We will work in the electron-hole picture which is particularly suited for describing the effects which arise after the optical excitation of an initially unexcited semiconductor. Notation from Ref. [35] will be used. The Hamiltonian has the form

$$H = H_c + H_{\text{ph}} + H_{\text{c-ph}} + H_{\text{c-f}}, \quad (1)$$

where  $H_c$  describes interacting carriers

$$\begin{aligned} H_c = & \sum_{q \in \text{CB}} \epsilon_q^c c_q^\dagger c_q - \sum_{q \in \text{VB}} \epsilon_q^v d_q^\dagger d_q \\ & + \frac{1}{2} \sum_{pqkl \in \text{CB}} V_{pqkl}^{\text{cccc}} c_p^\dagger c_k^\dagger c_l c_q + \frac{1}{2} \sum_{pqkl \in \text{VB}} V_{pqkl}^{\text{vvvv}} d_q^\dagger d_l^\dagger d_k d_p \\ & + \sum_{\substack{pq \in \text{VB} \\ kl \in \text{CB}}} (V_{plkq}^{\text{vcv}} - V_{pqkl}^{\text{vcc}}) c_k^\dagger d_q^\dagger d_p c_l, \end{aligned} \quad (2)$$

$$H_{\text{ph}} = \sum_{\mu} \hbar \omega_{\mu} b_{\mu}^{\dagger} b_{\mu} \quad (3)$$

is the free-phonon Hamiltonian,  $H_{\text{c-ph}}$  describes the carrier-phonon interaction

$$\begin{aligned} H_{\text{c-ph}} = & \sum_{\substack{pq \in \text{CB} \\ \mu}} (\gamma_{pq}^{\mu} c_p^{\dagger} c_q b_{\mu}^{\dagger} + \gamma_{pq}^{\mu*} c_q^{\dagger} c_p b_{\mu}) \\ & - \sum_{\substack{pq \in \text{VB} \\ \mu}} (\gamma_{pq}^{\mu} d_q^{\dagger} d_p b_{\mu}^{\dagger} + \gamma_{pq}^{\mu*} d_p^{\dagger} d_q b_{\mu}), \end{aligned} \quad (4)$$

whereas the coupling to the optical field is given by

$$H_{\text{c-f}} = -\mathbf{E}(t) \cdot \left( \sum_{\substack{p \in \text{VB} \\ q \in \text{CB}}} \mathbf{M}_{pq}^{\text{vc}} d_p c_q + \sum_{\substack{p \in \text{CB} \\ q \in \text{VB}}} \mathbf{M}_{pq}^{\text{cv}} c_p^{\dagger} d_q^{\dagger} \right). \quad (5)$$

Fermi operators  $c_q^{\dagger}$  ( $c_q$ ) create (annihilate) an electron of energy  $\epsilon_q^c$  in the single-particle state  $q$  in the conduction band, while Fermi operators  $d_q^{\dagger}$  ( $d_q$ ) create (annihilate) a hole of energy  $-\epsilon_q^v$  in the single-particle state  $q$  in the valence band. Matrix elements of the Coulomb interaction potential  $V(\mathbf{x} - \mathbf{y})$  are defined as

$$V_{pqkl}^{\lambda_p \lambda_q \lambda_k \lambda_l} = \int d\mathbf{x} d\mathbf{y} \phi_p^{\lambda_p*}(\mathbf{x}) \phi_q^{\lambda_q}(\mathbf{x}) V(\mathbf{x} - \mathbf{y}) \phi_k^{\lambda_k*}(\mathbf{y}) \phi_l^{\lambda_l}(\mathbf{y}), \quad (6)$$

where  $\phi_p^{\lambda_p}(\mathbf{x})$  are single-particle eigenfunctions for an electron in the state  $p$  and in the band  $\lambda_p$ . Bose operators  $b_{\mu}^{\dagger}$  ( $b_{\mu}$ ) create (annihilate) a phonon in mode  $\mu$ , while  $\gamma_{pq}^{\mu}$  are carrier-phonon matrix elements. We neglect intraband contributions to the carrier-field interaction and retain only interband dipole matrix elements.

We note that the Hamiltonian of interacting carriers [Eq. (2)] includes the limiting cases of Wannier and Frenkel excitons. Namely, when single-particle eigenfunctions are of the Bloch form labeled by a wave vector  $\mathbf{k}$ , then under suitable approximations, described, e.g., in Ref. [36], we obtain the Hamiltonian describing the limiting case of Wannier excitons. On the other hand, if single-particle eigenfunctions are taken to be atomic states labeled by a position vector  $\mathbf{R}$ , then using approximations that exploit localization properties of this basis set the Hamiltonian appropriate for the limiting case of Frenkel excitons is obtained [37].

We study the dynamics of exciton formation in photoexcited semiconductors in the framework of the density matrix theory. Differential equations for dynamic variables are formed and, due to the many-body nature of the problem, an infinite hierarchy of differential equations is obtained. The main approximation is then the truncation of the hierarchy, which can be based upon different physical pictures. The Hamiltonian defined by Eqs. (1)–(5) has the property that only the interaction with the optical field can change the number of pair excitations. The DCT scheme relies upon the aforementioned property of the Hamiltonian and classifies higher-order density matrices according to their leading order in the optical field [30,35,38]. Namely, when the system is initially in the

ground state represented by the vacuum of electron-hole pairs, the expectation value of the normal-ordered product of  $n_e$  electron operators  $c^\dagger$  and  $c$ ,  $n_h$  hole operators  $d^\dagger$  and  $d$  and an arbitrary number of phonon operators  $b^\dagger$  and  $b$  is at least of the order  $m = \max\{n_e, n_h\}$  in the applied field. Therefore, higher-order density matrices are also of higher order in the optical field and only a finite number of electronic density matrices contributes to the optical response at any given order in the optical field. The DCT scheme truncates only the electronic branch of the hierarchy and can be used along with any strategy to deal with the phonon-assisted branch of the hierarchy [7]. We limit ourselves to the case of weak optical field and low carrier densities, in which it is justified to neglect biexcitonic effects and keep only contributions up to the second order in the optical field. In Refs. [32,35] a reduced treatment of the phonon branch of the hierarchy, which can be combined with the DCT scheme for the electronic branch of the hierarchy, was presented. This treatment includes correlation expansion for phonon-assisted variables combined with the Markov approximation. As a result, phonon-assisted variables are eliminated from the formalism and only two types of electronic density matrices remain. These are the interband transition amplitude (excitonic amplitude)

$$Y_{ab} = \langle d_a c_b \rangle \quad (7)$$

and the electron-hole pair density (excitonic population)

$$N_{abcd} = \langle c_a^\dagger d_b^\dagger d_c c_d \rangle. \quad (8)$$

In this study, we adopt a different strategy for dealing with the phonon-assisted density matrices. In order to facilitate the truncation of the phonon-assisted branch of the hierarchy, the following generating functions for the phonon-assisted electronic density matrices are defined [35]:

$$Y_{ab}^{\alpha\beta} = \langle d_a c_b \hat{F}^{\alpha\beta} \rangle, \quad (9)$$

$$N_{abcd}^{\alpha\beta} = \langle c_a^\dagger d_b^\dagger d_c c_d \hat{F}^{\alpha\beta} \rangle, \quad (10)$$

$$F^{\alpha\beta} = \langle \hat{F}^{\alpha\beta} \rangle = \left\langle \exp \left( \sum_{\rho} \alpha_{\rho} b_{\rho}^\dagger \right) \exp \left( \sum_{\rho} \beta_{\rho} b_{\rho} \right) \right\rangle, \quad (11)$$

where  $\{\alpha_{\rho}\}$  and  $\{\beta_{\rho}\}$  are arbitrary sets of real parameters. As a consequence of the generating-function property, all phonon-assisted electronic density matrices can be obtained as derivatives of these functions taken at  $\alpha_{\mu} = \beta_{\mu} = 0$ . The electron and hole populations and correlations  $\langle c_a^\dagger c_b \rangle$  and  $\langle d_a^\dagger d_b \rangle$ , as well as their phonon-assisted counterparts, do not have to be considered as independent variables in the formalism since they can be eliminated in favor of  $N$  by identities (contraction identities) that are exact within the second-order treatment [35,38]. The differential equations for variables  $Y_{ab}^{\alpha\beta}$  and  $N_{abcd}^{\alpha\beta}$  are given in Appendix A.

The most general form of an electron-hole pair state is [36]

$$|p\rangle = \sum_{\substack{a \in \text{VB} \\ b \in \text{CB}}} \psi_{ab} c_b^\dagger d_a^\dagger |0\rangle, \quad (12)$$

where  $|0\rangle$  represents the state in which the conduction band is completely empty and the valence band is completely filled.

The excitonic basis is defined by the eigenvalue problem  $H_c |p\rangle = E |p\rangle$  which can be transformed into equations for amplitudes  $\psi_{ab}$ :

$$(\epsilon_b^c - \epsilon_a^v) \psi_{ab}^x + \sum_{\substack{p \in \text{VB} \\ q \in \text{CB}}} (V_{pqba}^{\text{vccv}} - V_{pabq}^{\text{vccc}}) \psi_{pq}^x = \hbar \omega_x \psi_{ab}^x. \quad (13)$$

The excitonic basis is orthonormal

$$\sum_{\substack{a \in \text{VB} \\ b \in \text{CB}}} \psi_{ab}^{\bar{x}*} \psi_{ab}^x = \delta_{x\bar{x}}. \quad (14)$$

We perform all calculations in the excitonic basis and expand all density matrices in the excitonic basis, for example,

$$Y_{ab} = \sum_x \psi_{ab}^x y_x, \quad (15)$$

$$N_{abcd} = \sum_{\bar{x}x} \psi_{ba}^{\bar{x}*} \psi_{cd}^x n_{\bar{x}x}, \quad (16)$$

and similarly for the corresponding phonon-assisted electronic density matrices; in the case of single-phonon assistance, the explicit definitions are

$$Y_{ab\mu^+} \equiv \langle d_a c_b b_{\mu}^\dagger \rangle = \sum_x \psi_{ab}^x y_{x\mu^+}, \quad (17a)$$

$$N_{abcd\mu^+} \equiv \langle c_a^\dagger d_b^\dagger d_c c_d b_{\mu}^\dagger \rangle = \sum_{\bar{x}x} \psi_{ba}^{\bar{x}*} \psi_{cd}^x n_{\bar{x}x\mu^+}. \quad (17b)$$

The creation operator for the exciton in the state  $x$  can be defined as

$$X_x^\dagger = \sum_{\substack{a \in \text{CB} \\ b \in \text{VB}}} \psi_{ba}^x c_a^\dagger d_b^\dagger. \quad (18)$$

The number of excitons in the state  $x$ , after performing the decoupling (which is exact up to the second order in the optical field)  $\langle c_a^\dagger d_b^\dagger d_c c_d \rangle = \langle c_a^\dagger d_b^\dagger \rangle \langle d_c c_d \rangle + \delta \langle c_a^\dagger d_b^\dagger d_c c_d \rangle$ , where  $\delta \langle c_a^\dagger d_b^\dagger d_c c_d \rangle$  stands for the correlated part of the electron-hole pair density, can be expressed as the sum

$$\langle X_x^\dagger X_x \rangle = |y_x|^2 + \bar{n}_{xx}, \quad (19)$$

where  $\bar{n}_{xx} = n_{xx} - y_x^* y_x$ . The first term in Eq. (19) describes the so-called coherent excitons, whereas the second term describes the incoherent excitons. Namely, an optical excitation of a semiconductor first induces single-particle excitations in form of optical polarizations and carrier densities. Optical polarizations decay very fast due to various scattering mechanisms present [15]. Therefore, their squared moduli, which are usually referred to as coherent excitonic populations [32], do not provide information about the true excitonic populations, which are the consequence of Coulomb-induced correlations between electrons and holes and which typically exist in the system for a long time after the decay of optical polarizations [7]. In order to describe true excitons, which are atomlike complexes of electrons and holes bound by the Coulomb attraction, we have to consider two-particle correlations between them, and not single-particle quantities [15]. The last conclusion justifies identification of the term  $\delta \langle c_a^\dagger d_b^\dagger d_c c_d \rangle$  with the incoherent excitonic populations.

The dynamic equations for the relevant variables should be compatible with the energy conservation in a system without external fields. Our system, however, interacts with external optical field, but, since we consider a pulsed excitation, the energy of the system should be conserved after the field has vanished. The total energy of the system, i.e., the expectation value of the Hamiltonian  $\langle H \rangle$  defined in Eqs. (1)–(5), is expressed as

$$\mathcal{E} = \mathcal{E}_c + \mathcal{E}_{\text{ph}} + \mathcal{E}_{\text{c-ph}} + \mathcal{E}_{\text{c-f}}, \quad (20)$$

where the carrier energy is

$$\mathcal{E}_c = \sum_x \hbar \omega_x n_{xx}, \quad (21)$$

the phonon energy is

$$\mathcal{E}_{\text{ph}} = \sum_{\mu} \hbar \omega_{\mu} \langle b_{\mu}^{\dagger} b_{\mu} \rangle, \quad (22)$$

the carrier-phonon interaction energy is

$$\mathcal{E}_{\text{c-ph}} = 2 \sum_{\bar{x}x\mu} \text{Re} \{ \Gamma_{\bar{x}x}^{\mu} n_{\bar{x}x\mu^+} \}, \quad (23)$$

and the carrier-field interaction energy is

$$\mathcal{E}_{\text{c-f}} = -\mathbf{E}(t) \sum_x (\mathbf{M}_x^* y_x + y_x^* \mathbf{M}_x). \quad (24)$$

In Eqs. (20)–(24) we have kept only contributions up to the second order in the external field and transferred to the excitonic basis. We also introduce excitonic dipole matrix elements

$$\mathbf{M}_x = \sum_{\substack{a \in \text{VB} \\ b \in \text{CB}}} \psi_{ab}^{x*} \mathbf{M}_{ba}^{\text{cv}}, \quad (25)$$

as well as matrix elements of the carrier-phonon interaction in the excitonic basis which describe the coupling to the phonon mode  $\mu$ :

$$\Gamma_{xx'}^{\mu} = \sum_{\substack{a \in \text{VB} \\ b \in \text{CB}}} \psi_{ab}^{x*} \left( \sum_{k \in \text{CB}} \gamma_{bk}^{\mu} \psi_{ak}^{x'} - \sum_{k \in \text{VB}} \gamma_{ka}^{\mu} \psi_{kb}^{x'} \right). \quad (26)$$

Within previous approaches to solving the hierarchy of equations obtained after performing the DCT scheme, single-phonon-assisted density matrices  $n_{\bar{x}x\mu^+}$ , which appear in Eq. (23), were not explicitly taken into account, but the respective differential equations were solved in the Markov and adiabatic approximations. However, it can be shown that the total energy under these approximations is not exactly conserved after the external field has vanished. In order to satisfy the energy conservation, we retain density matrices  $n_{\bar{x}x\mu^+}$  as independent dynamic variables in the formalism.

The dynamics should also conserve the particle number after the external field has vanished since all the other terms in the Hamiltonian given by Eqs. (1)–(5) commute with the total particle-number operator. The number of electrons (and also the number of holes, since carriers are generated in pairs in this model), with accuracy up to the second order in the

external field, is given as

$$N_{\text{tot}} = N_e = N_h = \sum_x n_{xx}. \quad (27)$$

The equations for the purely electronic relevant variables and phonon distribution function are

$$\begin{aligned} \partial_t y_x &= -i \omega_x y_x - \frac{1}{i\hbar} \mathbf{E}(t) \mathbf{M}_x \\ &+ \frac{1}{i\hbar} \sum_{\mu x'} \Gamma_{xx'}^{\mu} y_{x'\mu^+} + \frac{1}{i\hbar} \sum_{\mu x'} \Gamma_{x'x}^{\mu*} y_{x'\mu^-}, \end{aligned} \quad (28)$$

$$\begin{aligned} \partial_t n_{\bar{x}x} &= -i(\omega_x - \omega_{\bar{x}}) n_{\bar{x}x} - \frac{1}{i\hbar} \mathbf{E}(t) (y_{\bar{x}}^* \mathbf{M}_x - \mathbf{M}_{\bar{x}}^* y_x) \\ &+ \frac{1}{i\hbar} \sum_{\mu x'} \Gamma_{xx'}^{\mu} n_{\bar{x}x'\mu^+} - \frac{1}{i\hbar} \sum_{\mu \bar{x}'} \Gamma_{\bar{x}'\bar{x}}^{\mu} n_{\bar{x}'x\mu^+} \\ &+ \frac{1}{i\hbar} \sum_{\mu x'} \Gamma_{x'x}^{\mu*} n_{x'\bar{x}\mu^+} - \frac{1}{i\hbar} \sum_{\mu \bar{x}'} \Gamma_{\bar{x}\bar{x}'}^{\mu*} n_{x'\bar{x}\mu^+}, \end{aligned} \quad (29)$$

$$\partial_t \langle b_{\mu}^{\dagger} b_{\mu} \rangle = \frac{2}{\hbar} \sum_{\bar{x}x} \text{Im} \{ \Gamma_{\bar{x}x}^{\mu} n_{\bar{x}x\mu^+} \}. \quad (30)$$

Even at this level, without specifying the form of equations for one-phonon-assisted electronic density matrices, using Eq. (29) with vanishing electric field it is easily shown that, in the absence of external fields, our dynamics conserves the total number of particles.

We will neglect hot-phonon effects and assume that in all the equations for  $y_x$ ,  $n_{\bar{x}x}$ , and their phonon-assisted counterparts the phonon numbers assume their equilibrium values  $n_{\mu}^{\text{ph}} = (e^{\beta \hbar \omega_{\mu}} - 1)^{-1}$ . We will, however, retain Eq. (30) in the formalism because it is necessary to prove the energy conservation.

In equations for phonon-assisted electronic density matrices we neglect the coupling to the light field, i.e., we neglect contributions arising from the combined action of the phonon coupling and the interaction with the light field (so-called cross terms) [35,39]. The equations for the electronic density matrices with one-phonon assistance contain electronic density matrices with two-phonon assistance, from which we explicitly separate the factorized part and the correlated part, for example

$$\langle c_a^{\dagger} d_b^{\dagger} d_c c_d b_{\mu}^{\dagger} b_{\rho} \rangle = \langle c_a^{\dagger} d_b^{\dagger} d_c c_d \rangle \delta_{\mu\rho} n_{\mu}^{\text{ph}} + \delta \langle c_a^{\dagger} d_b^{\dagger} d_c c_d b_{\mu}^{\dagger} b_{\rho} \rangle, \quad (31)$$

$$\langle d_a c_b b_{\mu}^{\dagger} b_{\rho} \rangle = \langle d_a c_b \rangle \delta_{\mu\rho} n_{\mu}^{\text{ph}} + \delta \langle d_a c_b b_{\mu}^{\dagger} b_{\rho} \rangle. \quad (32)$$

We should bear in mind that the two-phonon-assisted electronic density matrices with two creation (annihilation) phonon operators, whose factorized part vanishes, should be considered on this level of truncation of the phonon branch [40]. Further comments on the factorization performed in Eq. (31) are given in Appendix B. The following equations for the electronic density matrices with single-phonon assistance are

obtained:

$$\begin{aligned} \partial_t n_{\bar{x}x\mu^+} = & -i(\omega_x - \omega_{\bar{x}} - \omega_\mu) n_{\bar{x}x\mu^+} + \frac{n_\mu^{\text{ph}}}{i\hbar} \sum_{x'} \Gamma_{x'\bar{x}}^{\mu*} n_{\bar{x}x'} \\ & - \frac{1+n_\mu^{\text{ph}}}{i\hbar} \sum_{\bar{x}'} \Gamma_{\bar{x}\bar{x}'}^{\mu*} n_{\bar{x}'x} \\ & - \frac{1}{i\hbar} \sum_{\rho\bar{x}'} (\Gamma_{\bar{x}\bar{x}'}^{\rho*} \delta n_{\bar{x}'x\mu^+\rho^-} + \Gamma_{\bar{x}'\bar{x}}^\rho \delta n_{\bar{x}x'\mu^+\rho^+}) \\ & + \frac{1}{i\hbar} \sum_{\rho x'} (\Gamma_{x'\bar{x}}^{\rho*} \delta n_{\bar{x}x'\mu^+\rho^-} + \Gamma_{xx'}^\rho \delta n_{\bar{x}x'\mu^+\rho^+}), \end{aligned} \quad (33)$$

$$\begin{aligned} \partial_t y_{x\mu^+} = & -i(\omega_x - \omega_\mu) y_{x\mu^+} + \frac{n_\mu^{\text{ph}}}{i\hbar} \sum_{x'} \Gamma_{x'\bar{x}}^{\mu*} y_{x'} \\ & + \frac{1}{i\hbar} \sum_{\rho x'} (\Gamma_{xx'}^\rho \delta y_{x'\mu^+\rho^+} + \Gamma_{x'\bar{x}}^{\rho*} \delta y_{x'\mu^+\rho^-}), \end{aligned} \quad (34)$$

$$\begin{aligned} \partial_t y_{x\mu^-} = & -i(\omega_x + \omega_\mu) y_{x\mu^-} + \frac{1+n_\mu^{\text{ph}}}{i\hbar} \sum_{x'} \Gamma_{xx'}^\mu y_{x'} \\ & + \frac{1}{i\hbar} \sum_{\rho x'} (\Gamma_{xx'}^\rho \delta y_{x'\rho^+\mu^-} + \Gamma_{x'\bar{x}}^{\rho*} \delta y_{x'\rho^-\mu^-}). \end{aligned} \quad (35)$$

The correlated parts of two-phonon-assisted density matrices appearing in Eqs. (33) ( $\delta n_{\bar{x}x\mu^+\rho^-}, \delta n_{\bar{x}x\mu^+\rho^+}$ ), (34), and (35) can be obtained solving their respective differential equations, in which all three-phonon-assisted density matrices have been appropriately factorized and their correlated parts have been neglected, in the Markov and adiabatic approximations. This procedure closes the phonon branch of the hierarchy. However, the full solution to these equations, when combined with Eq. (33), is cumbersome to evaluate, so further approximations are usually employed. The most common one is the so-called random phase approximation, which neglects sums over correlated parts of one-phonon-assisted electronic density matrices (which are complex quantities) due to random phases at different arguments of these density matrices [9]. After performing all the discussed approximations, the last two summands in Eq. (33), which represent the rate at which  $n_{\bar{x}x\mu^+}$  changes due to the coupling to electronic density matrices with higher phonon assistance, reduce to

$$(\partial_t n_{\bar{x}x\mu^+})_{\text{higher}} = -\gamma_{\bar{x}x\mu} n_{\bar{x}x\mu^+}, \quad (36)$$

where  $\gamma_{\bar{x}x\mu}$  is given as

$$\begin{aligned} \gamma_{\bar{x}x\mu} = & \frac{1}{2}(\Gamma_x + \Gamma_{\bar{x}}), \quad (37) \\ \Gamma_x = & \frac{2\pi}{\hbar} \sum_{\bar{x}\rho} [|\Gamma_{x\bar{x}}^\rho|^2 \delta(\hbar\omega_x - \hbar\omega_{\bar{x}} + \hbar\omega_\rho) n_\rho^{\text{ph}} \\ & + |\Gamma_{\bar{x}x}^\rho|^2 \delta(\hbar\omega_x - \hbar\omega_{\bar{x}} - \hbar\omega_\rho)(1 + n_\rho^{\text{ph}})]. \end{aligned} \quad (38)$$

Details of the procedure employed to close the phonon branch of the hierarchy are given in Appendix B.

It was recognized that this form of the coupling to higher-order phonon-assisted electronic density matrices is at variance with the energy conservation [9,10,41]. In this work, we will

use the following form of the coupling to higher-order phonon-assisted density matrices:

$$(\partial_t n_{\bar{x}x\mu}^{(+)})_{\text{higher}} = -\gamma_{\bar{x}x\mu} n_{\bar{x}x\mu}^{(+)} + \gamma_{\bar{x}x\mu} n_{\bar{x}x\mu}^{(+) *}, \quad (39)$$

where  $\gamma_{\bar{x}x\mu}$  is, as before, defined by Eqs. (37) and (38). This form of  $(\partial_t n_{\bar{x}x\mu}^{(+)})_{\text{higher}}$  is compatible with the energy conservation, as long as excitonic matrix elements of the carrier-phonon interaction  $\Gamma_{\bar{x}x}^\mu$  are purely real, which is the case relevant for our numerical investigation in Sec. III. Namely, as is shown in Appendix C, the rate at which the total energy changes after the pulse is equal to the rate at which the carrier-phonon interaction energy changes due to the coupling of the single-phonon-assisted electronic density matrices  $n_{\bar{x}x\mu^+}$  to density matrices with higher-order phonon assistance,

$$\begin{aligned} \partial_t \mathcal{E} = & (\partial_t \mathcal{E}_{\text{c-ph}})_{\text{higher}} \\ = & 2 \sum_{\bar{x}x\mu} \text{Re} \{ \Gamma_{\bar{x}x}^\mu (\partial_t n_{\bar{x}x\mu^+})_{\text{higher}} \}. \end{aligned} \quad (40)$$

It is then clear that, if all  $\Gamma_{\bar{x}x}^\mu$  are real, the form of  $(\partial_t n_{\bar{x}x\mu^+})_{\text{higher}}$  given in Eq. (39) does not violate the energy conservation. Furthermore, as  $n_{\bar{x}x\mu^+}$  describes the elementary process in which an exciton initially in the state  $x$  is scattered to the state  $\bar{x}$  emitting the phonon from the mode  $\mu$ , the reverse microscopic process, described by  $n_{x\bar{x}\mu^-} = n_{\bar{x}x\mu^+}^*$ , is also possible, so in the differential equation for  $n_{\bar{x}x\mu^+}$  the quantity  $n_{\bar{x}x\mu^+}^*$  may appear. In Appendix C, we comment on the energy conservation in greater detail.

Similar strategy can be adopted to simplify the coupling to electronic density matrices with higher phonon assistance in (34) and (35), with the final result

$$(\partial_t y_{x\mu}^{(\pm)})_{\text{higher}} = -\gamma_{x\mu} y_{x\mu}^{(\pm)}, \quad (41)$$

where

$$\gamma_{x\mu} = \frac{1}{2}\Gamma_x, \quad (42)$$

and  $\Gamma_x$  is defined in Eq. (38).

An alternative route to derive equations for the relevant variables is to rewrite the Hamiltonian given in Eq. (1) in terms of operators  $X_x, X_x^\dagger$  [see Eq. (18)], keeping only contributions whose expectation values are at most of the second order in the optical field. The result is

$$\begin{aligned} H = & \sum_x \hbar\omega_x X_x^\dagger X_x + \sum_\mu \hbar\omega_\mu b_\mu^\dagger b_\mu \\ & + \sum_{\mu\bar{x}x} \left( \Gamma_{\bar{x}x}^\mu X_{\bar{x}}^\dagger X_x b_\mu^\dagger + \Gamma_{\bar{x}x}^{\mu*} X_x^\dagger X_{\bar{x}} b_\mu \right) \\ & - \mathbf{E}(t) \sum_x (\mathbf{M}_x^* X_x + \mathbf{M}_x X_x^\dagger). \end{aligned} \quad (43)$$

The excitonic operators (up to the second order in the optical field) satisfy Bose commutation relations  $[X_x, X_{\bar{x}}^\dagger] = \delta_{x\bar{x}}$ . In this representation [42], the excitons are treated as noninteracting bosons and the form of the exciton-phonon interaction is transparent, with exciton-phonon coupling constants  $\Gamma_{\bar{x}x}^\mu$  defined in Eq. (26).

### III. ONE-DIMENSIONAL SEMICONDUCTOR MODEL AND NUMERICAL RESULTS

Numerical computations will be carried out on a two-band one-dimensional semiconductor model. We use a tight-binding model on a one-dimensional lattice with  $N$  sites and lattice spacing  $a$  to describe the semiconductor. Periodic boundary conditions are used. The Hamiltonian describing interacting carriers is given as

$$H_c = \sum_{i=0}^{N-1} \epsilon_0^c c_i^\dagger c_i - \sum_{i=0}^{N-1} J^c (c_i^\dagger c_{i+1} + c_{i+1}^\dagger c_i) - \sum_{i=0}^{N-1} \epsilon_0^v d_i^\dagger d_i + \sum_{i=0}^{N-1} J^v (d_i^\dagger d_{i+1} + d_{i+1}^\dagger d_i) + \frac{1}{2} \sum_{i,j=0}^{N-1} (c_i^\dagger c_i - d_i^\dagger d_i) V_{ij} (c_j^\dagger c_j - d_j^\dagger d_j). \quad (44)$$

It is assumed that the carrier transfer integrals  $J^c, J^v$  are nonzero only among nearest-neighbor pairs of sites. The Coulomb interaction is taken in the lowest monopole-monopole approximation [43], and the interaction potential  $V_{ij}$  is taken to be the Ohno potential

$$V_{ij} = \frac{U}{\sqrt{1 + \left(\frac{|i-j|a}{a_0}\right)^2}}. \quad (45)$$

$U$  is the onsite carrier-carrier interaction, while  $a_0$  is the characteristic length given as  $a_0 = e^2/(4\pi\epsilon_0\epsilon_r U)$ , where  $\epsilon_r$  is the static relative dielectric constant. This form of carrier-carrier interaction is an interpolation between the onsite Coulomb interaction  $U$  and the ordinary Coulomb potential (in which the static relative dielectric constant is taken)  $e^2/(4\pi\epsilon_0\epsilon_r r)$  when  $r \rightarrow \infty$  (see, e.g., the discussion on the effective electron-hole interaction in Ref. [5]). The interaction with phonons is taken to be of the Holstein form, where a charge carrier is locally and linearly coupled to a dispersionless optical mode

$$H_{c-ph} = \sum_{i=0}^{N-1} g^c c_i^\dagger c_i (b_i + b_i^\dagger) - \sum_{i=0}^{N-1} g^v d_i^\dagger d_i (b_i + b_i^\dagger), \quad (46)$$

where the free-phonon Hamiltonian is

$$H_{ph} = \sum_{i=0}^{N-1} \hbar\omega_{ph} b_i^\dagger b_i. \quad (47)$$

Despite the fact that the carrier-phonon interaction in real materials has a more complicated form, we choose for our numerical investigations its simplest possible form [Eq. (46)] capable of providing the energy relaxation of the electronic subsystem. The interaction with the electric field is

$$H_{c-f} = -d_{cv} E(t) \sum_{i=0}^{N-1} (d_i c_i + c_i^\dagger d_i^\dagger). \quad (48)$$

As the system described is translationally symmetric, we can transfer to the momentum space and obtain the same Hamiltonian as described in Eqs. (1)–(5) with the following

values of parameters:

$$\epsilon_k^{c/v} = \epsilon_0^{c/v} - 2J^{c/v} \cos(ka), \quad (49a)$$

$$\gamma_{k_1 k_2}^q = \delta_{k_2, k_1+q} \frac{g^c}{\sqrt{N}} \quad \text{for } k_1, k_2 \in \text{CB}, \quad (49b)$$

$$\gamma_{k_1 k_2}^q = \delta_{k_1, k_2+q} \frac{g^v}{\sqrt{N}} \quad \text{for } k_1, k_2 \in \text{VB}, \quad (49c)$$

$$V_{pqkl}^{vccc} = \delta_{k+q, p+l} V_{k-l}, \quad V_{plkq}^{vccv} = 0. \quad (49d)$$

The signs of the transfer integrals are  $J^c > 0$ ,  $J^v < 0$ . The constant energy  $\epsilon_0^c > 0$ , while  $\epsilon_0^v < 0$  is chosen so that the maximum of the valence band is the zero of the energy scale.  $V_{k-l}$  is the Fourier transformation of the Ohno potential and it is computed numerically as

$$V_k = \frac{1}{N^2} \sum_{i,j=0}^{N-1} V_{ij} e^{-ika(i-j)}. \quad (50)$$

The translational symmetry of our model enables us to solve efficiently the eigenvalue problem (13) which defines the excitonic basis. Instead of solving eigenvalue problem of a  $N^2 \times N^2$  matrix, we can solve  $N$ -independent eigenvalue problems of matrices of dimension  $N \times N$ , thus obtaining  $N^2$  excitonic eigenstates and their eigenenergies, which are counted by the center-of-mass wave vector  $Q$  and the band index  $\nu$ . Thus, the general index of an excitonic state  $x$  should be, in all practical calculations, replaced by combination  $(Q, \nu)$ . This has the following consequences on the matrix elements in the excitonic basis: dipole matrix elements reduce to

$$M_{(Q\nu)} = \delta_{Q,0} d_{cv} \sum_{k_e} \psi_{Q-k_e, k_e}^{(Q\nu)*}, \quad (51)$$

whereas carrier-phonon interaction matrix elements reduce to

$$\Gamma_{(Q\nu)(Q'\nu')}^q = \delta_{Q', Q+q} \frac{1}{\sqrt{N}} \sum_{k_e} \psi_{Q-k_e, k_e}^{(Q\nu)*} \times (g^c \psi_{Q-k_e, Q'-Q+k_e}^{(Q'\nu')} - g^v \psi_{Q'-k_e, k_e}^{(Q'\nu')}). \quad (52)$$

Due to the translational symmetry of our model, only the dynamic variables for which the total created wave vector is equal to the total annihilated wave vector will have nontrivial values in the course of the system's evolution. For example, from all density matrices  $\gamma_{(Q\nu)}$  only those with  $Q = 0$  can have nonzero values.

Our objective is to analyze, in the framework of this relatively simple model, the characteristic time scales of exciton formation and relaxation in a photoexcited semiconductor, along with the impact that various model parameters have on these processes. Basic parameters in our model are transfer integrals  $J^c, J^v$  (which determine bandwidths of the conduction and valence bands), electron-phonon coupling constants  $g^c, g^v$ , the phonon energy  $\hbar\omega_{ph}$ , the dielectric constant  $\epsilon_r$ , and the onsite Coulomb interaction  $U$ . We will, throughout the computations, assume for simplicity that  $J^c = J^v = J$  and  $g^c = g^v = g$ .

As is well known, the main differences between a typical organic and inorganic semiconductor can be expressed in terms of bandwidths, dielectric constant, and the carrier-phonon

interaction strength. Namely, inorganic semiconductors are characterized by wide bands and high value of dielectric constant, whereas organic semiconductors have narrow bands and small value of dielectric constant. The carrier-phonon interaction is stronger in organic than in inorganic semiconductors. Having all these facts in mind, we propose two sets of model parameters which assume values typical of an organic and inorganic semiconductor. Values of our model parameters are adjusted to material parameters of GaAs for the inorganic case and pentacene for the organic case. Values of carrier-phonon coupling constants are chosen to correspond to typical values for mobility and/or typical values for the polaron binding energy.

Typical bandwidths in organic semiconductors are  $W \sim 500$  meV [8], which corresponds to the transfer integral  $J \sim 125$  meV, whereas inorganic semiconductors usually exhibit bandwidths of several electronvolts [8] and we take in our calculations the value of the transfer integral  $J = 500$  meV. In both cases, the lattice constant was fixed to  $a = 1$  nm. The dielectric constant in a typical inorganic semiconductor is of the order of 10 and in the calculations we take the value of static dielectric constant of GaAs  $\epsilon_r = 12.9$ . For a representative value of the dielectric constant in organic semiconductors we take  $\epsilon_r = 3.0$  [4,8]. The value of the onsite Coulomb interaction  $U$  is chosen to give the correct order of magnitude for the exciton binding energy, which is calculated numerically. For the organic parameter set, we set  $U = 480$  meV, which gives the exciton binding energy around 320 meV, while for the inorganic parameter set  $U = 15$  meV and the corresponding exciton binding energy is roughly 10 meV.

The carrier-phonon coupling constants for the inorganic case are estimated from the mobility values. The mobility of carriers is estimated using the relation  $\mu = e\tau/m^*$ , where  $\tau$  is the scattering time and  $m^*$  is the effective mass of a carrier. For cosine bands considered in this work,  $m^* = \hbar^2/(2|J|a^2)$  in the vicinity of the band extremum. The scattering time is estimated from the expression for the carrier-phonon inelastic scattering rate based on the Fermi's golden rule, which around the band extremum  $k = 0$  assumes the following form:

$$\frac{1}{\tau(k)} = \frac{g^2}{\hbar|J|} \frac{n^{\text{ph}}}{\sqrt{1 - \left(\cos(ka) - \frac{\hbar\omega_{\text{ph}}}{2|J|}\right)^2}}, \quad (53)$$

where  $n^{\text{ph}} = (e^{\beta\hbar\omega_{\text{ph}}} - 1)^{-1}$ . Therefore, the carrier-phonon coupling constant in terms of the carrier mobility reads as

$$g = |J| \sqrt{\frac{2ea^2}{\hbar\mu n^{\text{ph}}}} \left[ 1 - \left( 1 - \frac{\hbar\omega_{\text{ph}}}{2|J|} \right)^2 \right]^{1/4}. \quad (54)$$

Using the value for the electron mobility in GaAs at 300 K  $\mu_e \approx 8500$  cm<sup>2</sup>/(Vs) [44], we obtain  $g \approx 25$  meV.

We can also estimate the carrier-phonon coupling constants from the polaron binding energy. As an estimate of this quantity, we use the result of the second-order weak-coupling perturbation theory at  $T = 0$  in the vicinity of the point  $k = 0$  [45]:

$$\epsilon_{\text{b}}^{\text{pol}}(k) = \frac{g^2}{2|J|} \frac{1}{\sqrt{(\cos(ka) + \frac{\hbar\omega_{\text{ph}}}{2|J|})^2 - 1}}. \quad (55)$$

TABLE I. Model parameters which are representative of a typical organic and inorganic semiconductor. References from which material parameters are taken are indicated.

Parameter	Inorganic	Organic
$E_g$ (meV)	1519 [32]	2000 [47]
$J$ (meV)	500	125
$\epsilon_r$	12.9 [32]	3.0 [8]
$g$ (meV)	25	40
$\hbar\omega_{\text{ph}}$ (meV)	36.4 [32]	10.0 [48,49]
$U$ (meV)	15	480

It is known that polaron binding energies in typical inorganic semiconductors are  $\epsilon_{\text{b}}^{\text{pol}} \sim 1$  meV and we used this fact along with Eq. (55) to check our estimate for  $g$  from the value of mobility; for  $g \approx 25$  meV, we obtain  $\epsilon_{\text{b}}^{\text{pol}} \approx 2$  meV. The polaron binding energies in polyacenes lie in the range between 21 and 35 meV [46]. The value of  $g$  in the set of model parameters representative of organic semiconductors was estimated from the polaron binding energy in pentacene, which is around 20 meV. We obtain that  $g \approx 40$  meV. The values used for the organic/inorganic set of parameters are listed in Table I.

The form of the electric field is assumed to be a rectangular cosine pulse

$$E(t) = E_0 \cos(\omega_c t) \theta(t + t_0) \theta(t_0 - t), \quad (56)$$

where  $\omega_c$  is the central frequency of the field and  $\theta(t)$  is the Heaviside step function. Time  $t_0$  is chosen large enough so that the pulse is so spectrally narrow that the notion of the central frequency makes sense. On the other hand, the pulse should be as short as possible, so that after its end we observe the intrinsic dynamics of our system, the one which is not accompanied by the carrier generation process, but merely shows how initially generated populations are redistributed among various states. Trying to reconcile the aforementioned requirements, we choose  $t_0 = 250$  fs. The amplitude of the electric field  $E_0$  and the interband dipole matrix element  $d_{\text{cv}}$  are chosen so that we stay in the low-density regime; particularly, we choose them so that the corresponding Rabi frequency  $\hbar\omega_R = d_{\text{cv}}E_0$  assumes the value of 0.2 meV, which is smaller than any energy scale in our problem and ensures that the excitation is weak.

In order to quantitatively study the process of exciton formation after a pulsed excitation of a semiconductor, we solved the system of quantum kinetic equations for electronic density matrices  $y_x, n_{\bar{x}x}$  and their single-phonon-assisted counterparts [Eqs. (28), (29), (33), (34), and (35) supplemented with Eqs. (36) and (41)] using the fourth-order Runge-Kutta algorithm. The computations are performed for the temperature  $T = 300$  K and the central frequency of the pulse equal to the single-particle gap ( $\hbar\omega_c = E_g$ ). The exciton is considered bound (unbound) if its energy  $\hbar\omega_{(Qv)}$  is smaller (larger) than the smallest single-particle energy difference  $\epsilon_{k_c}^c - \epsilon_{Q-k_c}^v$  [47]. The equation of the boundary line which

separates bound from unbound pair states reads as

$$\epsilon_{\text{sep}}(Q) = \epsilon_0^c - \epsilon_0^v - 2\sqrt{(J^c)^2 + (J^v)^2 - 2J^c J^v \cos(Qa)}. \quad (57)$$

An unbound exciton may be considered as (quasi)free electron and hole, so this way it is possible to distinguish between bound excitons and free carriers.

The pulsed excitation of a semiconductor leads, in the first step, to the generation of coherent electron-hole pairs that are described in our formalism by the coherent pair amplitudes  $y_x$ . The decay of the coherent pair occupation

$$N_{\text{coh}} = \sum_x |y_x|^2 \quad (58)$$

is due to the scattering processes which initiate already during the generation of the pairs and gives a direct measure of the loss of coherence [32]. At the same time, incoherent pair occupations start to grow, driven by the loss rate of coherent pair occupations [32,35]. In order to quantify the process of exciton formation, we will follow the time dependence of the total number of incoherent bound excitons

$$N_{\text{incoh,b}} = \sum_{x \in \text{bound}} (n_{xx} - |y_x|^2). \quad (59)$$

This quantity represents the number of truly bound electron-hole pairs which exist even after the optical field has vanished and as such is the direct measure of the efficiency of the exciton formation process. We will, when useful, also consider the number of incoherent excitons in a particular band  $\nu$ ,  $N_{\text{incoh},\nu}$ . The quantities  $N_{\text{incoh,b}}$  and  $N_{\text{incoh},\nu}$  will be normalized to the total number of excitons  $N_{\text{tot}}$  defined in Eq. (27).

### A. Numerical results: Organic set of parameters

We start this section by an overview of properties of the excitonic spectrum, shown in Fig. 1(a), which will be relevant for further discussions of the exciton formation process. The lowest excitonic band is energetically well separated from the rest of the spectrum, the energy separation between the minima of the bands  $\nu = 0$  and 1 being around 200 meV, which is much larger than both the value of  $k_B T$  at room temperature and the phonon energy in our model (see Table I). As a consequence, downward transitions that end at the lowest excitonic band start almost exclusively from the states on  $\nu = 1$  band and an exciton, which is at some instant in a state on the  $\nu = 0$  band, cannot be scattered to an unbound excitonic state.

We briefly comment on the size of the exciton for these values of model parameters. From the exciton wave function  $\psi_{Q-k_e, k_e}^{(Q\nu)}$  in  $k$  space, we can obtain the exciton wave function in real space performing the Fourier transformation

$$\begin{aligned} \psi_{r_e, r_h}^{(Q\nu)} &= \sum_{k_e} e^{i(Q-k_e)r_h} e^{ik_e r_e} \psi_{Q-k_e, k_e}^{(Q\nu)} \\ &= e^{iQ(r_e+r_h)/2} \sum_{k_e} e^{-i(Q-2k_e)(r_e-r_h)/2} \psi_{Q-k_e, k_e}^{(Q\nu)}. \end{aligned} \quad (60)$$

The exciton wave function in real space is a product of the plane wave which describes the motion of the center of mass

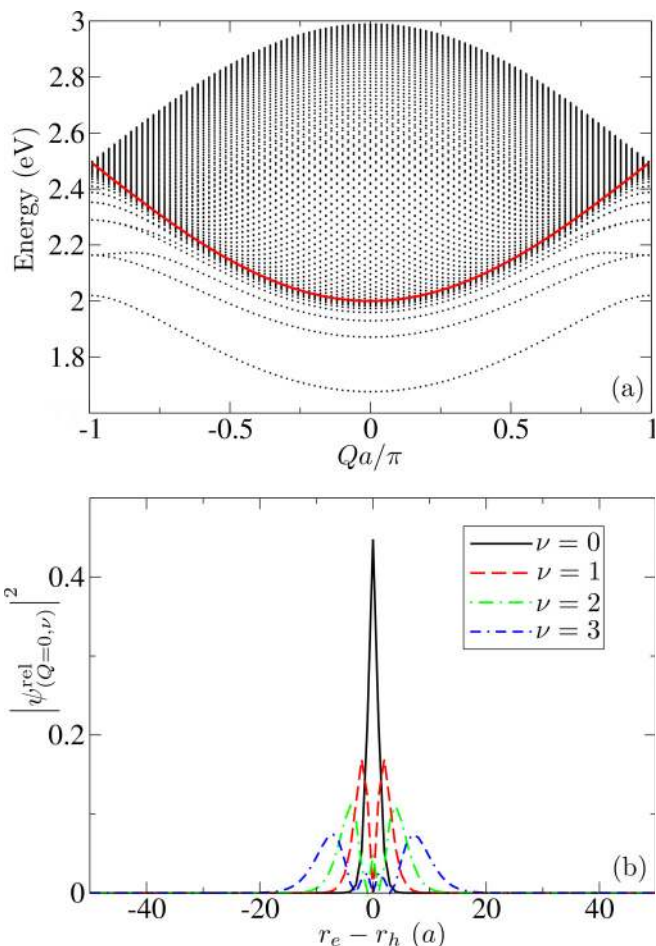


FIG. 1. (Color online) (a) Excitonic spectrum for the organic set of parameters. Dots represent individual excitonic states  $(Q, \nu)$ , while thick red line is the boundary between bound and unbound excitonic states computed using Eq. (57). (b) Squared modulus of the wave function which describes the relative motion of an electron-hole pair [Eq. (61)] calculated for different states  $(Q = 0, \nu)$ . Mean electron-hole separations in these states are  $0.7a$  ( $\nu = 0$ ),  $2.5a$  ( $\nu = 1$ ),  $4.6a$  ( $\nu = 2$ ), and  $7.8a$  ( $\nu = 3$ ). Computations are performed for  $N = 101$ .

with the wave vector  $Q$  and the wave function of the relative motion of an electron and a hole:

$$\psi_{(Q,\nu)}^{\text{rel}} = \sum_{k_e} e^{-i(Q-2k_e)(r_e-r_h)/2} \psi_{Q-k_e, k_e}^{(Q\nu)}. \quad (61)$$

The latter part is directly related to the exciton size. We calculated squared modulus of the wave function of the relative motion of a pair for states  $(Q = 0, \nu)$  in various bands. The result is shown in Fig. 1(b). It is clearly seen that an electron and a hole are tightly bound in these states and their relative separations are of the order of lattice constant, which is the typical value for the exciton radius in organic semiconductors. We point out that this does not mean that an exciton is localized; due to the translational symmetry of our system, it is delocalized over the whole lattice, as described by the plane-wave factor in the total wave function of a pair. Moreover, we note that the system size  $N = 101$  is large enough for the results to be numerically accurate, as it is much larger than the typical size of the exciton in a bound state.

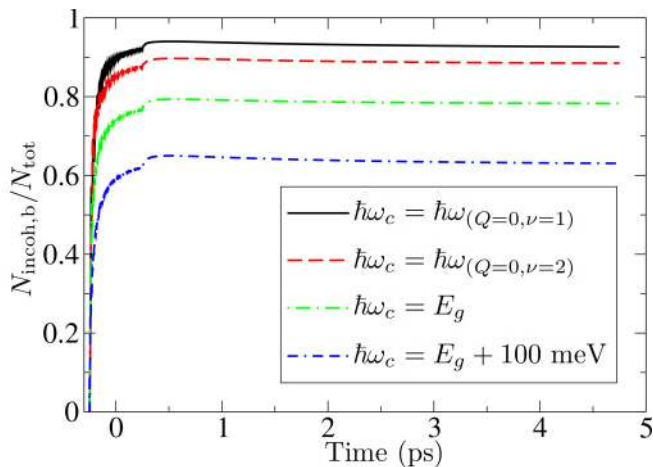


FIG. 2. (Color online) Time dependence of the relative number of incoherent bound excitons for different central frequencies of the pulse.

The impact that different parameters have on the exciton formation process is studied by changing one parameter, at the same time fixing the values of all the other parameters to the previously mentioned ones. We performed all the computations for a limited number of lowest excitonic bands, which crucially depends on the central frequency  $\omega_c$  of the excitation. For the given excitation, we took into account all the bands whose minima lie below  $\hbar\omega_c + \alpha k_B T$ , where  $\alpha \sim 5$  is a numerical constant.

We will first discuss the exciton formation process for different central frequencies of the exciting pulse. We have considered central frequencies in resonance with ( $Q = 0$ ,  $\nu = 1$ ) state, ( $Q = 0$ ,  $\nu = 2$ ) state, single-particle gap, and the central frequency which is 100 meV above the band gap. As can be noted from Fig. 2, raising the central frequency of the laser field leads to lower relative number of incoherent bound excitons. Namely, the higher is the central frequency, the higher (in energy) are the bands in which the initial coherent excitonic populations are created and the slower is the conversion of these coherent populations to incoherent populations in lower excitonic bands. However, in the long-time limit, the relative number of incoherent bound excitons should not depend on the central frequency of the laser, but tend to the value predicted by the Maxwell-Boltzmann distribution, which is above 99%. Such a high value is due to the large energy separation between the lowest excitonic band and the rest of the spectrum. We can thus infer, based on Fig. 2, that the semiconductor dynamics right after the pulsed excitation shows highly nonequilibrium features. Relaxation towards equilibrium occurs on a time scale longer than the picosecond one.

Next, we consider the dependence of the exciton formation process on temperature. The temperature enters our model only through phonon numbers  $n^{\text{ph}}$ . The overall behavior of the relative number of incoherent bound excitons for different temperatures is shown in Fig. 3. During the pulse, the relative number of incoherent bound excitons is highest for  $T = 300$  K and lowest for  $T = 100$  K, which is the consequence of the fact that scattering processes from higher excitonic bands (in which

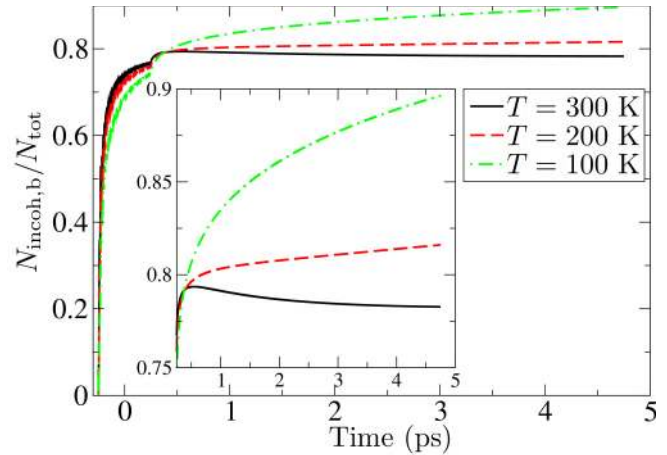


FIG. 3. (Color online) Time dependence of the relative number of incoherent bound excitons for different temperatures. The inset shows the portions of the same curves after the pulse.

initial coherent excitonic populations are created and which are situated both in the pair continuum and below it) towards lower excitonic bands are most efficient at  $T = 300$  K. After the generation of carriers has been completed, phonon-mediated processes lead to the redistribution of created incoherent excitons among different excitonic states and the relative number of incoherent bound excitons increases with decreasing the temperature, which is the expected trend. In the inset of Fig. 3 we also note that the relative number of incoherent bound excitons after the pulse experiences an initial growth followed by a slow decay at  $T = 300$  K, whereas at  $T = 100$  K it monotonically rises. The initial growth at  $T = 300$  K is attributed to downward scattering processes, but since at this temperature upward scattering events cannot be neglected, the following slow decay is due to the fact that some excitonic bands well below the pair continuum (bands  $\nu = 1, 2, 3$ ) lose excitons both by downward scattering and upward scattering to excitonic states which are near to or belong to the pair continuum [see Figs. 4(a) and 4(b)]. At  $T = 100$  K, these upward processes are much less probable than downward processes, thus the decay of the relative number of incoherent bound excitons is not observed; in Figs. 4(c) and 4(d) we see that lowest excitonic bands ( $\nu = 0, 1, 2$ ) gain excitons, whereas bands which are near to or belong to the pair continuum ( $\nu = 9, 11, 13, 15$ ) lose excitons. The population of the lowest excitonic band  $\nu = 0$  continually grows at all the temperatures studied, due to the large energetic separation between this band and the rest of the spectrum.

We briefly comment on the behavior of the number of coherent excitons  $N_{\text{coh}}$  and its temperature dependence. Right after the start of the pulse, coherent excitons comprise virtually the total excitonic population (see Fig. 5). Due to the carrier-phonon interaction, the relative number of coherent excitons decays during the pulse, so that at its end coherent excitons comprise around 1% of the total excitonic population. The conversion from coherent to incoherent populations is thus almost completed by the end of the pulse. From the inset of Fig. 5, we note that  $N_{\text{coh}}/N_{\text{tot}}$  exhibits a very fast decay after the pulse has vanished, with decay times of the order of 50 fs or less. Therefore, we infer that the transformation from coherent

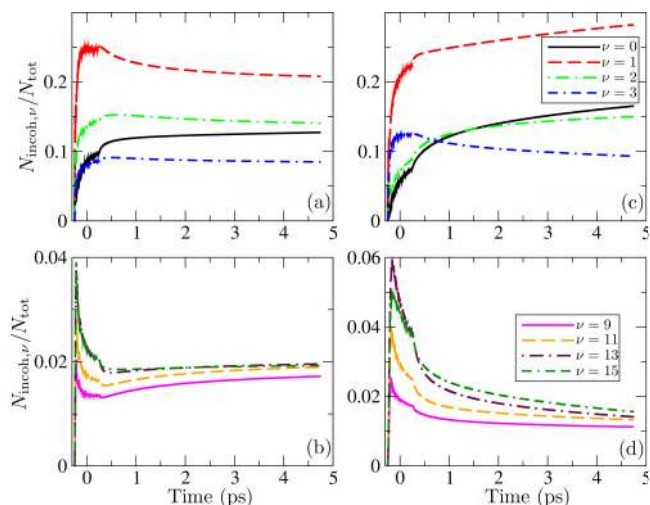


FIG. 4. (Color online) Time dependence of the relative population of various excitonic bands for different temperatures  $T = 300$  K for panels (a) and (b) and  $T = 100$  K for panels (c) and (d). Panels (a) and (c) concern bands which are well below the pair continuum ( $\nu = 0, 1, 2, 3$ ), whereas panels (b) and (d) deal with the bands which are near the continuum ( $\nu = 9$ ) or in the continuum ( $\nu = 11, 13, 15$ ).

to incoherent excitonic populations takes place on a 50-fs time scale. Based on Fig. 5, we also note that the lower is the temperature, the slower is the transformation from coherent to incoherent excitonic populations, which is the expected trend.

We continue our investigation by examining the effects that changes in the carrier-phonon coupling constant  $g$  have on the exciton formation process. Since increasing (lowering)  $g$  increases (lowers) semiclassical transition rates, just as increasing (lowering)  $T$  does, the changes in  $g$  and  $T$  should have, in principle, similar effects on the exciton formation process. Considering first the relative number of incoherent bound excitons, whose time dependence for different values of  $g$  is shown in Fig. 6(a), we note that after the end of the

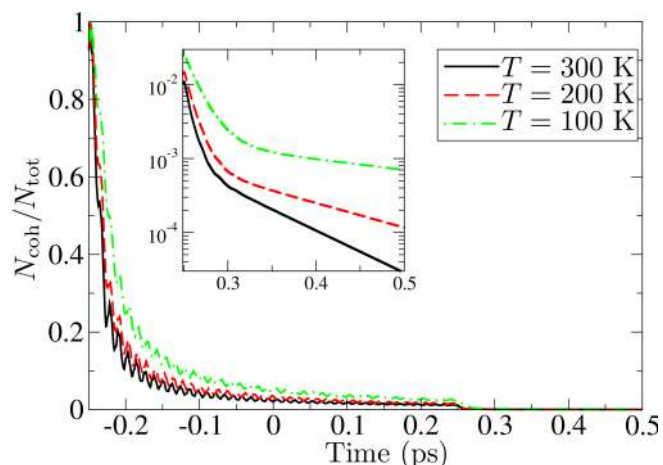


FIG. 5. (Color online) Time dependence of the relative number of coherent excitons for different temperatures. The inset shows the portions of the same curves (note the logarithmic scale on the vertical axis) after the pulse.

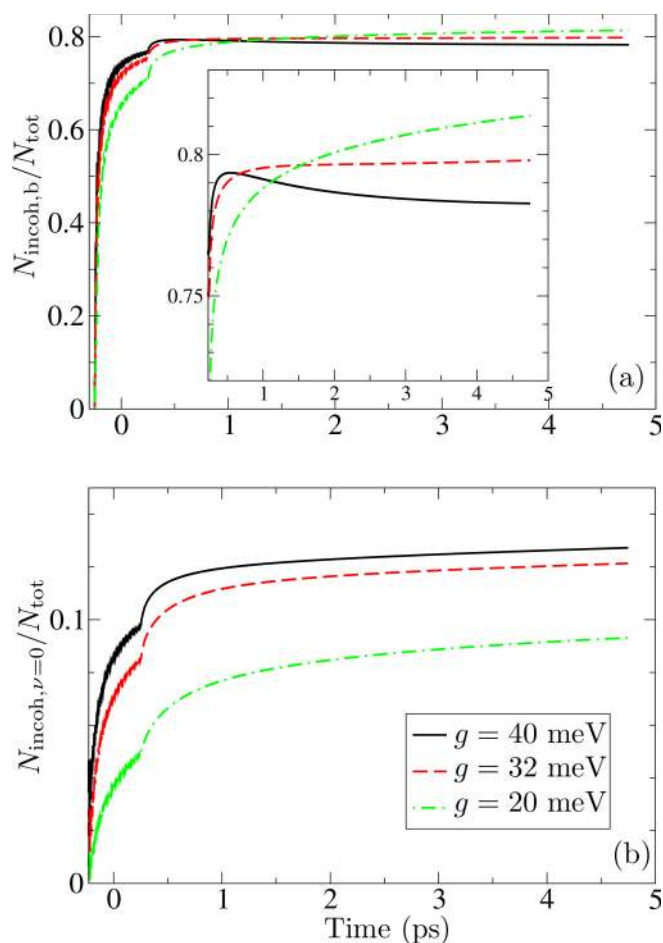


FIG. 6. (Color online) Time dependence of (a) the relative number of incoherent bound excitons, (b) the relative number of incoherent excitons in the  $\nu = 0$  band, for various values of  $g$ . The inset in the panel (a) shows the portions of the same curves after the pulse.

pulse it increases with decreasing  $g$ . However, during the pulse, higher values of  $g$  lead to more incoherent bound excitons, as is expected since scattering processes which populate low-energy states are more intensive for larger  $g$ . We also show the time dependence of the relative number of excitons in  $\nu = 0$  band in Fig. 6(b). It is observed that the lower is  $g$ , the lower is the number of excitons in the lowest excitonic band. This is due to the fact that populations on the lowest band are generated mainly via scattering processes from the  $\nu = 1$  band and these processes are less efficient for smaller  $g$ .

We conclude this section by studying the effects that changes in the onsite Coulomb interaction  $U$  have on the process of exciton formation. Changing  $U$  has profound effects on the excitonic spectrum. Exciton binding energy lowers with lowering  $U$  along with the energy separation between the band  $\nu = 0$  and the rest of the spectrum. We studied the impact of  $U$  on the exciton formation process for three values of  $U$ ,  $U = 480, 240$ , and  $48$  meV, for which the exciton binding energy is  $\sim 320, \sim 175$ , and  $\sim 40$  meV, respectively. Lowering  $U$  lowers the relative number of incoherent bound excitons, as is shown in Fig. 7. Smaller energy separation between the lowest excitonic band and the rest of the spectrum means that phonon-mediated transitions which start/end on the band  $\nu =$

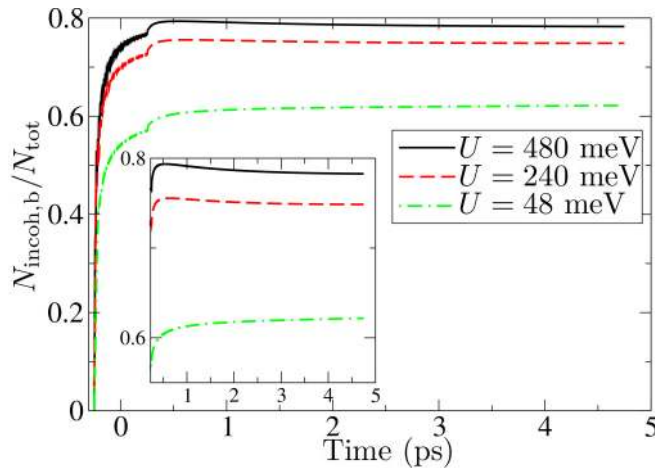


FIG. 7. (Color online) Time dependence of the relative number of incoherent bound excitons for various values of  $U$ . The inset shows the portions of the same curves after the pulse.

0 can end/start not predominantly on the band  $\nu = 1$ , but also on higher excitonic bands, which, for lower  $U$ , are more certain to belong to the electron-hole pair continuum than to the part of the spectrum which contains bound pair states. Thus, the lower is  $U$ , the more likely are the dissociation processes in which an exciton, initially in a bound state, after a phonon-mediated transition ends in an unbound pair state, which explains the observed trend in the relative number of incoherent bound excitons. This agrees with the usual picture according to which thermal fluctuations are likely to dissociate loosely bound electron-hole pairs. For  $U = 48$  meV, in the long-time limit and according to the Maxwell-Boltzmann distribution, around 78% of the total number of excitons should be in bound states, whereas for the other two values of  $U$  this number is above 99%. Thus, the dynamics observed is highly nonequilibrium, but unlike the cases  $U = 480$  and  $240$  meV, in which we cannot observe that the relative number of incoherent bound excitons starts to tend to its equilibrium value, for  $U = 48$  meV we observe such a behavior (see the inset of Fig. 7).

In summary, we list the time scales of the exciton formation and relaxation that stem from our computations. The transformation from coherent to incoherent excitons takes place in less than 50 fs. A significant number of incoherent bound excitons are established on a time scale of several hundreds of femtoseconds, whereas the subsequent relaxation of excitonic populations occurs on a time scale longer than the picosecond one. Further discussion of these results is deferred for Sec. IV.

### B. Numerical results: Inorganic set of parameters

In this section, we will investigate the exciton formation process in the case when material parameters assume values typical of inorganic semiconductors, i.e., relatively large bandwidths, large dielectric constant (weak Coulomb interaction), and weak carrier-phonon interaction. The excitonic spectrum is shown in Fig. 8(a). We see that almost all excitonic bands belong to the pair continuum, except for a couple of lowest bands, which is more clearly seen in the inset of Fig. 8(a). This is an entirely different situation from the one that we encounter

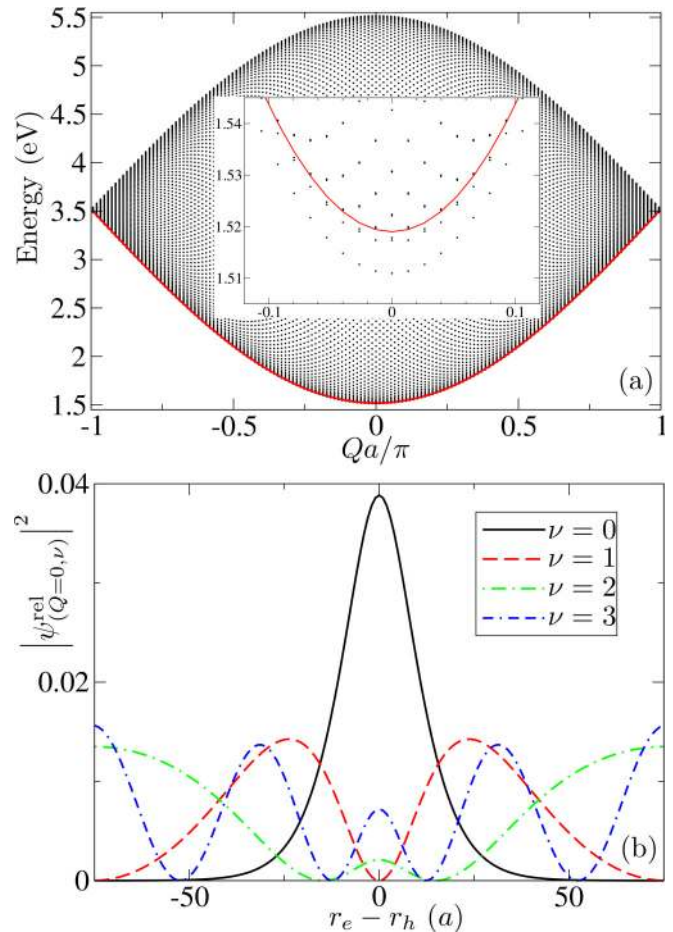


FIG. 8. (Color online) (a) Excitonic spectrum for the inorganic set of parameters. Dots represent individual excitonic states  $(Q, \nu)$ , while thick red line is the boundary between bound and unbound excitonic states computed using Eq. (57). The inset shows the same spectrum in the range of energies around the single-particle gap. (b) Squared modulus of the wave function which describes the relative motion of an electron-hole pair [Eq. (61)] calculated for different states  $(Q = 0, \nu)$ . Mean electron-hole separations are  $9.1a$  ( $\nu = 0$ ) and  $29.4a$  ( $\nu = 1$ ), while states  $(Q = 0, \nu = 2)$  and  $(Q = 0, \nu = 3)$  are not bound. Computations are performed for  $N = 151$ .

for the organic set of parameters, where large energy separation of the lowest excitonic band from the rest of the spectrum was crucial to understand the exciton formation process. As a consequence, excitons in bound states are likely to scatter to a state in the pair continuum, in contrast to the situation for the model parameters representative of an organic semiconductor.

Having noted the important characteristics of the excitonic spectrum, we move on to comment briefly on the exciton size for the inorganic set of parameters. We plot in Fig. 8(b) the squared modulus of the wave function of the relative motion of the pair, which is defined in Eq. (61). We note that for the inorganic set of parameters, electron and hole are not as tightly bound as for the organic set of parameters, which is in accord with the fact that excitons in a typical inorganic semiconductor have large radii, typically of the order of 10 lattice constants [5,6]. From Fig. 8(b), it is also clear that, if we are to see the lowest excitonic state ( $Q = 0, \nu = 0$ ) as a

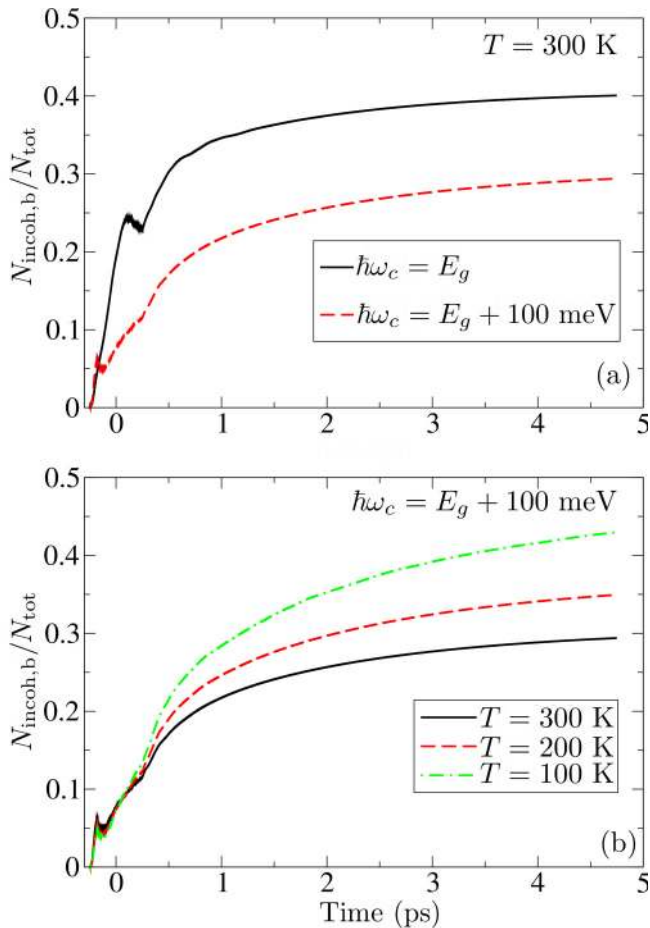


FIG. 9. (Color online) (a) Time dependence of the relative number of incoherent bound excitons for excitation resonant with the single-particle gap and the one which is 100 meV above it. The temperature in both cases is  $T = 300$  K. (b) Time dependence of the relative number of incoherent bound excitons for various temperatures. The central frequency of the laser pulse is 100 meV above the single-particle gap.

bound pair, we should take the system size  $N \gtrsim 120$ . We opted for  $N = 151$  because this value makes a good compromise between the minimal size of the system needed for the results to be numerically accurate and the computational time.

For the inorganic set of parameters, we note that incoherent unbound excitons comprise the major part of the total excitonic population [see Fig. 9(a)], which is different from the case when model parameters assume values representative of an organic semiconductor, when excitons in bound states prevail. Considering an unbound exciton as quasifree electron and hole, we interpret the last observation in the following manner: after an optical excitation of an organic semiconductor, (strongly) bound electron-hole pairs (excitons) are mainly generated, whereas in the case of an inorganic semiconductor an optical excitation predominantly generates (quasi)free charges. In Fig. 9, we also note that for higher central frequency of the laser field, the relative number of bound excitons is lower. However, in the long-time limit the number of incoherent bound excitons should assume the value predicted by the Maxwell-Boltzmann distribution, which is around 36.5%,

irrespective of the central frequency of the pulse. The values of the relative number of incoherent bound excitons at the end of our computations do not strongly deviate from the value predicted by the Maxwell-Boltzmann distribution, in contrast to the situation for the organic set of parameters, where this deviation was more pronounced (see Fig. 2). It can thus be inferred that nonequilibrium features of the semiconductor dynamics after a pulsed excitation are more pronounced for the organic than for the inorganic set of parameters.

Finally, we comment on the temperature dependence of the exciton formation process for the excitation whose central frequency is 100 meV above the single-particle gap. The lower is the temperature, the higher is the relative number of the incoherent bound excitons [see Fig. 9(b)]. During the pulse, higher temperature leads to higher relative number of incoherent bound excitons, which has already been explained in the section dealing with the organic set of parameters. The long-time limit values of the relative number of incoherent bound excitons are 44.7% for  $T = 200$  K and 62.7% for  $T = 100$  K. In all three cases, the dynamics is highly nonequilibrium, but it displays the trend of a slow, but monotonic, approach towards the equilibrium.

#### IV. DISCUSSION

In this section, we discuss the time scales of exciton formation and relaxation processes obtained from our calculations in light of recent subpicosecond time-resolved experiments. In Ref. [23], femtosecond-resolved fluorescence up-conversion spectroscopy was applied to investigate the exciton dynamics in pristine PCDTBT polymer. The results obtained were interpreted to originate from formation of free charges on less than 100 fs time scale, followed by formation of bound excitons in less than 1 ps and their further relaxation at a longer time scale. Similar results were obtained in Ref. [24] for P3HT polymer. Despite the fact that our Hamiltonian does not include the effects of disorder that are present in real materials and uses an oversimplified form of the carrier-phonon interaction, we obtain time scales consistent with these data in our computations. Namely, for the organic parameter set we find that significant population of bound excitons is formed on the time scale of several hundreds of femtoseconds and that their further relaxation occurs for at least several picoseconds. These conclusions are further corroborated by fitting the relative number of incoherent bound excitons  $N_{\text{incoh,b}}/N_{\text{tot}}$  after the carrier generation has been completed to a sum of three exponentially decaying terms. For the organic parameter set, we obtain characteristic time scales of  $\sim 50$  fs,  $\sim 500$  fs and  $\gtrsim 1$  ps. We attribute the fastest time scale to decoherence processes which are responsible for conversion from coherent ( $|y_x|^2$ ) to incoherent ( $\bar{n}_{xx}$ ) populations due to the interaction with phonons. The time scale of  $\sim 500$  fs may be associated with the buildup of the Coulomb-induced correlations between electrons and holes by formation of bound incoherent electron-hole pairs via phonon-assisted scattering processes. After this time scale, however, intraband coherences  $\bar{n}_{\bar{x}x}$  ( $\bar{x} \neq x$ ), as well as single-phonon-assisted density matrices  $n_{\bar{x}x\mu^+}$ , still have significant values. In the long-time limit, these variables asymptotically vanish, and we remain only with incoherent populations whose dynamics will

eventually lead to thermalized distribution of excitons [35]. As our computations are certainly not long enough to observe these effects, we speculate that the slowest time scale we obtain may be related to the decay of the intraband coherences and/or phonon-assisted variables.

Next, we comment on the relation of our results with recent experimental insights which have challenged the commonly accepted physical picture of the generation of free charges in bulk heterojunction solar cells. Namely, it is widely believed that physical processes leading to current generation are formation of bound excitons due to light absorption in the donor material, their diffusion to the donor/acceptor interface, and their subsequent separation at the interface [4]. From the discrepancy between the distance that a donor exciton can diffuse in 100 fs and the distance it has to cover in order to reach the donor/acceptor interface in efficient bulk heterojunction solar cells, Cowan *et al.* [25] conclude that the subpicosecond charge transfer to the acceptor occurs before exciton formation in the donor. The results of our computations, which indicate that the formation of incoherent bound excitons occurs on a  $\sim 500$ -fs time scale, are therefore consistent with their observations. The formation of hot charge transfer excitons which occurs in less than 100 fs and which is followed by their relaxation to lower energies and shorter electron-hole distances on a picosecond time scale was experimentally observed in a small molecule CuPc/fullerene blend using time-resolved second harmonic generation and time-resolved two-photon photoemission [28]. The presence of hot charge transfer excitons, which are delocalized, i.e., in which the electron-hole separation is rather large, and their essential role in subpicosecond charge separation in efficient OPV systems were also identified in Refs. [26,27,29]. Our simulation results that indicate exciton equilibration times longer than picoseconds are fully consistent with observations that during charge separation at the donor/acceptor interface the excitons remain out of equilibrium (hot excitons).

## V. CONCLUSION

In conclusion, we have investigated the exciton dynamics in a photoexcited semiconductor on a picosecond time scale. The study was conducted on the two-band semiconductor Hamiltonian, which includes relevant physical effects in the system, using the density matrix theory combined with the DCT scheme. We truncate the phonon branch of the hierarchy and propose the form of coupling between electronic density matrices with single-phonon assistance and higher-order phonon assistance so as to achieve the compatibility of the resulting equations with the energy and particle-number conservation in a system without external fields. The numerical

study aiming at identifying time scales of exciton formation and relaxation processes was performed on a one-dimensional model system for the values of model parameters representative of a typical organic and inorganic semiconductor. We concluded that the dynamics on a picosecond time scale shows highly nonequilibrium features, relaxation processes towards equilibrium occurring on a longer time scale. While for the organic set of parameters the excitons generated are mainly tightly bound, for the inorganic set of parameters the major part of excitons is in unbound pair states and may thus be considered as (quasi)free electrons and holes. In other words, a photoexcitation of an initially unexcited organic semiconductor leads to creation of bound electron-hole pairs, whereas in an inorganic semiconductor it leads to generation of free charges. This difference can be mainly attributed to different properties of the excitonic spectrum, which for the organic set of parameters exhibits large energy separation between the lowest excitonic band and the rest of the spectrum. Furthermore, although the carrier-phonon interaction is stronger for the organic set of parameters, we have noted that the number of excitons in bound states more strongly deviates from its equilibrium value for the organic set of parameters than for the inorganic one. This observation emphasizes the importance of nonequilibrium effects for the proper understanding of the ultrafast dynamics of photoexcited organic semiconductors and unraveling the working principles of organic photovoltaic devices.

## ACKNOWLEDGMENTS

We gratefully acknowledge the support by Serbian Ministry of Education, Science and Technological Development (Project No. ON171017) and European Community FP7 Marie Curie Career Integration Grant (ELECTROMAT) and the contribution of the COST Action MP1406. Numerical simulations were performed on the PARADOX supercomputing facility at the Scientific Computing Laboratory of the Institute of Physics Belgrade.

## APPENDIX A: EQUATIONS OF MOTION

In this appendix, we present equations of motion for relevant dynamic variables. These are the same equations as in Ref. [35], with only slight modifications in notation, which are exact up to the second order in the external field. We point out that, according to the generating function property, differential equations for the corresponding phonon-assisted density matrices are obtained after performing appropriate differentiations and setting  $\alpha_\mu = \beta_\mu = 0$ :

$$\begin{aligned}
 i\hbar \partial_t Y_{ab}^{\alpha\beta} = & (\epsilon_b^c - \epsilon_a^v) Y_{ab}^{\alpha\beta} + \sum_{\substack{p \in \text{VB} \\ q \in \text{CB}}} (V_{pqba}^{\text{vccv}} - V_{pabq}^{\text{vvcv}}) Y_{pq}^{\alpha\beta} + \sum_{\mu} \hbar\omega_{\mu} (\beta_{\mu} \partial_{\beta_{\mu}} - \alpha_{\mu} \partial_{\alpha_{\mu}}) Y_{ab}^{\alpha\beta} \\
 & + \sum_{\substack{k \in \text{CB} \\ \mu}} (\gamma_{bk}^{\mu} (\partial_{\alpha_{\mu}} + \beta_{\mu}) + \gamma_{kb}^{\mu*} \partial_{\beta_{\mu}}) Y_{ak}^{\alpha\beta} - \sum_{\substack{k \in \text{VB} \\ \mu}} (\gamma_{ka}^{\mu} (\partial_{\alpha_{\mu}} + \beta_{\mu}) + \gamma_{ak}^{\mu*} \partial_{\beta_{\mu}}) Y_{kb}^{\alpha\beta} - \mathbf{E}(t) \mathbf{M}_{ba}^{\text{cv}} F^{\alpha\beta}, \quad (\text{A1})
 \end{aligned}$$

$$\begin{aligned}
i\hbar \partial_t N_{abcd}^{\alpha\beta} &= (\epsilon_d^c - \epsilon_c^v + \epsilon_b^v - \epsilon_a^c) N_{abcd}^{\alpha\beta} + \sum_{\substack{p \in \text{VB} \\ q \in \text{CB}}} ((V_{pqdc}^{\text{vccv}} - V_{pcdq}^{\text{vccv}}) N_{abpq}^{\alpha\beta} - (V_{baqp}^{\text{vccv}} - V_{bpqa}^{\text{vccv}}) N_{qpdc}^{\alpha\beta}) \\
&+ \sum_{\mu} \hbar\omega_{\mu} (\beta_{\mu} \partial_{\beta_{\mu}} - \alpha_{\mu} \partial_{\alpha_{\mu}}) N_{abcd}^{\alpha\beta} + \sum_{\substack{k \in \text{CB} \\ \mu}} ((\gamma_{dk}^{\mu} (\partial_{\alpha_{\mu}} + \beta_{\mu}) + \gamma_{kd}^{\mu*} \partial_{\beta_{\mu}}) N_{abck}^{\alpha\beta} - (\gamma_{ka}^{\mu} \partial_{\alpha_{\mu}} + \gamma_{ak}^{\mu*} (\partial_{\beta_{\mu}} + \alpha_{\mu})) N_{kbcd}^{\alpha\beta}) \\
&- \sum_{\substack{k \in \text{VB} \\ \mu}} ((\gamma_{kc}^{\mu} (\partial_{\alpha_{\mu}} + \beta_{\mu}) + \gamma_{ck}^{\mu*} \partial_{\beta_{\mu}}) N_{abkd}^{\alpha\beta} - (\gamma_{bk}^{\mu} \partial_{\alpha_{\mu}} + \gamma_{kb}^{\mu*} (\partial_{\beta_{\mu}} + \alpha_{\mu})) N_{akcd}^{\alpha\beta}) - \mathbf{E}(t) (\mathbf{M}_{dc}^{\text{cv}} Y_{ba}^{\beta\alpha*} - \mathbf{M}_{ba}^{\text{vc}} Y_{cd}^{\alpha\beta}).
\end{aligned} \tag{A2}$$

## APPENDIX B: CLOSING THE HIERARCHY OF EQUATIONS

In Eq. (33), correlated parts of two-phonon-assisted density matrices  $\delta n_{\bar{x}\bar{x}\rho^+\sigma^-}$  and  $\delta n_{\bar{x}\bar{x}\rho^+\sigma^+}$  appear. In their differential equations, three-phonon-assisted density matrices are present. In order to close the hierarchy of equations, we factorize them into all possible combinations of phonon distribution functions and phonon-assisted electronic density matrices and neglect their correlated parts. The strategy for the factorization is the one we employed in Eq. (31) where we considered an exciton as a basic entity and did not take into account contributions arising from the excitonic amplitude (with possible phonon assistance). Namely, the two-phonon-assisted electronic density matrix  $\langle c_a^\dagger d_b^\dagger d_c c_d b_\mu^\dagger b_\rho \rangle$  can be written in terms of exciton creation and annihilation operators [see Eq. (18)] as  $\sum_{\bar{x}\bar{x}} \psi_{ba}^{\bar{x}*} \psi_{cd}^{\bar{x}} \langle X_{\bar{x}}^\dagger X_{\bar{x}} b_\mu^\dagger b_\rho \rangle$ . Since it appears in the equation of motion for one-phonon-assisted electronic density matrix  $n_{\bar{x}\bar{x}\mu}^{(+)}$ , which is coupled to Eq. (29) describing excitonic populations and intraband coherences, we treat an exciton as a basic entity and accordingly perform the factorization  $\langle X_{\bar{x}}^\dagger X_{\bar{x}} b_\mu^\dagger b_\rho \rangle = \langle X_{\bar{x}}^\dagger X_{\bar{x}} \rangle \langle b_\mu^\dagger b_\rho \rangle + \delta \langle X_{\bar{x}}^\dagger X_{\bar{x}} b_\mu^\dagger b_\rho \rangle$ . In the case of three-phonon-assisted electronic density matrices, the described factorization procedure, neglecting the correlated part, gives

$$\langle c_a^\dagger d_b^\dagger d_c c_d b_\mu^\dagger b_\rho \rangle = \delta_{\rho\sigma} \langle c_a^\dagger d_b^\dagger d_c c_d b_\mu^\dagger \rangle n_\rho^{\text{ph}} + \delta_{\mu\sigma} \langle c_a^\dagger d_b^\dagger d_c c_d b_\rho^\dagger \rangle n_\mu^{\text{ph}}. \tag{B1}$$

Performing transition to the excitonic basis, the following differential equation for the variable  $\delta n_{\bar{x}\bar{x}\rho^+\sigma^-}$  is obtained:

$$\begin{aligned}
\partial_t \delta n_{\bar{x}\bar{x}\rho^+\sigma^-} &= -i(\omega_x - \omega_{\bar{x}} + \omega_\sigma - \omega_\rho) \delta n_{\bar{x}\bar{x}\rho^+\sigma^-} + \frac{1 + n_\sigma^{\text{ph}}}{i\hbar} \sum_{x'} \Gamma_{xx'}^\sigma n_{\bar{x}\bar{x}'\rho^+} - \frac{n_\sigma^{\text{ph}}}{i\hbar} \sum_{\bar{x}'} \Gamma_{\bar{x}'\bar{x}}^\sigma n_{\bar{x}'\bar{x}\rho^+} \\
&- \frac{1 + n_\rho^{\text{ph}}}{i\hbar} \sum_{\bar{x}'} \Gamma_{\bar{x}\bar{x}'}^{\rho*} n_{x\bar{x}'\sigma^+} + \frac{n_\rho^{\text{ph}}}{i\hbar} \sum_{x'} \Gamma_{x'\bar{x}}^{\rho*} n_{x'\bar{x}\sigma^+},
\end{aligned} \tag{B2}$$

and similarly for the variable  $\delta n_{\bar{x}\bar{x}\rho^+\sigma^+}$ . Solving Eq. (B2) in the Markov and adiabatic approximations [39,40], the following result is obtained:

$$\begin{aligned}
\delta n_{\bar{x}\bar{x}\rho^+\sigma^-} &= (1 + n_\sigma^{\text{ph}}) \sum_{x'} \Gamma_{xx'}^\sigma \mathcal{D}(\hbar\omega_{x'} - \hbar\omega_x - \hbar\omega_\sigma) n_{\bar{x}\bar{x}'\rho^+} - n_\sigma^{\text{ph}} \sum_{\bar{x}'} \Gamma_{\bar{x}'\bar{x}}^\sigma \mathcal{D}(\hbar\omega_{\bar{x}} - \hbar\omega_{\bar{x}'} - \hbar\omega_\sigma) n_{\bar{x}'\bar{x}\rho^+} \\
&+ (1 + n_\rho^{\text{ph}}) \sum_{\bar{x}'} \Gamma_{\bar{x}\bar{x}'}^{\rho*} \mathcal{D}^*(\hbar\omega_{\bar{x}'} - \hbar\omega_{\bar{x}} - \hbar\omega_\rho) n_{x\bar{x}'\sigma^+} - n_\rho^{\text{ph}} \sum_{x'} \Gamma_{x'\bar{x}}^{\rho*} \mathcal{D}^*(\hbar\omega_x - \hbar\omega_{x'} - \hbar\omega_\rho) n_{x'\bar{x}\sigma^+},
\end{aligned} \tag{B3}$$

where  $\mathcal{D}(\epsilon) = -i\pi\delta(\epsilon) + \mathcal{P}(1/\epsilon)$ . We thus expressed two-phonon-assisted electronic density matrices in terms of one-phonon-assisted electronic density matrices. When these results are inserted in Eq. (33), we neglect all terms involving principal values which, in principle, lead to polaron shifts in energies [9,40]. Furthermore, we note that the inserted terms involve multiple summations over excitonic indices  $x$  and we use the random phase approximation to simplify the expression obtained. This approximation is easier to understand and justify when we transfer to a particular representation for the excitonic index  $x$ , for example, the one that we used in our computational study, where we took advantage of the translational symmetry and had  $x = (Q, \nu)$ . Electronic density matrices with one-phonon assistance  $n_{(\bar{Q}, \bar{\nu})(Q, \nu)q_\mu^\pm}$  are complex quantities, which acquire nontrivial values during the evolution provided that the condition  $\bar{Q} + q_\mu = Q$  is satisfied. Having in mind the selection rule for carrier-phonon matrix elements in the excitonic basis [see Eq. (52)], we can express the first term which describes the coupling of the one-phonon-assisted electronic density matrix  $n_{(Q-q_\mu, \bar{\nu})(Q, \nu)q_\mu^\pm}$  to density matrices with higher phonon assistance [see Eq. (33)] as

$$\begin{aligned}
& - \frac{1}{i\hbar} \sum_{\rho\bar{x}'} \Gamma_{\bar{x}\bar{x}'}^{\rho*} \delta n_{\bar{x}'\bar{x}\mu^+\rho^-} \\
& = \frac{\pi}{\hbar} \sum_{q_\rho, \nu', \bar{\nu}'} \Gamma_{(Q-q_\mu, \bar{\nu})(Q-q_\mu+q_\rho, \bar{\nu}')}^{q_\rho*} \Gamma_{(Q, \nu)(Q+q_\rho, \nu')}^{q_\rho} (1 + n_{q_\rho}^{\text{ph}}) \delta(\hbar\omega_{(Q+q_\rho, \nu')} - \hbar\omega_{(Q, \nu)} - \hbar\omega_{q_\rho}) n_{(Q-q_\mu+q_\rho, \bar{\nu}')(Q+q_\rho, \nu')q_\mu^\pm}
\end{aligned}$$

$$\begin{aligned}
& -\frac{\pi}{\hbar} \sum_{q_\rho, \bar{v}', \bar{v}''} \Gamma_{(Q-q_\mu, \bar{v})(Q-q_\mu+q_\rho, \bar{v}')}^{q_\rho*} \Gamma_{(Q-q_\mu, \bar{v}'')(Q-q_\mu+q_\rho, \bar{v}'')}^{q_\rho} n_{q_\rho}^{\text{ph}} \delta(\hbar\omega_{(Q-q_\mu+q_\rho, \bar{v}')} - \hbar\omega_{(Q-q_\mu, \bar{v}'')} - \hbar\omega_{q_\rho}) n_{(Q-q_\mu, \bar{v}'')(Q, v)q_\mu^+} \\
& -\frac{\pi}{\hbar} \sum_{q_\rho, \bar{v}', \bar{v}''} \Gamma_{(Q-q_\mu, \bar{v})(Q-q_\mu+q_\rho, \bar{v}')}^{q_\rho*} \Gamma_{(Q-q_\mu+q_\rho, \bar{v}')(Q+q_\rho, \bar{v}'')}^{q_\mu*} (1 + n_{q_\mu}^{\text{ph}}) \delta(\hbar\omega_{(Q+q_\rho, \bar{v}'')} - \hbar\omega_{(Q-q_\mu+q_\rho, \bar{v}')} - \hbar\omega_{q_\mu}) n_{(Q, v)(Q+q_\rho, \bar{v}'')q_\mu^+}^* \\
& +\frac{\pi}{\hbar} \sum_{q_\rho, \bar{v}', \bar{v}''} \Gamma_{(Q-q_\mu, \bar{v})(Q-q_\mu+q_\rho, \bar{v}')}^{q_\rho*} \Gamma_{(Q-q_\mu, \bar{v}')(Q, v)}^{q_\mu*} n_{q_\mu}^{\text{ph}} \delta(\hbar\omega_{(Q, v)} - \hbar\omega_{(Q-q_\mu, \bar{v}')} - \hbar\omega_{q_\mu}) n_{(Q-q_\mu, \bar{v}')(Q-q_\mu+q_\rho, \bar{v}'')q_\mu^+}^*. \tag{B4}
\end{aligned}$$

In the first, the third, and the fourth sums in the previous equation we perform summation of terms which involve complex-valued single-phonon-assisted electronic density matrices over the wave vector  $q_\rho$ , whereas in the second sum the summation is not carried out over any of the wave vectors describing the density matrix. In the lowest approximation, we can assume that all the sums apart from the second are negligible due to random phases at different wave vectors. For the sake of simplicity, in the second sum we keep only the contribution for  $\bar{v}'' = \bar{v}$ , thus expressing the coupling to higher-phonon-assisted density matrices only in terms of the single-phonon-assisted density matrix for which the equation is formed. Restoring the more general notation, we obtain the result

$$-\frac{1}{i\hbar} \sum_{\rho\bar{x}'} \Gamma_{\bar{x}\bar{x}}^{\rho*} \delta n_{\bar{x}'x\mu^+\rho^-} = -\frac{\pi}{\hbar} \left( \sum_{\rho\bar{x}} |\Gamma_{\bar{x}\bar{x}}^\rho|^2 n_\rho^{\text{ph}} \delta(\hbar\omega_{\bar{x}} - \hbar\omega_{\bar{x}} + \hbar\omega_\rho) \right) n_{\bar{x}x\mu^+}. \tag{B5}$$

Repeating similar procedure with the remaining three terms which describe coupling to density matrices with higher-order phonon assistance in Eq. (33), we obtain the result embodied in Eqs. (36)–(38).

Analogously, the following results for two-phonon-assisted electronic density matrices  $\delta y_{x\rho^+\sigma^-}, \delta y_{x\rho^+\sigma^+}$  are obtained, solving their respective differential equations in the Markov and adiabatic approximations

$$\delta y_{x\rho^+\sigma^-} = (1 + n_\sigma^{\text{ph}}) \sum_{x'} \Gamma_{xx'}^\sigma \mathcal{D}(\hbar\omega_{x'} - \hbar\omega_x - \hbar\omega_\sigma) y_{x'\rho}^{(+)} - n_\rho^{\text{ph}} \sum_{x'} \Gamma_{x'x}^{\rho*} \mathcal{D}^*(\hbar\omega_x - \hbar\omega_{x'} - \hbar\omega_\rho) y_{x'\sigma}^{(-)}, \tag{B6}$$

and similarly for the variable  $\delta y_{x\rho^+\sigma^+}$ . Inserting the results obtained in Eqs. (34) and (35) and performing the random phase approximation as described, the result given in Eqs. (41) and (42) is obtained.

### APPENDIX C: COMMENTS ON THE ENERGY CONSERVATION IN THE MODEL

In this appendix, we will comment on the energy conservation in the model after the external field has vanished. Using Eqs. (21), (22), (29), and (30), we obtain the rate at which the energy of carriers and phonons changes after the pulse

$$\partial_t (\mathcal{E}_c + \mathcal{E}_{\text{ph}}) = -\frac{2}{\hbar} \sum_{\mu\bar{x}x} (\hbar\omega_x - \hbar\omega_{\bar{x}} - \hbar\omega_\mu) \text{Im} \{ \Gamma_{\bar{x}x}^\mu n_{\bar{x}x\mu^+} \}, \tag{C1}$$

which exactly cancels the part from  $\partial_t \mathcal{E}_{c\text{-ph}}$  [see Eq. (23)] that originates from the free rotation term  $-i(\omega_x - \omega_{\bar{x}} - \omega_\mu) n_{\bar{x}x\mu^+}$  in Eq. (33). The terms in  $\partial_t \mathcal{E}_{c\text{-ph}}$  which arise from the second and third terms in Eq. (33) are identically equal to zero each since they are purely real, which is easily checked. Therefore, the rate at which the total energy changes after the pulse is equal to the rate at which the carrier-phonon interaction energy changes due to the coupling of single-phonon-assisted to higher-order phonon-assisted density matrices,  $(\partial_t \mathcal{E}_{c\text{-ph}})_{\text{higher}}$ , which is equal to [see Eq. (33)]

$$\begin{aligned}
(\partial_t \mathcal{E}_{c\text{-ph}})_{\text{higher}} = & -\frac{2}{\hbar} \text{Im} \left\{ \sum_{\substack{\mu\bar{x}x \\ \rho\bar{x}'}} \Gamma_{\bar{x}x}^\mu \Gamma_{\bar{x}\bar{x}'}^{\rho*} \delta n_{\bar{x}'x\mu^+\rho^-} \right\} - \frac{2}{\hbar} \text{Im} \left\{ \sum_{\substack{\mu\bar{x}x \\ \rho\bar{x}'}} \Gamma_{\bar{x}x}^\mu \Gamma_{\bar{x}'\bar{x}}^\rho \delta n_{\bar{x}'x\mu^+\rho^+} \right\} \\
& + \frac{2}{\hbar} \text{Im} \left\{ \sum_{\substack{\mu\bar{x}x \\ \rho\bar{x}'}} \Gamma_{\bar{x}x}^\mu \Gamma_{x'x}^{\rho*} \delta n_{\bar{x}x'\mu^+\rho^-} \right\} + \frac{2}{\hbar} \text{Im} \left\{ \sum_{\substack{\mu\bar{x}x \\ \rho\bar{x}'}} \Gamma_{\bar{x}x}^\mu \Gamma_{xx'}^\rho \delta n_{\bar{x}x'\mu^+\rho^+} \right\}. \tag{C2}
\end{aligned}$$

The first and the third terms on the right-hand side of Eq. (C2) are separately equal to zero (since the quantities under the sign of the imaginary part are purely real), whereas the second and the fourth terms exactly cancel each other, so the total energy is conserved. In particular, this is true for the form of the correlated parts of two-phonon-assisted density matrix  $\delta n_{\bar{x}x\rho^+\sigma^-}$  given in Eq. (B3) and the similar form of the density matrix  $\delta n_{\bar{x}x\rho^+\sigma^+}$ . In Eq. (C2), all the sums are performed over all indices that are present in a particular expression, so the crux of the proof that the energy is conserved is the interchange of dummy indices combined with the properties  $\delta n_{\bar{x}x\rho^+\sigma^-}^* = \delta n_{x\bar{x}\sigma^+\rho^-}$  and  $\delta n_{\bar{x}x\rho^+\sigma^+} = \delta n_{x\bar{x}\sigma^+\rho^+}$ . However, when we apply the random phase approximation, the aforementioned properties are lost and the energy is not conserved any more. For example,

the first term on the right-hand side in Eq. (C2) after performing the random phase approximation is not equal to zero, but to  $-\frac{2\pi}{\hbar}(\sum_{\rho\bar{x}}|\Gamma_{\bar{x}\bar{x}}^{\rho}|^2n_{\rho}^{\text{ph}}\delta(\hbar\omega_{\bar{x}}-\hbar\omega_{\bar{x}}+\hbar\omega_{\rho}))\text{Re}\{\sum_{\mu\bar{x}x}\Gamma_{\bar{x}x}^{\mu}n_{\bar{x}x\mu^+}\}$  [see Eq. (B5)], which is just one term of the total rate  $(\partial_t \mathcal{E}_{\text{c-ph}})_{\text{higher}}$  when we use the result from Eq. (36).

- 
- [1] W. Tress, *Organic Solar Cells: Theory, Experiment, and Device Simulation*, Vol. 208 (Springer, Berlin, 2014).
- [2] C. Deibel and V. Dyakonov, *Rep. Prog. Phys.* **73**, 096401 (2010).
- [3] J.-L. Brédas, J. E. Norton, J. Cornil, and V. Coropceanu, *Acc. Chem. Res.* **42**, 1691 (2009).
- [4] T. M. Clarke and J. R. Durrant, *Chem. Rev.* **110**, 6736 (2010).
- [5] R. S. Knox, *Theory of Excitons* (Academic, New York, 1963).
- [6] J. Singh and H. E. Ruda, in *Optical Properties of Condensed Matter*, edited by J. Singh (Wiley, Hoboken, NJ, 2006).
- [7] V. M. Axt and T. Kuhn, *Rep. Prog. Phys.* **67**, 433 (2004).
- [8] H. Bässler and A. Köhler, in *Unimolecular and Supramolecular Electronics I*, edited by R. M. Metzger (Springer, Berlin, 2012).
- [9] T. Kuhn, in *Theory of Transport Properties of Semiconductor Nanostructures*, edited by E. Schöll (Chapman and Hall, London, 1998).
- [10] F. Rossi and T. Kuhn, *Rev. Mod. Phys.* **74**, 895 (2002).
- [11] H. Haug and A.-P. Jauho, *Quantum Kinetics in Transport and Optics of Semiconductors* (Springer, Berlin, 1996).
- [12] P. E. Selbmann, M. Gulia, F. Rossi, E. Molinari, and P. Lugli, *Phys. Rev. B* **54**, 4660 (1996).
- [13] M. Gulia, F. Rossi, E. Molinari, P. E. Selbmann, and P. Lugli, *Phys. Rev. B* **55**, R16049 (1997).
- [14] M. Kira and S. Koch, *Prog. Quantum Electron.* **30**, 155 (2006).
- [15] M. Kira and S. Koch, *Semiconductor Quantum Optics* (Cambridge University Press, New York, 2012).
- [16] M. Kira, W. Hoyer, T. Stroucken, and S. W. Koch, *Phys. Rev. Lett.* **87**, 176401 (2001).
- [17] W. Hoyer, M. Kira, and S. Koch, *Phys. Status Solidi B* **234**, 195 (2002).
- [18] W. Hoyer, M. Kira, and S. W. Koch, *Phys. Rev. B* **67**, 155113 (2003).
- [19] M. N. Kobrak and E. R. Bittner, *Phys. Rev. B* **62**, 11473 (2000).
- [20] K. Tandon, S. Ramasesha, and S. Mazumdar, *Phys. Rev. B* **67**, 045109 (2003).
- [21] N. S. Sariciftci, L. Smilowitz, A. J. Heeger, and F. Wudl, *Science* **258**, 1474 (1992).
- [22] I.-W. Hwang, D. Moses, and A. J. Heeger, *J. Phys. Chem. C* **112**, 4350 (2008).
- [23] N. Banerji, S. Cowan, M. Leclerc, E. Vauthey, and A. J. Heeger, *J. Am. Chem. Soc.* **132**, 17459 (2010).
- [24] N. Banerji, S. Cowan, E. Vauthey, and A. J. Heeger, *J. Phys. Chem. C* **115**, 9726 (2011).
- [25] S. R. Cowan, N. Banerji, W. L. Leong, and A. J. Heeger, *Adv. Funct. Mater.* **22**, 1116 (2012).
- [26] G. Grancini, M. Maiuri, D. Fazzi, A. Petrozza, H.-J. Egelhaaf, D. Brida, G. Cerullo, and G. Lanzani, *Nat. Mater.* **12**, 29 (2013).
- [27] A. A. Bakulin, A. Rao, V. G. Pavelyev, P. H. M. van Loosdrecht, M. S. Pshenichnikov, D. Niedzialek, J. Cornil, D. Beljonne, and R. H. Friend, *Science* **335**, 1340 (2012).
- [28] A. E. Jailaubekov, A. P. Willard, J. R. Tritsch, W.-L. Chan, N. Sai, R. Gearba, L. G. Kaake, K. J. Williams, K. Leung, P. J. Rossky, and X.-Y. Zhu, *Nat. Mater.* **12**, 66 (2013).
- [29] S. Gélinas, A. Rao, A. Kumar, S. L. Smith, A. W. Chin, J. Clark, T. S. van der Poll, G. C. Bazan, and R. H. Friend, *Science* **343**, 512 (2014).
- [30] V. Axt and A. Stahl, *Z. Phys. B* **93**, 195 (1994).
- [31] V. Axt and A. Stahl, *Z. Phys. B* **93**, 205 (1994).
- [32] K. Siantidis, V. M. Axt, and T. Kuhn, *Phys. Rev. B* **65**, 035303 (2001).
- [33] K. Siantidis, V. Axt, J. Wühr, and T. Kuhn, *Phys. Status Solidi A* **190**, 743 (2002).
- [34] K. Siantidis, T. Wolterink, V. Axt, and T. Kuhn, *Phys. B (Amsterdam)* **314**, 220 (2002).
- [35] V. M. Axt and S. Mukamel, *Rev. Mod. Phys.* **70**, 145 (1998).
- [36] E. Hanamura and H. Haug, *Phys. Rep.* **33**, 209 (1977).
- [37] M. Combescot and W. Pogosov, *Phys. Rev. B* **77**, 085206 (2008).
- [38] V. M. Axt, K. Victor, and A. Stahl, *Phys. Rev. B* **53**, 7244 (1996).
- [39] T. Kuhn and F. Rossi, *Phys. Rev. B* **46**, 7496 (1992).
- [40] J. Schilp, T. Kuhn, and G. Mahler, *Phys. Rev. B* **50**, 5435 (1994).
- [41] J. Schilp, T. Kuhn, and G. Mahler, *Phys. Status Solidi B* **188**, 417 (1995).
- [42] W. M. Zhang, T. Meier, V. Chernyak, and S. Mukamel, *Phys. Rev. B* **60**, 2599 (1999).
- [43] W. Huhn and A. Stahl, *Phys. Status Solidi B* **124**, 167 (1984).
- [44] *Handbook Series on Semiconductor Parameters*, Vol. 1, edited by M. Levinshtein, S. Rumyantsev, and M. Shur (World Scientific, Singapore, 1996).
- [45] Y.-C. Cheng and R. J. Silbey, *J. Chem. Phys.* **128**, 114713 (2008).
- [46] M. Pope and C. E. Swenberg, *Electronic Processes in Organic Crystals and Polymers* (Oxford University Press, Oxford, 1999).
- [47] P. Cudazzo, F. Sottile, A. Rubio, and M. Gatti, *J. Phys.: Condens. Matter* **27**, 113204 (2015).
- [48] A. Troisi and G. Orlandi, *Phys. Rev. Lett.* **96**, 086601 (2006).
- [49] K. Fujii, S. Kera, M. Oiwa, K. K. Okudaira, K. Sakamoto, and N. Ueno, *Surf. Sci.* **601**, 3765 (2007).

**Nonequilibrium optical conductivity in materials with localized electronic states**

Veljko Janković\* and Nenad Vukmirović†

*Scientific Computing Laboratory, Institute of Physics Belgrade, University of Belgrade, Pregrevica 118, 11080 Belgrade, Serbia*

(Received 8 September 2014; revised manuscript received 20 November 2014; published 1 December 2014)

A wide range of disordered materials contain electronic states that are spatially well localized. In this work, we investigated the electrical response of such systems in nonequilibrium conditions to external electromagnetic field. We obtained the expression for optical conductivity valid for any nonequilibrium state of electronic subsystem. In the case of incoherent nonequilibrium state, this expression contains only the positions of localized electronic states, Fermi's golden rule transition probabilities between the states, and the populations of electronic states. The same form of expression is valid both in the case of weak electron-phonon interaction and weak electron-impurity interaction that act as perturbations of electronic Hamiltonian. The derivation was performed by expanding the general expression for ac conductivity in powers of small electron-phonon interaction or electron-impurity interaction parameter. Applications of the expression to two model systems, a simple one-dimensional Gaussian disorder model, and the model of a realistic three-dimensional organic polymer material, were presented as well.

DOI: [10.1103/PhysRevB.90.224201](https://doi.org/10.1103/PhysRevB.90.224201)

PACS number(s): 72.80.Ng, 72.80.Le

**I. INTRODUCTION**

Electronic transport in semiconductors has been attracting significant research attention for more than half a century. Particular classes of semiconductors where interesting physical effects arise in electronic transport are semiconductors where a certain type of disorder is present in the system which leads to localization of electronic states. These include amorphous inorganic semiconductors (such as amorphous Si or Ge) [1], inorganic crystals doped with randomly positioned impurities [2,3], and organic semiconductors based on conjugated polymers or small molecules [4–10]. The latter class of materials triggered a particular interest in the past two decades due to their low production cost, which led to the development of a variety of organic electronic devices [11–17].

There is currently a solid understanding of equilibrium electronic transport in disordered systems with localized electronic states. dc transport in such systems can be modeled using an equivalent network of resistors that connect each two sites where electronic states are localized [18,19]. Electronic conductivity or mobility in the material can then be calculated by finding the equivalent resistance of the network or estimated using percolation theory. However, dc mobility which quantifies electronic transport properties over long length scales is in many cases not the most relevant quantity when the description of electronic transport processes is concerned. In particular, in organic solar cells based on a bulk heterojunction of two organic semiconductors, charge carriers travel over very short length (on the order of nanometers) and time (on the order of picoseconds) scales before they reach the interface of two semiconductors [20–22]. The high frequency (terahertz) ac mobility is a much better measure of charge transport over such short time scales.

The approaches for simulation of ac conductivity are usually based on Kubo's formula which expresses the ac conductivity in terms of the mean square displacement of a diffusing carrier [23–27]. Such approaches therefore assume

that carriers are in equilibrium and that they are only slightly perturbed by external alternating electric field. However, in many realistic situations, the carriers are not in equilibrium; a typical example concerns the carriers created by external optical excitation across the band gap of a semiconductor. While general approaches for the treatment of nonequilibrium electronic transport, such as the density matrix formalism [28] or the nonequilibrium Green's function formalism [29–31], do exist, it is in practice quite difficult to apply them to disordered materials, where one needs to consider large portions of material to obtain reliable information about its properties.

The main goal of this work was to derive a simple expression that relates the optical conductivity of a material with localized electronic states to its microscopic parameters. To accomplish this goal, we first derive in Sec. II the relation between nonequilibrium optical conductivity and the corresponding current-current correlation function. Then, in Sec. III we derive an expression for the conductivity of the system of localized states with electron-phonon interaction that acts as perturbation valid for arbitrary nonequilibrium state of the electronic subsystem. In the case of incoherent nonequilibrium state, the obtained expression appears to have a rather simple form—the only quantities that appear in it are the positions of localized states, their populations, and the phonon-induced transition probabilities between the states. In Sec. IV we show that the same expression is obtained if additional static potential acts as a perturbation. In Sec. V, we present the results obtained from the application of the derived formula to a simple one-dimensional hopping model and to a realistic disordered conjugated polymer material. We discuss our results in light of the other results that exist in the literature in Sec. VI.

**II. GENERAL EXPRESSION FOR NONEQUILIBRIUM OPTICAL CONDUCTIVITY**

In this section, we consider an arbitrary quantum system described by the Hamiltonian  $\hat{H}$  whose state is given by the statistical operator  $\hat{\rho}(t)$ . We will derive the time evolution of  $\hat{\rho}(t)$  due to a weak external perturbation  $\hat{H}'(t)$  which is turned on at  $t = 0$ . Next, for the system that contains charged

\*veljko.jankovic@ipb.ac.rs

†nenad.vukmirovic@ipb.ac.rs

particles, we will find the current density caused by external electric field that acts as a perturbation. While the results of this section are mostly available in the literature, we repeat them here for completeness of the paper, as well as to introduce the notation and terminology for the remainder of the paper.

### A. Evolution of the density matrix

The equation for the density matrix  $\hat{\rho}(t)$  describing the state of the system for  $t > 0$  is

$$i\hbar \frac{d\hat{\rho}(t)}{dt} = [\hat{H} + \hat{H}'(t), \hat{\rho}(t)]. \quad (1)$$

We search for the solution of Eq. (1) in the form  $\hat{\rho}(t) = \hat{\rho}_{\text{free}}(t) + \hat{f}(t)$ , where

$$\hat{\rho}_{\text{free}}(t) = e^{-i\frac{\hat{H}}{\hbar}t} \hat{\rho}(0) e^{i\frac{\hat{H}}{\hbar}t} \quad (2)$$

is the statistical operator of the system in the absence of external perturbation,  $\hat{\rho}(0)$  is the statistical operator describing the state of the system just before the external perturbation is turned on, while  $\hat{f}(t)$  is the contribution to the statistical operator due to linear response of the system. It satisfies the differential equation

$$i\hbar \frac{d\hat{f}(t)}{dt} - [\hat{H}, \hat{f}(t)] = [\hat{H}'(t), \hat{\rho}_{\text{free}}(t)], \quad (3)$$

with the initial condition  $\hat{f}(0) = \hat{0}$ . After solving the last equation up to linear terms, we obtain [32]

$$\hat{\rho}(t) = e^{-i\frac{\hat{H}}{\hbar}t} \hat{\rho}(0) e^{i\frac{\hat{H}}{\hbar}t} + \frac{1}{i\hbar} e^{-i\frac{\hat{H}}{\hbar}t} \int_0^t dt' [\hat{H}'(t'), \hat{\rho}(0)] e^{i\frac{\hat{H}}{\hbar}t'}, \quad (4)$$

where  $\hat{H}'_I(t) = e^{i\frac{\hat{H}}{\hbar}t} \hat{H}'(t) e^{-i\frac{\hat{H}}{\hbar}t}$ . Equations given in this section are strictly valid only for an isolated quantum system and do not include the relaxation of the system from some nonequilibrium to the equilibrium state. In realistic systems, interaction of the system with the environment leads to relaxation of the system to the equilibrium state. Therefore, the equations that we will derive are valid only if the characteristic time of external perturbation is short compared to the relaxation time  $\tau$ . Since we shall study the response to the electric field oscillating with a frequency  $\omega$ , the aforementioned condition reads

$$\omega\tau \gg 1. \quad (5)$$

In that case, the relaxation of the system towards equilibrium during one period of the perturbation is negligible and can be ignored in the considerations.

### B. Nonequilibrium optical conductivity

Next, we assume that the system contains mobile charged particles and that external electric field acts as a perturbation. The system responds to external electric field by nonzero value of current density. The current density operator is given by [33]

$$\hat{j}_a(\mathbf{r}) = \frac{1}{2m} \sum_n q(\hat{\mathbf{p}}_n \delta^{(3)}(\mathbf{r} - \hat{\mathbf{r}}_n) + \delta^{(3)}(\mathbf{r} - \hat{\mathbf{r}}_n) \hat{\mathbf{p}}_n)_a, \quad (6)$$

where  $q$  and  $m$  are the charge and the mass of a carrier, respectively, while  $\hat{\mathbf{p}}_n$  and  $\hat{\mathbf{r}}_n$  are the momentum and the

position operator for a single carrier, and  $a$  denotes the component of the current density operator ( $x$ ,  $y$ , or  $z$ ). Using Eq. (4), we find that the current density at time  $t$  is given as

$$\begin{aligned} \langle \hat{j}_a(\mathbf{r}) \rangle_t &= \text{Tr}(\hat{\rho}(t) \hat{j}_a(\mathbf{r})) \\ &= \text{Tr}(\hat{\rho}(0) \hat{j}_a(t, \mathbf{r})) \\ &\quad + \frac{1}{i\hbar} \int_0^t dt' \text{Tr}(\hat{\rho}(0) [\hat{j}_a(t, \mathbf{r}), \hat{H}'_I(t')]), \end{aligned} \quad (7)$$

where  $\hat{j}_a(t, \mathbf{r}) = e^{i\frac{\hat{H}}{\hbar}t} \hat{j}_a(\mathbf{r}) e^{-i\frac{\hat{H}}{\hbar}t}$ . The first term in Eq. (7) does not depend on the electric field, while we are interested in the response of the system to the applied electric field. Consequently, we shall further only consider the second term in Eq. (7) given as

$$\mathcal{J}_a(t, \mathbf{r}) = \frac{1}{i\hbar} \int_0^t dt' \text{Tr}(\hat{\rho}(0) [\hat{j}_a(t, \mathbf{r}), \hat{H}'_I(t')]). \quad (8)$$

We shall also assume that we are dealing with a spatially homogeneous system at the macroscopic scale. The current density averaged over the volume of the system

$$\mathcal{J}_a(t) = \frac{1}{V} \int d^3\mathbf{r} \mathcal{J}_a(t, \mathbf{r}) \quad (9)$$

will be considered as the response to the applied field. The Hamiltonian of interaction with electric field  $\mathbf{E}(t)$  is given as [34]

$$\hat{H}'(t) = -\hat{\mathbf{\Pi}} \cdot \mathbf{E}(t), \quad (10)$$

where  $\hat{\mathbf{\Pi}}$  is the electric dipole moment operator defined as

$$\hat{\mathbf{\Pi}} = q \sum_n \hat{\mathbf{r}}_n. \quad (11)$$

Using Eqs. (9), (8), and (10), the quantity  $\mathcal{J}_a(t)$  can be expressed as

$$\mathcal{J}_a(t) = \int_0^t dt' \sigma_{ab}(t, t') E_b(t'), \quad (12)$$

where the tensor

$$\sigma_{ab}(t, t') = \frac{i}{\hbar V} \text{Tr}(\hat{\rho}(0) [\hat{J}_a(t), \hat{\Pi}_b(t')]) \quad (13)$$

describes the linear response to the applied electric field. In Eq. (13), the operator  $\hat{J}_a(t)$  is defined as

$$\hat{J}_a(t) = \int d^3\mathbf{r} \hat{j}_a(t, \mathbf{r}) = \frac{q}{m} \sum_n (\hat{\mathbf{p}}_n)_a. \quad (14)$$

The operators  $\hat{\Pi}_a(t)$  and  $\hat{J}_b(t)$  satisfy the equal time commutation relation

$$[\hat{\Pi}_a(t), \hat{J}_b(t)] = i\hbar \frac{Nq^2}{m} \delta_{ab}, \quad (15)$$

where  $N$  is the number of carriers, and the continuity equation

$$\hat{j}_a(t) = \frac{d}{dt} \hat{\Pi}_a(t). \quad (16)$$

When the condition

$$[\hat{\rho}(0), \hat{H}] = \hat{0} \quad (17)$$

is satisfied, the tensor  $\sigma_{ab}(t, t')$  defined in Eq. (13) does not depend separately on  $t$  and  $t'$ , but only on their difference

$u = t - t'$ . The optical conductivity tensor can then be defined as  $\sigma_{ab}(\omega) = \int_0^{+\infty} du \sigma_{ab}(u) e^{i\omega u}$  and reads

$$\sigma_{ab}(\omega) = \frac{i}{\hbar V} \int_0^{+\infty} dt e^{i\omega t} \text{Tr}(\hat{\rho}(0)[\hat{J}_a(t), \hat{\Pi}_b(0)]). \quad (18)$$

Using Eqs. (16) and (15), Eq. (18) can be cast into a more familiar form ( $n = N/V$  is the concentration of carriers)

$$\sigma_{ab}(\omega) = i \frac{nq^2}{m\omega} \delta_{ab} + \frac{1}{\hbar\omega V} \int_0^{+\infty} dt e^{i\omega t} \times \text{Tr}(\hat{\rho}(0)[\hat{J}_a(t), \hat{J}_b(0)]). \quad (19)$$

The equation for the optical conductivity (19) can be considered as a generalization to the nonequilibrium stationary case of well-known results [35] which relate optical conductivity to the equilibrium current-current correlation function. Generalizations of this sort have already been proposed in the literature [in the context of the fluctuation-dissipation theorem, which relates the dissipative part of the optical conductivity to the (non)equilibrium current fluctuations] [36,37].

In the case, when  $[\hat{\rho}(0), \hat{H}] \neq \hat{0}$ , the tensor  $\sigma_{ab}(t, t')$  defined in Eq. (13) depends separately on  $t$  and  $t'$

$$\sigma_{ab}(t, t') = -\frac{1}{i\hbar V} \text{Tr}(e^{-\frac{i}{\hbar}\hat{H}t} \hat{\rho}(0) e^{\frac{i}{\hbar}\hat{H}t'} [\hat{J}_a(0), \hat{\Pi}_b(-(t-t'))]). \quad (20)$$

Using Eqs. (16) and (15), one obtains the following expression:

$$\sigma_{ab}(t, t') = \frac{nq^2}{m} \delta_{ab} - \frac{i}{\hbar V} \int_0^{t-t'} d\tau \times \text{Tr}(e^{-\frac{i}{\hbar}\hat{H}(t-\tau)} \hat{\rho}(0) e^{\frac{i}{\hbar}\hat{H}(t-\tau)} [\hat{J}_a(\tau), \hat{J}_b(0)]). \quad (21)$$

### III. OPTICAL CONDUCTIVITY IN THE PRESENCE OF ELECTRON-PHONON INTERACTION

In this section, we derive the expression for optical conductivity of a system with localized electronic states in the presence of weak electron-phonon interaction. In Sec. III A we introduce the Hamiltonian of the system, derive the current operator, and obtain the frequency-time representation of the conductivity tensor. In Sec. III B, we derive the expression for conductivity valid for the arbitrary reduced density matrix of the electronic subsystem and in the limit of low carrier concentration. For incoherent density matrix of the electronic subsystem, this expression contains only the populations of single-particle electronic states, their spatial positions, and Fermi's golden rule transition probabilities between these states.

#### A. Model Hamiltonian and preliminaries

We consider the system of electrons and phonons described by the Hamiltonian

$$\hat{H} = \hat{H}_0 + \hat{H}_{\text{e-ph}} = \hat{H}_e + \hat{H}_{\text{ph}} + \hat{H}_{\text{e-ph}}, \quad (22)$$

where

$$\hat{H}_0 = \hat{H}_e + \hat{H}_{\text{ph}} = \sum_{\alpha} \epsilon_{\alpha} \hat{c}_{\alpha}^{\dagger} \hat{c}_{\alpha} + \sum_k \hbar\omega_k \hat{b}_k^{\dagger} \hat{b}_k \quad (23)$$

is the Hamiltonian of noninteracting electrons and phonons, while

$$\hat{H}_{\text{e-ph}} = \sum_k \sum_{\alpha\alpha'} (g_{\alpha\alpha',k}^{-} \hat{c}_{\alpha}^{\dagger} \hat{c}_{\alpha'} \hat{b}_k + g_{\alpha\alpha',k}^{+} \hat{c}_{\alpha}^{\dagger} \hat{c}_{\alpha'} \hat{b}_k^{\dagger}) \quad (24)$$

is the electron-phonon interaction Hamiltonian. In previous expressions,  $\hat{b}_k^{\dagger}$  ( $\hat{b}_k$ ) are the creation (annihilation) operators for the phonon mode  $k$  that satisfy bosonic commutation relations,  $\hat{c}_{\alpha}^{\dagger}$  ( $\hat{c}_{\alpha}$ ) are creation (annihilation) operators for electronic single-particle state  $\alpha$  that satisfy fermion anticommutation relations,  $\hbar\omega_k$  is the energy of a mode  $k$  phonon, while  $\epsilon_{\alpha}$  is the energy of electronic state  $\alpha$ . Matrix elements of electron-phonon interaction satisfy the relation

$$g_{\alpha\alpha',k}^{\pm} = g_{\alpha'\alpha,k}^{\mp*} \quad (25)$$

and their particular form depends on details of the electron-phonon interaction mechanism.

We will assume that the phonon subsystem is in thermal equilibrium and therefore we will adopt the following factorization of the initial density matrix  $\hat{\rho}(0)$ :

$$\hat{\rho}(0) = \hat{\rho}_e \hat{\rho}_{\text{ph,eq}}. \quad (26)$$

The operator  $\hat{\rho}_{\text{ph,eq}}$  describes the phonon subsystem in equilibrium at the temperature  $T_{\text{ph}} = \frac{1}{k_B \beta_{\text{ph}}}$  and it is given as

$$\hat{\rho}_{\text{ph,eq}} = \frac{e^{-\beta_{\text{ph}} \hat{H}_{\text{ph}}}}{\text{Tr}_{\text{ph}} e^{-\beta_{\text{ph}} \hat{H}_{\text{ph}}}}, \quad (27)$$

whereas  $\hat{\rho}_e$  is the reduced density matrix of the electronic subsystem. The state of the system described by Eq. (26) assumes that electrons are out of equilibrium, while the phonons are in equilibrium. Such states can arise naturally in several relevant physical scenarios. A typical example of such a scenario is a semiconductor structure excited with photons whose energy is larger than the band gap of the structure. Most of the energy of incident photons is then transferred to electronic degrees of freedom and therefore it is quite reasonable to assume that electrons are out of equilibrium, while the phonons are in equilibrium.

The electric dipole moment operator  $\hat{\Pi}_a$  introduced in Eq. (11) can be expressed in the second quantization representation as

$$\hat{\Pi}_a = q \sum_{\alpha\beta} x_{\alpha;\alpha\beta} \hat{c}_{\alpha}^{\dagger} \hat{c}_{\beta}, \quad (28)$$

where  $x_{\alpha;\alpha\beta} \equiv \langle \alpha | \hat{x}_a | \beta \rangle$  are the matrix elements of the single electron position operator. Using Eq. (16), we find that the operator  $\hat{J}_a$  reads  $\hat{J}_a = \hat{J}_a^{(1)} + \hat{J}_a^{(2)}$ , where

$$\hat{J}_a^{(1)} = \frac{iq}{\hbar} \sum_{\alpha\beta} (\epsilon_{\alpha} - \epsilon_{\beta}) x_{\alpha;\alpha\beta} \hat{c}_{\alpha}^{\dagger} \hat{c}_{\beta} \quad (29)$$

describes the contribution to the operator  $\hat{J}_a$  due to direct interaction of electrons with electric field, while

$$\hat{J}_a^{(2)} = \frac{iq}{\hbar} \sum_k \sum_{\alpha\beta} (F_{\alpha;\alpha\beta,k}^{-} \hat{c}_{\alpha}^{\dagger} \hat{c}_{\beta} \hat{b}_k + F_{\alpha;\alpha\beta,k}^{+} \hat{c}_{\alpha}^{\dagger} \hat{c}_{\beta} \hat{b}_k^{\dagger}) \quad (30)$$

describes the contribution arising from electron-phonon interaction. The coefficients  $F_{a;\alpha\beta,k}^\pm$  are given by

$$F_{a;\alpha\beta,k}^\pm = \sum_{\alpha'} (g_{\alpha'\beta,k}^\pm x_{a;\alpha'\beta} - x_{a;\alpha\alpha'} g_{\alpha'\beta,k}^\pm) \quad (31)$$

and satisfy the relation

$$F_{a;\alpha\beta,k}^\pm = -F_{a;\beta\alpha,k}^{\mp*} \quad (32)$$

In this work, we are mainly interested in the case of localized electronic states when the matrix elements of the position operator between different states are negligible. This condition can be mathematically expressed as

$$x_{a;\alpha\beta} = \delta_{\alpha\beta} x_{a;\alpha} \quad (33)$$

Therefore, in the case of localized electronic states,  $\hat{J}_a^{(1)} = 0$  and consequently  $\hat{J}_a = \hat{J}_a^{(2)}$ .

Next, we treat electron-phonon interaction as a perturbation and perform the expansion of Eq. (21) with respect to small interaction constants  $g_{\alpha\beta,k}^\pm$ . The evolution operator that appears in Eq. (21) can be expanded in Dyson series as

$$e^{-\frac{i}{\hbar}\hat{H}t} = e^{-\frac{i}{\hbar}\hat{H}_0t} + \frac{1}{i\hbar} \int_0^t dt' e^{-\frac{i}{\hbar}\hat{H}_0(t-t')} \hat{H}_{\text{e-ph}} e^{-\frac{i}{\hbar}\hat{H}_0t'} + \dots \quad (34)$$

Consequently, the expansion of the time-dependent operator  $\hat{J}_a(\tau)$  from Eq. (21) reads

$$\hat{J}_a(\tau) = e^{\frac{i}{\hbar}\hat{H}_0\tau} \hat{J}_a e^{-\frac{i}{\hbar}\hat{H}_0\tau} + \left[ e^{\frac{i}{\hbar}\hat{H}_0\tau} \hat{J}_a e^{-\frac{i}{\hbar}\hat{H}_0\tau}, \int_0^\tau \frac{dt'}{i\hbar} e^{\frac{i}{\hbar}\hat{H}_0t'} \hat{H}_{\text{e-ph}} e^{-\frac{i}{\hbar}\hat{H}_0t'} \right] + \dots \quad (35)$$

Furthermore, the expansion of the first term under trace in Eq. (21) gives

$$\begin{aligned} & e^{-\frac{i}{\hbar}\hat{H}(t-\tau)} \hat{\rho}(0) e^{\frac{i}{\hbar}\hat{H}(t-\tau)} \\ &= \hat{\rho}(0) + \sum_{n=1}^{+\infty} \frac{1}{n!} \left( -\frac{i(t-\tau)}{\hbar} \right)^n [\hat{H}, \dots, [\hat{H}, \hat{\rho}(0)] \dots]_n. \end{aligned} \quad (36)$$

Our aim is to obtain the first nonzero term in the expansion of Eq. (21) in the case of localized electronic states. It is therefore sufficient to take only the first term in the expansion given by Eq. (35) and to isolate the contribution from the expansion given in Eq. (36) which does not contain electron-phonon coupling constants. One can show by direct inspection, using the factorization of the initial density matrix given by Eq. (26), that every summand under the sum on the right hand side of Eq. (36) has only one term which does not contain electron-phonon coupling constants and which is of the type  $\frac{1}{n!} \left( -\frac{i(t-\tau)}{\hbar} \right)^n [\hat{H}_e, \dots, [\hat{H}_e, \hat{\rho}_e] \dots]_n \hat{\rho}_{\text{ph,eq}}$ . All these

contributions can be resummed so that we finally obtain the zeroth-order term in the expansion given by Eq. (36)

$$e^{-\frac{i}{\hbar}\hat{H}(t-\tau)} \hat{\rho}(0) e^{\frac{i}{\hbar}\hat{H}(t-\tau)} = e^{-\frac{i}{\hbar}\hat{H}_e(t-\tau)} \hat{\rho}(0) e^{\frac{i}{\hbar}\hat{H}_e(t-\tau)} + \dots \quad (37)$$

The first nontrivial term in the expansion of Eq. (21) in the case of localized electronic states is thus given by

$$\begin{aligned} \sigma_{ab}(t,t') &= \frac{nq^2}{m} \delta_{ab} - \frac{i}{\hbar V} \int_0^{t-t'} d\tau \\ &\times \text{Tr}(\hat{\rho}(0) e^{\frac{i}{\hbar}\hat{H}_e(t-\tau)} [\hat{J}_a^{(2),0}(\tau), \hat{J}_b^{(2)}(0)] e^{-\frac{i}{\hbar}\hat{H}_e(t-\tau)}), \end{aligned} \quad (38)$$

where  $\hat{J}_a^{(2),0}(\tau) = e^{\frac{i}{\hbar}\hat{H}_0\tau} \hat{J}_a^{(2)} e^{-\frac{i}{\hbar}\hat{H}_0\tau}$ . Next, we consider the frequency-time representation of the conductivity tensor which can be defined as

$$\sigma_{ab}(t,\omega) = \int_0^{+\infty} du \sigma_{ab}(t,t-u) e^{i\omega u}. \quad (39)$$

When  $\sigma_{ab}(t,t')$  depends only on the difference  $t-t'$ , Eq. (39) defines the conventional optical conductivity tensor  $\sigma_{ab}(\omega)$ . The frequency-time representation of the conductivity tensor given in Eq. (38) is

$$\begin{aligned} \sigma_{ab}(t,\omega) &= \frac{inq^2}{m\omega} \delta_{ab} + \frac{1}{\hbar\omega V} \int_0^{+\infty} du e^{i\omega u} \\ &\times \text{Tr}(\hat{\rho}(0) e^{\frac{i}{\hbar}\hat{H}_e(t-u)} [\hat{J}_a^{(2),0}(u), \hat{J}_b^{(2)}(0)] e^{-\frac{i}{\hbar}\hat{H}_e(t-u)}). \end{aligned} \quad (40)$$

In the case when  $\sigma_{ab}(t,\omega)$  varies slowly with  $t$  on the  $1/\omega$  time scale, it can be interpreted as the conventional optical conductivity tensor at time  $t$ .

We also note that when the condition of localized electronic states [Eq. (33)] is not satisfied, the dominant term in the  $\hat{J}_a$  operator is the  $\hat{J}_a^{(1)}$  term. The leading terms in expansions (35) and (36) are then given by first terms in Eqs. (35) and (37), where  $\hat{J}_a$  is replaced by  $\hat{J}_a^{(1)}$  in Eq. (35). These terms are independent of electron-phonon coupling constants and lead to the following expression for the frequency-time representation of the conductivity tensor:

$$\begin{aligned} \sigma_{ab}(t,\omega) &= \frac{inq^2}{m\omega} \delta_{ab} + \frac{1}{\hbar\omega V} \int_0^{+\infty} du e^{i\omega u} \\ &\times \text{Tr}(\hat{\rho}(0) e^{\frac{i}{\hbar}\hat{H}_e(t-u)} [\hat{J}_a^{(1),0}(u), \hat{J}_b^{(1)}(0)] e^{-\frac{i}{\hbar}\hat{H}_e(t-u)}). \end{aligned} \quad (41)$$

The physical origin of this term is direct absorption of electromagnetic radiation by the electronic subsystem. However, since this term vanishes for a system with localized electronic states, which is of main interest in this work, this term will not be considered in the remainder of the paper. The focus will be on the term from Eq. (40) which arises due to phonon-assisted transitions between states, as will become evident in Sec. III B.

## B. Frequency dependence of mobility in low carrier density limit

We will now start from Eq. (40) for the frequency-time representation of conductivity to derive the expression for the optical conductivity that explicitly contains the populations of electronic states (diagonal elements of  $\hat{\rho}_e$ ) and coherences (off-diagonal elements of  $\hat{\rho}_e$ ). By replacing Eq. (30) into the expression for mean value

$\text{Tr}(\hat{\rho}(0) e^{\frac{i}{\hbar}\hat{H}_e(t-u)}[\hat{J}_a^{(2),0}(u), \hat{J}_b^{(2)}]e^{-\frac{i}{\hbar}\hat{H}_e(t-u)})$  and tracing out the phonon degrees of freedom one obtains

$$\begin{aligned} & \text{Tr}(\hat{\rho}(0) e^{\frac{i}{\hbar}\hat{H}_e(t-u)}[\hat{J}_a^{(2),0}(u), \hat{J}_b^{(2)}]e^{-\frac{i}{\hbar}\hat{H}_e(t-u)}) \left(\frac{iq}{\hbar}\right)^{-2} \\ &= \sum_k \sum_{\alpha\beta\gamma\delta} (F_{a;\alpha\beta,k}^- F_{b;\gamma\delta,k}^+ e^{-\frac{i}{\hbar}(\epsilon_\gamma - \epsilon_\delta + \hbar\omega_k)u} - F_{a;\alpha\beta,k}^+ F_{b;\gamma\delta,k}^- e^{-\frac{i}{\hbar}(\epsilon_\gamma - \epsilon_\delta - \hbar\omega_k)u}) e^{\frac{i}{\hbar}(\epsilon_\alpha - \epsilon_\beta + \epsilon_\gamma - \epsilon_\delta)t} \langle \hat{c}_\alpha^\dagger \hat{c}_\beta \hat{c}_\gamma^\dagger \hat{c}_\delta \rangle_e \\ &+ \sum_k \sum_{\alpha\beta\gamma} (F_{a;\alpha\gamma,k}^- F_{b;\gamma\beta,k}^+ e^{-\frac{i}{\hbar}(\epsilon_\gamma - \epsilon_\beta + \hbar\omega_k)u} - F_{b;\alpha\gamma,k}^+ F_{a;\gamma\beta,k}^- e^{-\frac{i}{\hbar}(\epsilon_\alpha - \epsilon_\gamma + \hbar\omega_k)u}) N_k e^{\frac{i}{\hbar}(\epsilon_\alpha - \epsilon_\beta)t} \langle \hat{c}_\alpha^\dagger \hat{c}_\beta \rangle_e \\ &+ \sum_k \sum_{\alpha\beta\gamma} (F_{a;\alpha\gamma,k}^+ F_{b;\gamma\beta,k}^- e^{-\frac{i}{\hbar}(\epsilon_\gamma - \epsilon_\beta - \hbar\omega_k)u} - F_{b;\alpha\gamma,k}^- F_{a;\gamma\beta,k}^+ e^{-\frac{i}{\hbar}(\epsilon_\alpha - \epsilon_\gamma - \hbar\omega_k)u}) (1 + N_k) e^{\frac{i}{\hbar}(\epsilon_\alpha - \epsilon_\beta)t} \langle \hat{c}_\alpha^\dagger \hat{c}_\beta \rangle_e. \end{aligned} \quad (42)$$

Here,  $N_k$  is the number of phonons in mode  $k$  given by the Bose-Einstein distribution,  $\langle \dots \rangle_e$  denotes averaging with respect to  $\hat{\rho}_e$ , and coefficients  $F_{\alpha\beta,k}^\pm$  are given as [by the virtue of the definition of the localized electronic states from Eq. (33)]

$$F_{a;\alpha\beta,k}^\pm = g_{\alpha\beta,k}^\pm (x_{a;\beta} - x_{a;\alpha}). \quad (43)$$

See Eqs. (31) and (32).

In the limit of low carrier densities, only single-particle electronic excitations are relevant. One can therefore restrict the Hilbert space of the system to the space given as a product of single-particle electronic space and the phonon space. In this restricted space, the operators  $\hat{c}_\alpha^\dagger \hat{c}_\beta$  and  $\hat{c}_\alpha^\dagger \hat{c}_\beta \hat{c}_\gamma^\dagger \hat{c}_\delta$  reduce respectively to  $|\alpha\rangle\langle\beta|$  and  $\delta_{\beta\gamma}|\alpha\rangle\langle\delta|$ , while the Hamiltonian in this restricted space reads

$$\begin{aligned} \hat{H} &= \sum_\alpha \epsilon_\alpha |\alpha\rangle\langle\alpha| + \sum_k \hbar\omega_k \hat{b}_k^\dagger \hat{b}_k \\ &+ \sum_k \sum_{\alpha\alpha'} (g_{\alpha\alpha',k}^- |\alpha\rangle\langle\alpha'| \hat{b}_k + g_{\alpha\alpha',k}^+ |\alpha\rangle\langle\alpha'| \hat{b}_k^\dagger). \end{aligned} \quad (44)$$

The average values of the expressions appearing in Eq. (42) are then given as

$$\langle \hat{c}_\alpha^\dagger \hat{c}_\beta \rangle_e = \text{Tr}_e(\hat{\rho}_e \hat{c}_\alpha^\dagger \hat{c}_\beta) = \langle \beta | \hat{\rho}_e | \alpha \rangle \quad (45)$$

and

$$\langle \hat{c}_\alpha^\dagger \hat{c}_\beta \hat{c}_\gamma^\dagger \hat{c}_\delta \rangle_e = \text{Tr}_e(\hat{\rho}_e \hat{c}_\alpha^\dagger \hat{c}_\beta \hat{c}_\gamma^\dagger \hat{c}_\delta) = \delta_{\beta\gamma} \langle \delta | \hat{\rho}_e | \alpha \rangle. \quad (46)$$

Combining Eqs. (45), (46), (42), and (40), the following equation for the frequency-time representation of the conductivity tensor is obtained:

$$\sigma_{ab}(t, \omega) = i \frac{nq^2}{m\omega} \delta_{ab} - f_{ab}(t, \omega) - f_{ab}(t, -\omega)^*, \quad (47)$$

where  $f_{ab}(t, \omega)$  is defined as

$$\begin{aligned} f_{ab}(t, \omega) &= \frac{q^2}{\hbar^2 \omega V} \sum_k \sum_{\alpha\beta\gamma} e^{\frac{i}{\hbar}(\epsilon_\alpha - \epsilon_\beta)t} \langle \beta | \hat{\rho}_e | \alpha \rangle \\ &\times (F_{a;\alpha\gamma,k}^- F_{b;\gamma\beta,k}^+ \mathcal{D}(\epsilon_\beta - \epsilon_\gamma - \hbar\omega_k + \hbar\omega)(1 + N_k) \\ &+ F_{a;\alpha\gamma,k}^+ F_{b;\gamma\beta,k}^- \mathcal{D}(\epsilon_\beta - \epsilon_\gamma + \hbar\omega_k + \hbar\omega)N_k). \end{aligned} \quad (48)$$

Function  $\mathcal{D}(\epsilon)$  is given as

$$\mathcal{D}(\epsilon) = \pi \delta(\epsilon) + i \mathcal{P}(1/\epsilon). \quad (49)$$

In the expressions (47) and (48), there are two clear signatures of nonequilibrium: the explicit time dependence and the

presence of off-diagonal elements of  $\hat{\rho}_e$  (coherences). Both of these effects would be absent for the system in equilibrium.

Next, we consider the case when the reduced density matrix of the electronic subsystem is an analytic function of the electronic Hamiltonian  $\hat{H}_e$ , when we have

$$\langle \beta | \hat{\rho}_e | \alpha \rangle = \delta_{\alpha\beta} r_\alpha, \quad (50)$$

where

$$r_\alpha = \langle \alpha | \hat{\rho}_e | \alpha \rangle \quad (51)$$

is the average occupation of electronic state  $\alpha$ . Then in Eq. (48) we remain only with the average occupations of individual electronic states and since the quantity  $f_{ab}(t, \omega)$  does not depend explicitly on  $t$ ,  $\sigma_{ab}(t, \omega)$  also does not depend on  $t$  and represents the frequency-dependent conductivity tensor. Starting from Eqs. (47) and (48) one can show that under the aforementioned condition the following relation for the real part of the optical conductivity holds:

$$\begin{aligned} \text{Re } \sigma_{ab}(\omega) &= \frac{q^2}{2\hbar\omega V} \sum_{\alpha\beta} (x_{a;\beta} - x_{a;\alpha})(x_{b;\beta} - x_{b;\alpha}) r_\beta \\ &\times [w_{\beta\alpha, \text{ph}}(\epsilon_\beta - \epsilon_\alpha + \hbar\omega) \\ &- w_{\beta\alpha, \text{ph}}(\epsilon_\beta - \epsilon_\alpha - \hbar\omega)], \end{aligned} \quad (52)$$

where the terms  $w_{\beta\alpha, \text{ph}}$  are of the form

$$\begin{aligned} w_{\beta\alpha, \text{ph}}(\epsilon_\beta - \epsilon_\alpha) &= \frac{2\pi}{\hbar} \sum_k [ |g_{\alpha\beta,k}^-|^2 \delta(\epsilon_\beta - \epsilon_\alpha + \hbar\omega_k) N_k \\ &+ |g_{\alpha\beta,k}^+|^2 \delta(\epsilon_\beta - \epsilon_\alpha - \hbar\omega_k) (1 + N_k) ]. \end{aligned} \quad (53)$$

These are identical to the rates that would be obtained by applying Fermi's golden rule to calculate the transition probability from the state  $\beta$  to the state  $\alpha$  due to electron-phonon interaction. Equation (52) gives a rather simple expression for the dissipative part of the optical conductivity as it involves the positions of electronic states, their occupations, and Fermi's golden rule transition probabilities. Equations (52) and (53) also offer an intuitive interpretation of elementary processes giving contribution to the dissipative part of the optical conductivity in the lowest nontrivial order of the perturbation expansion. These processes are one-particle transitions  $\beta \rightarrow \alpha$  induced by emission (absorption) of one phonon accompanied by emission (absorption) of the quantum of the external electromagnetic field  $\hbar\omega$ . One should note that within our

lowest-order perturbative approach, one does not take into account multiphonon transitions which may be important in some systems.

From the definition of mobility, one then also obtains for the real part of ac mobility

$$\begin{aligned} \text{Re } \mu_{ab}(\omega) &= \frac{q}{2\hbar\omega} \sum_{\alpha\beta} (x_{a;\beta} - x_{a;\alpha})(x_{b;\beta} - x_{b;\alpha}) \frac{r_\beta}{\sum_\gamma r_\gamma} \\ &\times [w_{\beta\alpha,\text{ph}}(\epsilon_\beta - \epsilon_\alpha + \hbar\omega) \\ &- w_{\beta\alpha,\text{ph}}(\epsilon_\beta - \epsilon_\alpha - \hbar\omega)]. \end{aligned} \quad (54)$$

Equation (54) was derived under the assumption that hopping rates have the mathematical form given by Eq. (53). In Sec. V, the hopping rates given by Eqs. (70) and (66) will be used. Equation (70) can be derived from Eq. (53) under the assumption that electron-phonon coupling elements are proportional to wave function moduli overlap (see Ref. [38]). Equation (66) can then be obtained from Eq. (70) if one assumes that wave function overlaps decay exponentially with distance between states and that phonon density of states (DOS) is such that energy dependence in Eq. (70) disappears. Therefore, both Eqs. (70) and (66) are compatible with the mathematical structure of Eq. (53) and it is appropriate to use them in Eq. (54).

#### IV. OPTICAL CONDUCTIVITY IN THE PRESENCE OF IMPURITY SCATTERING

In this section, we will show that similar expressions for optical conductivity are obtained if electrons interact with an additional static potential, rather than with phonons. A typical cause of such potential could be the impurities that are present in the material.

Therefore, we consider the Hamiltonian

$$\hat{H} = \hat{H}_0 + \hat{U} = \sum_\alpha \epsilon_\alpha \hat{c}_\alpha^\dagger \hat{c}_\alpha + \sum_{\alpha\beta} A_{\alpha\beta} \hat{c}_\alpha^\dagger \hat{c}_\beta, \quad (55)$$

where  $\hat{H}_0$  is the noninteracting part of the Hamiltonian, while  $\hat{U}$  describes the interaction of electrons with static potential. The operator  $\hat{J}_a$  can be computed using Eq. (16) and reads

$$\begin{aligned} \hat{J}_a &= \hat{J}_a^{(\text{dir})} + \hat{J}_a^{(\text{imp})} \\ &= \frac{iq}{\hbar} \sum_{\alpha\alpha'} x_{a;\alpha\alpha'} (\epsilon_\alpha - \epsilon_{\alpha'}) \hat{c}_\alpha^\dagger \hat{c}_{\alpha'} + \frac{iq}{\hbar} \sum_{\alpha\beta} \mathcal{A}_{a;\alpha\beta} \hat{c}_\alpha^\dagger \hat{c}_\beta. \end{aligned} \quad (56)$$

The  $\hat{J}_a^{(\text{dir})}$  operator is analogous to the operator  $\hat{J}_a^{(1)}$  in the case of a system with electron-phonon interaction and describes direct interaction of electrons with perturbing electric field. On the other hand, the  $\hat{J}_a^{(\text{imp})}$  operator describes the contribution to  $\hat{J}_a$  due to the interaction with the static potential (or, in particular, with impurities). The coefficients  $\mathcal{A}_{a;\alpha\beta}$  that appear in Eq. (56) are given as

$$\mathcal{A}_{a;\alpha\beta} = \sum_{\alpha'} (A_{\alpha\alpha'} x_{a;\alpha'\beta} - x_{a;\alpha\alpha'} A_{\alpha'\beta}) \quad (57)$$

and satisfy [compare to Eq. (32)]

$$\mathcal{A}_{a;\beta\alpha} = -\mathcal{A}_{a;\alpha\beta}^* \quad (58)$$

We will treat the interaction with the static potential as a perturbation and we will derive the formula for optical conductivity in the lowest order of the perturbation expansion with respect to small coefficients  $A_{\alpha\beta}$ . We will assume that electronic states are localized; see Eq. (33). This way, the expression for the operator  $\hat{J}_a$  simplifies to

$$\hat{J}_a = \hat{J}_a^{(\text{imp})} = \frac{iq}{\hbar} \sum_{\alpha\beta} A_{\alpha\beta} (x_{a;\beta} - x_{a;\alpha}) \hat{c}_\alpha^\dagger \hat{c}_\beta. \quad (59)$$

The starting point for the perturbation expansion is again Eq. (21). Following a discussion, similar to that conducted in Sec. III, we obtain that the first nonzero term in the expansion of Eq. (21) in the case of localized electronic states is quadratic in quantities  $A_{\alpha\beta}$  and that the corresponding expression for the time-frequency representation of the conductivity tensor [Eq. (39)] reads

$$\begin{aligned} \sigma_{ab}(t, \omega) &= \frac{inq^2}{m\omega} \delta_{ab} + \frac{1}{\hbar\omega V} \int_0^{+\infty} dt e^{i\omega t} \\ &\times \text{Tr}(\hat{\rho}(0) e^{\frac{i}{\hbar} \hat{H}_0(t-u)} [\hat{J}_a^{(\text{imp}),0}(u), \hat{J}_b^{(\text{imp})}] e^{-\frac{i}{\hbar} \hat{H}_0(t-u)}). \end{aligned} \quad (60)$$

The notation  $\hat{J}_a^{(\text{imp}),0}(t)$  again suggests that the time dependence is governed by the noninteracting Hamiltonian.

In the low density limit, the projection of the Hamiltonian onto the single-particle subspace reads

$$\hat{H}_0 = \sum_\alpha \epsilon_\alpha |\alpha\rangle\langle\alpha| + \sum_{\alpha\beta} A_{\alpha\beta} |\alpha\rangle\langle\beta|, \quad (61)$$

with the average values  $\langle \hat{c}_\alpha^\dagger \hat{c}_\beta \rangle = \langle \beta | \hat{\rho}(0) | \alpha \rangle$ . Deriving Eq. (60) we obtain the expression for the frequency-time representation of the conductivity tensor which bears formal resemblance to the analogous expression [Eq. (47)] in the case with electron-phonon interaction,

$$\sigma_{ab}(t, \omega) = i \frac{nq^2}{m\omega} \delta_{ab} - f_{ab}(t, \omega) - f_{ab}(t, -\omega)^*, \quad (62)$$

where  $f_{ab}(t, \omega)$  is defined as

$$\begin{aligned} f_{ab}(t, \omega) &= \frac{q^2}{\hbar^2\omega V} \sum_{\alpha\beta\gamma} e^{\frac{i}{\hbar}(\epsilon_\alpha - \epsilon_\beta)t} \langle \beta | \hat{\rho}_e | \alpha \rangle A_{\alpha\gamma} (x_{a;\gamma} - x_{a;\alpha}) \\ &\times A_{\gamma\beta} (x_{b;\beta} - x_{b;\gamma}) \mathcal{D}(\epsilon_\beta - \epsilon_\gamma + \hbar\omega). \end{aligned} \quad (63)$$

Again, when the initial density matrix  $\hat{\rho}(0)$  is an analytic function of the electronic part of the Hamiltonian  $\hat{H}_0$ , the quantity  $f_{ab}(t, \omega)$  defined in Eq. (63) contains only populations of the individual electronic states  $r_\alpha = \langle \alpha | \hat{\rho}(0) | \alpha \rangle$  and does not depend explicitly on time. Thus  $\sigma_{ab}(t, \omega)$  is the optical conductivity tensor (entirely expressed in terms of populations of electronic states). The final expression for the real part of ac mobility in the presence of interaction with impurities reads

$$\begin{aligned} \text{Re } \mu_{ab}(\omega) &= \frac{q}{2\hbar\omega} \sum_{\alpha\beta} (x_{a;\beta} - x_{a;\alpha})(x_{b;\beta} - x_{b;\alpha}) \frac{r_\beta}{\sum_\gamma r_\gamma} \\ &\times [w_{\beta\alpha,\text{imp}}(\epsilon_\beta - \epsilon_\alpha + \hbar\omega) \\ &- w_{\beta\alpha,\text{imp}}(\epsilon_\beta - \epsilon_\alpha - \hbar\omega)], \end{aligned} \quad (64)$$

where the terms  $w_{\beta\alpha,\text{imp}}$  are of the form

$$w_{\beta\alpha,\text{imp}}(\epsilon_\beta - \epsilon_\alpha) = \frac{2\pi}{\hbar} |A_{\alpha\beta}|^2 \delta(\epsilon_\beta - \epsilon_\alpha). \quad (65)$$

We emphasize the formal analogy between Eqs. (54) and (64) for the ac mobility. The form of both equations is the same, regardless of the particular interaction mechanism (electron-phonon interaction or interaction with an additional static potential) which causes transitions between localized states.

## V. NUMERICAL RESULTS

### A. One-dimensional model with Miller-Abrahams rates and Gaussian density of states

In this section, we apply the derived formulas to a one-dimensional Gaussian disorder model. The assumption of the model is that the states are located on the sites of a one-dimensional lattice with spacing  $a$  and that the energies of the states are drawn from a Gaussian distribution with standard deviation  $\sigma$ . The transition rates were assumed to take the Miller-Abrahams form and only the hops between

nearest neighbors were considered. Under these assumptions, the transition rate from the state  $\beta$  to the state  $\gamma$  has the form

$$w_{\beta\gamma} = w_0 e^{-a/a_{\text{loc}}} \exp\left(\frac{\epsilon_\beta - \epsilon_\gamma - |\epsilon_\beta - \epsilon_\gamma|}{2k_B T}\right), \quad (66)$$

where  $a_{\text{loc}}$  is the localization length which is assumed equal for all sites,  $T$  is the temperature, and  $w_0$  is a constant prefactor. Real part of the frequency dependent mobility can under all these assumptions be written in the form

$$\text{Re } \mu_{xx}(\omega) = \sum_{\gamma} \mu_{\gamma,\gamma+1}(\omega), \quad (67)$$

where  $\mu_{\gamma,\gamma+1}(\omega)$  is the contribution of the pair of sites  $(\gamma, \gamma + 1)$  given as

$$\mu_{\gamma,\gamma+1}(\omega) = \frac{qa^2}{2k_B T} w_0 e^{-a/a_{\text{loc}}} M(x). \quad (68)$$

In the last equation,  $x$  is a dimensionless parameter defined as  $x = \beta\hbar\omega$  [ $\beta = 1/(k_B T)$ ], while  $M(x)$  is the function that reads

$$M(x) = \begin{cases} \frac{r_{\min}}{\sum_{\delta} r_{\delta}} e^{-x_{\gamma,\gamma+1}} \times 2 \frac{\sinh x}{x}, & x < x_{\gamma,\gamma+1}, \\ \frac{r_{\max}}{\sum_{\delta} r_{\delta}} \frac{1}{x} (1 - e^{x_{\gamma,\gamma+1}} e^{-x}) + \frac{r_{\min}}{\sum_{\delta} r_{\delta}} \frac{1}{x} (1 - e^{-x_{\gamma,\gamma+1}} e^{-x}), & x > x_{\gamma,\gamma+1}, \end{cases} \quad (69)$$

where  $x_{\gamma,\gamma+1} = \beta|\epsilon_\gamma - \epsilon_{\gamma+1}|$  and  $r_{\max}$  ( $r_{\min}$ ) is the population of the state with larger (smaller) energy among the states  $\gamma$  and  $\gamma + 1$ .

The frequency range in which this formula can be applied is determined by the condition (5) where  $\tau$  is the relaxation time towards equilibrium. The relaxation time  $\tau$  must be larger than the reciprocal value of largest hopping rates  $\tau \gtrsim w_0^{-1} e^{a/a_{\text{loc}}}$ , so that the relevant frequencies obey the condition  $f \gtrsim (2\pi)^{-1} w_0 e^{-a/a_{\text{loc}}}$ .

The calculations were performed for a lattice with  $10^5$  sites, where the following values of the parameters were used:  $T = 300$  K,  $\sigma = 100$  meV,  $a = 1$  nm,  $a_{\text{loc}} = 2a/9$ , and  $w_0 = 1.0 \times 10^{14}$  s $^{-1}$ . Two different cases for initial populations of localized states were considered. In case 1, we assume that initial distribution of carriers are nonequilibrium, but still of Maxwell-Boltzmann form with electronic temperatures  $T_e$  which can be different than  $T$ . Therefore, in this case  $r_\gamma = e^{-\beta_e \epsilon_\gamma}$ , where  $\beta_e = 1/(k_B T_e)$ . In case 2, we assume that only the states in some narrow energy window are initially populated, while the other states are not populated. The initial populations are then given as  $r_\gamma = 1$  for  $\epsilon_{\min} < \epsilon_\gamma < \epsilon_{\max}$ ,  $r_\gamma = 0$  otherwise. The results for different values of the parameter  $T_e$  in case 1 and different intervals  $(\epsilon_{\min}, \epsilon_{\max})$  in case 2 are shown in Figs. 1 and 2.

As can be immediately seen from expressions in Eqs. (67)–(69), for sufficiently high frequencies  $f$ , such that  $hf > \max_{\gamma} |\epsilon_\gamma - \epsilon_{\gamma+1}|$ , real part of the ac mobility decreases as  $\text{Re } \mu_{xx}(f) \sim 1/f$ . On the other hand, for sufficiently low frequencies  $f$ , such that  $hf < \min_{\gamma} |\epsilon_\gamma - \epsilon_{\gamma+1}|$ , real part of the mobility tends to a constant value which depends on the particular choice of  $r_\gamma$ .

In case 1 and in the intermediate frequency range real part of the ac mobility reaches its maximum value. The height of this maximum (measured relative to the low-frequency limit of the mobility) decreases with increasing the temperature  $T_e$ . The position of the maximum moves towards lower frequencies with increasing the temperature  $T_e$ . Namely, the position of the maximum of the mobility spectrum is determined by the positions of the maximum of the function  $M(x)$ . For all values

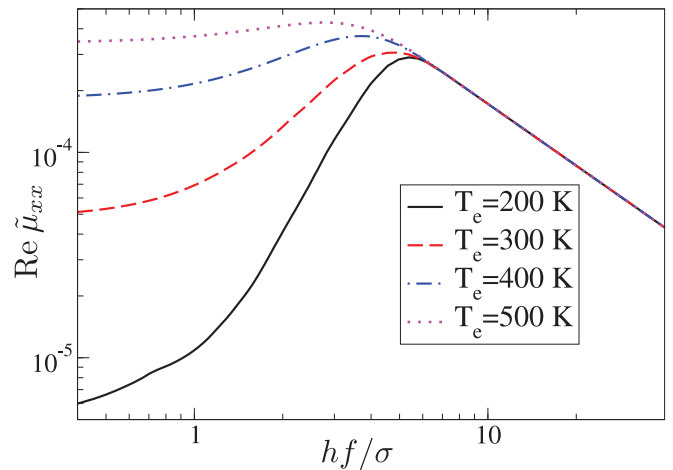


FIG. 1. (Color online) Frequency dependence of real part of the normalized mobility  $\tilde{\mu}_{xx} = \mu_{xx}/(qa^2\beta w_0 e^{-a/a_{\text{loc}}}/2)$  for different electronic temperatures  $T_e$  in one-dimensional Gaussian disorder model. The nonequilibrium populations of electronic states were assumed as  $r_\gamma = e^{-\beta_e \epsilon_\gamma}$ .

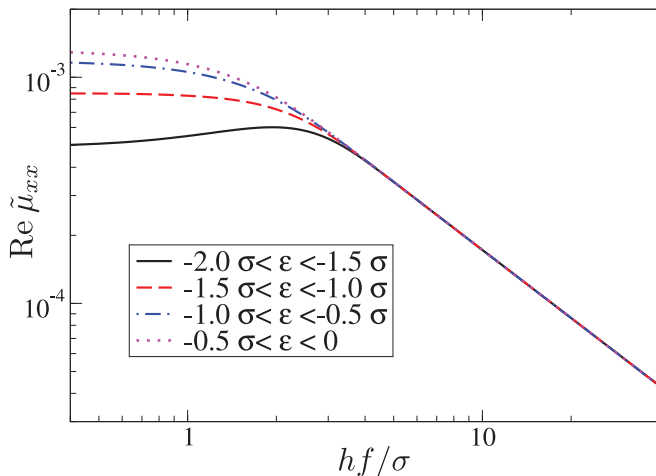


FIG. 2. (Color online) Frequency dependence of real part of the normalized mobility  $\tilde{\mu}_{xx} = \mu_{xx}/(qa^2\beta w_0 e^{-a/a_{loc}}/2)$  for different choices of the energy interval  $\epsilon \in (\epsilon_{\min}, \epsilon_{\max})$  of the populated states in one-dimensional Gaussian disorder model. The nonequilibrium populations of electronic states were assumed as  $r_\gamma = 1$  for  $\epsilon_{\min} < \epsilon_\gamma < \epsilon_{\max}$ , and  $r_\gamma = 0$  otherwise.

of the parameter  $T_e$  considered in Fig. 1, it can be shown (by direct inspection) that the function  $M(x)$  has its maximum at  $x = x_{\gamma, \gamma+1}$ . At low temperatures  $T_e$  the lowest energy states have the highest values of the factors  $r_\gamma$  and the typical energy difference  $|\epsilon_\gamma - \epsilon_{\gamma+1}|$  of the pair of neighboring sites giving significant contribution to the mobility (at least one of the states should have high enough population factor) is fairly high, so that the peak of the contribution  $\mu_{\gamma, \gamma+1}$  is at high frequencies. This typical energy difference decreases with increasing the temperature  $T_e$  (since higher energy states, which are more numerous, also have appreciable values of population factors), which leads to the shift of the peak position towards lower frequencies. For small enough  $|\epsilon_\gamma - \epsilon_{\gamma+1}|$  (compared to  $k_B T$ ), the function  $M(x)$ , for  $x < x_{\gamma, \gamma+1}$ , can be approximated by a constant, which leads to flattening of the maximum, as seen at higher electronic temperatures in Fig. 1.

A similar analysis can be used to understand the shapes of the mobility spectra for case 2 shown in Fig. 2. The contribution to the mobility of the pair  $(\gamma, \gamma+1)$  reaches its maximum at frequency  $f_*$  such that  $hf_* > |\epsilon_\gamma - \epsilon_{\gamma+1}|$ . When the interval  $(\epsilon_{\min}, \epsilon_{\max})$  is in the tail of the Gaussian, the typical energy difference  $|\epsilon_\gamma - \epsilon_{\gamma+1}|$  is rather high for the pairs contributing significantly to the mobility, so that the maximum of the mobility spectrum is at high frequencies. Moving the interval towards the center of the Gaussian, the typical energy difference decreases and so does the position of the maximum of the mobility spectrum. For sufficiently small energy difference (compared to  $k_B T$ ), the function  $M(x)$  can be well approximated by a constant in the range  $x < x_{\gamma, \gamma+1}$  which explains the disappearance of the maximum.

Since the flattening of the maximum in the mobility spectrum appears due to the presence of carriers at higher energies under nonequilibrium conditions, this flattening may be considered as a signature of nonequilibrium effects in the system. It is less pronounced when nonequilibrium distribution is of Maxwell-Boltzmann type with a different electronic

temperature and more pronounced in the case when the carriers are present only at energies in a certain spectral window—a situation where the carrier distribution more strongly differs from the equilibrium one.

## B. Model of a disordered conjugated polymer material

Next, we apply the derived formula for frequency dependence of the mobility to a realistic polymer material—strongly disordered poly(3-hexylthiophene) (P3HT) polymer. The positions of electronic states, hopping probabilities between the states, and the energies of states were extracted from our previous calculations reported in Ref. [39]. For completeness, we briefly summarize the methodology employed in these calculations. First, the positions of atoms were obtained from classical molecular dynamics simulations using a simulated annealing procedure. 50 different realizations of the  $5 \text{ nm} \times 5 \text{ nm} \times 5 \text{ nm}$  portion of material (that consists of 12024 atoms) were obtained from these simulations and were subsequently used in electronic structure calculations. Charge patching method [40] was used to obtain the single-particle Hamiltonian that approximates well the Hamiltonian that would be obtained from density functional theory in local density approximation. This Hamiltonian was diagonalized using the overlapping fragments method [41]. The transition rates for downhill transitions between the states were then calculated as

$$w_{\alpha\beta} = \alpha^2 S_{\alpha\beta}^2 [N(\epsilon_{\alpha\beta}) + 1] D_{\text{ph}}(\epsilon_{\alpha\beta}) / \epsilon_{\alpha\beta}, \quad (70)$$

where  $D_{\text{ph}}(E)$  is the phonon DOS normalized such that  $\int_0^\infty D_{\text{ph}}(E) dE = 1$ ,  $\epsilon_{\alpha\beta} = |\epsilon_\alpha - \epsilon_\beta|$ ,  $N(E)$  is the phonon occupation number given by the Bose-Einstein distribution at a temperature  $T$ ,  $S_{\alpha\beta} = \int d^3 \mathbf{r} |\psi_\alpha(\mathbf{r})| \cdot |\psi_\beta(\mathbf{r})|$  is the overlap of the wave function moduli, and  $\alpha$  is a constant factor equal to  $10^7 \text{ eV s}^{-1/2}$ . The phonon energies and the phonon DOS were calculated from the classical force field that was used in molecular dynamics simulations by diagonalizing the corresponding dynamical matrix, as reported in Ref. [42]. Equation (70) gives a good approximation of the transition rates that would be obtained from Eq. (53), as shown in Ref. [38]. The value of the parameter  $\alpha$  in Eq. (70) was chosen to provide the best fit of Eqs. (70) to (53).

Frequency dependence of the real part of hole mobility was then calculated using Eqs. (52) and (70) where all data from 50 different realizations of the 12024 atom system were used. The results obtained from the calculation are presented in Fig. 3. We note that the data from electronic structure calculations that were performed are not sufficient to yield convergent results for the mobility. This can be evidenced from the noisy dependence in Fig. 3 and from the fact that the mobility obtained from a smaller number of realizations of the system is different than the one in Fig. 3. Larger number of calculations or the calculations performed on larger systems would be needed to obtain converged value of the mobility. However, such calculations require a huge computational cost and we cannot currently perform them. Nevertheless, from the set of calculations that were performed one can identify the main trends in the frequency dependence of the mobility. As in the simple model discussed in Sec. V A, the real part of the mobility exhibits a peak at a frequency that corresponds to typical transition energies in the system, which is then followed

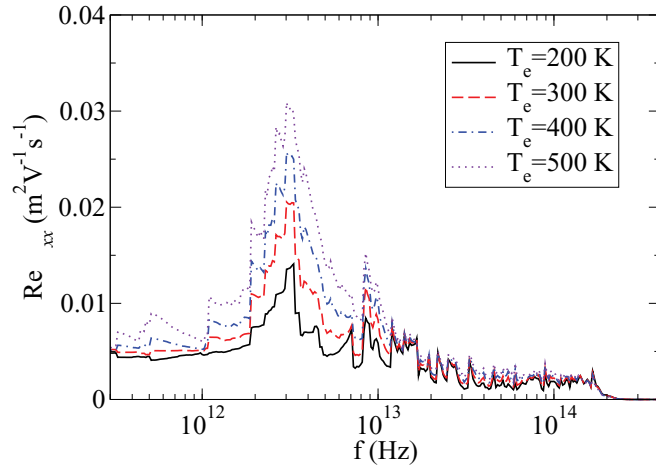


FIG. 3. (Color online) Frequency dependence of real part of hole mobility in disordered P3HT polymer for different electronic temperatures  $T_e$  and the lattice temperature  $T = 300$  K.

by a decay at higher frequencies. The mobility also increases with an increase in electronic temperature, as expected.

We next compare the results obtained in this work to measurements of high-frequency P3HT hole mobility reported in the literature. These measurements are typically based on time-resolved terahertz spectroscopy [43] and cover the frequencies around 1 THz. At these frequencies our simulations yield the mobilities on the order of (50–100)  $\text{cm}^2/(\text{V s})$ . In Ref. [44] the mobilities on the order of 10  $\text{cm}^2/(\text{V s})$  were extracted from the fits to measurements. On the other hand, the mobilities on the order of 50  $\text{cm}^2/(\text{V s})$  were obtained in Ref. [45]. Therefore, the simulation yields the same order of magnitude of the terahertz mobility as previously reported in experiments.

## VI. DISCUSSION

In this section, we discuss our results in light of other results that exist in the literature and concern optical conductivity in a system with localized states.

Our result for nonequilibrium optical conductivity should, of course, in the special case of equilibrium reduce to the formula valid in equilibrium case. A well-known expression for the real part of optical conductivity in equilibrium that relates it to the mean square displacement of a diffusing carrier reads (see, for example, Ref. [24])

$$\text{Re}\sigma(\omega) = -\frac{q^2\omega^2}{V} \frac{\tanh(\beta\hbar\omega/2)}{\hbar\omega} \text{Re} \int_0^{+\infty} dt e^{i\omega t} \Delta X^2(t), \quad (71)$$

where  $\Delta X^2(t) = \langle (\hat{X}(t) - \hat{X}(0))^2 \rangle$ ,  $\hat{X}$  is the sum of position operators of all electrons, and  $\langle \dots \rangle = \text{Tr}(e^{-\beta\hat{H}} \dots) / \text{Tr} e^{-\beta\hat{H}}$  is the thermodynamic average at the temperature  $T = 1/(\beta k_B)$ . While, at first sight, Eq. (71) seems to lead to rather different results for the lowest-order optical conductivity than the one embodied in Eq. (52), a detailed proof can be conducted, showing that the two expressions are identical for the system with localized states in equilibrium. The details of this proof are given in the Appendix.

A somewhat different version of Eq. (71) is often encountered in the literature which contains the  $\beta/2$  term instead of the  $\frac{\tanh(\beta\hbar\omega/2)}{\hbar\omega}$  term and reads [23,26,27,46]

$$\text{Re}\sigma(\omega) = -\frac{q^2\omega^2\beta}{2V} \text{Re} \int_0^{+\infty} dt e^{i\omega t} \Delta X^2(t). \quad (72)$$

When the condition  $\beta\hbar\omega \ll 1$  is satisfied these two expressions are approximately equal. However, at high frequencies these two expressions essentially differ. While Eq. (71) leads to the real part of the conductivity that vanishes at sufficiently high frequencies, Eq. (72) gives a constant real part of the mobility at these frequencies which is not the correct trend. Therefore, Eq. (72) should be applied only if the condition  $\beta\hbar\omega \ll 1$  is satisfied.

An expression for optical conductivity in the form similar to the one given in Eq. (52) has also been previously obtained for the case of equilibrium [47,48]. These expressions [Eq. (12) in Ref. [47] and Eq. (3.21) in Ref. [48]] in the limit of low concentration are the special case of Eq. (52) for the case of equilibrium in the limit  $\hbar\omega \ll k_B T$ . It is very interesting that our main result given by Eq. (52) has the same mathematical form as the expressions for the case of equilibrium. Therefore, we have generalized the result that was known for the case of equilibrium to the case of nonequilibrium systems that satisfy the assumptions of factorization of the density matrix into the electron and the phonon part [Eq. (26)] and weak relaxation at relevant time scales [Eq. (5)].

As we have already pointed out, our results are not expected to be valid at low frequencies, such that the period of perturbation is larger than the carrier relaxation time. For that reason, one can certainly not assume that dc mobility or conductivity is equal to the low frequency limit of our results. There is an additional reason that our results cannot be extended to low frequencies. It has been pointed out in Refs. [47,48] that conductivity at low frequencies cannot be obtained from a formal expansion in powers of electron-phonon interaction strength, which is an approach used in our work.

From the previous discussion, we can conclude that our results reduce to previous results from the literature for the case of equilibrium state. On the other hand, there have been almost no works in the literature with an attempt to obtain similar results for the system out of equilibrium. The exceptions are Refs. [36,37] where Eq. (19) was derived. However, we are not aware of any attempt to obtain a more specific form of nonequilibrium conductivity in a system with localized states and the main contribution of our work is that it covers this so far unexplored area.

## VII. CONCLUSION

In conclusion, we have developed an approach for the treatment of nonequilibrium optical conductivity in a system with localized electronic states and weak electron-phonon or electron-impurity interaction. Starting from nonequilibrium generalization of Kubo's formula and performing the expansion of optical conductivity in powers of small electron-phonon interaction parameter, we obtain a relatively simple expression for the optical conductivity of the material. In the special case of incoherent nonequilibrium state the expression contains

only the positions of electronic states, their nonequilibrium populations, and Fermi's golden rule transition probabilities between the states. Interestingly, the same mathematical form of the expression is valid both in the case of electron-phonon and electron-impurity interaction. Our result opens the way to better understanding of the response of nonequilibrium systems to electromagnetic radiation. A typical example where our results can be applied is photoexcited semiconductor where electrons and holes are formed by the optical excitation. If that semiconductor is then probed by low energy (terahertz) excitation, the response will depend on the nonequilibrium distribution of excited carriers. Our final expressions should be able to predict the response of the system to such probes.

The application of the derived formula to two model systems was presented to illustrate the features that one may expect to see in terahertz conductivity spectra.

### ACKNOWLEDGMENTS

This work was supported by European Community FP7 Marie Curie Career Integration Grant (ELECTROMAT), Serbian Ministry of Education, Science and Technological Development (Project No. ON171017) and FP7 projects PRACE-3IP and EGI-InSPIRE. V.J. also acknowledges the support by the Fund for Young Talents of the Serbian Ministry of Youth and Sport.

### APPENDIX: PROOF OF EQUIVALENCE OF THE LOWEST-ORDER OPTICAL CONDUCTIVITY CALCULATED FROM EQ. (71) AND THE EXPRESSION IN EQ. (52)

The operator  $\hat{X}(t) - \hat{X}(0)$  appearing in Eq. (71) can be expressed as [see Eqs. (11) and (16)]

$$q(\hat{X}(t) - \hat{X}(0)) = \int_0^t dt' \hat{J}_x(t'), \quad (\text{A1})$$

so that in the case of localized carriers, when  $\hat{J}_x = \hat{J}_x^{(2)}$ , the operator  $(\hat{X}(t) - \hat{X}(0))^2$  is quadratic in electron-phonon coupling constants. If we are to obtain the conductivity up to quadratic terms in small interaction constants  $g_{\alpha\beta,k}^{\pm}$ , it is clear that the following factorization of the equilibrium statistical operator should be adopted [compare to the decomposition of the initial density matrix in Eq. (26)]

$$\frac{e^{-\hat{H}/(k_B T)}}{\text{Tr} e^{-\hat{H}/(k_B T)}} \approx \frac{e^{-\hat{H}_e/(k_B T)}}{\text{Tr}_e e^{-\hat{H}_e/(k_B T)}} \frac{e^{-\hat{H}_{ph}/(k_B T)}}{\text{Tr}_{ph} e^{-\hat{H}_{ph}/(k_B T)}}, \quad (\text{A2})$$

and that time dependencies appearing in (71) should be taken with respect to the noninteracting Hamiltonian  $\hat{H}_0$ . The average value  $\langle (\hat{X}(t) - \hat{X}(0))^2 \rangle$  is then transformed into

$$\begin{aligned} \langle (\hat{X}(t) - \hat{X}(0))^2 \rangle &= \sum_k \sum_{\alpha\beta\gamma\delta} (x_\beta - x_\alpha)(x_\delta - x_\gamma) \langle \hat{c}_\alpha^\dagger \hat{c}_\beta \hat{c}_\gamma^\dagger \hat{c}_\delta \rangle_e \left( g_{\alpha\beta,k}^- g_{\gamma\delta,k}^+ \frac{e^{\frac{i}{\hbar}(\epsilon_\alpha - \epsilon_\beta - \hbar\omega_k)t} - 1}{\epsilon_\alpha - \epsilon_\beta - \hbar\omega_k} \frac{e^{\frac{i}{\hbar}(\epsilon_\gamma - \epsilon_\delta + \hbar\omega_k)t} - 1}{\epsilon_\gamma - \epsilon_\delta + \hbar\omega_k} (1 + N_k) \right. \\ &\quad \left. + g_{\alpha\beta,k}^+ g_{\gamma\delta,k}^- \frac{e^{\frac{i}{\hbar}(\epsilon_\alpha - \epsilon_\beta + \hbar\omega_k)t} - 1}{\epsilon_\alpha - \epsilon_\beta + \hbar\omega_k} \frac{e^{\frac{i}{\hbar}(\epsilon_\gamma - \epsilon_\delta - \hbar\omega_k)t} - 1}{\epsilon_\gamma - \epsilon_\delta - \hbar\omega_k} N_k \right), \end{aligned} \quad (\text{A3})$$

where  $\langle \dots \rangle_e$  denotes averaging with respect to the electronic part of the decomposition (A2). Combining Eqs. (71) and (A3) and in the limit of low carrier densities, when Eqs. (46), (50), and (51) can be used, the following expression for the optical conductivity ( $\omega \neq 0$ ) is obtained:

$$\text{Re} \sigma_{xx}(\omega) = \frac{q^2}{2\hbar\omega V} \tanh\left(\frac{\hbar\omega}{2k_B T}\right) \sum_{\alpha\beta} (x_\beta - x_\alpha)^2 r_\beta [w_{\beta\alpha,ph}(\epsilon_\beta - \epsilon_\alpha - \hbar\omega) + w_{\beta\alpha,ph}(\epsilon_\beta - \epsilon_\alpha + \hbar\omega)], \quad (\text{A4})$$

where the transition probabilities  $w_{\beta\alpha,ph}$  are defined in Eq. (53) and the average occupation of electronic state  $\beta$  is  $r_\beta = e^{-\epsilon_\beta/(k_B T)}/\text{Tr}_e e^{-\hat{H}_e/(k_B T)}$ . In order to prove that the relation (52) (in which we take  $r_\beta = e^{-\epsilon_\beta/(k_B T_{ph})}/\text{Tr}_e e^{-\hat{H}_e/(k_B T_{ph})}$ ) gives the same result for the lowest-order optical conductivity as Eq. (A4) (assuming that  $T = T_{ph}$ ), we note that the transition probabilities satisfy the detailed-balance condition (in the low-density limit and in the presence of external harmonic perturbation)

$$\frac{w_{\beta\alpha,ph}(\epsilon_\beta - \epsilon_\alpha + \hbar\omega)}{w_{\alpha\beta,ph}(\epsilon_\alpha - \epsilon_\beta - \hbar\omega)} = e^{-(\epsilon_\alpha - \epsilon_\beta - \hbar\omega)/(k_B T)} = \frac{r_\alpha}{r_\beta} \frac{1 + \tanh\frac{\hbar\omega}{2k_B T}}{1 - \tanh\frac{\hbar\omega}{2k_B T}}. \quad (\text{A5})$$

Interchanging the dummy electronic indices  $\alpha, \beta$  in the first summand in Eq. (52) we obtain

$$\text{Re} \sigma_{xx}(\omega) = \frac{q^2}{2\hbar\omega V} \sum_{\alpha\beta} (x_\beta - x_\alpha)^2 [-r_\alpha w_{\alpha\beta,ph}(\epsilon_\alpha - \epsilon_\beta - \hbar\omega) + r_\beta w_{\beta\alpha,ph}(\epsilon_\beta - \epsilon_\alpha + \hbar\omega)], \quad (\text{A6})$$

whereas performing the same operation on Eq. (A4) gives

$$\text{Re } \sigma_{xx}(\omega) = \frac{q^2}{2\hbar\omega V} \tanh\left(\frac{\hbar\omega}{2k_B T}\right) \sum_{\alpha\beta} (x_\beta - x_\alpha)^2 [r_\alpha w_{\alpha\beta,\text{ph}}(\epsilon_\alpha - \epsilon_\beta - \hbar\omega) + r_\beta w_{\beta\alpha,\text{ph}}(\epsilon_\beta - \epsilon_\alpha + \hbar\omega)]. \quad (\text{A7})$$

The right-hand sides of Eqs. (A6) and (A7) are equal since, by the condition (A5), single summands under the double sums are mutually equal.

- 
- [1] N. F. Mott and E. A. Davis, *Electronic Processes in Non-Crystalline Materials*, 2nd ed. (Clarendon Press, Oxford, 1979).
- [2] B. I. Shklovskii and A. L. Efros, *Electronic Properties of Doped Semiconductors* (Springer, Berlin, 1984).
- [3] H. Böttger and V. V. Bryksin, *Hopping Conduction in Solids* (VCH Publishing, Berlin, 1986).
- [4] *Physics of Organic Semiconductors*, edited by W. Brütting (Wiley, Weinheim, 2005).
- [5] *Introduction to Organic Electronic and Optoelectronic Materials and Devices*, edited by S.-S. Sun and L. R. Dalton (Taylor & Francis, Boca Raton, 2008).
- [6] M. Pope and C. E. Swenberg, *Electronic Processes in Organic Crystals and Polymers* (Oxford University Press, Oxford, 1999).
- [7] M. Schwoerer and H. C. Wolf, *Organic Molecular Solids* (Wiley, Weinheim, 2007).
- [8] T. U. Kampen, *Low Molecular Weight Organic Semiconductors* (Wiley, Weinheim, 2010).
- [9] *Organic Electronics*, edited by H. Klauk (Wiley, Weinheim, 2006).
- [10] *Charge Transport in Disordered Solids with Applications in Electronics*, edited by S. Baranovskii (Wiley, Chichester, England, 2006).
- [11] H. Sirringhaus, P. J. Brown, R. H. Friend, M. M. Nielsen, K. Bechgaard, B. M. W. Langeveld-Voss, A. J. H. Spiering, R. A. J. Janssen, E. W. Meijer, P. Herwig, and D. M. de Leeuw, *Nature (London)* **401**, 685 (1999).
- [12] R. J. Kline, M. D. McGehee, and M. F. Toney, *Nat. Mater.* **5**, 222 (2006).
- [13] J. H. Burroughes, D. D. C. Bradley, A. R. Brown, R. N. Marks, K. Mackay, R. H. Friend, P. L. Burns, and A. B. Holmes, *Nature (London)* **347**, 539 (1990).
- [14] B. K. Yap, R. Xia, M. Campoy-Quiles, P. N. Stavrinou, and D. D. C. Bradley, *Nat. Mater.* **7**, 376 (2008).
- [15] N. S. Sariciftci, D. Braun, C. Zhang, V. I. Srdanov, A. J. Heeger, G. Stucky, and F. Wudl, *Appl. Phys. Lett.* **62**, 585 (1993).
- [16] F. Laquai and D. Hertel, *Appl. Phys. Lett.* **90**, 142109 (2007).
- [17] Y. Kim, S. Cook, S. M. Tuladhar, S. A. Choulis, J. Nelson, J. R. Durrant, D. D. C. Bradley, M. Giles, I. McCulloch, C.-S. Ha, and M. Ree, *Nat. Mater.* **5**, 197 (2006).
- [18] A. Miller and E. Abrahams, *Phys. Rev.* **120**, 745 (1960).
- [19] V. Ambegaokar, B. I. Halperin, and J. S. Langer, *Phys. Rev. B* **4**, 2612 (1971).
- [20] N. S. Sariciftci, L. Smilowitz, A. J. Heeger, and F. Wudl, *Science* **258**, 1474 (1992).
- [21] I.-W. Hwang, D. Moses, and A. J. Heeger, *J. Phys. Chem. C* **112**, 4350 (2008).
- [22] S. R. Cowan, N. Banerji, W. L. Leong, and A. J. Heeger, *Adv. Funct. Mater.* **22**, 1116 (2012).
- [23] H. Scher and M. Lax, *Phys. Rev. B* **7**, 4491 (1973).
- [24] S. Ciuchi, S. Fratini, and D. Mayou, *Phys. Rev. B* **83**, 081202 (2011).
- [25] S. Fratini, S. Ciuchi, and D. Mayou, *Phys. Rev. B* **89**, 235201 (2014).
- [26] F. C. Grozema and L. D. A. Siebeless, *Int. Rev. Phys. Chem.* **27**, 87 (2008).
- [27] H. Němec, P. Kužel, and V. Sundström, *J. Photochem. Photobiol. A: Chem.* **215**, 123 (2010).
- [28] F. Rossi and T. Kuhn, *Rev. Mod. Phys.* **74**, 895 (2002).
- [29] L. V. Keldysh, *Sov. Phys. JETP* **20**, 1018 (1965).
- [30] L. P. Kadanoff and G. Baym, *Quantum Statistical Mechanics* (Benjamin, New York, 1962).
- [31] H. Haug and A.-P. Jauho, *Quantum Kinetics in Transport and Optics of Semiconductors* (Springer, Berlin, 1996).
- [32] J. Rammer, *Quantum Field Theory of Non-Equilibrium States* (Cambridge University Press, Cambridge, UK, 2007).
- [33] G. Mahan, *Many-Particle Physics* (Kluwer Academic, New York, 2000).
- [34] C. Jacoboni, *Theory of Electron Transport in Semiconductors* (Springer, Berlin, 2010).
- [35] P. B. Allen, in *A Standard Model for Ground- and Excited-state Properties*, edited by S. G. Louie and M. L. Cohen (Elsevier Science, Amsterdam, 2006).
- [36] U. Gavish, Y. Imry, and B. Yurke, [arXiv:cond-mat/0404270](https://arxiv.org/abs/cond-mat/0404270).
- [37] U. Gavish, B. Yurke, and Y. Imry, *Phys. Rev. Lett.* **93**, 250601 (2004).
- [38] N. Vukmirović and L.-W. Wang, *Appl. Phys. Lett.* **97**, 043305 (2010).
- [39] N. Vukmirović and L.-W. Wang, *J. Phys. Chem. B* **115**, 1792 (2011).
- [40] N. Vukmirović and L.-W. Wang, *J. Chem. Phys.* **128**, 121102 (2008).
- [41] N. Vukmirović and L.-W. Wang, *J. Chem. Phys.* **134**, 094119 (2011).
- [42] N. Vukmirović and L.-W. Wang, *Nano Lett.* **9**, 3996 (2009).
- [43] R. Ulbricht, E. Hendry, J. Shan, T. F. Heinz, and M. Bonn, *Rev. Mod. Phys.* **83**, 543 (2011).
- [44] X. Ai, M. C. Beard, K. P. Knutsen, S. E. Shaheen, G. Rumbles, and R. J. Ellingson, *J. Phys. Chem. B* **110**, 25462 (2006).
- [45] P. D. Cunningham and L. M. Hayden, *J. Phys. Chem. C* **112**, 7928 (2008).
- [46] N. Vukmirović, C. S. Ponceca, H. Němec, A. Yartsev, and V. Sundström, *J. Phys. Chem. C* **116**, 19665 (2012).
- [47] E. O. Manucharyants and I. P. Zvyagin, *Phys. Status Solidi B* **65**, 665 (1974).
- [48] R. Barrie and P. C. W. Holdsworth, *J. Phys.: Condens. Matter* **1**, 557 (1989).

# Dynamics of Photoexcited Charges in Organic Heterojunctions – Insights from Theory and Simulation

Veljko Janković<sup>1</sup> and Nenad Vukmirović<sup>1</sup>,

<sup>1</sup>Scientific Computing Laboratory, Center for the Study of Complex Systems, Institute of Physics Belgrade, University of Belgrade, Pregrevica 118, 11080 Belgrade, Serbia, email: [nenad.vukmirovic@ipb.ac.rs](mailto:nenad.vukmirovic@ipb.ac.rs)

**Abstract**—The process of exciton splitting at heterojunctions of two organic semiconductors in organic photovoltaic devices was investigated. Theoretical model is based on a Hamiltonian taking into account the effects of electronic coupling, interaction of carriers with external electromagnetic field, Coulomb interaction between electrons and holes and carrier-phonon interaction. Exciton dynamics at subpicosecond timescales was investigated within density matrix theory complemented with the dynamics controlled truncation scheme. Our results indicate that the efficiency of charge separation on subpicosecond timescales is low and that the majority of space-separated charges that occur on these timescales are directly optically generated. Next, we investigated charge separation process on longer timescale by considering it as a sequence of phonon-assisted transitions between electron-hole pair states at the interface. We found that donor exciton separation yields larger than 90% can be achieved in agreement with experimentally observed internal quantum efficiencies close to 100% in most efficient organic photovoltaic devices.

## I. INTRODUCTION

Significant research attention in the last two decades was devoted to the development of photovoltaic devices based on organic semiconductors which offer the advantage of easy and cheap processing. Nevertheless, understanding of the details of the processes that take place in a solar cell device is still limited. It is well understood that binding between an electron and a hole that are created by an incident photon is sufficiently strong to form a bound electron-hole pair (exciton). For this reason, efficient devices can be obtained only if they are composed of (at least) two semiconductors (donor and acceptor) whose band edge alignment is chosen to energetically allow the dissociation of an exciton into an electron in the acceptor and a hole in the donor. A simple picture of photon-to-charge conversion process suggests that it takes place by photon absorption that creates an exciton, exciton diffusion to an interface between the two materials, exciton separation to charges at opposite sides of an interface, and charge transport from an interface to external contacts [1, 2].

To better understand the mechanism of exciton splitting at the interface, several ultrafast spectroscopy studies that probe the dynamics at subpicosecond timescales have been performed in the last decade [3, 4, 5, 6]. These studies

typically register response signals with subpicosecond decay times, which are often interpreted to originate from ultrafast separation of donor excitons into space-separated charges. Nevertheless, the nature of exciton evolution on these timescales and the mechanism of its possible separation remains unclear.

In this presentation, we will review our recent results on exciton dynamics at photoexcited organic heterojunctions [7-9].

## II. METHODS

We model the heterojunction of two organic semiconductors using a microscopic Hamiltonian that takes into account the effects of electronic coupling, interaction of carriers with external electromagnetic field, attractive Coulomb interaction between electrons and holes and interaction of charges with lattice vibrations. We consider a one-dimensional model of a semiconductor in which it is represented using a lattice of sites. Each site provides at least one electron and at least one hole level from which the conduction and valence band of the material are derived. Interaction with phonons is modeled using local Holstein interaction, while electron-hole interaction is modeled in the lowest monopole-monopole approximation with the Ohno interaction potential between the charges.

The parameters of the model – electronic coupling between the sites, site energies, electron-phonon interaction parameters, on-site Coulomb interaction parameter – were chosen to yield values of band gaps, band offsets, bandwidths and exciton binding energies that are representative of typical organic photovoltaic materials.

To model exciton dynamics on ultrafast timescales, we use the density matrix theory along with the dynamics controlled truncation scheme. We consider the case of low excitation field and low carrier densities when it is appropriate to work in the subspace of single electron-hole excitations. The carrier branch of the hierarchy of equations in density matrix approach was truncated by keeping the contributions up to second order in the excitation field. The phonon branch is truncated in such a way to ensure the conservation of particle number and energy [7].

### III. RESULTS

Our results indicate that space-separated charges present around 100 fs after the optical excitation, originate mainly from direct optical generation. There is also a certain degree of donor exciton population transfer but it is not the main source of space-separated charges, see Figs. 1(a) and (b). We also find that such a conclusion is insensitive to the values of model parameters since similar behavior is obtained when material parameters were changed within reasonable limits [8].

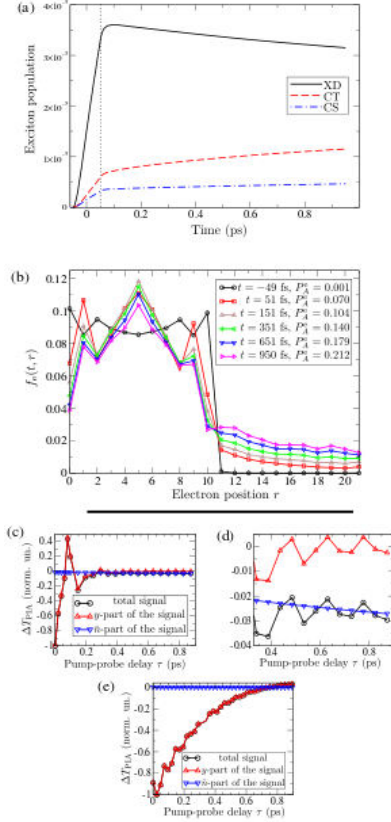


Fig. 1. (a) Dependence of the number of incoherent excitons in donor (XD), charge transfer (CT) and charge separated (CS) states. Optical excitation is centered at photon energy of 1500 meV and lasts from -50 to 50 fs. (b) Time evolution of spatial electron probability distribution. (c) and (d) Simulated photoinduced absorption signal from space separated states after pumping at photon energy of 1500 meV. (e) Simulated PIA signal from donor states after pumping to lowest donor state.

Our analysis indicates that microscopic mechanism responsible for direct optical generation of space-separated charges is resonant mixing between donor states and states of space-separated charges. We find that the efficiency of charge separation at these time scales is quite low, as can be seen for example in Fig. 1(a).

Next, within our theoretical approach we simulate the photoinduced absorption (PIA) signal obtained in ultrafast pump-probe experiments [3]. Our results indicate that for interpretation of PIA signal it is of essential importance to

consider not only the excitonic populations, but also the coherences between the exciton and ground state, as well as the coherences between exciton states. Calculated signals presented in Figs. 1(c)-(e) qualitatively agree with experimental signals obtained in [3]. In the case of excitation well above the lowest donor exciton, PIA signal from space-separated states [labeled as total signal in Figs. 1(c) and (d)] is initially dominated by the contribution of coherences between the exciton and ground state [labeled as y-part of the signal in Figs. 1(c) and (d)], while at longer times the contribution of excitonic populations dominates [labeled as  $\bar{n}$ -part of the signal in Fig. 1(d)]. On the other hand, in the case of excitation to the lowest donor exciton, PIA signal completely originates from the contribution of coherences between the exciton and ground state, see Fig. 1(e). Therefore, such a signal does not originate from ultrafast transfer of donor excitons to states of space-separated charges, but rather from relatively slow conversion from coherences to populations of lowest donor state.

Overall, our simulations at subpicosecond timescale do not show that there is ultrafast charge transfer and cannot explain high internal quantum efficiencies observed in best solar cell devices. For this reason, we investigated charge separation process on longer timescale by considering it as a sequence of phonon-assisted transitions between electron-hole pair states at the interface. Our preliminary results indicate that donor exciton separation yields larger than 90% can be achieved in agreement with experimentally observed internal quantum efficiencies close to 100% in most efficient organic photovoltaic devices.

### ACKNOWLEDGMENT

We gratefully acknowledge the support by the Ministry of Education, Science and Technological Development of the Republic of Serbia (Project No. ON171017) and the European Commission under H2020 project VI-SEEM, Grant No. 675121, as well as the contribution of the COST Action MP1406.

### REFERENCES

- [1] J. L. Bredas, J. E. Norton, J. Cornil, and V. Coropceanu, *Acc. Chem. Res.* vol. 42, pp. 1691-1699 (2009).
- [2] T. M. Clarke and J. R. Durrant, *Chem. Rev.* vol. 110, pp. 6736-6767 (2010).
- [3] G. Grancini, M. Maiuri, D. Fazzi, A. Petrozza, H.-J. Egelhaaf, D. Brida, G. Cerullo, and G. Lanzani, *Nature Mater.* vol. 12, pp. 29-33 (2013).
- [4] A. E. Jaiilaubekov, A. P. Willard, J. R. Tritsch, W.-L. Chan, N. Sai, R. Gearba, L. G. Kaake, K. J. Williams, K. Leung, P. J. Rossky, and X.-Y. Zhu, *Nature Mater.* vol. 12, pp. 66-73 (2013).
- [5] S. Gelinas, A. Rao, A. Kumar, S. L. Smith, A. W. Chin, J. Clark, T. S. van der Poll, G. C. Bazan, and R. H. Friend, *Science* vol. 343, pp. 512-516 (2014).
- [6] A. A. Paraecattil and N. Banerji, *J. Am. Chem. Soc.* 136, pp. 1472-1482 (2014).
- [7] V. Janković and N. Vukmirović, *Phys. Rev. B* vol. 92, p. 235208 (2015).
- [8] V. Janković and N. Vukmirović, *Phys. Rev. B* vol. 95, p. 075308 (2017).
- [9] V. Janković and N. Vukmirović, *J. Phys. Chem. C* vol. 121, pp. 19602-19618 (2017).

START AT	SUBJECT	View All	NUM.	ADD
16:00	<p>Importance of Carrier Delocalization and Disorder for Incoherent Charge Separation at Organic Bilayers</p> <p>Authors : Veljko Jankovic, Nenad Vukmirovic Affiliations : Scientific Computing Laboratory, Center for the Study of Complex Systems, Institute of Physics Belgrade, University of Belgrade, Pregrevica 118, 11080 Belgrade, Serbia; Scientific Computing Laboratory, Center for the Study of Complex Systems, Institute of Physics Belgrade, University of Belgrade, Pregrevica 118, 11080 Belgrade, Serbia</p> <p>Resume : Recent studies [1,2,3] have challenged the view that free-charge generation in all-organic blends predominantly occurs on ultrafast time scales via delocalized hot charge transfer states. However, the mechanisms behind very efficient and weakly electric field-dependent charge separation on longer time scales remain highly debated. We investigate field-dependent charge separation in a one-dimensional lattice model of an all-organic bilayer. Charge separation is considered as a sequence of phonon-assisted transitions among eigenstates of an electron-hole pair supported by the interface. We find that the yield of charge separation starting from the strongly bound charge transfer state is weakly field-dependent and above 50% even at zero electric field. Moderate diagonal static disorder and good charge delocalization increase the yield by strengthening the transitions from the initial state toward long-lived states with increased electron-hole separation, from which further separation proceeds without kinetic obstacles. We also observe almost field-independent (at low to moderate fields) charge separation starting from a donor exciton state, while the yield varies from around 40% (from the lowest-energy donor state) to around 80% (from states energetically well above the lowest-energy donor state). [1] Vandewal et al., Nat. Mater. 13, 63 (2013). [2] Jankovic and Vukmirovic, Phys. Rev. B 95, 075308 (2017). [3] Grupp et al., J. Phys. Chem. Lett. 8, 4858 (2017).</p>		J.12.7	

## Origin of Space-separated Charges in Photoexcited Organic Heterojunctions on Subpicosecond Time Scales

Veljko Janković and Nenad Vukmirović

*Scientific Computing Laboratory, Centre for the Study of Complex Systems, Institute of Physics Belgrade, University of Belgrade, Pregrevica 118, 11080 Belgrade, Serbia*

e-mail: veljko.jankovic@ipb.ac.rs

The promise of economically viable and environmentally friendly conversion of sunlight into electrical energy has driven vigorous and interdisciplinary research on donor/acceptor heterojunction organic photovoltaics. However, the actual mechanism of the emergence of free charges on subpicosecond (<100-fs) time scales following the excitation of a heterojunction remains elusive.

We investigate subpicosecond exciton dynamics in the lattice model of an all-organic heterojunction. Exciton generation by means of a photoexcitation, exciton dissociation, and further charge separation are treated on equal footing and on a fully quantum level using the density matrix formalism combined with the dynamics controlled truncation scheme [1]. Our results indicate that the space-separated charges appearing on <100-fs time scales following the photoexcitation are predominantly directly optically generated [2], in contrast to the usual viewpoint that they originate from ultrafast population transfer from initially generated excitons in the donor material. The space-separated states acquire nonzero oscillator strengths from donor excitons thanks to the strong resonant mixing between these two groups of exciton states. The results of ultrafast pump-probe experiments are commonly interpreted in terms of exciton populations only. Our theoretical insights into the ultrafast pump-probe spectroscopy highlight the importance of coherences, which cannot be disregarded on such short time scales, in the interpretation of pump-probe spectra [2].

### REFERENCES

- [1] V. Janković and N. Vukmirović, Phys. Rev. B 92, 235208 (2015).
- [2] V. Janković and N. Vukmirović, Phys. Rev. B 95, 075308 (2017).



The Abdus Salam  
**International Centre  
for Theoretical Physics**



**Workshop on  
Spectroscopy and Dynamics of  
Photoinduced Electronic Excitations**

**8 - 12 May 2017**

**TO WHOM IT MAY CONCERN**

This is to certify that

**Veljko Jankovic**

has presented a poster entitled

**Origin of Space-separated Charges in Photoexcited Organic  
Heterojunctions on Ultrafast Time Scales**

at the Poster Session held during the Workshop on Spectroscopy and Dynamics of Photoinduced Electronic Excitations held at ICTP, Trieste, Italy, from 8 to 12 May 2017.

A handwritten signature in blue ink that reads 'R. Gebauer'.

**Ralph Gebauer  
Workshop Organizer**

Trieste, 11 May 2017



The Abdus Salam  
**International Centre  
for Theoretical Physics**



MAX-PLANCK-GESELLSCHAFT



This is to certify that

**Veljko JANKOVIC**

participated in and completed the  
**Workshop on  
Spectroscopy and Dynamics of  
Photoinduced Electronic Excitations**

Co-sponsors:  
The Max Planck Society, Psi-K

8 - 12 May 2017  
ICTP, Trieste, Italy

Organizers:  
Ralph Gebauer (ICTP),  
Angel Rubio (MPI for the Structure and Dynamics of Matter),  
Nicola Seriani (ICTP)

Fernando Quevedo, Director

---

## Poster

---

**Title:** Origin of Space-separated Charges in Photoexcited Organic Heterojunctions on Ultrafast Time Scales

**Abstract:** The promise of economically viable and environmentally friendly conversion of sunlight into electrical energy has driven vigorous and interdisciplinary research on donor/acceptor heterojunction organic photovoltaics. However, the actual mechanism of the emergence of free charges on subpicosecond (<100-fs) time scales following the excitation of a heterojunction remains elusive. We investigate subpicosecond exciton dynamics in the lattice model of an all-organic heterojunction. Exciton generation by means of a photoexcitation, exciton dissociation, and further charge separation are treated on equal footing and on a fully quantum level using the density matrix formalism combined with the dynamics controlled truncation scheme [1]. Our results indicate that the space-separated charges appearing on <100-fs time scales following the photoexcitation are predominantly directly optically generated [2], in contrast to the usual viewpoint that they originate from ultrafast population transfer from initially generated excitons in the donor material. The space-separated states acquire nonzero oscillator strengths from donor excitons thanks to the strong resonant mixing between these two groups of exciton states. The results of ultrafast pump-probe experiments are commonly interpreted in terms of exciton populations only. Our theoretical insights into the ultrafast pump-probe spectroscopy highlight the importance of coherences, which cannot be disregarded on such short time scales, in the interpretation of pump-probe spectra [2].

[1] V. Janković and N. Vukmirović, Phys. Rev. B 92, 235208 (2015).

[2] V. Janković and N. Vukmirović, Phys. Rev. B 95, 075308 (2017).

---

## Research Experience

---

**Research experience:** Since the beginning of my doctoral programme, I have been focused on the theory and modelling of the ultrafast dynamics of electronic excitations in photoexcited semiconductors. I am particularly interested in the ultrafast exciton dynamics in organic semiconductors, which hold promise for applications in organic solar cells. Using relatively simple, but physically grounded models, I have investigated the exciton formation in the model of a neat organic semiconductor and the exciton dissociation in the model of an all-organic heterointerface. During my MSc studies, I studied the nonequilibrium electronic transport in systems with localized electronic states under the influence of terahertz fields.

**Gordon Research Conferences: Participation Certificate****From:** "Gordon Research Conferences" <agrasso@grc.org>**To:** [veljko@ipb.ac.rs](mailto:veljko@ipb.ac.rs)**Date:** 2016-06-11 07:01

[visit us on the web at http://www.grc.org](http://www.grc.org)

**Certificate of Participation**

06/11/2016

Veljko Jankovic  
Institute of Physics Belgrade  
Pregrevica 118  
Belgrade, 11080  
Serbia

***This is a certificate of participation for:***

Conference: Electronic Processes in Organic Materials  
Dates: 06/05/2016 - 06/10/2016  
Location: Renaissance Tuscany Il Ciocco in Lucca (Barga) Italy

This letter certifies your participation as a Poster Presenter at the Gordon Research Conference on Electronic Processes in Organic Materials held 06/05/2016 - 06/10/2016 at Renaissance Tuscany Il Ciocco in Lucca (Barga) Italy.

Presented poster titled: TBD Exciton Formation and Relaxation Dynamics in Photoexcited Organic Semiconductors and Their Heterojunctions: Numerical Study

Nancy Ryan Gray, PhD, President and Chief Executive Officer  
Gordon Research Conferences

A handwritten signature in black ink, appearing to read 'Nancy Ryan Gray', is positioned below the typed name.

---

*\*Please notify us if you are not the intended recipient of this email.*

Follow GRC: [Facebook](#) | [Twitter](#)

This email message from Gordon Research Conferences is intended only for the individual or entity to which it is addressed. This email may contain confidential or privileged information. If you are not the intended recipient, any disclosure, copying, use, or distribution of the information included in this message and any attachments is prohibited. If you have received this communication in error, please notify us by reply e-mail and immediately and permanently delete this message and any attachments. Thank you.

## Gordon Research Seminar 2016

### Exciton Formation and Relaxation Dynamics in Photoexcited Organic Semiconductors and Organic Semiconductor Heterojunctions: Numerical Study

Veljko Jankovic and Nenad Vukmirovic

*Scientific Computing Laboratory, Institute of Physics Belgrade, University of Belgrade, Pregrevica 118, 11080 Belgrade, Serbia*

Recent years have seen vigorous and interdisciplinary research activity in the field of organic photovoltaics with the aim of deeper understanding of ultrafast processes which govern their operation. We have investigated the dynamics of exciton formation and relaxation on a picosecond time scale following a pulsed photoexcitation of a semiconductor [1]. The study is conducted on the two-band semiconductor Hamiltonian, which includes relevant physical effects in the system, employing the density matrix theory combined with the dynamics controlled truncation scheme. We truncate the phonon branch of the resulting hierarchy of equations and propose the form of coupling among single-phonon-assisted and higher-order phonon-assisted density matrices so as to ensure the energy and particle-number conservation in a system without external fields. Time scales relevant for the exciton formation and relaxation processes are determined from numerical investigations performed on a one-dimensional model for the values of model parameters representative of a typical organic semiconductor and organic semiconductor heterojunction. We find that in a neat organic semiconductor the phonon-mediated conversion from coherent to incoherent excitonic populations happens on a 50 fs time scale, followed by the formation of bound excitons on a several-hundred-femtosecond time scale and their subsequent relaxation and equilibration which takes at least several picoseconds. At a heterojunction of two organic semiconductors, we find that the strong (resonant) mixing between interfacial excitonic states and excitonic states in neat materials, as well as proper accounting for interband excitonic coherences, are critical for the accurate description of charge transfer from the donor to the acceptor and subsequent charge separation. Time scales that emerge from our numerical study are consistent with recent experimental reports on the exciton formation and relaxation in conjugated polymer-based materials. We believe that the insights obtained from our study of a typical organic/organic heterojunction may contribute to more profound understanding of fundamental OPV physics.

#### References

[1] V. Jankovic and N. Vukmirovic, *Phys. Rev. B* **92**, 235208 (2015)

## ID 68 - Poster

### Nonequilibrium Electrical Transport in Materials with Localized Electronic States

V. Jankovic<sup>1</sup>, \*N. Vukmirovic<sup>1</sup>

<sup>1</sup>Institute of Physics Belgrade, Scientific Computing Laboratory, Belgrade, Serbia

A broad range of disordered materials contain electronic states that are spatially well localized. In this work we studied the electrical response of such materials to external terahertz electromagnetic field [1]. We obtained expressions for nonequilibrium terahertz conductivity of a material with localized electronic states and weak electron-phonon or electron-impurity interaction. The expression is valid for any nonequilibrium state of the electronic subsystem prior to the action of external field. It gives nonequilibrium optical conductivity in terms of microscopic material parameters and contains both coherences and populations of the initial electronic subsystem's density matrix. Particularly, in the case of incoherent nonequilibrium state of the electronic subsystem, the optical conductivity is entirely expressed in terms of the positions of electronic states, their nonequilibrium populations, and Fermi's golden rule transition probabilities between the states. The same mathematical form of the expression is valid both in the case of electron-phonon and electron-impurity interaction. Moreover, our result for the nonequilibrium optical conductivity has the same form as the expressions previously obtained for the case of equilibrium. Our results are expected to be valid at sufficiently high frequencies, such that the period of the external field is much smaller than the carrier relaxation time. We apply the derived expressions to two model systems, a simple one-dimensional Gaussian disorder model and the model of a realistic three-dimensional organic polymer material obtained using previously developed multiscale methodology [2]. We note that the simple one-dimensional model captures the essential features of the mobility spectrum of a more realistic system. Furthermore, our simulations of the polymer material yield the same order of magnitude of the terahertz mobility as previously reported in experiments.

[1] V. Janković and N. Vukmirović, Phys. Rev. B 90, 224201 (2014).

[2] N. Vukmirović and L.-W. Wang, Nano Lett. 9, 3996 (2009).

# Nonequilibrium High-frequency Conductivity in Materials with Localized Electronic States

Veljko Janković and Nenad Vukmirović

*<sup>a</sup>Scientific Computing Laboratory, Institute of Physics Belgrade, University of Belgrade, Pregrevica 118, 11080 Belgrade, Serbia*

**Abstract.** A broad range of disordered materials contain electronic states that are spatially well localized. These include amorphous inorganic semiconductors, inorganic crystals doped with randomly positioned impurities and organic semiconductors based on conjugated polymers or small molecules. Usual approaches to simulation of ac conductivity of these materials rely on Kubo's formula which expresses the ac conductivity in terms of the mean square displacement of a diffusing carrier. Such approaches therefore assume that carriers are in equilibrium and that they are only slightly perturbed by external alternating electric field. However, in many realistic situations, the carriers are not in equilibrium; a typical example concerns the carriers created by external optical excitation across the band gap of a semiconductor.

In this work we obtain the expression for the optical conductivity in a material with localized electronic states and weak electron-phonon or electron-impurity interaction [1]. The expression is valid for any nonequilibrium state of the electronic subsystem prior to the action of electric field. It gives nonequilibrium optical conductivity in terms of microscopic material parameters and contains both coherences and populations of the initial electronic subsystem's density matrix. Particularly, in the case of incoherent nonequilibrium state of the electronic subsystem, the optical conductivity is entirely expressed in terms of the positions of electronic states, their nonequilibrium populations, and Fermi's golden rule transition probabilities between the states. The same mathematical form of the expression is valid both in the case of electron-phonon and electron-impurity interaction. Moreover, our result for the nonequilibrium optical conductivity has the same form as the expressions previously obtained for the case of equilibrium. The derivation was performed by expanding the general expression for ac conductivity in powers of small electron-phonon or electron-impurity interaction parameter. Our results are expected to be valid at sufficiently high frequencies, such that the period of the electric field is much smaller than the carrier relaxation time. We apply the derived expressions to two model systems, a simple one-dimensional Gaussian disorder model and the model of a realistic three-dimensional organic polymer material obtained using previously developed multiscale methodology [2]. We note that the simple one-dimensional model captures the essential features of the mobility spectrum of a more realistic system. Furthermore, our simulations of the polymer material yield the same order of magnitude of the terahertz mobility as previously reported in experiments.

## REFERENCES

1. Janković V., and Vukmirović N., Phys. Rev. B 90, 224201 (2014).
2. Vukmirović N., and Wang L. W., Nano Lett. 9, 3996 (2009).

## Nonequilibrium Terahertz Conductivity in Systems with Localized Electronic States

Veljko Janković and Nenad Vukmirović

Scientific Computing Laboratory, Institute of Physics Belgrade, University of Belgrade, Pregrevica 118,  
11080 Belgrade, Serbia  
veljko.jankovic@ipb.ac.rs

A broad range of disordered materials contain electronic states that are spatially well localized. These include amorphous inorganic semiconductors, inorganic crystals doped with randomly positioned impurities and organic semiconductors based on conjugated polymers or small molecules. Usual approaches to simulation of ac conductivity rely on Kubo's formula which expresses the ac conductivity in terms of the mean square displacement of a diffusing carrier. Such approaches therefore assume that carriers are in equilibrium and that they are only slightly perturbed by external alternating electric field. However, in many realistic situations, the carriers are not in equilibrium; a typical example concerns the carriers created by external optical excitation across the band gap of a semiconductor.

In this work we obtain the expression for the optical conductivity in a material with localized electronic states and weak electron-phonon or electron-impurity interaction [1]. The expression is valid for any nonequilibrium state of the electronic subsystem prior to the action of electric field. Particularly, in the case of incoherent nonequilibrium state of the electronic subsystem, the optical conductivity is entirely expressed in terms of the positions of electronic states, their nonequilibrium populations, and Fermi's golden rule transition probabilities between the states. The same mathematical form of the expression is valid both in the case of electron-phonon and electron-impurity interaction. Moreover, our result for the nonequilibrium optical conductivity has the same form as the expressions previously obtained for the case of equilibrium. The derivation was performed by expanding the general expression for ac conductivity in powers of small electron-phonon or electron-impurity interaction parameter. Our results are expected to be valid at sufficiently high frequencies, such that the period of the electric field is much smaller than the carrier relaxation time. We apply the derived expressions to two model systems, a simple one-dimensional Gaussian disorder model and the model of a realistic three-dimensional organic polymer material obtained using previously developed multiscale methodology [2]. We note that the simple one-dimensional model captures the essential features of the mobility spectrum of a more realistic system. Furthermore, our simulations of the polymer material yield the same order of magnitude of the terahertz mobility as previously reported in experiments.

### References

- [1] V. Janković and N. Vukmirović, Phys. Rev. B **90**, 224201 (2014).
- [2] N. Vukmirović and L.-W. Wang, Nano Lett. **9**, 3996 (2009).

# Nonequilibrium terahertz conductivity in materials with localized electronic states

Veljko Janković<sup>1</sup> and Nenad Vukmirović<sup>1</sup>

<sup>1</sup>*Scientific Computing Laboratory, Institute of Physics Belgrade, University of Belgrade, Pregrevica 118, 11080 Belgrade, Serbia*  
email: veljko.jankovic@ipb.ac.rs

A broad range of disordered materials contain electronic states that are spatially well localized. In this work [1] we studied the electrical response of such materials to external terahertz electromagnetic field. We obtained expressions for nonequilibrium terahertz conductivity of a material with localized electronic states and weak electron-phonon or electron-impurity interaction. The expression is valid for any nonequilibrium state of the electronic subsystem prior to the action of external field. It gives nonequilibrium optical conductivity in terms of microscopic material parameters and contains both coherences and populations of the initial electronic subsystem's density matrix. Particularly, in the case of incoherent nonequilibrium state of the electronic subsystem, the optical conductivity is entirely expressed in terms of the positions of electronic states, their nonequilibrium populations, and Fermi's golden rule transition probabilities between the states. The same mathematical form of the expression is valid both in the case of electron-phonon and electron-impurity interaction. Moreover, our result for the nonequilibrium optical conductivity has the same form as the expressions previously obtained for the case of equilibrium. Our results are expected to be valid at sufficiently high frequencies, such that the period of the external field is much smaller than the carrier relaxation time. We apply the derived expressions to two model systems, a simple one-dimensional Gaussian disorder model and the model of a realistic three-dimensional organic polymer material obtained using previously developed multiscale methodology [2]. We note that the simple one-dimensional model captures the essential features of the mobility spectrum of a more realistic system. Furthermore, our simulations of the polymer material yield the same order of magnitude of the terahertz mobility as previously reported in experiments.

## REFERENCES

- [1] V. Janković and N. Vukmirović, *Phys. Rev. B* **90**, 224201 (2014).
- [2] N. Vukmirović and L.-W. Wang, *Nano Lett.* **9**, 3996 (2009).